Calibration of SNO for the Detection of ^{8}B Neutrinos

by

Richard James Ford

A thesis submitted to the Department of Physics
in conformity with the requirements for
the degree of Doctor of Philosophy

Queen's University
Kingston, Ontario, Canada
December, 1998

To my parents

Abstract

The Sudbury Neutrino Observatory (SNO) is a second generation water Čerenkov detector using 1000 tonnes of heavy water to study neutrino astrophysics. Using deuterium neutrino reactions, SNO will measure the flux and energy spectrum of solar electron neutrinos, and will measure the flavour-blind flux of neutrinos.

A nitrogen/multi-dye laser diffuser ball has been designed and installed in SNO for calibration of the electronics, photomultiplier tubes (PMTs) and optical parameters. The laser provides pulsed radiation at 337.1 nm with a 600 psec width and pulse rate up to 50 Hz. The laser can be used directly or as a pump for one of four dye laser resonators, which provides five wavelength selections from $337 - 500$ nm. The light is delivered to a pseudo-isotropic diffuser ball (the laserball) by a $100\,\mu$m UV-VIS fibre bundle with less than 1 nsec dispersion at 337 nm. The laserball can be deployed throughout the detector with the rope manipulator system. The laserball output is adjustable from 0.01 to 1000 photo-electrons (PE) and has a pulsewidth of 0.90 nsec at 386 nm and 1.18 nsec at 337.1 nm.

A method has been developed for measuring the optical attenuation and scattering in SNO using the laserball and single photo-electron (SPE) PMT time histograms. At SPE intensity the nanosecond PMT timing can be used to separate direct and scattered light, and the extinction coefficients determined using varying path lengths from the source.

A calibration function has been developed that accounts for the position and direction dependence of the response for electrons and gamma rays. The calibration function uses simplified or parameterized distributions for the Čerenkov output and detector geometry. The function is fast enough to be built in to neutrino spectrum analysis and can be used to evaluate the uncertainties in the position response.

The laserball system has been tested and used to provide a PMT and electronics calibration of the detector for analysis of the airfill commissioning runs. The electronics channels were calibrated for charge pedestals and slopes, time offsets and slopes and discriminator walk (slewing). The PMT occupancies were measured and a method was developed for measuring the mean SPE gain. Finally, event reconstruction was studied for the airfill data, and a time biased reconstruction algorithm was created for cutting flashing PMT events.

Co-authorship

The work, results and conclusions presented in this thesis are original except for most of chapters 1 and 2 and parts of sections 3.1 and 3.2. In section 3.2 I have made use of the deuterium cross-section computer code made available by J. Bahcall. This is referenced and accredited in the text.

The Sudbury Neutrino Observatory is a large collaboration, and the construction of SNO is the result of efforts by over a hundred people. The ideas, construction, analysis and results discussed in the body of the thesis are the work of the author with the following exceptions and notes:

SNOMAN is the primary SNO analysis and Monte Carlo package. The software was developed by the Oxford University group and created by many people across the collaboration, including the author.

The Queen's Monte Carlo was written by Peter Skensved (Queen's).

The laserball system presented in chapter 4 was designed and fabricated by the author. The rope manipulator and umbilical system was produced by the calibration group at Queen's University.

Sean White (Queen's) performed some of the later measurements of fibre-optic dispersion.

Bryce Moffat (Queen's) helped with the production version of the diffuser ball.

The SNO electronics was designed at the University of Pennslyvania, and they have independently produced an electronics calibration.

The SNO event display program, used for the graphical and data acquisition part of the optical on-line monitoring tool, is written by Phil Harvey (Queen's). Phil Harvey and Tom Radcliffe (Queen's) wrote most of the source manipulator control code.

Acknowledgements

I have benefitted greatly from the advice and guidance of my supervisor Professor Aksel Hallin, who usually let me do things my way, but was always available for help and encouragement. I also thank Professors Art McDonald, Hay-Boon Mak, Hamish Leslie, Tom Radcliffe, Emmanuel Bonvin and Peter Skensved for useful discussions, support and other help. I also thank Hugh Evans, Barry Robertson, Fraser Duncan and Hardy Seifert for co-ordination and help with on-site installations.

Fellow graduate students Chris Jillings, Andre Hamer, Bryce Moffat, Mark Boulay, Matt Dayon, Ed Korpach and Lorne Erhardt helped out in various ways, and otherwise made Queen's a fun place to work.

Chuck Hearn's wisdom in all things mechanical made possible much of the hardware in this thesis (and in SNO). The help of Bob Stevenson and Alvin Bell with electronics is greatly appreciated. Thanks to Phil Harvey for his event display program, the manipulator control code, and various computer help over the years. I would also like to thank Alison Cunningham, Lisa Neumann and Margaret Morris from the office for various help with travel, purchasing and bureaucracy.

I also thank collaboration members for useful discussions; especially Dave Wark, Bill Frati, Josh Klein, Steve Biller and Nick West.

The support from my parents and family is especially appreciated. Finally I thank distant friends Tig Starr and Steve Urh for fun diversions.

Contents

List of Figures

List of Tables

List of Acronyms

AC	Adsorption column
ADC	Analogue to digital converter
AV	Acrylic vessel in SNO containing the D_2O
Borexino	Liquid scintillator neutrino detector (Gran Sasso)
CC	Charged current
CCC	PMT number based on crate/card/channel
CERNLIB	CERN software library
CFD	Constant fraction discriminator
CKM	Cabibbo-Kobayashi-Maskawa weak mixing matrix for quarks
CMA	Control, monitors and alarms system
CMOS	Complementary Metal-Oxide Semiconductor
CNO	Solar carbon-nitrogen-oxygen fusion cycle
CPU	Central processing unit
CTC	Crate trigger card
CVC	Conserved vector current
CVD	Chemical vapour deposition
D_2O	Heavy water
DAC	Digit to analogue converter
DAQ	Data acquisition system
DB	Daughter board
DPE	Double photo-electron
D-T	Deuteron-tritium accelerator (neutron generator)
DTiO	Deuterated titanium oxide
ECA	Electronics calibration SNOMAN processor
ECL	Emitter-Collector Logic
eCPU	Embedded CPU
EDTA	Ethylene Diamine Tetraacetic Acid
EGS4	Electron-gamma shower particle transport package
ES	Electron scattering
ESUM	Charge sum trigger signal
EVB	Event builder
FEC	Front end card
FPGA	Field programmable gate array
FWHM	Full width at half maximum

GALLEX	Gallium experiment (Gran Sasso)
GEANT	CERNLIB Monte Carlo code system
GPS	Global positioning system
GT	Global trigger
GT	Gamow-Teller
H_2O	Normal (light) water
HEPDB	CERNILB database management system
Homestake	Homestake mine chlorine neutrino experiment
HV	High voltage
HX	Heat exchanger
INCO	International Nickel Company
IR	Infrared electromagnetic radiation (light)
LED	Light emitting diode
LGT	Low gain PMT
LMA	large mixing angle
MB	Mother board
MC	Monte Carlo
MCA	Multi-channel analyser
MCNP	Monte Carlo code for Neutron and Photon transport
MDPM	Macintosh dual port memory
MPE	Multiple photo-electron
MSW	Mikheyev, Smirnov, Wolfenstein matter oscillation effect
MTC/A	Master trigger card (analogue)
MTC/D	Master trigger card (digital)
MWE	Mean water equivalent
NC	Neutral current
NCDs	Neutral current detectors
NFIT	Number of PMTs fit in an event
NHIT	Number of PMTs fired in an event
OCA	Optical calibration SNOMAN processor
OWL	Outward looking PMT
pC	Pico-Coulomb (unit of charge)
PCA	PMT calibration SNOMAN processor
PE	Photo-electrons
PDG	Process degasser
PIN	Intrinsic layer between p and n type semiconductors.
PMT	Photomultiplier tube
PMTIC	PMT HV interface card
pp	Solar proton-proton fusion cycle
PSUP	PMT support structure
QE	Quantum efficiency
QHL	High gain long integrate charge sample

QHS	High gain short integrate charge sample
QLX	Low gain long integrate charge sample
QMC	Queen's Monte Carlo
QvT	Scatter plot of PMT charge versus time
QUSN7	SNO custom CMOS electronics chip
RF	Radio frequency radiation
RMS	Root mean square
RO	Reverse osmosis unit
ROV	Remote submersible vehicle
SAGE	Soviet American gallium experiment
SBC	Single board computer
SDPM	SUN dual port memory
SK	Super-Kamiokande neutrino detector
SM	Standard model of particle physics
SMA	Small mixing angle
SN	Supernova
SNO	Sudbury Neutrino Observatory
SNOD	SNO discriminator chip
SNODB	SNO database implemented using HEPDB
SNOINT	SNO integrator chip
SNOMAN	SNO Monte Carlo and analysis program
SNP	Solar neutrino problem
SNU	Solar neutrino unit
SPE	Single photo-electron
SSM	Standard solar model
STR	SNO technical report
TAC	Time to amplitude converter
TCP/IP	Transmission Control Protocol / Internet Protocol
TDC	Time to digital converter
TTS	Transit time spread (FWHM)
TUB	Trigger utility board
UFR	Ultra-filtration unit
U/G	Underground
UV	Ultraviolet electromagnetic radiation (light)
UVA	UV absorbing
UVT	UV transmitting
VME	Virtual Machine Extension BUS
WIMP	Weakly interacting massive particle
XL1/XL2	Custom VME translation cards
XSNOED	SNO event display program
ZDAB	SNO ZEBRA bank for raw PMT event data
ZEBRA	CERNLIBs FORTRAN memory management package

Chapter 1

Introduction

The Sudbury Neutrino Observatory (SNO) [1, 2] is a second generation Čerenkov detector using 1000 tonnes of heavy water as a target to study neutrino astrophysics. Located 6800 feet underground, SNO is designed to measure the flux and energy spectrum of solar electron neutrinos, and the total flux of all neutrino flavours emitted from the sun. The deuterium neutrino reactions with heavy water permit a solar model independent test of neutrino oscillation hypotheses, which attempt to explain the current global solar neutrino deficit [3, 9, 10]. Construction of SNO was completed in the spring of 1998 and the detector is now being filled with water.

This thesis defines the procedure for calibration of the SNO detector. Calibration is essential, since we must determine the fraction of all electron neutrinos that can be observed above a detector threshold. Uncertainties and variations in the shape of the detector response function will translate into significant uncertainties in the flux of electron neutrinos. I describe the nitrogen/dye laser system that I have designed, built and commissioned in the SNO detector. This is the primary source for electronics and PMT calibrations, and for the determination of spatial variations within the detector. I then describe algorithms developed for optical calibration, and a response function technique that will allow us to correct the fitted data for the detector spatial variations. The laser light source has been tested by providing a complete electronics and PMT calibration, and investigating the optics of the empty detector. The PMT calibration was then used to study event reconstruction in airfill and the efficiency for cutting flashing PMT events.

The earth's proximity to the sun allows the sun to be investigated in detail not possible for other stars. Since the sun is a typical main sequence star this affords the opportunity for rigorous testing of the predictions from models of stellar evolution, and, perhaps, extensions to the standard electro-weak particle model. Also the sun may be used to infer the initial chemical composition of the local interstellar medium. Eddington first proposed that the solar energy source must be nuclear in the 1920's; and in the late 1930's Gamow, Weizsacher, Bethe and others developed the CNO and *pp* fusion reaction cycles [12]. However, testing the details of these models is difficult since the solar luminosity and emission spectrum depend mainly on the solar mass, radiation opacities, and solar surface physics, but not on the nuclear cross-sections or on details of the solar internal structure. While the outer layers of the sun are quite complex due to turbulent convective motions and differential rotations, the inner core is predicted to obey a simple equation of state in quasi-static equilibrium. Examination of the solar interior requires probing techniques such as helioseismology and the detection of solar neutrinos. Neutrino detection, in particular, is very valuable since neutrinos emerge from the solar interior without interaction, thus providing a deep probe into the regions of emission.

Models of the solar interior have been refined over the last 30 years and now make quite precise predictions for the flux and energy spectrum of solar neutrinos [13–19]. However, also in this period the Homestake chlorine neutrino detector has detected only 30% of the expected neutrino flux [28]. More recently, direct counting experiments using water [29, 30], and gallium radiochemical detectors [33, 34] have confirmed the neutrino shortfall. The experiments together have now established that the shortfall is dependent on the detector energy spectrum sensitivity, so that the combined data present a possible distortion of the neutrino spectral shape. This is called the solar neutrino problem (SNP), and it now appears likely that the solution of the SNP requires physics beyond the standard model of particle physics (see Bahcall [3, 4]).

Solar neutrinos may also provide opportunity for measurements of neutrino properties. Neutrinos are weakly interacting spin-$\frac{1}{2}$ particles produced in nuclear beta decay. In the standard model of particle physics there are three neutrino generations (called flavours: electron-, muon- and tau-) which are all massless, electrically neutral and have zero magnetic moment. A possible extension to the standard model has massive neutrinos that are not simultaneously diagonalized with the flavour states, so that the propagated neutrino states contain mixed flavours [6]. Then the flavour states would oscillate in flight, similar to kaon oscillations. A possible consequence of neutrino oscillations is resonantly enhanced oscillations within the dense solar core (the MSW effect [36]). The MSW effect can explain the neutrino deficit energy dependence, and the measured spectral distortions can provide a measurement of the corresponding neutrino Δm^2 and mixing angle. Other proposed extensions including a neutrino magnetic moment, neutrino decay, or an isolated right handed helicity neutrino state (called sterile neutrinos) have also been considered [3, 8].

Since the neutrino mass must certainly be small,[1] the sun-earth system might provide a laboratory for precision neutrino measurements. The sun provides the large fluxes and low energies not possible in terrestrial accelerator labs, and the earth sun distance allows for quantum mechanical mixing (the so-called long baseline experiment). A neutrino mass would have large implications for the large scale structure of the universe, where massive neutrinos are a candidate for hot dark matter.[2]

Finally, detection of neutrinos from the supernova 1987A gave life to a new field of neutrino astronomy. Measurement of the arrival times of the supernova neutrinos in Kamiokande and IMB provided an independent limit of the neutrino mass and the first neutrinos observed from stellar collapse [8]. The experimental program at SNO includes a supernovae watch, and the detection of atmospheric neutrinos and ultra-high energy neutrinos (supernova relics).

This chapter provides the background material for the thesis. The standard solar model is presented, and previous solar neutrino experimental results are described. This leads to the solar neutrino problem (SNP) which is discussed along with possible astrophysical and particle physics solutions. The SNO detector is then introduced as

[1] The neutrino mass is known to be small due to tritium beta decay endpoint experiments and accelerator oscillation searches (present limit $m_{\nu_{e(1)}} < 15\,\mathrm{eV}$ [5]). See Boehm and Vogel [6].

[2] From observation of large galaxy clusters and distant type 1a supernovae astronomers now seem to favour a low value (about $70\,\mathrm{km\,s^{-1}Mpc^{-1}}$) for the Hubble constant H_0 (with Ω_m about 0.3) where a massive neutrino may still account for the non-luminous mass [7].

the experiment that can uncover the physics behind the solar neutrino problem.

1.1 Standard Solar Model

The standard solar model (SSM) is any solar model using "standard model" physics, the best nuclear cross-section data, measured solar observables, and a common set of assumptions to iterate the equation of state from an initial primordial composition to the present age. We use the SSM of Bahcall and Pinsonneault [17, 18] as the standard for comparison and discussion. The usual assumptions are:

1. The sun is spherically symmetric, has no mass loss or accretion during the lifetime, and no change in angular momentum.

2. The sun is in hydrostatic equilibrium, that is, the gas and radiation pressure is balanced by gravity.

3. Energy within the sun is transported only by electromagnetic radiation or convection.

4. The elemental composition is modified only by nuclear reactions, and the pre-main sequence star is turbulently mixed and homogeneous.

Recent upgrades to the standard solar models have slightly relaxed some of these assumptions, for example by adding gravitational diffusion, pre-main sequence evolution or some turbulent mixing [15, 18, 19]. Non-standard solar models have been considered to explain the SNP by postulating unexpected conditions such as unstable core oscillations, low initial metalicity, various turbulent mixing scenarios or new weakly interacting particles (WIMPS) [3].

The sun is a typical main sequence star that is fueled by the nuclear fusion of hydrogen into helium. The main solar measured parameters are listed in table 1.1. As a medium mass star most of the solar luminosity (about 98.5%) is derived from the *pp* fusion sequence (see figure 1.1), with the remainder from the CNO cycle reactions (figure 1.2). The *pp* chain can represented by the net reaction

$$4p + e^- \longrightarrow \alpha + e^+ + 2\nu_e + 26.73\,\mathrm{MeV} \tag{1.1}$$

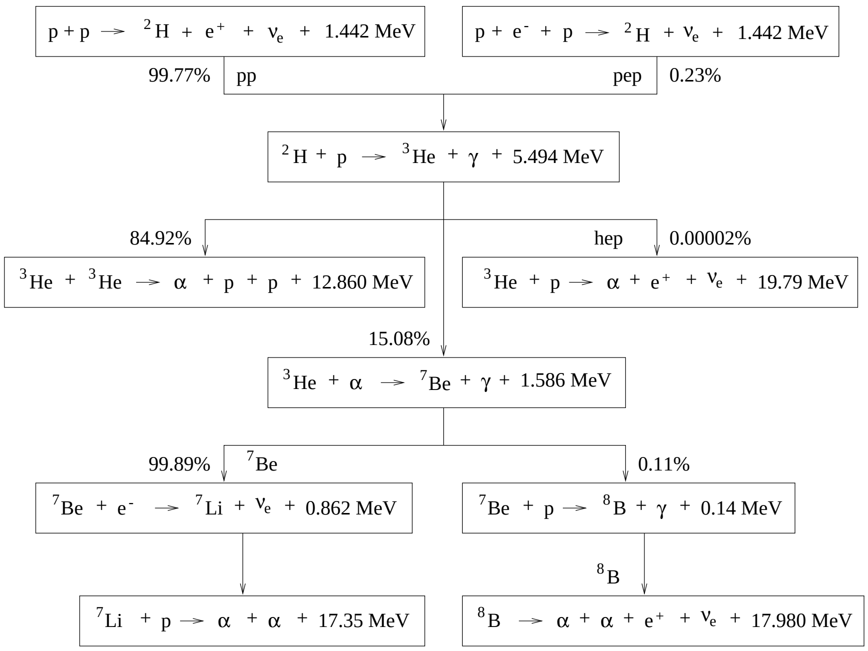

Figure 1.1: The *pp* chain solar fusion cycle with the *pp*, *pep*, *hep*, ^{7}Be and ^{8}B neutrino producing reactions identified. Termination fractions are from Bahcall [3].

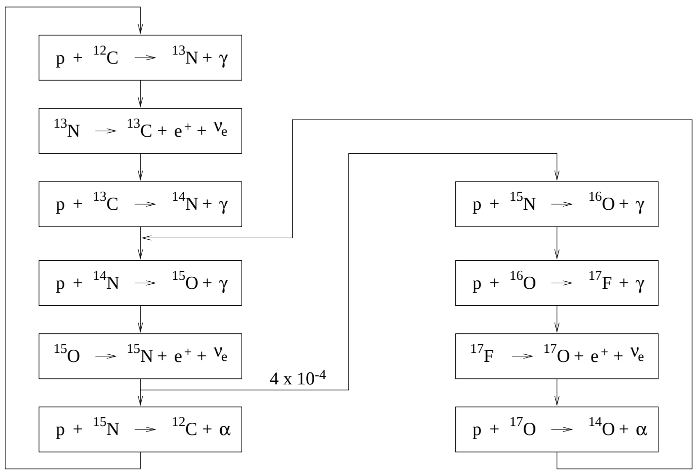

Figure 1.2: The CNO solar fusion cycle [3].

where about 2% (0.6 MeV) of the energy is carried away by the neutrinos. While the solar core temperature is high, the thermal energy of the gas plasma is small compared to the Coulomb barrier for fusion. Hydrostatic equilibrium and the equation of state provides a stable pressure well below the Coulomb repulsion so that the sun evolves slowly to its present age of 4.6 billion years.

Parameter	Value
Mass ($M_\odot$)	$(1.9891 \pm 0.0004) \times 10^{33}$ g
Radius ($R_\odot$)	$(6.9599 \pm 0.0002) \times 10^{10}$ cm
Luminosity ($L_\odot$)	$(3.846 \pm 0.004) \times 10^{10}$ ergs s^{-1}
Neutrino Luminosity	$0.022 L_\odot$
Age	$(4.52 \pm 0.04) \times 10^{9}$ yr
Oblateness	$\leq 2 \times 10^{-5}$
$(Z/X)_\odot$	$0.0245 \pm 10\%$

Table 1.1: Observed solar parameters[15].

The standard solar model calculation and nuclear reaction rates are developed in appendix A; here I discuss an outline of the method and the principal uncertainties. The starting point is an equation for hydrostatic equilibrium and an equation of state for a ideal gas under thermal and radiation pressure, with modifications for electron degeneracy and screening interactions. These equations, along with expressions for the radiative opacities and nuclear fusion energy, form a simultaneous set of differential equations whose solution is iterated over suitable time steps and over thin spherical shells. Over shells where the temperature gradient is unstable against convective motion the equation of state is replaced by the convection equation where the pressure gradient is proportional to the temperature gradient.

The calculation proceeds by stepping the solution up to the present age (set by terrestrial and meteoritic dating), then iterating the whole procedure by adjusting any variable starting parameters, for example the initial chemical composition and a mixing length parameter. The calculation end condition is the satisfactory convergence to the solar observables: mass, radius, luminosity, and relative photospheric

Parameter	BP95	BTM98	DS96	Experimental
$\rho_c\,(\mathrm{g/cm^3})$	156.2	151.9	155.4	
$T_c \times 10^6\,(\mathrm{K})$	15.84	15.67	15.61	
Y_c	0.646	0.635	0.638	
Z_c	0.0211	0.02084	0.0194	
$T_s\,(\mathrm{K})$	5800	5800	5803	5780
Y_s	0.247 (0.243)	0.243	0.238	0.249 ± 0.003
Z_s	0.0180	0.0181	0.017	
$R_{cz}/R_\odot$	0.712 (0.714)	0.715	0.713	0.713 ± 0.001
$T_{cz} \times 10^6\,(\mathrm{K})$	2.20	2.17	2.11	
Y_0	-	0.273	-	
$(Z/X)_0$	-	0.0277	Meteoritic	
$^{37}\mathrm{Cl}$ $(\sum \phi_\nu \sigma)$ SNU	9.3 (7.7)	7.2	4.1	2.56 ± 0.25
$^{71}\mathrm{Ga}$ $(\sum \phi_\nu \sigma)$ SNU	137 (129)	127	115	73 ± 11
$^{8}\mathrm{B}$ ϕ_ν $(10^6\,\mathrm{cm^{-2}s^{-1}})$	6.5 (5.2)	4.8	2.5	2.44 ± 0.11

Table 1.2: Predicted solar parameters and detected neutrino rates for three recent solar models: BP95 (Bahcall and Pinsonneault [17]), MTM98 (Brun, Turck-Chièze and Morel [15]) and DS96 (Dar and Shaviv [19]). The subscripts have the following meaning: s=surface, c=core, 0=initial and cz=base of convective zone. Bahcall's 1995 model is used instead of his recent 1998 model [18] since his new thermodynamical quantities are unpublished. However, where available, Bahcall's 1998 model predictions are include in brackets since his adoption of the new INT $^7\mathrm{Be}(p,\gamma)^8\mathrm{B}$ cross-section $S_{17}(0)$ factor [24] have reduced his ^{8}B neutrino rate predictions significantly. See text for references on experimental values.

metalicity[3] (Z/X). Other parameters such as the surface temperature, convective zone depth and pressure mode oscillation speeds are then compared to measured values. The model then predicts other solar characteristics such as the initial mass, helium abundance and the neutrino flux and spectra (see table 1.2). The neutrino spectra for Bahcall's SSM are plotted in figure 1.3 along with the detector thresholds for the neutrino experiments discussed in the next section.

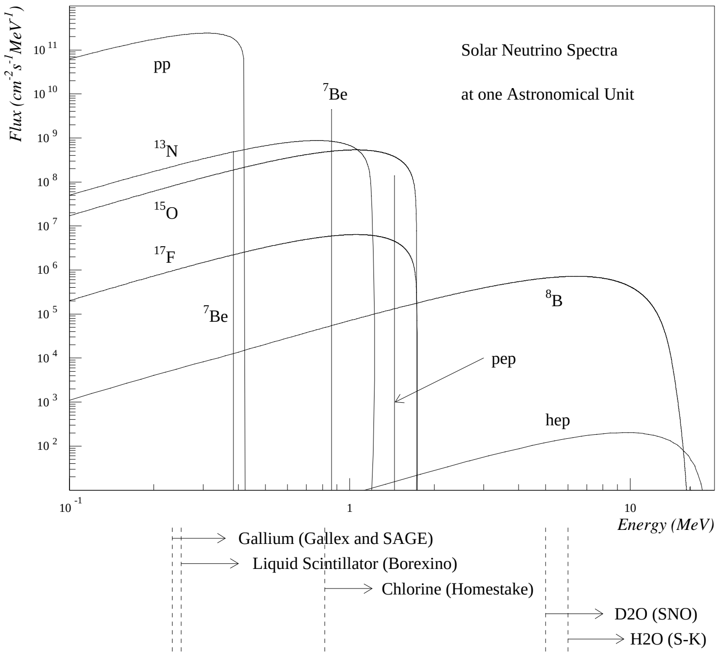

Figure 1.3: Solar neutrino energy spectra for the *pp* and CNO reaction chains (data from Bahcall [17]). The spectra are plotted as flux at one astronomical unit per MeV bin, while for the mono-energetic neutrinos the line height is the flux in $\mathrm{cm}^{-2}\mathrm{s}^{-1}$.

The main uncertainties in the solar models affecting the neutrino flux are the zero-extrapolated reaction shape factors (the astrophysical S-factors $S(0)$), the present

[3]In astrophysics notation X, Y and Z refer to fractional abundances of hydrogen, helium and all heavier elements, thus $X + Y + Z = 1$. Z is called the metalicity.

surface metalicity $(Z/X)_\odot$, radiation opacities, solar luminosity, effects of helium and heavy element diffusion and solar age.

The largest uncertainties are due to the nuclear reaction rates which are parameterized by a shape factor $S(E)$, after factoring out the large Coulomb energy dependence. The reaction rates are necessarily measured at terrestrial energies, then the S-factors must be extrapolated to near zero energy, and there is significant uncertainty in doing so. For the ^{8}B neutrino flux the main uncertainty is the $^7\mathrm{Be}(p,\gamma)^8\mathrm{B}$ rate ($S_{17}(0)$) which is uncertain to 20% due to conflicting experiments [24]. The S-factor adopted by the recent solar models are shown in table 1.3. The ^{8}B flux also depends on the radiation opacities since these neutrinos are produced deeper in the core compared to the pp and ^{7}Be flux (due to stronger temperature dependence of the solar $^7\mathrm{Be}(p,\gamma)^8\mathrm{B}$ rate).

Reaction	S-factor	BP98 [18]	BTM98 [15]	DS96 [19]
		(eV barn)	(eV barn)	(eV barn)
$^1\mathrm{H}(p,e^+\nu)^2\mathrm{H}$	$S_{11}(0)$	4.00×10^{-19}	4.00×10^{-19}	4.07×10^{-19}
$^3\mathrm{He}(^3\mathrm{He},2p)^4\mathrm{He}$	$S_{33}(0)$	5.3×10^6	5.4×10^6	5.6×10^6
$^3\mathrm{He}(\alpha,\gamma)^7\mathrm{Be}$	$S_{34}(0)$	530	530	450
$^7\mathrm{Be}(p,\gamma)^8\mathrm{B}$	$S_{17}(0)$	19	19	17

Table 1.3: Astrophysical S-factors for the main nuclear reactions influencing neutrino production rates as adopted by the three recent solar models.

The largest uncertainty for the ^{7}Be flux is in $S_{34}(0)$ which is known to 10% [24]. The pp neutrino flux does not suffer from these uncertainties since S_{11} is more certain, the pp flux does not depend much on the heavy element composition, and it is better constrained by solar luminosity.

Despite these significant uncertainties, the overall models are now quite constrained by new earth and satellite-borne helioseismology data [20–23]. These experiments detect the very large mode solar surface oscillations, which then predict the sound speed depth profile to astonishing precision. The present solar models agree quite well with the measured sound speed profile and convective zone depth, but this agreement rapidly deteriorates if the temperature profile is significantly modified, for example by more helium diffusion.

The ^{8}B and ^{7}Be flux also depend on the initial metalicity which is assumed to be well represented by the present surface metalicity. The Convective zone and surface are well mixed, so that the present solar surface represents the primordial constituents, since the whole star is turbulent before the zero age main sequence.

1.2 Current Experimental Results

The first experiment with sensitivity to solar neutrinos was the ^{37}Cl detector built by Davis and collaborators at the 4850 ft level of the Homestake Gold mine near Lead, South Dakota [26]. The detector has been operating since 1968. The deep mine detector was constructed to remove uncertainty in the termination of the reactions for the *pp* chain, and because of the realization by Bahcall that the ^{8}B neutrino capture rate on ^{37}Cl over 6 MeV was enhanced by a factor of 10 due to transition to an analogue state of ^{37}Ar [27].

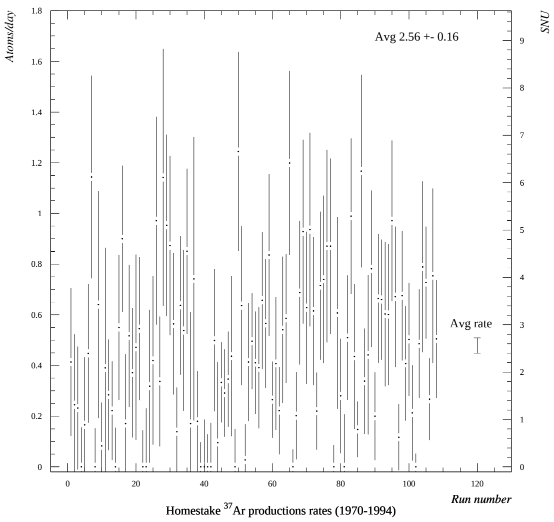

Figure 1.4: ^{37}Ar extraction data for 108 runs (1970-1995) of the Homestake chlorine solar neutrino experiment [28].

The Homestake detector is a 6 m diameter tank containing 615 tonnes of perchloroethylene (C_2Cl_4). The neutrino capture reaction

$$^{37}\mathrm{Cl} + \nu_e \longrightarrow ^{37}\mathrm{Ar} + e^-, \qquad E_\nu > 814\,\mathrm{keV} \tag{1.2}$$

is sensitive mainly to the solar ^{8}B and ^{7}Be neutrinos due to the 814 KeV threshold. Every 1 to 3 months the ^{37}Ar atoms are swept from the volume by helium bubblers and counted in low background proportional gas counters. The ^{37}Ar atoms have a 35 day half life and are detected by Auger electron emission from K and L shell electron capture decay. The data for 108 runs from 1970 to 1995 is shown in figure 1.4 and has an overall average of [28]

$$\langle \phi_{\nu_e} \sigma \rangle_{\mathrm{Cl}} = 2.56 \pm 0.16(\mathrm{stat}) \pm 0.14(\mathrm{sys}) \quad \mathrm{SNU} \tag{1.3}$$

where a SNU (solar neutrino unit) is one capture per 10^{36} target atoms per second. The solar model predicted capture rates (flux times cross-section) for the neutrino flux components are shown in table 1.4 for the Bahcall-Pinsonneault (BP98) model and total 7.7 ± 1.2 SNU for chlorine.

Neutrino Source	Flux (cm^{-2}/s)	Cl (SNUs)	Ga (SNUs)
pp	5.94×10^{10}	0.00	69.6
pep	1.39×10^{8}	0.2	2.8
hep	2.10×10^{3}	0.0	0.0
^{7}Be	4.80×10^{9}	1.15	34.4
^{8}B	5.15×10^{6}	5.9	12.4
^{13}N	6.05×10^{8}	0.1	3.7
^{15}O	5.32×10^{8}	0.4	6.0
^{17}F	6.33×10^{6}	0.0	0.1
Total		$7.7^{+1.2}_{-1.0}$	129^{+8}_{-6}

Table 1.4: Solar neutrino fluxes and predicted capture rates for the chlorine and gallium detectors. A SNU (solar neutrino unit) is 10^{-36} events per target atom per second. Data is for the Bahcall and Pinsonneault 1998 model[18].

The Kamiokande water Čerenkov detector was originally constructed as a proton decay experiment 1000 m under the Japanese Alps in the Mitsui Mining and Smelting

Company zinc mine near Kamioka. It was adapted in 1987 for solar neutrino sensitivity (Kamiokande-II) by instrumenting the outer volume as a muon anti-counter, upgrading the water purification to remove uranium and radium elements, and adding an inert cover gas. The detector was upgraded (Kamiokande-III) in 1990 with new electronics, PMT reflectors to increase the photocathode coverage, and further upgrades to the water purification system. Until decommissioning in 1995 Kamiokande achieved 2079 days of live time, covering most of solar cycle 22, with a final analyzed sample of 6368 events with energies from $7-20\,\mathrm{MeV}$. The detector properties and performance are detailed in table 1.5.

The neutrino interaction with light water is by neutrino-electron scattering. The angular distribution is calculated from the differential cross-section and is strongly forward peaked. The theoretical angular distribution is convolved with the detector angular resolution (by Monte Carlo), and then fit to the data binned by reconstructed angle to the sun (as in figure 1.5). This resulted in 597^{+41}_{-40} events above background observed at Kamiokande compared to 1121^{+13}_{-157} predicted from the Bahcall-Pinsonneault solar model[18]. The detected solar neutrino flux and ratio to the standard solar model is

$$\phi_{\mathrm{Kam}} = 2.80 \pm 0.19(\mathrm{stat}) \pm 0.33(\mathrm{sys}) \times 10^6\,\mathrm{cm}^{-2}\mathrm{s}^{-1} \tag{1.4}$$

$$\frac{\phi_{\mathrm{Kam}}}{\mathrm{SSM}_{\mathrm{BP98}}} = 0.533 \pm 0.088(\mathrm{theory}) \pm 0.036(\mathrm{stat}) \pm 0.063(\mathrm{sys}). \tag{1.5}$$

Also the Kamiokande data shows no significant difference between the daytime and night-time fluxes, and there is no anti-correlation with solar activity (sun spots). A day/night flux difference is expected for some neutrino oscillation parameters (discussed in the next section) due to regeneration with the earth. A sun spot correlation would be expected if the neutrinos had a magnetic moment sufficiently large the explain the solar neutrino problem.

The Kamiokande detector is now superceded by the new 50 kilotonne Super-Kamiokande (S-K) constructed at the same site. Super-Kamiokande has been operational since April 1996 and has reported results from analysis of the first 300 days of data. See table 1.5 for detector properties. The Super-Kamiokande detector advances the water Čerenkov solar neutrino experiment with its very high statistics capability

	Kamiokande-III	Super-K
Depth	1000m (2700 MWE)	1000m (2700 MWE)
Volume	3000 tonnes	50,000 tonnes
Fiducial volume	680 tonnes	22,500 tonnes
PMTs	948 50cm	11,200 50cm
Photocathode coverage	40%	25%
Analysis threshold	7-9 MeV	6.5 MeV
PMT hits per MeV	4 at 10 MeV	6 at 10 MeV
Trigger efficiency	50% at 5 MeV	50% at 5.5 MeV
Angular resolution	26° at 10 MeV	25° at 10 MeV
Vertex reconstruction	1.2 m at 10 MeV	0.7 m at 8.6 MeV
Energy resolution	$18\% \times\sqrt{\frac{10\,\mathrm{MeV}}{T_e}}$	$15\% \times\sqrt{\frac{10\,\mathrm{MeV}}{T_e}}$
Energy calibration	5.3%	1%
Event rate	0.86 per day (SSM)	67 per day (SSM)

Table 1.5: Detector properties and performance of the Kamiokande-III and Super-Kamiokande detectors. MWE is the mean water equivalent depth.

Figure 1.5: Fitted $\cos\theta_{\mathrm{sun}}$ for Super-Kamiokande data for $T_e > 6.5\,\mathrm{MeV}$ after fiducial and spallation cuts for 300 days [30].

and a more precise (1%) energy calibration using an electron LINAC. The detected solar neutrino flux and ratios to the SSM are

$$\phi_{\rm SK} = 2.44 \pm 0.06({\rm stat}) \pm 0.09({\rm sys}) \times 10^6\,{\rm cm}^{-2}{\rm s}^{-1} \tag{1.6}$$

$$\frac{\phi_{\rm SK}}{{\rm SSM}_{\rm BP98}} = 0.474 \pm 0.078({\rm theory}) \pm 0.012({\rm stat}) \pm 0.017({\rm sys}). \tag{1.7}$$

Two gallium experiments, GALLEX and SAGE, detect neutrinos via inverse beta decay on ^{71}Ga, which makes up 39.6% of natural gallium

$$^{71}{\rm Ga} + \nu_e \longrightarrow ^{71}{\rm Ge} + e^-, \qquad E_\nu > 233\,{\rm keV}. \tag{1.8}$$

The low 233 keV threshold makes gallium sensitive to the very high flux *pp* solar neutrinos, which contribute 54% to the expected event rate, with the remainder of the events coming from ^{7}Be and ^{8}B neutrinos (26% and 11%). Every several weeks the ^{71}Ge atoms are extracted and counted in low background proportional counters. With an 11.4 day half-life ^{71}Ge decays back to ^{71}Ga emitting X-rays and Auger electrons from K and L shell electron capture. The expected neutrino capture rates per target mass (in SNUs) is given in table 1.4.

The GALLEX experiment [33] contains 30.3 tonnes of gallium in a $GaCL_3$:HCL solution in the Gran Sasso underground laboratory which provides 3500 m of water-equivalent shielding. The Ge atoms produced by neutrino capture (equation 1.8) form $GeCl_4$, a volatile compound, which is swept out in a gas stream and converted to GeH_4 for counting. The combined result of 65 GALLEX runs (GALLEX I-IV) is

$$\langle \phi_{\nu_e} \sigma \rangle_{\rm Ga} = 76.4 \pm 6.3({\rm stat}) \pm 4.9({\rm sys}) \quad {\rm SNU}. \tag{1.9}$$

The SAGE experiment is located at the Baksan Laboratory at 4715 m water-equivalent depth in Russia's Caucasus mountains. The detector contains 55 tonnes of pure Gallium metal. For each extraction the metal is liquefied by heating and dissolved in HCL acid solution, and the Ge chemically removed. The results from the combined 65 SAGE runs produced

$$\langle \phi_{\nu_e} \sigma \rangle_{\rm Ga} = 70.0 \pm 6.3({\rm stat}) \pm 4.9({\rm sys}) \quad {\rm SNU}. \tag{1.10}$$

Both GALLEX and SAGE have been calibrated with a strong ^{51}Cr neutrino source. The ratio of the expected neutrino event rate to the measured rate is 0.92 ± 0.07 for GALLEX and 0.95 ± 0.11 for SAGE.

1.3 Possible Solutions to the Solar Neutrino Problem

The solar neutrino predicted experimental rates are given in table 1.6 for several solar models, and plotted in figure 1.6 as a function of the mean detected neutrino energy. Good spectral data is not available, since the radio-chemical experiments have no spectral information, while the spectral sensitivity of light water Čerenkov detectors is very weak. However, together the experiments reveal both a suppression and a distortion of the solar neutrino spectrum. Furthermore, the suppression of the neutrino fluxes can be deduced independent of solar models from the luminosity sum rule [38]. From 1.1 the net fusion reaction yields two neutrinos along with $Q = 26.7\,\mathrm{MeV}$ of energy. By subtracting the mean neutrino energy for each flux from Q, and setting equal to the solar luminosity, we have an equation for the neutrino fluxes

$$\frac{L_\odot}{4\pi D_{\text{earth-sun}}} = \sum_i \left(\frac{Q}{2} - \langle E_{\nu_e}(i)\rangle\right) \phi_{\nu_e}(i) \tag{1.11}$$

The experimental results give three more equations for the neutrino fluxes

$$\phi_{\nu_e}(^8\mathrm{B}) = (2.44 \pm 0.10) \times 10^6 \mathrm{cm}^{-2}\mathrm{s}^{-1} \qquad \text{(Super-K)} \tag{1.12}$$

$$\sum_i \sigma_i \phi_{\nu_e}(i) = 72.5 \pm 11 \text{ SNU} \qquad \text{(SAGE/GALLEX)} \tag{1.13}$$

$$\sum_i \sigma_i \phi_{\nu_e}(i) = 2.56 \pm 0.23 \text{ SNU} \qquad \text{(Homestake)} \tag{1.14}$$

The fluxes are reduced to four variables by adding the *pep* to the *pp* (they are proportional), and ^{13}N to ^{15}O, and ignoring the small contribution to the luminosity by the ^{8}B flux [39]. The equations can then be solved for the fluxes. The result is that the $\phi(^7\mathrm{Be})$ and $\phi(\mathrm{NO})$ flux are slightly negative, and taken to be practically zero. However, this is not possible since ^{7}Be precedes ^{8}B in the *pp* cycle. We see how this result comes about, as the ^{8}B flux, fixed by S-K, summed to the *pp* flux already totals more than the rate seen in the radio-chemical detectors, leaving no room for the ^{7}Be flux. Thus the solar neutrino problem (SNP) consists of the overall suppression of all fluxes, and the complete suppression of the ^{7}Be flux, and can be formulated independent of the solar models.

	Experiment	BP95 [17]	BP98 [18]	TC93 [12]	BTM98 [15]	DS96 [19]
Homestake	2.56 ± 0.23	9.3 ± 1.4	7.7 ± 1.2	6.4 ± 1.4	7.2 ± 1.5	4.1 ± 1.2
Kamiokande	2.80 ± 0.38					
Super-K	2.44 ± 0.10	6.5 ± 1.1	5.2 ± 1.0	4.4 ± 1.1	4.8 ± 1.1	2.5 ± 0.7
Combined	2.46 ± 0.14					
SAGE	67 ± 8					
GALLEX	78 ± 8	137 ± 8	129 ± 8	122 ± 7	127 ± 8	115 ± 6
Combined	72.5 ± 6					

Table 1.6: Predicted experimental rates for several solar models.

Attempts to explain the cause of the solar neutrino problem fall into two categories; astrophysical or particle physics sources. Astrophysical solutions involve non-standard solar models or large systematic problems with the inputs to the standard solar model. Non-standard solar models typically modify the solar temperature profile, while particle physics solutions postulate extended neutrino properties, in particular mass or a magnetic moment. The neutrino spectra are given by the weak interaction physics of beta decay, and are not affected by the solar model. Thus any evidence of spectral distortion points to new neutrino properties.

Bahcall and Ulrich obtained the approximate correlation between solar core temperature and neutrino flux by calculating 1000 solar models with the input parameters (eg. S-factors) randomly varied over their uncertainty ranges [13]. They fit simple

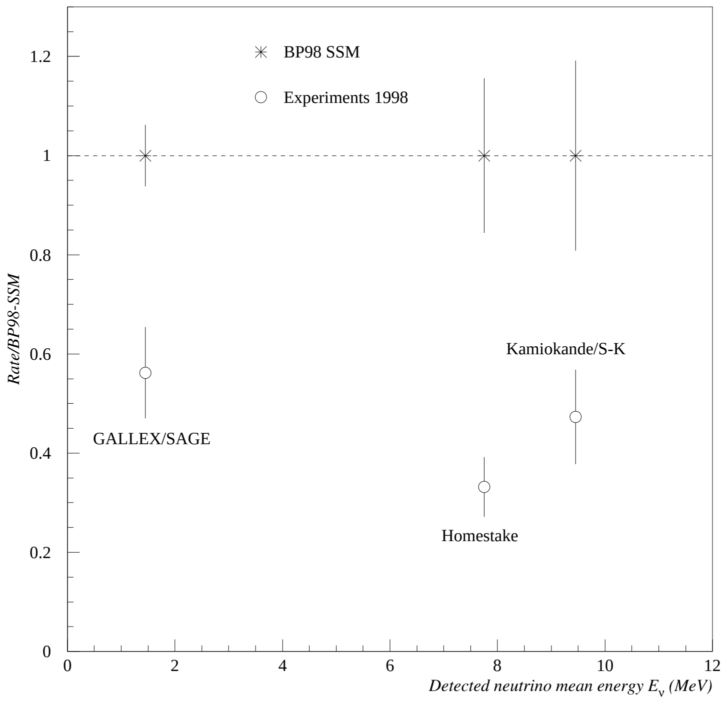

Figure 1.6: Experiment versus theory for solar neutrino experiments. The detected solar neutrino rates for the gallium, chlorine and Kamiokande experiments are plotted as a ratio to the BP98 solar model and as a function of the mean neutrino energy detected in each experiment.

power laws as

$$\phi(pp) \sim T_c^{-1.2}, \;\; \phi(^7\mathrm{Be}) \sim T_c^8, \;\; \phi(^8\mathrm{B}) \sim T_c^{18}. \tag{1.15}$$

This result can be understood by examining the regions of emission (figure 1.7). For models in which the central temperature is highest, the ^{8}B flux is greatly increased. However, the surface boundary condition then requires that the temperature fall more rapidly with radius, so that the ^{7}Be is increased less, and the *pp* flux, further out, is reduced. A non-standard solar model would require a dramatic temperature inversion. Suggested methods include out of equilibrium ^{3}He mixing or filament ^{3}He mixing [40]. However, these models are very strongly constrained by the helioseismological data.

Figure 1.7: Neutrino production as a function of solar radius.

In the Dar and Shaviv solar model [19] the nuclear S-factors are chosen to maximize the neutrino production. While they manage to obtain agreement for the ^{8}B flux (due to the large S_{17} uncertainty), their prediction for the chlorine and gallium experiments are consistent with the other models.

If neutrinos have mass then it is possible that the flavour expectation value (the probability of observing a particular neutrino flavour state) may oscillate if the flavour states are an admixture of the propagated mass eigenstates. The detectors, sensitive mainly to electron neutrinos, would see a reduced flux, depending on the vacuum mixing angle θ_v and the mass difference squared Δm^2 [35]. However, at most we can get a factor of two suppression using an unexpectedly large mixing angle, which poorly explains the SNP.

An attractive oscillation hypothesis is the MSW effect [36] where neutrino forward scattering in the dense sun can phase shift the electron neutrino to cause a resonant oscillation enhancement. The time evolution equation will have an extra potential in the mass matrix for the electron flavour due to the charged weak current. Considering only two flavour oscillations the time evolution equation (with traceless mass matrix) is

$$i\frac{d}{dt}\begin{pmatrix} \nu_e \\ \nu_\mu \end{pmatrix} = \begin{pmatrix} -\frac{\Delta m^2}{2E}\cos 2\theta_v + \sqrt{2}G_F n_e & \frac{\Delta m^2}{2E}\sin^2\theta_v \\ \frac{\Delta m^2}{2E}\sin^2\theta_v & \frac{\Delta m^2}{2E}\cos 2\theta_v - \sqrt{2}G_F n_e \end{pmatrix}\begin{pmatrix} \nu_e \\ \nu_\mu \end{pmatrix}. \tag{1.16}$$

The MSW effect is derived in appendix B. The result is that for a particular neutrino energy range the oscillation is resonantly enhanced at the electron density

$$n_e = \frac{\Delta m^2 \cos 2\theta_v}{2\sqrt{2}G_F E} \tag{1.17}$$

and complete flavour conversion is possible for even small values of θ_v and Δm^2. The MSW effect requires only that neutrinos have mass. Whether or not MSW accounts for the SNP depends on the Δm^2 and $\sin^2 2\theta_v$ parameters. In turn the solar neutrino experimental results can be used to derive the Δm^2 and $\sin^2 2\theta_v$ parameters under the MSW hypothesis. The best fit solutions for the current experiments (S-K, GALLEX, SAGE, Homestake) are, in preferred order [9]: (i) small angle mixing or non-adiabatic (SMA) $\Delta m^2 = 5.4 \times 10^{-6}, \sin^2 2\theta_v = 6.0 \times 10^{-3}$, (ii) large angle angle (LMA) $\Delta m^2 = 1.8 \times 10^{-5}, \sin^2 2\theta_v = 0.76$, (iii) or a third less likely solution with small Δm^2 called the low probability solution (LOW) $\Delta m^2 = 7.9 \times 10^{-8}, \sin^2 2\theta_v = 0.96$. A pure vacuum mixing solution (VAC) with parameters $\Delta m^2 = 8.0 \times 10^{-11}, \sin^2 2\theta_v = 0.75$, while much lower probability, is still not ruled out [9].

The treatment for three neutrinos is more complicated but follows the same formalism. However, the two neutrino treatment is most relevant, because the masses are predicted to be hierarchical [11], so that only one resonance will contribute considering the solar density and the current parameter ranges. Of course the Δm^2 quoted here may actually be the mass difference between the electron and tau neutrinos. The survival probability as a function of neutrino energy is plotted in figure 1.8 for the three solutions using the Parke formula [37] to calculate level crossing corrections to the adiabatic conversion probability (see appendix B). Comparing figures 1.8 and 1.6 we see why the MSW effect is preferred. The SMA solution provides for complete suppression of the ^{7}Be neutrinos and partial suppression of the *pp* and ^{8}B neutrinos. The MSW effect can also cause flavour regeneration within the earth to yield a day/night flux difference. S-K has not observed such an effect which rules out part of the Δm^2, $\sin^2 2\theta_v$ space [30].

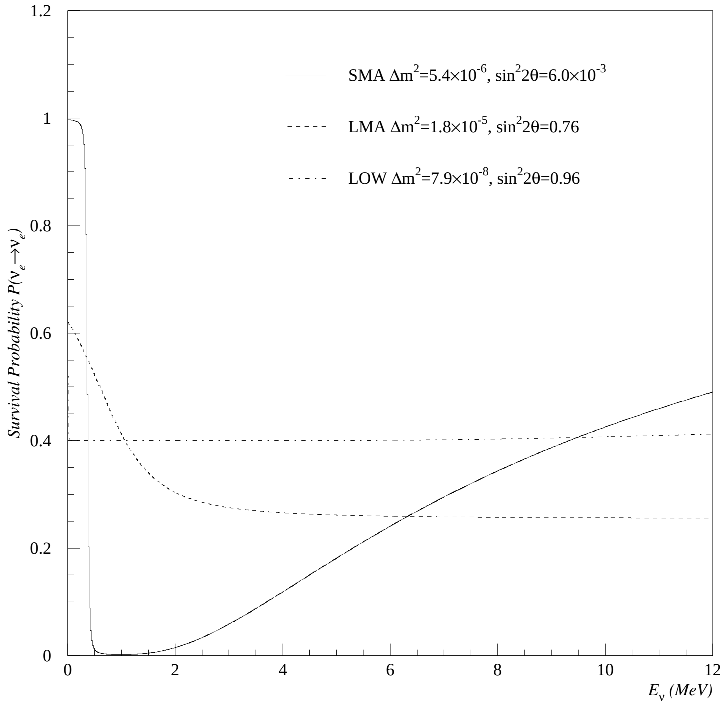

Figure 1.8: The MSW survival probabilities for electron neutrinos produced at the solar core evaluated with the Parke Formula for the three best fit solutions [9].

Other possible solutions such as weakly interacting massive particles (WIMPs), sterile neutrinos, neutrino decay or a neutrino magnetic moment have also been considered. WIMPs can provide a way to cool the solar core, but cannot explain the ^{7}Be suppression relative to the ^{8}B neutrinos [3]. Neutrino decay is essentially ruled out by observation of neutrinos from supernova 1987A [42]. A neutrino magnetic moment large enough to cause a spin flip in the sun should yield a rate correlation with solar magnetic phenomena (sunspots or solar equatorial variation), which is not supported by the data [30]. Finally, oscillation to sterile neutrinos is a possibility that can be explored at SNO. A reduced neutral current flux, and distortion of the charged current spectrum are indications of conversion to sterile types.

If neutrino flavour mixing is the solution to the SNP, then this needs to be examined in the context of other experimental searches for neutrino oscillations. Other neutrino oscillation experiments are reactor experiments, accelerator detectors and atmospheric neutrino detectors. Reactor experiments probe the disappearance $\bar{\nu}_e \longrightarrow \bar{\nu}_\mu$ by measuring the positron spectrum in neutron coincidence from

$$\bar{\nu}_e + p \longrightarrow e^+ + n \tag{1.18}$$

at various distances from the reactor [8]. Results from the CHOOZ detector [44] show no evidence for oscillation, and they rule out a segment of the Δm^2, $\sin^2 2\theta_v$ space roughly bounded by $\Delta m^2 > 10^{-3}\,\mathrm{eV}^2$ and $\sin^2 2\theta_v > 0.2$.

Two medium neutrino energy $(30-50\,\mathrm{MeV})$ accelerator experiments report results from decays of muons and pions produced at the beam dump of $800\,\mathrm{MeV}$ proton beams [8]. The LSND experiment, with 170 tonnes of mineral oil based scintillator, finds excess ν_e capture events indicating oscillation in the $\nu_\mu - \nu_e$ channel [45]. The oscillation probability yields an area in the Δm^2, $\sin^2 2\theta_v$ space, not ruled out by reactor experiments (CHOOZ), corresponding to about $\Delta m^2 \sim 1\,\mathrm{eV}^2$ and $\sin^2 2\theta_v \sim 10^{-2}$. The KARMEN experiment sees no evidence for oscillations [46], although it does not yet overlap the entire LSND parameter space. Further, NOMAD, a high energy accelerator detector, reports $\sin^2 2\theta_v \sim 2 \times 10^{-3}$ for $\Delta m^2 > 1\,\mathrm{eV}^2$, which further rules out much of the LSND parameter space [47].

High energy neutrinos (sub- and multi-GeV) are produced in the earth's atmosphere from cosmic ray muon and pion decay. These neutrinos are convenient for oscillation searches as the baseline is a function of the zenith angle, varying from several kilometers overhead to the $12,750\,\mathrm{km}$ terrestrial diameter. The flux of ν_μ and ν_e depends on the geomagnetic field and assumptions about the primary cosmic ray spectrum. The ν_μ/ν_e ratio, while energy dependent, is better determined, and the experimental quantity of interest is the double ratio of the observed to calculated ν_μ/ν_e ratios (including a Monte Carlo of detector efficiencies). Two experiments (Fréjus [48] and NUSEX [49]) found ratios of $R = 1$, but recent experiments (Super-Kamiokande [31], IMB [50] and Soudan-2 [51]) with much higher significance report ratios of about $R = 0.6$. Further, Super-Kamiokande finds an up-down zenith angle asymmetry for muon neutrinos and finds the best fit MSW parameters correspond to (ν_μ, ν_τ) oscillations with $\sin^2 2\theta_v = 1.0$, $\Delta m^2 = 2.2 \times 10^{-3}\,\mathrm{eV}^2$ [31]. Their fit for (ν_μ, ν_e) oscillations is poorer, with parameters $\sin^2 2\theta_v = 0.93$, $\Delta m^2 = 3.2 \times 10^{-3}\,\mathrm{eV}^2$. However, the $\nu_\mu - \nu_e$ fit is entirely ruled out by the CHOOZ reactor experiment.

While there appears to be a wealth of evidence for neutrino oscillations (and hence for neutrino mass), that evidence is mostly indirect and some of it contradictory. Solar neutrino experiments favour a small mass difference, $\Delta m^2 \sim 10^{-5}\,\mathrm{eV}^2$, while the zenith angle dependence of the atmospheric muon neutrino anomaly indicates a larger mass difference, $\Delta m^2 \sim 10^{-3}\,\mathrm{eV}^2$. This indicates a hierarchical neutrino mass model [11], but leaves no room for the LSND value of $\Delta m^2 \sim 1\,\mathrm{eV}^2$. Also, it is surprising that while current solar neutrino data flavours a small mixing angle for $\nu_e - \nu_\mu$, the S-K zenith angle data for $\nu_\mu - \nu_\tau$ neutrino oscillations requires a large mixing angle.

1.4 The SNO Experiment

The Sudbury Neutrino Observatory has been constructed to address the solar neutrino problem and to study the properties of neutrinos. This will be achieved in SNO by a sensitive measurement of the solar neutrino flux via the weak neutral current (NC) and the charged current (CC) reactions using 1000 tonnes of heavy water. SNO is a direct counting water Čerenkov detector sensitive to the ^{8}B and hep solar neutrinos. With separate measurements of the electron neutrino flux (CC) and the flux of all neutrino flavours combined (NC), SNO can determine if neutrino oscillations are occurring, since the ratio of these fluxes (CC/NC) will be smaller than one. Also, the the CC reaction preserves the neutrino spectrum shape so that further investigation of particular MSW scenarios is possible through examination of spectrum shape distortions. SNO is also sensitive to neutrinos and anti-neutrinos from supernova events that may occur within the galaxy.

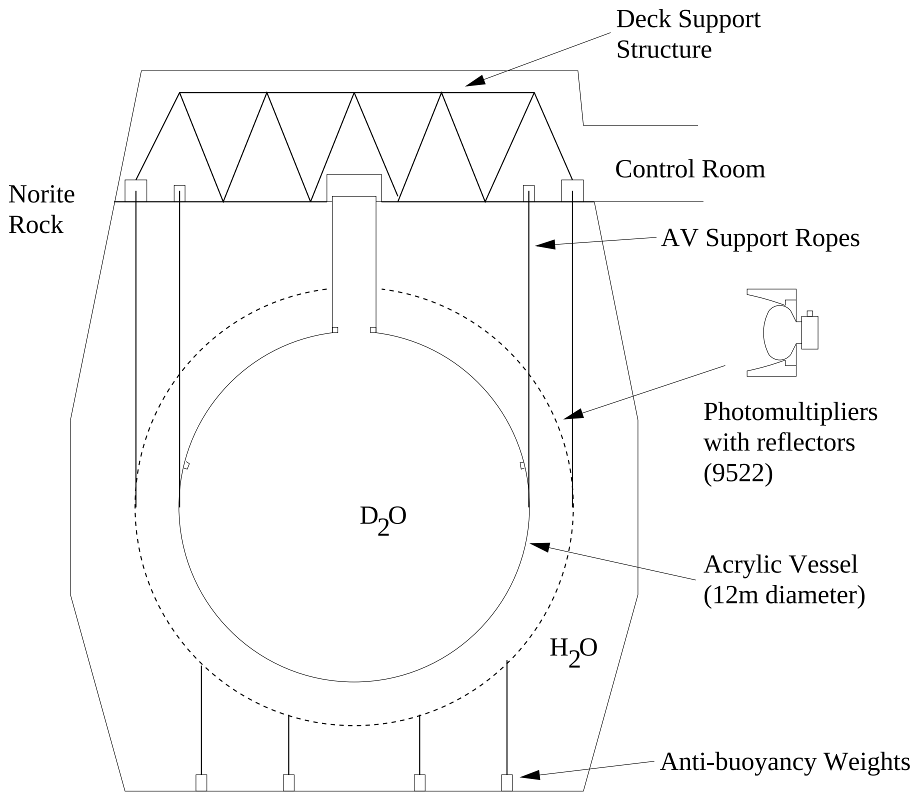

Figure 1.9: The Sudbury Neutrino Observatory.

The SNO detector is at 5900 m water equivalent depth underground where the rock shielding reduces the background cosmic ray muon intensity to less than 100 $\mathrm{m}^{-2}\mathrm{y}^{-1}$. Within a barrel shaped cavity 32 m high and 22 m in diameter, the heavy water is buoyed by 7600 tonnes of light water in a 12 m diameter acrylic vessel of 5 cm thickness. The Čerenkov radiation is detected by 9522 20 cm photomultipliers (PMTs) supported on an 18 m diameter steel geodesic structure. The PMTs have non-imaging reflectors to increase the total photocathode coverage to 64%. The cavity is lined with a 8 mm thick Urylon (polyurethane) liner which provides a water barrier and is also impermeable to radon. The light water shields the detector from γ radiation from the host rock, and from the radiation from trace radioactive impurities in the PMTs.

The CC reaction is detected via the Čerenkov light emission from the relativistic electron in neutrino capture on deuterium (called inverse beta decay). The energy spectrum is almost preserved since the electron gains most of the energy. There is also a dependence in the cross-section on the angle to the sun. At 5-20 MeV solar neutrino energies, the event energy is proportional to the number of PMTs hit with single photo-electron intensity. The NC reaction is detected by capture of the free neutron on deuterium, which yields a 6.25 MeV gamma ray. Gamma rays are detected by the relativistic electron following Compton scattering of gamma rays off electrons. Events are reconstructed with a statistical fitter using the light photon arrival times at the PMTs to produce a reconstructed location and direction. SNO will also run with 2 other neutron detection schemes for NC measurement; $MgCl_2$ salt and neutral current detectors (NCDs). With salt the neutron is captured on ^{35}Cl which yields 8.6 MeV in gamma rays and has a large capture cross-section. The NCDs are an array of ^{3}He filled proportional counters which produce a signal pulse following the neutron capture on ^{3}He.

The detector background signals are $\beta-\gamma$ decays within the D_2O and $\beta-\gamma$ decays and α captures from the rock and PMTs which can mimic detector events. These decays are mostly from the ^{232}Th and ^{238}U radio-nuclide chains, and in particular ^{208}Tl and ^{214}Bi which have decay energies extending to 5 MeV. In addition the ^{208}Tl and ^{214}Bi isotopes emit gamma rays of 2.615 MeV and 2.445 MeV which can photodisintegrate the deuteron to create a neutron background. These backgrounds are reduced by a very careful selection of construction materials and by very clean construction procedures to reduce contamination from mine dust which contains U and Th. The major control of radioactive background is the heavy and light water filtration systems which will reduce the levels of ^{232}Th and ^{238}U to parts per 10^{-15} g/g for the heavy water. The analysis threshold will be about 5 MeV where the neutrino spectra rise substantially above the steep low energy background spectra (see figure 2.2). SNO will be calibrated with several gamma ray, optical, and neutron sources to map the detector response in energy and position.

Chapter 2

The Sudbury Neutrino Observatory

The Sudbury Neutrino Observatory is a second generation heavy water Čerenkov detector in the final stage of construction and will begin commissioning and data taking in the fall of 1998. SNO will be sensitive to solar neutrinos with capability to measure the flux and energy spectrum of electron neutrinos and the flavour-blind flux of all three neutrino flavours. This chapter provides a complete description of the detector and the physics. Emphasis is placed on describing those components of the detector that are most relevant for the work in this thesis, notably the calibration hardware and sources, the photomultipliers, electronics and the expected signals.

2.1 Neutrino Interactions and Event Detection

Using deuterium in heavy water as a target, SNO will detect neutrinos in three channels: the charged current reaction (CC), the neutral current reaction (NC), and electron scattering (ES) (see figure 2.1). The charged current reaction is the inverse beta decay of deuterium

$$\nu_e + d \longrightarrow p + p + e^- \qquad (Q = -1.44\,\mathrm{MeV}). \tag{2.1}$$

The CC reaction is a Gamow-Teller transition and by kinematics the electron energy spectrum is closely matched to the neutrino energy spectrum. The angular distribution, excluding small weak magnetism and radiative corrections, is $1 - \frac{1}{3}\cos\theta$, which permits a correlation analysis with the angle θ between the event direction and the direction to the sun. The expected event rate is 10.6 events per day for a 5 MeV threshold and a 775 tonne fiducial target (see table 2.1), assuming the Super-Kamiokande measurement of 0.47 standard solar model neutrino flux [30]. The energy spectrum will provide sensitivity to possible MSW spectral distortions.

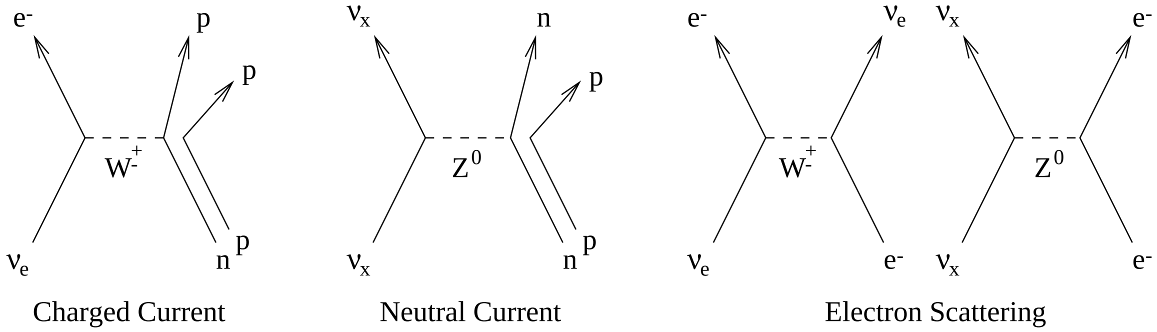

Figure 2.1: Interaction diagrams for the charged current, neutral current and electron scattering reactions of neutrinos on deuterium.

The neutral current reaction is the neutrino induced disintegration of the deuteron

$$\nu_x + d \longrightarrow p + n + \nu_x \qquad (Q = -2.22\,\mathrm{MeV}), \tag{2.2}$$

where ν_x is any flavour neutrino. The reaction has a threshold of 2.223 MeV, and is observed by the subsequent detection of the neutron. The neutron will thermalize in the heavy water and can be captured on deuterium with 23% efficiency to yield a 6.25 MeV gamma ray. The event is detected by Čerenkov light from Compton scattered electrons. The expected neutron production rate is 13.4 per day assuming the full Bahcall-Pinsonneault 1998 standard solar model prediction. After collecting sufficient charged current statistics, SNO will then increase the neutral current efficiency in two ways: by adding magnesium chloride salt and, separately, by installing neutral current detectors. With 2500 kg of $MgCl_2$ in a 0.2% D_2O brine the neutron will capture on ^{35}Cl with 83% efficiency to produce a gamma ray cascade totalling 8.6 MeV. With a threshold of 5 MeV about 6.6 NC events per day will be reconstructed inside the 775 tonne fiducial target (see table 2.1). For the second NC measurement, a 1 m grid array of ^{3}He filled gas proportional counters will be installed inside the acrylic vessel. The neutral current counters will provide event by event neutron detection with a 45% capture probability. The above neutron capture efficiencies depend on Monte Carlo of neutron transport in D_2O and probably have an uncertainty of several percent.

The third neutrino reaction with heavy water is neutrino-electron scattering

$$\nu_x + e^- \longrightarrow \nu_x + e^- \tag{2.3}$$

This is the reaction observed in light water Čerenkov detectors, but the event rate in SNO will be about one tenth of the charged current rate, depending on the flux of non-electron neutrinos for which the cross-section is one sixth of the electron neutrino cross-section. The angular distribution is

$$\cos\theta_{\text{sun}} = \frac{T_e(E_\nu + m_e)}{\sqrt{T_e^2 + 2T_e m_e}} \tag{2.4}$$

where T_e is the kinetic energy of the scattered electron and θ_{sun} is the angle between the electron and the neutrino. The angular distribution is strongly forward peaked and will be dominated by the angular resolution in SNO. The electron scattering reaction will provide a good second determination of the electron neutrino flux due to the angular distribution, but it will offer very little energy spectrum sensitivity after integration over the scattered electron energy.

The expected PMT hits distribution (the uncalibrated energy spectrum where the number of fired PMTs is referred to as NHIT) for the neutrino and background signals is shown in figure 2.2. The expected detector events rates for the CC, NC and ES reactions are given in table 2.1 at thresholds of 5 and 6 MeV with cuts for position reconstruction efficiencies. The details of the neutrino spectrum and the detector response used for table 2.1 are discussed in chapter 3.

The SNO detector will also detect anti-neutrinos in the heavy water by

$$\overline{\nu}_e + d \rightarrow n + n + e^+ \tag{2.5}$$

and in the light water region by

$$\overline{\nu}_e + p \rightarrow n + e^+ \tag{2.6}$$

Detection Process	Threshold	Events/year $R_{\text{fit}} < 600\,\text{cm}$	$R_{\text{fit}} < 550\,\text{cm}$
Charged Current	5 MeV	5016	3854
(0.47 SSM)	6 MeV	4154	3192
Electron Scattering	5 MeV	529	406
$(0.47\,\text{SSM}\,\nu_e + 0.53\,\text{SSM}\,\nu_\mu)$	6 MeV	371	285
Neutral Current - No salt	5 MeV	660	587
(full SSM, 4899 neutrons)	6 MeV	291	263
Neutral Current - 0.2% salt	5 MeV	2819	2409
(full SSM, 4899 neutrons)	6 MeV	1774	1530

Table 2.1: Expected event rates in SNO. The rates are calculated using the ^{8}B neutrino spectrum and neutrino reaction cross-sections discussed in chapter 3. The full SSM is for the BP98 model [18], and the 0.47 SSM is the ^{8}B flux as measured by Super-K [30]. The response and detector resolution function are discussed in chapter 3. The 5 and 6 MeV thresholds are assumed to be 41 and 49 PMT hits for both electrons (CC, ES) and gammas (NC). The NC rates are calculated using the SNOMAN neutron transport code. The cuts on the reconstructed event radius (R_{fit}) correspond to 1007 tonnes and 775 tonnes fiducial mass for 600 cm and 550 cm. The ES cross section is calculated using the Weinberg angle $\sin^2\theta_W = 0.231$ [5].

which provides sensitivity to supernovae and atmospheric neutrinos. In the event of a supernova within our galaxy, SNO can separately measure the charged current, neutral current and anti-neutrino fluxes of neutrinos.

2.2 The SNO Detector

2.2.1 The SNO Cavity

The SNO detector is located at the 6800 foot level (2073 m) of INCO's Creighton nickel mine near Sudbury, Ontario. The cavity is 300 m away from mining activity in the norite 'hanging wall' rock. The norite rock has good ground stability, lower levels of uranium and thorium and provides a 5900 m mean water equivalent cosmic ray shield. The cavity is barrel shaped which provides good geo-seismic stability and extra water shielding at the vessel equator. The cavity is 32 m high and 22 m in diameter at the mid-height. Ground control is accomplished with some 800 cable bolts cemented 10 m into the rock wall with steel screening and sprayed concrete (shotcrete). The deck support trusses are anchored on 16 rock bolts 15 m long. Ten sets of coils are fixed around the cavity wall to cancel the vertical component of the terrestrial magnetic field, which is 475 milli-Gauss at 15° from vertical. Finally the cavity is sprayed with eight layers of Urylon (polyurethane) to create an 8 mm barrier that is impermeable to water and reduces radon diffusion by a factor of 10^{-7}.

2.2.2 The Acrylic Vessel

The 1000 tonnes of heavy water is contained in a UVT acrylic spherical vessel (AV) 12 m in diameter with a 8 m high and 1.5 m diameter UVA acrylic chimney (see figure 1.9). The acrylic serves to isolate the D_2O to maintain its isotopic purity while transmitting the short wavelength Čerenkov radiation. The vessel is constructed from 125 spherically thermoformed panels bonded together underground. The AV thickness is nominally 5.5 cm, except for the equatorial band which is 11.4 cm to accommodate the support ropes. The bonds are 3 mm thick and made from partially polymerized acrylic adhesive by fabricating precision bonding dams which allowed for

Figure 2.2: Expected signal and background NHIT spectrum in SNO for one year of counting and one year of neutral current without salt assuming 0.47 SSM for charged current channel and full SSM in the neutral current channel. The PMT background is scaled by a factor 750 to yield 3.3×10^{10} events.

20% material shrinkage without forming exotherm or shrink voids. The AV panels and bonds are tested for radioactivity by neutron activation, mass spectroscopy and alpha counting.

The vessel is supported on 10 loops of 3.3 cm Vectran fibre rope 30 m long through rope grooves in the equatorial AV panels. Vectran was selected for its low radioactivity and long term strength in ultrapure water. The ropes are connected to see-saw rockers on the deck with load cell monitors.

The heavy water will be buoyed by 7600 tonnes of high purity light water. The light water shields the PMTs from γ-rays from the host rock and also shields the heavy water from radio-impurities in the PMTs. The AV was designed using numerical modeling to withstand the tensile load of hanging dry under its own weight and the compression load of heavy/light water fill, and various transients due to the possibility of a rope breaking or large seismic activity close to the SNO cavity.

2.2.3 Water Systems and Cover Gas

The water volumes in SNO provide both the detector target and the shielding and must be maintained at unprecedented high purity levels, as discussed in the following section on backgrounds. The water systems consist of separate H_2O and D_2O systems, each of which consists of a receiving circuit and a recirculation loop. The water systems will recirculate the water to provide temperature and purity equilibrium, while removing heat, radon, leached compounds, biological activity, and uranium and thorium chain elements. All components of the water systems are selected to meet requirements for amounts of leached contaminants, and the radon diffusion rate. The systems were constructed with a strict program of quality assurance to obtain the high cleanliness levels. The D_2O volume must be homogeneous, while the light water will be circulated from within the PMT support sphere to the outside cavity to minimize contamination from the cavity wall.

The H_2O receiving circuit (figure 2.3) accepts piped water from the mine potable water plant and removes sand, silt, bacteria, algae, inorganic salts, organic molecules and gases. The receiving circuit consists of a deaerator tank, multimedia filters, soft-

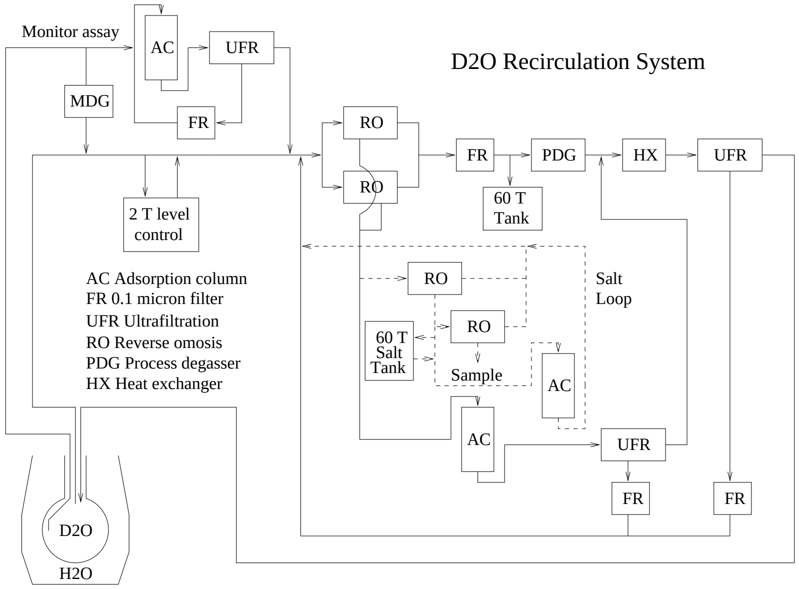

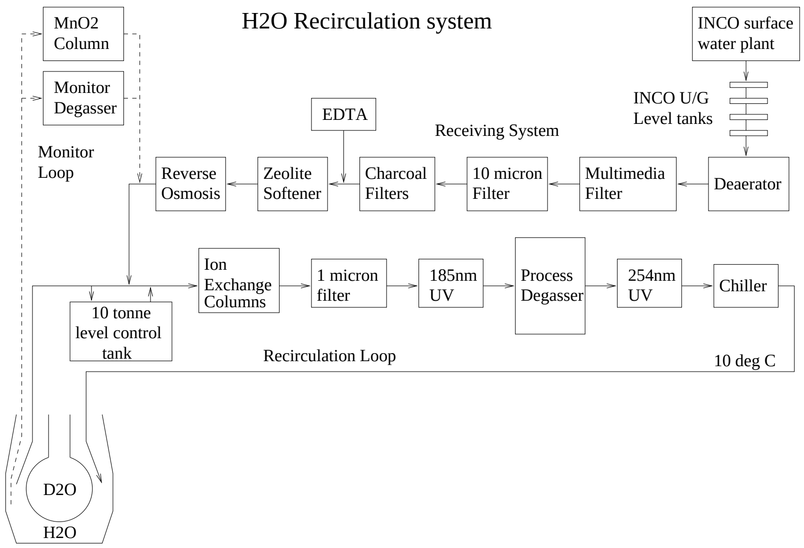

Figure 2.3: Outline schematic of the heavy water and light water purification systems.

eners and reverse osmosis units (ROs) before entering the recirculation loop. The H_2O recirculation loop includes ion exchangers, UV lamps, $1\,\mu$ filters, a process degasser and heat exchangers. The process degasser is a 6 m stainless steel column where oxygen, nitrogen, and radon gases are pumped off as the the water is run through shower heads in a 20 Torr vacuum. The recirculation flow rate is 150 l/min and the water is regularly assayed for radioactivity, pH, conductivity, suspended solids, bacteria and anions. The water is pumped into the cavity volume between the acrylic vessel and the PMTs, and pumped out from the volume behind the PMTs. Circulation is restricted between these regions since the outer volume is expected to be of much lower purity as it is in contact with the cavity walls and all of the PMT support structure surfaces and PMT cables.

The D_2O (figure 2.3) system must provide extremely pure water, remove heat and radon gas, provide level control, maintain strict control of the D_2O inventory and provide assay facilities. The D_2O is delivered from Ontario Hydro's Bruce heavy water plant and shipped underground in 6 tonne mine rail tanks. The D_2O is initially purified through ion exchange columns and then through filters coated with DTiO to remove the critical Th, Ra and Pb contaminants. The D_2O is stored in a 60 tonne polypropylene-lined tank to maintain an inventory for filling. The D_2O recirculation loop consists of parallel reverse osmosis (RO) units, 0.1 micron filters, the process degasser, heat exchangers and DTiO seeded ultra-filtration units. The RO concentrate passes through MnO_x adsorption columns where Th, Ra, and Pb is retained on coated beads. There is also an additional reverse osmosis loop for desalination following the $MgCl_2$ cycle as a neutral current detection option. Radioactivity monitoring is accomplished by α-counting the long lived Ra and Rn, which will not be in secular equilibrium. In one method the α's from ^{222}Rn emanation are counted using α scintillation in Lucas cells. A second method uses cryogenic trapping of the washed adsorbate from the MnO_x columns and counting with a windowless PIN diode.

The surface of the H_2O and D_2O are controlled with a cover gas system to prevent radon in the air from contacting the water. The cover gas is liquid nitrogen boil-off gas maintained at a small positive pressure. There are a series of buffer tanks to protect the vessel from transient changes in mine air pressure.

2.2.4 SNO Photomultiplier Tubes

The R1408 20 cm photomultiplier tube (PMT) manufactured by Hammamatsu was selected for SNO to provide the best compromise between high photocathode coverage, good single photon detection efficiency, small transit time spread, low noise rate, good reliability and low cost. Other important PMT characteristics are the charge resolution (evaluated by the peak-to-valley ratio in the single photo-electron charge spectrum), pre-pulsing, late-pulsing and after-pulsing rates and the voltage dependence of the noise rate. Long term deployment at high pressure under water also meant special attention to the design of the base housing, cable connector and cable. The materials for the glass, PMT base, base housing, cable and connector must have high resistance to leaching in ultrapure water and have very low radioactivity (U and Th chain impurities).

Of particular concern was U and Th activity in the glass which produces neutrons by (α,n) on Si, Al and Mg, which then capture in the large mass of the steel PMT support structure to produce high energy gammas. High energy gammas are also created directly from (α,pγ) on ^{27}Al. These high energy gammas penetrating to the D_2O will raise the detector threshold and contribute to the neutral current background by photo-disintegration of the deuteron. The SNO PMT glass bulbs are mushroom shaped for pressure stability and use a specially developed low radioactivity glass (Schott 8246), which also has excellent short wavelength light transmission.

The R1408 PMT is a 9 dynode Venetian blind design with two focusing grids and a compact dynode stack. The upper half of the PMT envelope has a 25 nm thick bialkali photocathode (K_2CsSb), while the lower half is aluminized. The PMT base operates with high voltage at the anode with the HV and the signal carried on the same cable (RG59/U). Set to operate at a constant gain of 10^7 the anode voltages range from 1700V to 2100V. The PMT bases were installed at Queen's University, and then the PMTs were tested for single photo-electron (SPE) response [52]. A total of 9829 PMTs were accepted for use in SNO with RMS timing resolution of

1.5 ns, noise rate 2.3 kHz at 20°C (about 1 kHz at 10°C in SNO), and a mean relative efficiency 1.1 times that of the prototype tubes. The bases were constructed with a kapton board and surface mount components to minimize the U and Th content.

The PMTs are assembled into hexagonal ABS plastic housings which incorporates a Winston cone aluminized reflector [53] to increase the effective photocathode coverage to 64% of the total 4π solid angle. The reflector also serves to limit the PMT field of view to the D_2O volume to further reduce background events. The hexagonal housings are clustered into panels of 7 to 21 PMTs which then mounted on to the steel geodesic icosahedron PMT support structure (PSUP). The PSUP also provides a light shield from the higher activity outer volume and creates a high impedance water flow to prevent mixing of the less pure outside shield water.

2.2.5 Electronics and Data Acquisition

The SNO electronics are a combination of custom and commercial integrated circuits in a custom architecture to meet the SNO requirements of 10,000 channels with 0.1-1000 photo-electrons (PE) dynamic range, sub-nanosecond timing, programmable channel parameters (thresholds, trigger etc), testing diagnostics and low cost. The electronics need to be able to handle a high trigger rate, up to 1 kHz for backgrounds and calibration, with almost zero dead time, and have a large burst trigger rate (1 MHz) for the possibility of detecting supernovae events.

The electronics are divided into 19 crates, each with a custom backplane (SNOBus) to process 512 PMT signals arranged in 16 front end cards (FECs) of 32 channels each. PMT interface cards (PMTICs) provide the high voltage (HV) isolation and trimming with breakdown/over-voltage protection and programmable calibration pulses. The FECs reside on one side of the SNOBus while the PMTIC cards with cable supports mate from the other side.

Each FEC has a mother board (MB) and 4 resident daughter boards (DBs) (to minimize cross-talk) which contain the bipolar chips (discriminators, amplifiers and integrators) and the CMOS chip (analogue/digital storage, TACs and trigger logic) for 4 channels [54]. There is a high and low gain amplifier for each channel which is sampled at a short and longer time for 4 possible charge readings, any three of which are stored. There is one CMOS chip (QUSN7) per channel containing dual time to amplitude converters (TACs) and sixteen analogue storage cells for 4 charges (the three charge samples plus the TAC level). The TAC starts charging on any discriminator gate and is stopped if and when a global-trigger valid signal (GT valid) is received. The two TACs alternate to allow a stable reset with no dead time. On a GT valid the 4 charge samples (charge and TAC) are stored on QUSN7 along with the analogue cell number and a GT sequence number generated on the MB to enable later event building. The QUSN7 chip also has a rate counter, error bits and a data available flag.

The MB has four $2\,\mu$sec ADCs and a field programmable gate array (FPGA) sequencer. The sequencer selects each QUSN7 in turn and reads out each analogue cell for the ADC and stores the digital data, along with the GT sequence and flags, in on-board SIMM DRAM memory. It is this combination of analogue storage and large front end memory that provides the deadtime-less operation and huge burst rate capability.

The trigger is initiated with current pulses generated on QUSN7 with a 100 nsec resolving time, and a delayed 20 nsec pulse for some background analyses. These pulses are summed on the DB, then on the FEC, then summed over each FEC on the crate trigger card. The MTC/A then sums over the 19 crate trigger cards and compares the sum to a threshold setting. Although there are potentially 9522 channels in this sum, the comparator needs a dynamic range less than 100 hits, since the threshold will be about 45 hits (5 MeV). On the MTC/D the summed trigger is ORed with any additional (calibration) triggers and latched with the 50MHz clock. Channels associated with the outward looking PMTs (OWLs) and the low gain dynode taps (LGTs) are summed separately with different trigger conditions. A second trigger is generated in a similar way by summing directly a copy of the PMT analogue pulses (ESUM). This trigger is appropriate for certain background events that may deposit a large charge in one or several PMTs but with a low number of total PMTs hits. There is also a 10 MHz GPS corrected clock for long term timing precision, and the synchronization of astronomical events (eg. supernovae) with other observatories.

The data acquisition system consists of a VME crate with a Motorola 68040 single board computer (eCPU), SNOBus to VME translators for each crate (XL1s), a PCI-VME interface for Macintosh dual port memory (MDPM), and a SUN-VME interface for SUN dual port memory (SDPM). The eCPU reads each FEC/crate in turn through the XL1 by addressing each FEC according to an algorithm that depends on previous activity. The eCPU reads all PMT data and trigger information from the MTC and stores it in the SUN's circular buffer (the SDPM). The eCPU reads data and commands from the Mac dual port memory for controlling the HV, initializing and programming the sequencers on each FEC and setting all FEC parameters (discriminators etc.).

The SDPM is read by a SUN Ultra Sparc1 167MHz workstation which builds the events according to GT number and writes the data stream to disk and tape (DLT4000). The SUN also ships data to surface for tape archive via a dedicated ethernet link. There is a dispatcher server to broadcast a fraction of the events over ethernet for other computer clients to monitor, run event displays or check data integrity. The events are stored in a buffer for a short period of time to wait for the possibility of late hits. The data stream is written in CERNLIB ZEBRA exchange format.

A 225 MHz Macintosh Power PC (the DAQ Mac) provides a user friendly graphical interface for the control and monitoring of the entire detector. The FECs and MTC are programmed, controlled and monitored via the VME eCPU commands communicated through the MDPM. Commands are, for example, setting discriminator thresholds, ramping high voltage, PMTIC relays, sequencer upload, reading rate monitors, synchronizing the GT counters and many other control and monitor tasks. The DAQ Mac also provides a graphical interface for computerized control of the calibration source manipulator and other calibration hardware (see next section) through a TCP/IP ethernet link. The DAQ can insert status information into the data stream through the MDPM.

There is also a laboratory wide control, monitors and alarms system (CMA). This is to monitor and control such variables as air monitoring and handling (cooling, temperature, humidity, pressure, hazardous gases), PSUP and AV loadcells, deck superstructure (corbels) monitor, lab electrical, magnetic field compensation, DAQ HV monitors, water system monitoring, seismic sensors, and fire protection. The CMA provides a central database for lab systems status for safety, systems maintenance and for possible correlation with detector event data. The CMA is implemented by Intec Control Paragon TNT automation software for Windows NT using a Sciemetric Instruments analogue/digital control system. The CMA can be monitored and controlled at locations underground or on surface. Many of the inputs are from other computers (eg. DAQ and calibration) while other inputs are direct analogue or digital data.

Finally the raw data stream is processed by a run logger and a data bank validation processor (a checksum) before available for off-line analysis. General analysis uses the SNOMAN code (SNO Monte carlo and ANalysis, described in chapter 3.3) which accesses the SNO database to calibrate the PMT data for each event (pedestals and time calibration etc). A typical SNOMAN analysis would then apply various cuts to the event data, then reconstruct the event with a fitter, then possibly apply further cuts before histogramming the data in energy (NHITs) (or other binning, eg. time or angle to the sun). A more flexible method of analysis is to store various computed event quantities (eg. NHIT, fit radius, etc) as a CERNLIB Ntuple for later histogramming with cuts.

2.2.6 Neutral Current Detectors

Neutron detectors are designed for SNO to detect neutral current events on an event-by-event basis to provide a precision measurement for the CC/NC ratio. The detectors are vertical strings of ^{3}He-filled proportional counters arranged on a 1 m grid within the D_2O. Neutrons are thermalized in the heavy water and captured in the tubes by ^{3}He(n,p)^{3}H which has a large 5330 barn cross-section. The tubes are 5 cm in diameter, and 96 strings are made from tubes $2 - 2.7$ m long, for a total length of 750 m. The counter strings will be attached to anchors on the bottom of the AV using a remote submersible vehicle (ROV). The anode wire (50 μm copper) is at 1800V and the counters are at 2.5 atm pressure with 15% CF_4 for charge amplification. The tubes are made from chemical vapour deposition nickel (CVD) on an anodized aluminum mandrel to provide the cleanest low-background tubes. The counters are stored for 18 months underground to allow cosmogenic activities to cool down. The longest lived being ^{60}Co with a 78 day half-life. The deuterium photo-disintegration background is expected to be less than 300 neutrons per year based on neutron activation and direct counting assays of the components. This neutron production rate corresponds to 38 μg U or 3.3 μg Th in equilibrium. The neutron capture probability is 45%, but this is reduced to 25% for unambiguous discrimination from alphas (using track length versus energy). The counters will absorb about 12% of optical photons from charged current interactions.

2.3 Detector Performance and Backgrounds

SNO is designed for superior energy resolution, angular resolution, and vertex reconstruction. The anticipated performance characteristics are summarized in table 2.2.

Parameter	Value
Location	46° 28'30"N, 81° 22'4"W
Depth	5900 MWE
Mass D_2O	1016.5 tonnes
Fiducial Mass	774.3 tonnes
Inward PMTs	9456
Outward PMTs	92
Low gain PMTs	66
Photocathode coverage	64%
NHIT response (10 MeV)	8.2 PMTs/MeV
Energy resolution (10 MeV)	14%
Threshold	5 MeV
Position resolution (10 MeV)	21 cm
Angular resolution (10 MeV)	24°

Table 2.2: SNO detector parameters and performance for electrons.

With the low counting rates expected for neutrinos it is critical for SNO to be free from background signals that are not easily distinguishable from the neutrino detection channels. The primary shield is SNO's location deep underground which removes all cosmic rays except muons and neutrinos, and reduces the muon flux to about $95\,\mathrm{m}^{-2}\mathrm{year}^{-1}$ (about 59 per day through the 8.5 m PMT sphere). The muons will be unmistakable as they fire almost every PMT in the lower half of the detector in time sequence Čerenkov rings. SNO is instrumented with 92 outward looking PMTs to see muons that will graze the light water volume and perhaps scatter light into the inner volume. Muons will also produce spallation daughters on ^{16}O which are identified by delayed high energy betas (up to the 13 MeV endpoint). The 29 muons per day passing through the heavy water will produce about 1.8 spallations per day.

The greater background concerns are naturally occurring radioactivities in the surrounding rock and detector components, in particular ^{40}K, ^{235}U, and the decay chains associated with ^{232}Th and ^{238}U. In addition to the β-rays and γ-rays from these decay chains, there are also high energy gamma ray and neutron backgrounds from (α,pγ) and (α,n), (n,γ) reactions on light elements at the cavity wall or the PMTs and PMT support structure (PSUP).

The charged current background is made up from i) high energy tail due to poor energy resolution from the low energy γ and β internal radioactivity, ii) high energy γ's from the cavity or PMTs that penetrate to the D_2O volume, and iii) low and high energy β's and γ's that convert outside the D_2O volume but occasionally get mis-reconstructed within the D_2O by the fitter.

The neutral current background is due to free neutrons from photo-disintegration of the deuteron by γ's with energies above the 2.22 MeV Q value. The main source is ^{232}Th and ^{238}U chain radio-nuclides (see figure 2.4) within the D_2O and acrylic vessel, due to ^{208}Tl and ^{214}Bi which produce 2.615 MeV and 2.445 MeV γ's, respectively (see figure 2.5). Since these γ's will mostly Compton scatter off electrons, a calculation using the Klein-Nishina and photo-disintegration cross-sections shows that 1 in 485 2.615 MeV γ's and 1 in 688 2.445 MeV γ's will produce a neutron. The neutral current background will also be a source of background for the charged current, following

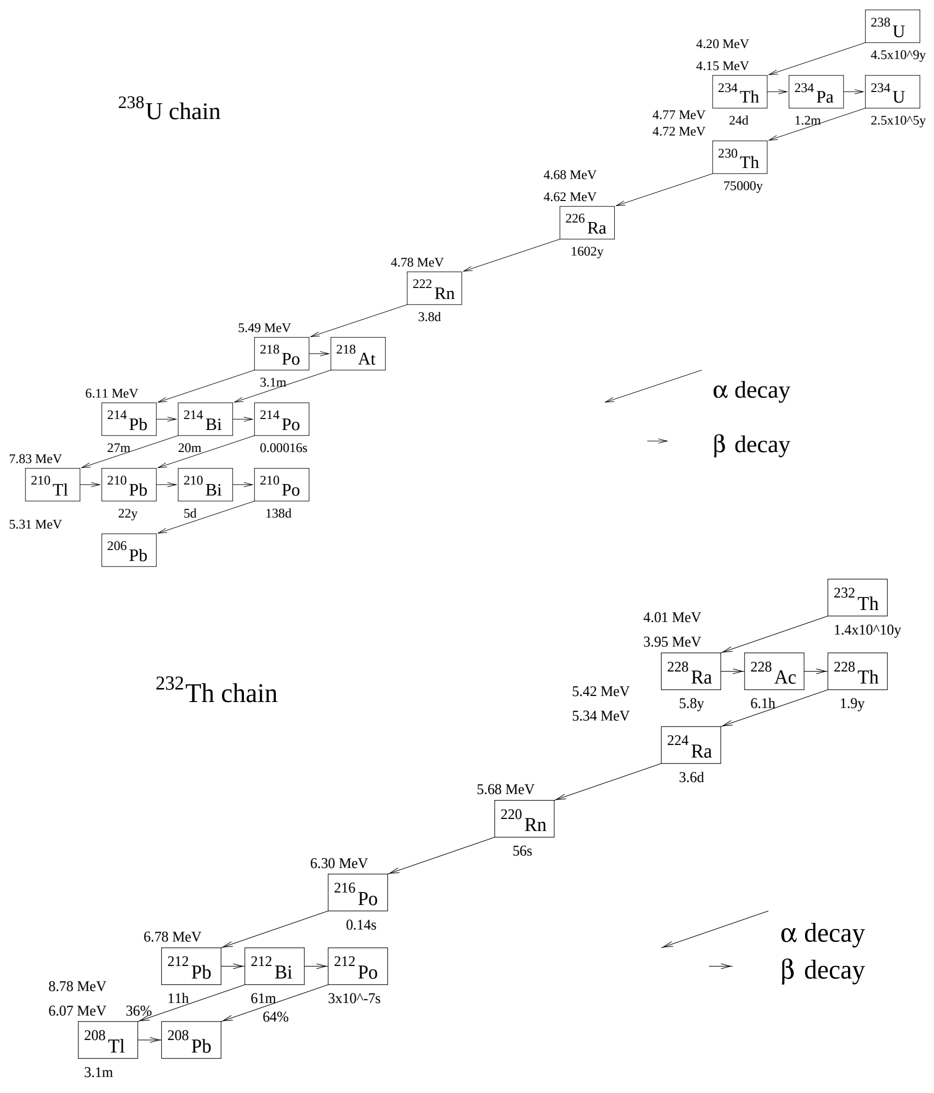

Figure 2.4: The ^{232}Th and ^{238}U decay chains.

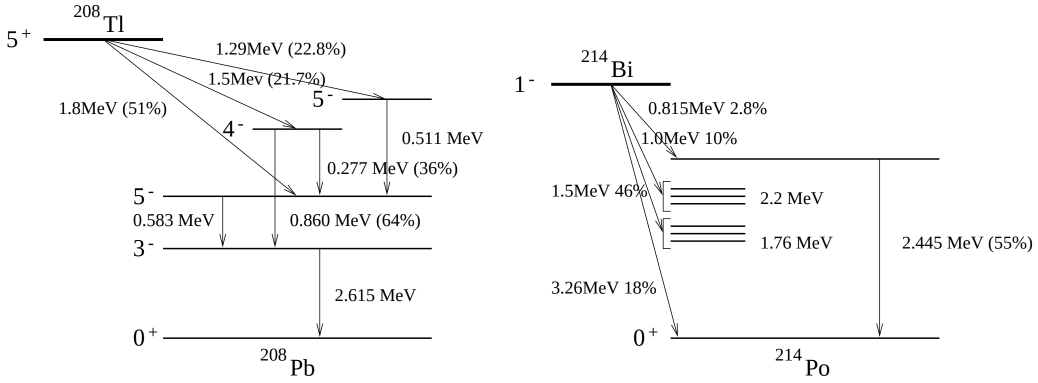

Figure 2.5: Simplified decay schemes for ^{214}Bi and ^{208}Tl.

neutron capture on deuterium or chlorine in the salt.

These background concerns lead to the present detector design with light water shielding both the PMTs from the rock and the D_2O from the PMTs, and the close attention to the radio-purities of construction materials, and the attention to cleanliness during construction. Neutron transport and shielding calculations [55] established the target maximum impurity concentrations given in table 2.3 assuming the background rates should by less than 1% of signal. For all detector components the targets have been met or exceeded.

	Design		Actual	
Material	^{232}Th g/g	^{238}U g/g	^{232}Th g/g	^{238}U g/g
Norite			3.3×10^{-6}	1.2×10^{-6}
PMTs	1×10^{-7}	1×10^{-7}	3×10^{-8}	3×10^{-8}
Acrylic	1.9×10^{-12}	3.6×10^{-12}	1×10^{-13}	1×10^{-13}
$MgCl_2$	1×10^{-12}	1×10^{-12}	1×10^{-12}	1×10^{-12}
H_2O	2.2×10^{-14}	1.5×10^{-14}	1.0×10^{-14}	5×10^{-13}
D_2O	1.1×10^{-14}	1.1×10^{-14}	3×10^{-15}	1.0×10^{-14}

Table 2.3: Trace radioactivity in SNO materials.

The NHIT spectra for the expected signals and backgrounds are shown in figure 2.2 for events reconstructed within a 550 cm fiducial radius (approximately 750 tonnes).

At very low energies (3−4 MeV) the background is dominated by PMT β−γ's, while at threshold (5 MeV) the D_2O and acrylic internal activities dominate. The high energy tail for the internal backgrounds is due to photodisintegration of the deuteron, thus the neutral current background scales directly with the charged current background for the dominant internal sources. The total (summed) background spectrum as referred to as the "background wall" due the very rapid fall off at threshold. This "wall" effect of the background spectrum means that uncertainty in the detector energy calibration translates into an uncertainty in the background rate. For example, a 100 keV shift up in the energy scale amounts to a 30% reduction in the background flux at fixed threshold.

2.4 Detector Calibration

To achieve the physics objectives of SNO experiment the detector response to electrons, gamma rays, and neutrons must be calibrated. A comprehensive calibration of the detector will be the result of various source deployments and Monte Carlo simulations.

The philosophy in calibration is that given a fitted event, the calibrations will provide the event energy with an uncertainty. The fitted event will have a certain number of fitted PMT hits, a position, a direction and a goodness of fit estimation. The calibration will be a detector response function that incorporates the measured optical parameters. The response function will be verified and scaled with Monte Carlo simulations of the response to electrons over the variable detector parameter space. In turn the Monte Carlo is scaled and constrained by the various calibration sources that will be deployed throughout the detector.

The detector calibration consists of several tasks: electronics calibration, optical calibration and the determination of the detector response for electrons, gamma rays and neutrons. The electronics calibration involves determining the PMT time offsets, charge pedestals, time slopes, charge gain and threshold for each PMT channel. The charge versus time (QvT) correction must also be mapped, and the time resolution measured for each channel. The optical calibration will determine the optical response of the detector, which depends on the light attenuation lengths, light scattering distributions, and PMT light detection efficiencies. The energy calibration will determine the detector hit pattern response to electrons and gamma rays, including the energy scale, energy resolution, and angular resolution. Finally the efficiency for neutron detection will be measured as a function of source location.

2.4.1 Calibration Source Manipulator

The response of the SNO detector to electrons and gamma rays is quite complicated due to light absorption and lensing effects in the acrylic, and light absorption in heavy water. In particular the NHIT response varies with the event position radius due to the variation in optical path lengths through the heavy water and the acrylic panels. Also the neutral current detection efficiency will drop rapidly close to the AV. For these reasons it is critical for SNO to be able to calibrate by moving sources within the heavy water and to access regions outside the AV.

The manipulator system allows calibration sources to be moved to off-axis positions throughout the D_2O; it consists of the sources, a source manipulator, and an umbilical storage/retrieval system. The source manipulator is a carriage located in a plane by three 1/16" ropes (figure 2.6). The centre rope connects directly to the source carriage, while the side ropes run through pulleys on the carriage to fixed locations on the acrylic vessel 10° above the equator. In this way the source carriage can visit 70% of the plane with a position accuracy of better than 5 cm under reasonable tension conditions. There will be two manipulator source planes within the D_2O vessel. The ropes are operated by tension and length feedback control employing stepper motors, optical shaft encoders, load cells and real-time control software. At the neck/vessel junction of the acrylic vessel, the manipulator ropes run over a smooth ring that mounts inside of the various water pipes and the NCD cable ring. The sources mount to a flange on the carriage, with an optional buoyancy control weight cylinder.

The source umbilicals are standardized flexible cables that provide a connection between the sources and other equipment on deck, for example power lines, fibre-

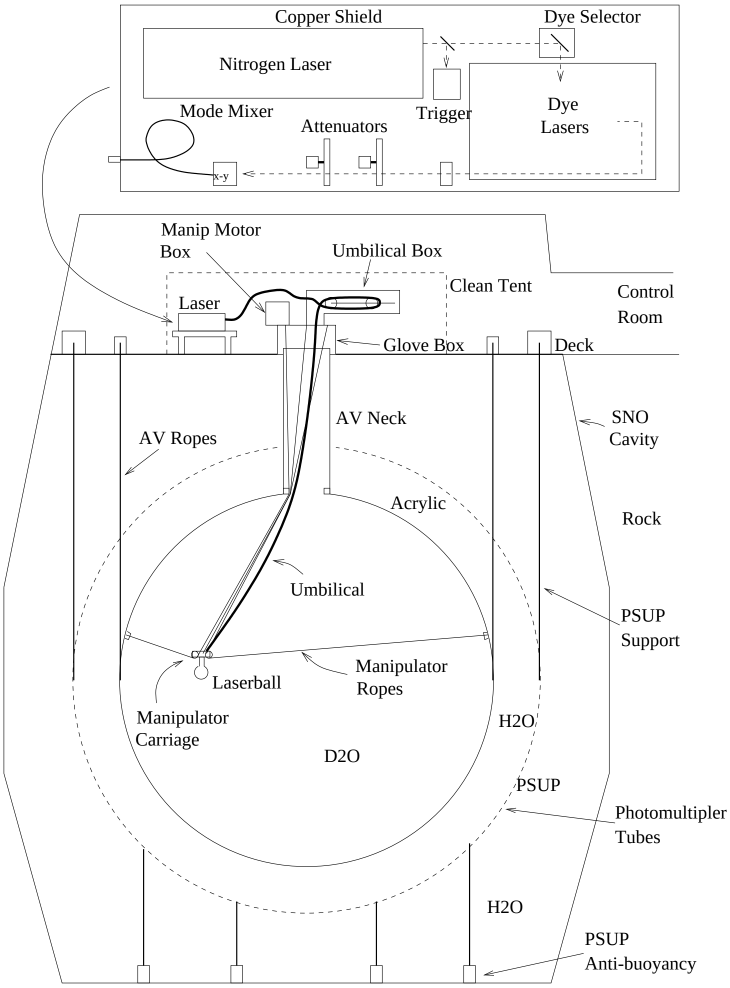

Figure 2.6: SNO calibration source manipulator system.

optics or gas capillary tubes. The umbilical retrieval mechanism stores and feeds out the umbilical in a way that does not involve rotating or twisting connections (figure 2.7). The pulley carriage is held under tension with a compressed air piston, and the umbilical is fed out with a motorized pinch roller, with length and tension control from an optical shaft encode and load cell. The umbilical is a 1/2" o.d. silicone tubing, selected for its flexibility and cleanliness. The required cable components are helically wound and pulled through the tubing, then the umbilical is potted with RTV silicone (GE-RTV615). The umbilical runs through the centre of the source carriage to a compression fitting at the top of the source. The cable connections are then internal to the source.

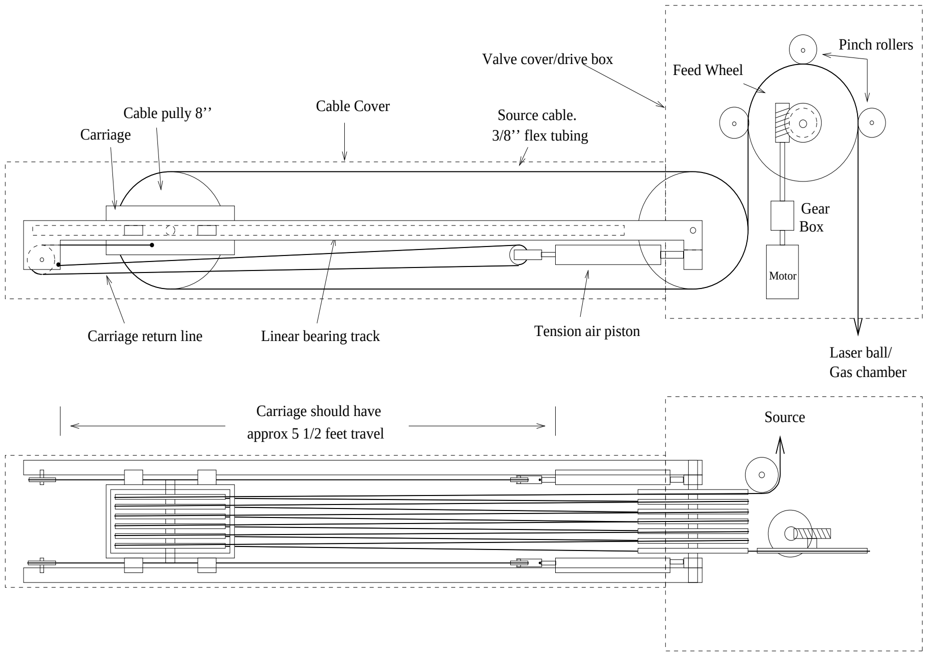

Figure 2.7: SNO umbilical retrieval mechanism.

2.4.2 Optical Sources

The optical sources are used to provide the electronics calibration and the optical calibration. To provide these calibrations an optical source must be pulsed so that the light will trigger the detector as an event which can be distinguished from other events or noise. The source should also have long term stability, good pulse-to-pulse stability, and have a large intensity range. A very short pulse width, a nanosecond or less, is required for timing calibration of the PMTs and to study effects of light scattering. Finally the light should be reasonably isotropic within the detector and have one or several light frequencies in the 300-400 nm range where the detector optical efficiency has the greatest variation.

An N_2/dye laser with a fibre-optic cable to a diffuser ball is the primary light source. The laser (Laser Photonics Inc. LN203C) provides pulsed radiation at 337.1 nm with a 600 psec pulse width and peak power of 150 kW. The laser pulses up to 45 Hz and can be used directly or as a pump for several dye lasers which provide wavelengths in the range of $360 - 700$ nm. Neutral density filters mounted into two selector wheels allow remote intensity adjustment. The laser light is delivered to a diffuser ball via a fibre optic bundle cabled within an umbilical. The diffuser ball gets attached to the calibration manipulator carriage for deployment within the detector (see figure 2.6). This system, called the laserball, was designed and constructed by the author and is described in detail in chapter 4. The laserball has been used extensively in SNO commissioning and electronics calibration. Some of this data and analysis is discussed in chapter 6.

A second optical source uses single bubble sono-luminescence (SBSL), which occurs when an air bubble is introduced into water at the node of an intense spherically symmetric sound field. The light production mechanism is still unknown, but it has a very short (< 0.1 nsec) pulse width, a frequency distribution corresponding to about 10,000 - 40,000°C and it occurs at the apex of the compression phase [56].

The SNO sono-luminescence source consists of a 250 cc boiling flask with two cylindrical piezo-electric transducers. This is housed within a sphere of two 15 cm radius hemispherical acrylic sections to provide an air buffer. The flask is filled with pure distilled water to the neck level, and driven at the natural monopole resonance (28.5 kHz) with a matched inductive circuit. The circuit consists of a stable function generator (Hewett Packard 8904A), a 500 W sound amplifier and a tunable inductor in series with the piezo-transducers. A small microphone transducer aids in scanning the frequency to find the natural resonance.

A bubble is generated remotely with a nichrome heater wire within the water. The bubble stability is monitored by observing the spikes on the microphone voltage trace. As sono-luminescence output begins, the light output is monitored with a small PMT (Hammamatsu R5600) within the acrylic source housing. The light output contains the order of a million blue photons and is very isotropic over time scales of seconds or longer. The SNO detector will provide an opportunity to investigate short time period behavior of the sono-luminescence bubble. The heater wire also provides some control over the light intensity, which decreases with increased water temperature. The short pulse width and isotropic output will make the sono-luminescence source useful to check PMT timing calibrations and some optical analysis.

The rotating source is a Nichia blue LED (NSPB500) with a fast pulser circuit set at the focus of a 10 cm parabolic reflector. The source is rotated by stepper motors on two orthogonal axes. The second axis steps after every complete revolution on the first axis, so that the pulsed light beam systematically sweeps through the full solid angle. The beam focus is adjustable to illuminate about 20-200 PMTs with the source at the centre of the detector. The pulse rate is 5 kHz.

The rotating source will be used prior to the first electronics calibration to verify that the channels are connected properly (both in hardware and software). The data will be stored as a histogram for each channel of the distance from the PMT to the mean position of the hit PMTs. If the peak is not within the beam footprint size then the PMT is connected to the wrong channel, or there is an error in a software mapping.

During the final construction stages of the PMT support structure (PSUP) new LED products became available from Nichia corporation. These indium-gallium nitride single quantum well (NSPB500) and double hetero-structure (NLPB500) devices offer high intensity blue radiation (420-480 nm) with nanosecond rise times. The DH device can even emit in the UV (380 nm) when strongly over driven in pulse mode [57]. Several of these devices have been packaged with a pulser circuit and mounted at various locations on the lower PSUP. These beacons may prove useful for verification of water transparency and the acrylic vessel and source positions. Also these devices can be incorporated into other calibration sources or potted into the umbilicals.

2.4.3 Gas Transport Sources

The gas transport sources consist of a D-T generator neutron source, a neutron target chamber, gas capillaries and decay chambers that can be deployed within the detector. The D-T generator, producing 14 MeV neutrons, is enclosed in concrete 30 m from the detector. Various target chambers can be moved into the neutron flux by stepper motor control. Gases from the target chamber are routed via capillaries to the deck area and down into the source umbilicals. The decay chambers can attach to the manipulator carriage and connect to the umbilical gas lines.

Three gas transport sources are currently being manufactured: a ^{16}N gamma ray source, a ^{17}N neutron source and a ^{8}Li beta source [58]. The ^{16}N is produced via (n, p) on oxygen and decays with 7.13 second half-life by a beta delayed 6.13 MeV (68%) or 7.12 MeV (4.9%) gamma ray. The target will be carbon dioxide; but oxygen gas, carbon dioxide or oxygen rich material such as glass fibres, cotton or cellulose can also be used. ^{16}N can also be produced with (n, α) on ^{19}F using targets such as Teflon. The decay chamber is 19 cm long and 7 cm radius, it is made from 5 mm thick steel so that the 10 MeV endpoint electrons are absorbed, but not the gamma rays. A beta tag is provided by a 10 mm thick scintillator sleeve on the inside of the chamber with a 2" PMT. The ^{16}N source will produce about 300 events/sec.

The ^{17}N isotope is produced in a similar way from the rare ^{17}O isotope. It has a 4 second half-life and decays with a beta delayed neutron. With a similar decay chamber, the anticipated yield is about 10 neutrons per second.

The ^{8}Li is produced by (n, α) on ^{11}B and is transported on a helium NaCl aerosol to the decay chamber. With a one second half-life it decays to a broad 2+ state of ^{8}Be which subsequently breaks into two alphas. The chamber wall is only 0.0020" thick so that the beta passes with only a 250 keV energy loss. The decay chamber is 1 m long and has a counter wire with a signal line from both ends. This permits tagging of the decay with the alpha and localization of the event by charge division from the two signals. The expected event rate is about 1 Hz. The significant advantage of calibrating with the ^{8}Li source is that the beta decay final state for ^{8}Be is the same as for the ^{8}B decay, and hence cancels some of the theoretical uncertainties in the ^{8}B solar neutrino spectrum [67].

2.4.4 Tagged Sources

Two high energy gamma ray sources are presently under development. These accelerator sources consist of a cold Penning trap ion source, electro-optics for beam extraction and acceleration, and a fixed target. Getter pumps are used to control the partial pressure of the hydrogen discharge gas in these sources. The first source employs a tritium target inside a 10 inch diameter by 24 inch stainless steel capsule [59]. The gamma-rays are generated through proton capture on tritium, which has a Q-value of 19.8 MeV. The beam voltage is $20-30$ kV. The second source has a ^{7}Li target producing gamma rays at 14.3 MeV and 17.3 MeV [60]. The beam voltage is 70 kV.

A source is constructed from a NaI crystal coupled to a PMT. The crystal is activated within the neutron source pit to produce the ^{24}Na isotope. ^{24}Na has a 15 hour half-life and beta decays ($Q = 5.51$ MeV) with a 1.37 MeV and a 2.75 MeV gamma ray. The trigger can be gated on the energy deposited in the NaI such that the 1.37 MeV, the 2.75 MeV, or the sum gamma ray peaks are preferentially selected.

Neutron sources are fabricated using ^{252}Cf with several activities mounted in plastic scintillators. The ^{252}Cf half-life is 2.64 years, it decays with a spontaneous fission branch at 3.09% which will provide neutrons and a trigger from fragment beta-gammas. The scintillator trigger will emit about 25,000 photons, resulting in about 2000 - 3000 PMT hits, depending on position. The 97% branch is to ^{248}Cm with only low energy gammas (< 100 keV), and a 3.5×10^{5} year half-life.

Triggered sources have been developed which permit specific backgrounds in SNO to be calibrated [61]. The source is a Lexan housed proportional counter with a radioactive source (eg.^{228}Th) deposited on the anode wire. The wall thickness is

0.7 mm with the Čerenkov production in the wall compensating for the beta particle energy loss. The counter has a 12 μm stainless steel wire in a 50.6 mm long by 5.0 mm radius volume of P10 gas (90% Ar, 10% methane). The cathode consists of a 20 μm aluminum foil on the inner wall of the Lexan, which also serves to block scintillated and arc light from the counter gas avalanche. The pulses are digitized for a pulse shape analysis. The counter wire will also provide a detector trigger so that delayed coincidences and tagged betas can be detected in SNO with a low threshold.

2.4.5 Electronics Calibration

Electronics calibration determines the constants that allows converting the digitized values for the PMT charge and time into photoelectrons (PE) and time. The charge is first converted to pico-Coulombs, then to PE's after calibration of the channel gain. The time is converted to nano-seconds using a function for each TAC, then corrected for discriminator walk and multiple photoelectron threshold effects by mapping the charge versus time (QvT) for each channel.

The charge calibration begins by finding the charge pedestals, which is the ADC value for zero charge. The integrators deliberately leak some charge onto the capacitors after the discriminator fires so that the integrators are operating linearly down to zero charge. The DAQ performs pedestal runs by sending an event trigger to each QUSN7 in sequence for a fixed number of measurements (eg. 20), then the mean and RMS is calculated. Pedestal runs can operate concurrently with neutrino runs, with the calibration data mixed into the data stream. The DAQ then begins a sequence where each PMTIC receives a charge injection with increasing amplitudes. A best fit slope is calculated off-line to obtain the charge slope calibration. Finally the PMT PE gain calibration is obtained from single photoelectron (SPE) laserball runs and fits to the shape of the SPE charge spectrum.

The time zero offset is obtained from a laserball calibration run with the laserball at the centre of the detector. The time offsets account for transit and propagation delay differences between channels and is essential for event reconstruction, which requires the relative photon arrival times at the PMTs. The time slope is found similar to the charge slope via time delayed pulses on the PMTICs. The walk correction is found by mapping the QvT for a series of laserball runs that completely cover the intensity range from SPE to 100's of PE.

Note that full charge and time calibrations are required for each of the 16 analogue storage cells on every channel. Detailed issues about electronics and PMT calibrations are described in chapter 6 where the author's independent electronic/PMT calibration method was developed during SNO commissioning.

2.4.6 Optical Calibration

The optical calibration is the determination of the heavy water, light water and acrylic attenuation coefficients and scattering coefficients. Also, the relative PMT quantum efficiencies, PMT occupancies and the overall optical gain of the detector are to be monitored over time. Understanding the optical condition of the detector is central to the electron response calibration and extraction of the neutrino physics. The detector optics will be analyzed from the arrival time distribution for each PMT using the laserball at various detector positions and wavelengths. The PMT time histograms can be integrated over several time slices that correspond to prompt light, scattered light and distinct reflection paths. With the laserball at several positions there will be many different path lengths through each of the D_2O, acrylic and H_2O to permit multi-parameter fitting to the extinctions. Also effects such as changes in diffuse scattering off the acrylic or PMT reflectors will cause shape changes in the time histograms.

The measured optical constants will then become the inputs for a calculated detector response function for electrons and gamma rays. This idea is developed in chapter 5.

2.4.7 Energy Calibration

After correcting for the relative response due to position and direction, an event is assigned an energy according to a calibrated NHIT scale. The ^{16}N source will set the absolute scale and provide a measurement of the energy resolution for a 6.1 MeV gamma ray. The difference in response between gamma rays and electrons is well modeled with the EGS4 code and will not contribute significantly to the uncertainty. The 6.25 MeV gammas from neutron capture with the ^{252}Cf will also be used. The noise rate will be counted with scalars on each PMT so that the zero offset (about 1 PMT hit) can be calculated. Event noise is also measured from PULSE-GT events, where a GT signal is sent to all crates without any trigger conditions having been met. The PULSE-GT events are initiated from a pulser (eg. at 5 Hz) and provide a sample of the quiescent detector. The high energy end of the energy scale is more difficult but not as critical. The (p, γ) accelerator sources (^{3}H and ^{7}Li) will be deployed as they become available to provide higher energy calibration points.

The ^{8}Li source provides a beta spectrum where the shape can be fitted to the Monte Carlo of the ^{8}Li spectrum to yield an energy scale. Theoretical uncertainties in the energies of the ^{8}Be* final states cause a spectrum scale uncertainty of about 70 KeV (1σ) [65]. A ^{8}B neutrino charged current analysis is possible by considering the ratio of the detected neutrino spectrum to the ^{8}Li source spectrum [67]. Much of the theoretical uncertainty involving the forbidden and radiative corrections then cancel in the ratio.

2.4.8 Position and Angular Resolution

Position resolution is measured by reconstruction of low intensity laserball events and from a Čerenkov source (^{90}Sr encapsulated in acrylic). The detector position resolution can also be measured with the ^{8}Li gas source. The event position is known to about 10 cm, which is sufficient for measuring the expected 25 cm detector position resolution. This includes uncertainties in the source manipulator position and charge division position determination from the gas chamber counter wire.

The detector angular resolution cannot be properly measured without a collimated electron source. However, it can be verified against the Monte Carlo using the ^{16}N gamma source. If the fitted event position is taken to be the point of momentum transfer from the gamma ray to the electron then the initial direction is the vector to this position from the source position. A cut on large radial distances reduces the source angle uncertainty, while a cut on the larger NHIT events will select mostly those events of large momentum transfers to the electron in the first scatter.

There is also a unique opportunity to make this measurement in a clean way during partial heavy water fill, with the ^{16}N source about 3 m above the water interface. This configuration avoids the problem of events close to the source that may get improperly misfit at a distance from the source. The mis-reconstructed events are difficult to separate for the source in water due to the much larger number of gamma conversions close to the source.

2.4.9 Neutral Current Calibration

The neutral current (flavour independent) reaction in SNO is detected by the subsequent neutron capture on deuterium, added chlorine ($MgCl_2$) or in the neutral current detectors (NCDs). The capture efficiency must be measured since it will fall off rapidly near the H_2O and may vary slightly with any water impurities and detector asymmetry (water pipes etc).

The neutron efficiency will be measured with the ^{252}Cf source using the scintillator tag with a time window of 10's of milliseconds. Background events above 5 MeV within this time window are negligible. The proportional counter background source can also provide tagged neutrons (with ^{228}Th) using pulse shape discrimination of the wire pulse.

Chapter 3

Neutrino Detection and Event Simulation

The SNO detector is sensitive to solar neutrinos from the decay of ^{8}B, and *hep* neutrinos over 15 MeV (figure 1.3). The shape of the ^{8}B energy spectrum depends only on the physics of beta decay and not on the structure of the sun. Thus detecting any change from the expected beta decay spectrum will be evidence for new neutrino physics. In this chapter we make a calculation of the ^{8}B neutrino spectrum and compare to recently published spectra. The CC and NC reactions on deuterium are discussed and the ^{8}B spectrum is then used to calculate the expected signal in SNO. We then describe the SNO Monte Carlo and discuss the predicted SNO detector response and event reconstruction (event fitters). Some useful parameterizations are provided for the SNO energy response (gain and resolution), angular resolution, threshold efficiencies and systematic fitter effects. Finally, the expected detected energy spectra in SNO for ^{8}B neutrinos with no MSW oscillations, and for the large angle and small angle oscillation hypotheses are presented.

3.1 ^{8}B Neutrino Spectrum

^{8}B decays to an excited state in ^{8}Be via a Gamow-Teller transition with the emission of a positron. The ^{8}Be* is unstable and subsequently decays into two alpha particles resulting in a broad width for the ^{8}Be* final state (see figure 3.1). The ^{8}B (and ^{8}Li) β and neutrino spectra thus require averaging over the intermediate ^{8}Be 2^+ level, the profile for which is not well known. The spectrum can be calculated by using the measured 2α data to represent the ^{8}Be 2^+ level profile. A further complication is that forbidden and radiative corrections are significant at the high endpoint energies. The mass-8 system has been studied for violation of the conserved vector current (CVC) or G-parity hypotheses, and a neutrino spectrum has been calculated by Bahcall and Holstein [63] for solar neutrino studies. A difficulty is that the 2α data suffer systematic uncertainties in the energy loss at the detectors. The uncertainties are worse at low energies, which correspond to high neutrino energies, the region of interest for solar neutrinos. Napolitano [64] measured the ^{8}B positron spectrum, and used this to qualify available 2α data to produce a best neutrino spectrum. Bahcall *et al* [65] have recently extended this procedure using new β^+ data, improved radiative and recoil corrections, and parameterizing the 2α low energy uncertainty as a calibration scale bias to produce a best neutrino spectrum. De Braeckeleer has recently remeasured the 2α spectrum and produced a ^{8}B neutrino spectrum consistent with previous spectra [66].

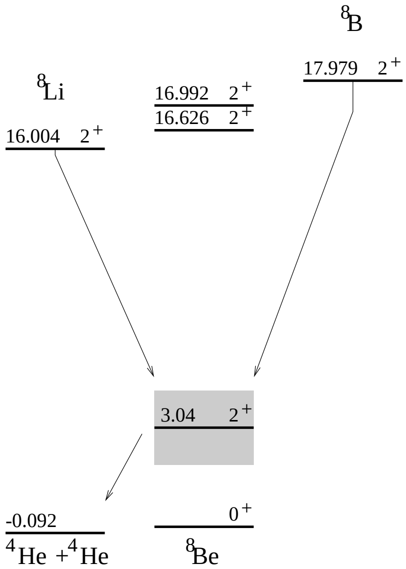

Figure 3.1: Energy levels in the mass $A = 8$ system.

I calculate here the ^{8}B neutrino spectrum to obtain a form useful for interpretation of the uncertainties and to predict the expected spectrum in SNO. I follow the method of Napolitano for the intermediate level averaging, radiative and recoil corrections, and then use Bahcall's 2α scale bias from his best fit to the positron data. The differential neutrino energy spectrum is, as a function of the intermediate level Q

$$\frac{dN}{dE_\nu} = CE_\nu^2(Q-E_\nu+m_e)\sqrt{(Q-E_\nu)^2+2((Q-E_\nu)}R(E_\nu,Q)S(E_\nu,Q)F(-Z,Q-E_\nu,A) \tag{3.1}$$

where $R(E_\nu, Q)$ and $S(E_\nu, Q)$ are the radiative and forbidden corrections and

$$Q = E(^8\mathrm{B}) - E(^8\mathrm{Be}^{2+}) - 2m_e = 17.979 - (2E_\alpha - 0.092) - 2m_e. \tag{3.2}$$

Retaining only the leading terms, the corrections are

$$S(E_\nu, Q) = 1.0 - \left(\frac{2Q}{3m_N}\right)\left(\frac{1}{A}+\frac{d}{Ac}-\frac{b}{Ac}\right)\left(\frac{10E_e}{3m_N}\right)\left(\frac{1}{A}-\frac{2b}{5Ac}\right). \tag{3.3}$$

The weak magnetism coefficient b (induced tensor term in the vector current) has been measured in several experiments and has the value $b/Ac = 6.5 \pm 0.2$ [66]. However, b/Ac varies with Q, so we choose the form $b/Ac = 8 - 0.2Q$ [64]. The induced pseudo-tensor coefficient d is the largest correction (about 2%) and has the experimental value $b/Ac = 1.8 \pm 1.0$ [66] (although a theoretical determination yields $b/Ac = 5$ [66]).

In figure 3.2 the 2α data of Wilkinson and Alburger [62] is shown and the neutrino spectrum derived from it. Also plotted is the spectrum from Napolitano and Bahcall for comparison, and the ratio of the spectrum to the Bahcall best fit. We have used the 2α energy scale calibration published by Barker (thin catcher (detector)) and Warburton [62] (thick catcher) which include energy loss corrections. The plot of the spectra ratios also shows spectra produced using the thick and thin catcher data without any recoil correction, and Bahcall's 3σ spectra produced by his estimate of all the theoretical uncertainties. The largest uncertainty is the energy loss calibration in the 2α data. Also plotted is the neutrino Kurie plot using the peak value for Q (marked $\bar{Q}$)

$$\sqrt{\frac{dN/dE_\nu}{E_\nu^2 F(-Z,\bar{Q}-E_\nu,A)\left(1-\frac{m^2}{2E_e^2}\right)}} \quad \text{vs. } E_\nu, \tag{3.4}$$

where the curved shape shows the effect of the intermediate state averaging.

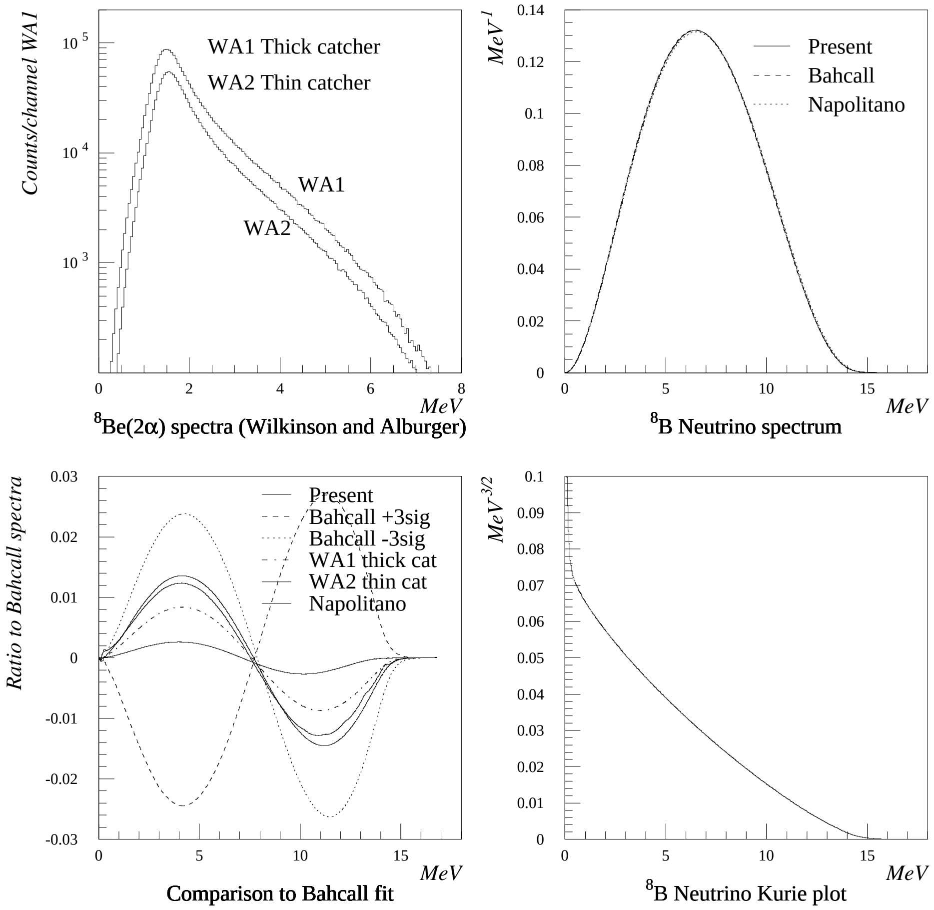

Figure 3.2: The ^{8}B α data and neutrino spectrum. The upper left is the alpha spectra data from Wilkinson and Alburger using the energy scale calibration from Barker [62]. The upper right plot shows the present ^{8}B neutrino spectrum derived from the α data compared to complete calculations by Bahcall [65] and Napolitano [64]. In the lower left plot we compare the spectra by taking the ratio to Bahcall's spectrum and compare to Bahcall's 3 sigma limits and to Napolitano's spectrum and calculations using the thick and thin catcher alpha data. The final plot shows the neutrino Kurie plot evaluated using the mean excitation value of the broad 2^+ state in the Fermi function.

SNO plans to calibrate SNO using the ^{8}Li gas transport source (see chapter 2.4) which is the analogue of the ^{8}B decay. Since ^{8}Li decays via the same ^{8}Be(2α) level then the uncertainties in the 2α scale calibration cancel. Jonkmans *et al* [67] have recently examined in detail all the recoil corrections using R-matrix fits to profile the ^{8}Be 2^+ level. They find that in the ratio of the normalized charged-current to ^{8}Li spectra the recoil correction uncertainties mostly disappear. Thus using the ^{8}Li spectrum in SNO as the energy scale calibration for neutrino analysis improves the sensitivity for shape discrimination.

3.2 Neutrino Detection Cross-sections

The charged current reaction is the neutrino inverse beta decay of the deuteron

$$\nu_e + d \longrightarrow p + p + e^- \qquad (Q = -1.44\,\mathrm{MeV}) \tag{3.5}$$

The deuteron has isospin $T = 0$ and is in the spin-1 $^3S_1$ state except for a small (4%) $^3D_1$ state admixture. At low energies the di-proton is only in the $^1S_0$ state (exclusion principle) so that $\Delta J = 1$ and the transition is Gamow-Teller (except for the small $^3D_1 \longrightarrow {}^1D_2$). The differential cross-section was first calculated by Kelly and Überall [68] and refined by Ellis and Bahcall [69] using the effective range approximation for the S-wave matrix element. The differential rate has the form

$$d\sigma \sim |I|^2 \left(1 - \frac{1}{3}\frac{\vec{p_\nu} \cdot \vec{p_e}}{E_\nu E_e}\right) m_p p d\Omega_p E_e p_e d\Omega_e dE_e \tag{3.6}$$

where p is the relative momentum between the two protons. We see the 1:2 forward-backward angular correlation, and that the cross-section increases as E_ν^2, since to recoil order the energy constraint is

$$E_\nu - Q = T_e + \frac{p^2}{m_p} \tag{3.7}$$

The cross-sections are shown in figure 3.3 together with the recoil electron energy distribution and the angular correlations. The recoil electron energy is peaked near $E_\nu - Q$, but not as much as would be suggested by the kinematics. In the final

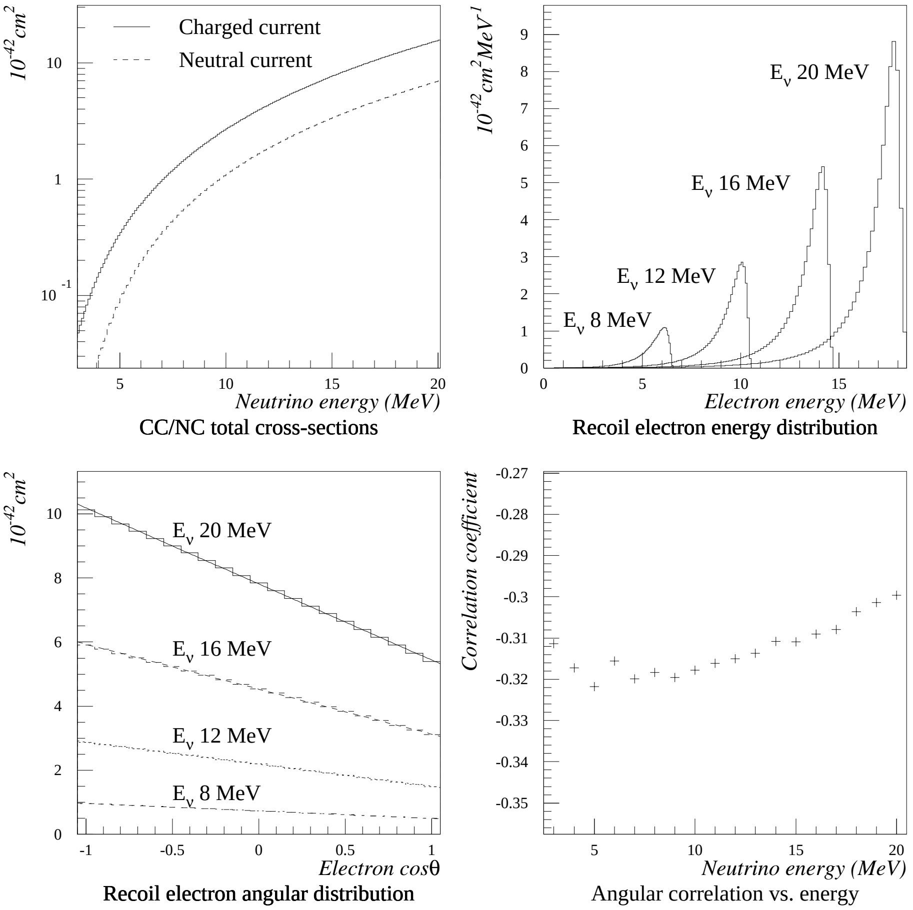

Figure 3.3: Neutrino-deuterium CC and NC cross-sections. The upper left plot is the total cross-section versus neutrino energy. The upper right plots show the differential cross-section as a function of the electron recoil energy for several neutrino energies. The overall E_ν^2 dependence of the total cross-section is also evident in this plot. The lower left plot is the differential cross-section as a function of the angle cosine for the recoil electron calculated by integrating the double differential cross-section over the electron kinetic energy for several neutrino energies. From this, fits to the angular distribution correlation coefficient are plotted as a function of the neutrino energy on the lower right. Code by Bahcall and Lisi [76] is used for the differential cross-section (see text).

state, the di-proton state is unbound causing the Coulomb repelled protons to acquire part of the final state energy. Recent calculations by Ying, Haxton, and Henley and Kubodera and Nozawa have included relativistic effects, forbidden matrix elements, higher partial waves and exchange currents [70]. These improvements have very little effect on the recoil spectrum, but add about 6% to the cross-section. The full 6% correction is conservatively taken to be the uncertainty in the cross-section [71]. Bahcall and Lisi's differential cross-section code, used in the calculations for figure 3.3 [76], uses the S-wave effective range calculation with a normalization to the Kubodera and Nozawa cross-section.

The neutral current cross-section has also been calculated by Kubodera and Nozawa [70] and is plotted in figure 3.3. SNO will only measure the total neutron production rate for neutrinos above the 2.22 MeV threshold. Kubodera and Nozawa estimate a 10% 3σ uncertainty in the cross-section. However, most of the theoretical uncertainties relating to deuteron partial waves and exchange currents will cancel in the CC/NC ratio.

3.3 SNOMAN Monte Carlo

The detailed simulation of SNO signals and backgrounds is necessary for analysis, to guide design and construction decisions, and to develop fitters, event cuts and other analysis tools. Calculation of the detector response requires integration over all possible process distributions, and would be very computationally expensive to compute numerically. Usually such a complex detector response is simulated using the Monte Carlo method that computes the integral by random sampling of the integrand. The response is calculated by simulating events, for example, by choosing an electron energy and then deciding how it will scatter, and taking the directions of Čerenkov photons from weight distributions. The Monte Carlo method requires selecting a value x from a distribution $f(x)$. If f is normalized then the cumulative probability density function $F(s) = \int_0^s f(x)dx$ is on the range [0-1], and s is derived from

$$s = F^{-1}(y) \tag{3.8}$$

where y is a uniform random number [0-1]. As an example, consider a particle in a scattering medium. The unscattered probability distribution is $f(x) = \frac{1}{\lambda}\exp\left(\frac{-x}{\lambda}\right)$, so that the distance traveled before scattering is $-\lambda\log(y)$, where $1/\lambda$ is the scattering coefficient. Some distributions can be sampled more rapidly by trial-and-reject if the distribution and its domain are bounded.

The SNO off-line analysis and detector simulation software, SNOMAN (SNO Monte carlo and ANalysis) [72], is a set of data driven FORTRAN processors with CERNLIB's ZEBRA memory manager. The processors are routines that process the event data in sequence for each event; processors include, for example, Monte Carlo, PMT calibration, event fitting and histogramming. The code includes an event data structure and a titles management system that ensures that the correct time dependent constants are used for detector data analysis. The Monte Carlo processor includes a detailed description of the detector and PMT geometry, generation and tracking of electrons, gamma rays, neutrons, muons and optical photons, and the response of the PMTs, trigger logic, and electronics. Data constants banks (titles) can be loaded from titles files or from the SNO database (SNODB) which is a master-slave multi-node database based on CERNLIB HEPDB.

The Monte Carlo evolves particle histories by storing tracks and interaction vertices in the data structure. Electrons and gamma rays are propagated using EGS4 routines, neutron tracks are evolved with MCNP routines, muons are tracked using code from GEANT, and the photons propagated using optical transport code produced by SNO. The geometry is handled external to the EGS4, MCNP, and GEANT packages. After each Monte Carlo event, the electronics values (PMT charges and TACs) for the PMT calibration are reversed (un-calibrated), so that the event in the data structure appears the same as an event input directly from the detector data stream (except that the Monte Carlo events have additional track data). Finally, other processors such as the electronics calibrator (ECA), PMT calibrator (PCA), time fitter (FTT), events classifiers, viewers etc. can be run in a single event loop.

A second Monte Carlo (called the Queen's Monte Carlo QMC) has been developed by Skensved [73]. The QMC was used for some of the optical analysis discussed in chapter 4.

3.4 SNO Detector Response and Event Fitting

The SNOMAN Monte Carlo is now used to study the SNO response for detecting electrons and gamma rays and the results of event reconstruction. Simulations were run with the following input data:

1. Čerenkov optical wavelengths restricted to $200 - 700$ nm and a statistical reduction factor (cerfac $= 0.28$) to be accounted for by increasing the PMT efficiency to a peak of 100%.

2. Fresnel and Rayleigh scattering and photo-disintegration switched on.

3. The "grey-disk" PMT model, which has the hit efficiency and reflection probability coded as distributions derived from a full 3-D simulation [79]. The PMT quantum efficiency (QE) has been set to the recent absolute QE measurement [74]. The photocathode has a peak efficiency of 23.6% at 430 nm (see figure 4.3). The PMT noise rate is set to 1500 Hz.

4. Trigger (simulated) hardware threshold of 10 hits.

5. D_2O attenuation coefficients according to [77]. The extinction length is 50 m at 400 nm, see figure 4.1.

6. AV attenuation coefficients measured at Chalk River [78], and AV diffuse scattering deduced from airfill laserball time distribution data (see chapter 6). AV belly plates and bonded joints are also in the Monte Carlo.

7. EGS4 parameters (step length, AP, ECUT) set as in standard SNOMAN by M. Lay [79] for the correct energy loss, straggling, and Čerenkov production for low energy electrons.

The expected detector performance based on Monte Carlo runs of electrons is shown in the plot in figure 3.4. With the best current measurement of the absolute

PMT detection efficiency [74], and conservative estimates of the water transparency, the mean number of hit PMTs is 8.2/MeV at 10 MeV. The PMTs/MeV scale is very linear in the region of interest (4 – 20 MeV) and is represented by the functions

$$\begin{aligned} \text{NHIT} &= 7.70E + 4.51 \qquad \text{electrons} \qquad (3.9) \\ \text{NHIT} &= 7.46E - 1.27 \qquad \text{gammas} \qquad (3.10) \end{aligned}$$

The resolution can be modeled as a Gaussian $R(E', E)$ with a detected energy E for an electron/gamma actual energy E'

$$R(E', E) = \frac{1}{\sqrt{2\pi}\sigma} \exp\left(\frac{-(E' - E)^2}{2\sigma^2}\right) \qquad (3.11)$$

where the 1-sigma width as a percentage of the peak is given by

$$\left(\frac{\sigma}{E}\right)\% = a + bE + cE^2, \qquad 3 \leq E \leq 20\,\text{MeV} \qquad (3.12)$$

with a, b and c given in figure 3.4. Note that the purely statistical form $\sigma = \sigma_{10}\sqrt{E/10}$ employed by many authors analyzing the expected response is not a good fit for SNO. In particular the statistical form results in too much threshold spreading and it slightly underestimates the high energy tail.

Most SNO analyses will employ an NHIT cut as an energy cutoff above the trigger level. The efficiency as a function of electron energy is shown for such a cutoff in figure 3.4. This efficiency is dependent on the shape of the low energy resolution, and on the reconstruction for which fitter failure and mis-fitting has a strong NHIT dependence at low energy. The suggested Fermi function forms shown in the figure are meant as illustrations only. If the response function presented above is used with an NHIT cut then this efficiency is already included. Note that there will be a further threshold efficiency factor due to the hardware trigger; this will be measured in SNO.

In SNO a substantial background reduction is gained by using the hit PMT locations and times to predict the location of the initial interaction. This is called event reconstruction, or event fitting, and the algorithms are referred to as fitters. After fitting, events can be cut based on fit positions within a fiducial volume, and a response calibration can be refined to use the fitted position and direction. The free

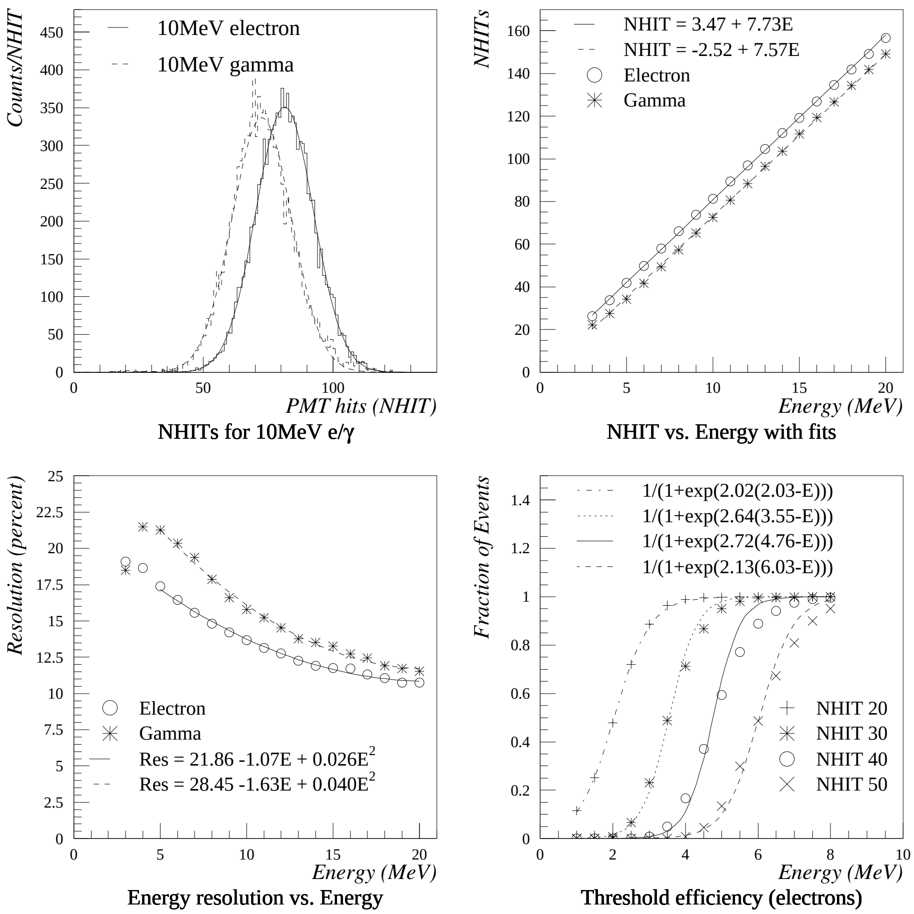

Figure 3.4: Expected SNO performance based on SNOMAN Monte Carlo simulations with the version 3.080 PMT response. The upper left plot is the NHIT distribution for 10 MeV electrons and gammas with the peaks at 81 and 73 hits. The upper right plot shows NHIT parameterizations for the linear region (3 to 20 MeV). At the lower left are parameterizations for the 1-sigma resolution for electrons and gammas as a percent of the peak. In the lower right are plots of the efficiency for NHIT cuts due to resolution and mis-fitting as a function of electron energy. All plots had the cut for event reconstruction within the AV.

parameters (x,y,z and t) can be determined from any 4 PMTs, but since many PMTs may be noise or scattered light hits it is best to use a statistical minimization with a large over-constraint using all the PMTs. The time fitter uses the time of flight for Čerenkov light to find the most probable event position. The PMT hit time t_i is the event time t, plus the channel time offset t_{0i}, plus the time of flight

$$t_i = t + t_{0i} + d_i/c \pm \sigma_i \tag{3.13}$$

if the PMT was hit by direct light. The relative channel time offsets are subtracted in the PMT calibration, and the σ_i is mainly the PMT transit time spread. The fitted position $\vec{r}$ and time t is found by minimizing the time residuals weighted by the transit time spread

$$\chi^2 = \frac{1}{\mathrm{NFIT} - 4} \sum_i \left(\frac{1}{c} \left| \vec{r_i} - \vec{r} \right| + t - t_i \right)^2 / \sigma_i^2 \tag{3.14}$$

where $\vec{r_i}$ is the position of the ith PMT. In SNOMAN this is minimized using the Levenberg-Marquardt algorithm (mrqmin in Numerical Recipes [75]). The event direction is then the mean of the vector directions from the fitted position to each of the PMTs.

The major difficulty with all fitters is the influence of noise hits and scattered or reflected light. Minimization routines assuming Gaussian distributions are strongly influenced by out of time hits. It would not be serious if the tails were at least symmetric, but of course this is not the case as scattered and reflected light is always late. The fit will tend to move toward an unphysical region, or not converge at all. The worse case is when it seems to fit well, but to a wrong location, with a reasonable χ^2. An algorithm to circumvent this problem is to throw away the furthest out of time PMT, and then repeat the fit. The fit is seeded at a location given by the average position of the PMTs, then this refitting procedure is repeated until all the time residuals are smaller than a tolerance, about 8 nanoseconds. This tolerance represents a tuning between removing indirect light, and throwing away some real statistical hits. Another method is to trim PMTs at the start that are more than 50 nsec (one PSUP radius) from the main prompt time peak at the expected NHIT trigger time. Then the initial fit should be more reasonable, and the fit can then be refined using the method above. Since no more than 20% of the light should be reflected or scattered then a high portion of time-rejected hits is a good cut indicating a non-physical (eg. breakdown) or unusual event (eg. flasher). Other fitter algorithms have been developed for SNO including a simulated annealing routine (the elastic fitter), a grid χ^2 fitter (the box fitter) and a routine using a sample of 4-PMT combinations (the quad fitter). Systematics due to event mis-reconstruction maybe reduced using a combination of fitters.

The reconstruction mis-location distribution (distance from the true electron position to the fitter reconstructed position) is peaked at 21 cm with a 34 cm mean for 10 MeV electrons (figure 3.5). The vertex reconstruction is significantly worse for gamma rays (peak 32 cm, mean 65 cm). This is because gammas Compton scatter several times with typically a radiation length in between (40 cm)[1] to give several vertices. Indeed this has been used to develop methods for distinguishing electrons from gamma rays.[2] While these classification schemes are not sufficiently robust for event-by-event differentiation, the possibility of separating distributions is promising. The reconstruction accuracy is not a strong function of energy, except that it is considerably worse at very low energy. The peak of the mis-location distribution roughly has the form

$$|R_{\text{dev}}| = 13 + \frac{1}{0.013E - 0.001} \text{ cm} \tag{3.15}$$

The angular resolution (the dot product between the initial trajectory and the reconstructed direction) is remarkable in that it is almost perfectly an exponential function and that it is almost the same for electrons and gammas (figure 3.5). We measure the angular resolution by the cosine at one decade,

$$\cos\theta/\text{decade} = \frac{b - \log 10}{b} \tag{3.16}$$

[1]We are actually below the energy for the radiation length in water (47cm over 1 GeV). The attenuation length ranges from 20 cm at 2 MeV to 60 cm at 100 MeV.

[2]This is called pattern recognition, and many methods have been attempted. Usually the technique is to evaluate a likelihood for double Čerenkov rings, or other figures of merit related to the PMT hit distribution. A particularly promising method uses a neural network to 'train' a classifier.

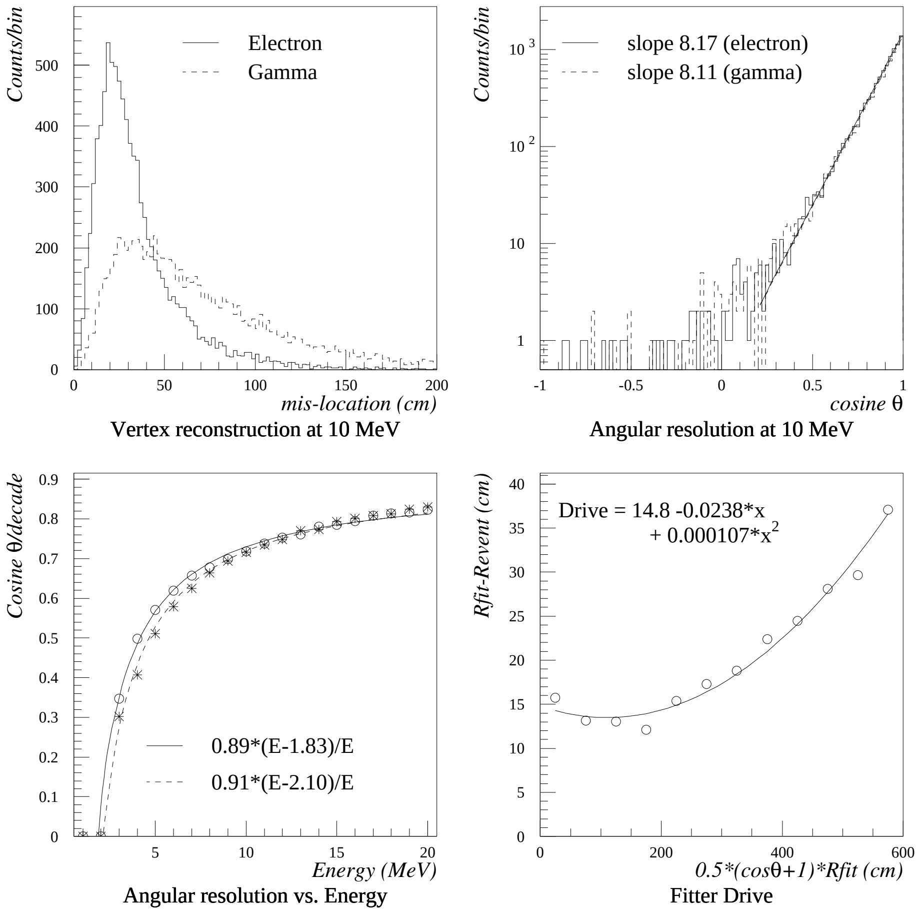

Figure 3.5: Expected SNO reconstruction (fitter) performance based on SNOMAN Monte Carlo simulations with the version 3.080 PMT response. The upper left plot is the vertex position reconstruction; for electrons is peaked at 21 cm with a mean of 34 cm and for gamma rays it is peaked at 32 cm with a mean of 65 cm. The angular reconstruction distribution is exponential with slope parameters shown in the upper right plot. By fitting exponentials the angular resolution is characterized by a cosine width per decade as a function of electron and gamma energy (lower left). In the lower right plot a systematic reconstruction shift (fitter drive) is parameterized by a quantity which indicates how the electron moves away from the centre of the AV (see text).

where b is the exponential slope for the distribution $\exp(a+bx)$. The energy dpendence of the angular resolution is parameterized with

$$\text{Angular resolution}(\cos\theta_{10}) = c_1 \frac{E - c_2}{E} \tag{3.17}$$

where the constants c_1 and c_2 are given in figure 3.5 for electrons and gammas. To convert this to a half width at half height or at the 1/e point use $\cos\theta_2 = 1+(\cos\theta_{10} - 1)\frac{\log 2}{\log 10}$ or $\cos\theta_e = 1 + (\cos\theta_{10} - 1)\frac{1}{\log 10}$. Thus the half height angular resolution at 10 MeV corresponds to 23.8° .

A significant feature of the time fitter is called fitter drive, which is a systematic mis-reconstruction due to the late light problem discussed earlier. The effect is systematic due to geometry and path length degeneracy, and tends to pull events within the AV to larger radii. Consider electrons at large AV radii and traveling outward. Since scattering is fairly isotropic then scattered light is as likely to go forward as backward, yet the backward scattered light will result in larger time residuals. Also the forward scattered light is largely in-time with the direct light (the Čerenkov cone) and hence does not contribute significantly to the χ^2. The fitter compensates for the larger time residuals in the backward light by moving the fitted position forward to a larger radius. When the electron is at a large radius but moving towards the centre, the backward (non-degenerate) light will have smaller time residuals since the PMTs are closer. Hence the drive effect is smaller. The size of the fitter drive depends on the event radius and the trajectory angle, but since the effect is greater for larger radii with an outward trajectory then we can parameterize it in terms of the quantity

$$z = 0.5(1 + \cos\theta)R_{\text{fit}}. \tag{3.18}$$

The fitter drive effect can be compensated by the transformation

$$R_{\text{ev}} = R_{\text{fit}} - 14.8 + 0.0238z - 0.000107z^2 \text{ cm}, \tag{3.19}$$

which maps the event back to a smaller radius.

We end this chapter by presenting the expected energy spectrum in SNO for ^{8}B neutrinos with the large and small mixing angle MSW scenarios and the no oscillations case (figure 3.6). The spectra are calculated using the ^{8}B(2α) data in section 3.1, and the Parke formula for the MSW survival probabilities (appendix B). The differential cross-section is integrated over the neutrino survival spectrum to get the SNO electron shape

$$\frac{dN}{dT_e} = \int dE_\nu \, \lambda_\nu(E_\nu) P(E_\nu) \int dT'_e \, R(T'_e, Te) \left(\frac{d\sigma(E_\nu)}{dT'_e} \right), \tag{3.20}$$

where $\lambda_\nu(E_\nu)$ is the ^{8}B neutrino spectrum (3.1) and $P(E_\nu)$ is the MSW electron neutrino survival probability for transit through the sun. The response function used is a Gaussian (equation 3.11) with the width as in equation 3.12.

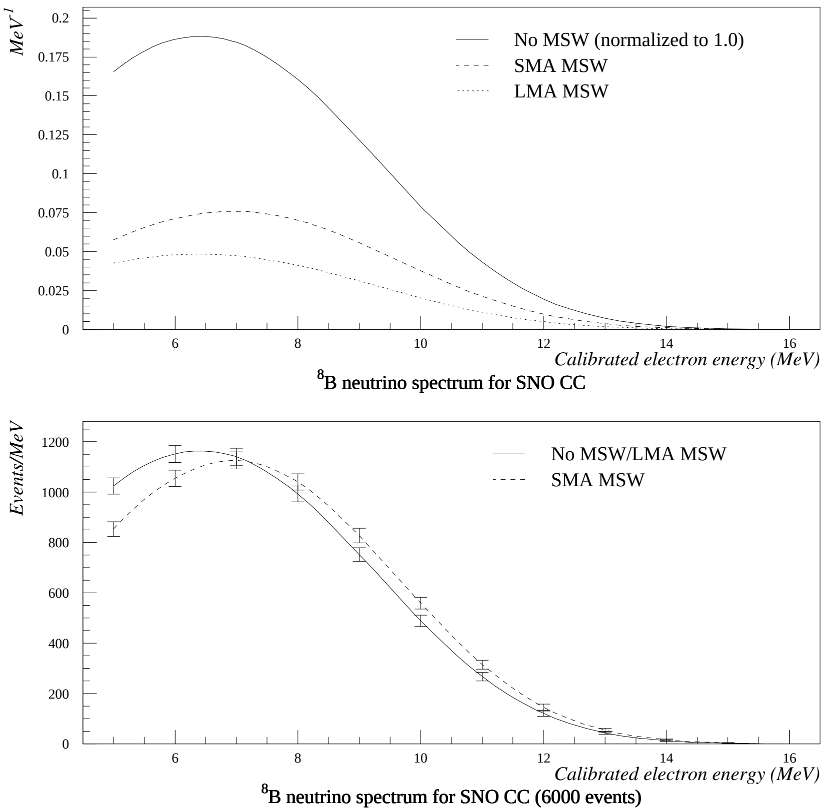

Figure 3.6: Electron recoil spectral shape in SNO for solar ^{8}B neutrinos for the large and small mixing angle MSW scenarios and the no oscillations case.

From the upper plot we see that both MSW solutions produce a strong charged current flux suppression, while the small angle solution also causes a spectrum distortion. The re-normalized spectra are shown in the lower plot with statistical error bars for 6000 events (less than two years for 0.47 SSM). Thus SNO will be able to verify an oscillation effect (by the CC/NC ratio) and distinguish the MSW solutions by shape distortion.

With a 5 MeV threshold the mean value of the spectum is 7.47 MeV and 7.68 MeV for the SMA and LMA solutions, for a difference of 210 keV. Assuming Gaussian statistics for each bin then 6000 events (1.56 years at 5 MeV threshold) will contribute 110 keV uncertainty to the mean. Taking the neutrino spectrum shape uncertainty as a 104 keV energy shift [65], then adding the uncertainies in quadrature leaves a 145 keV error budget for the energy scale calibration to distinguish between the MSW spectral shapes. This error budget is eliminated for a 6 MeV threshold. The error budget improves by calibration with the ^{8}Li source which removes the uncertainty in the ^{8}B neutrino spectrum [67].

Chapter 4

Optical Calibration

Understanding the optical condition of the SNO detector is important for the analysis of neutrino and background events in the detector. The detector response to electrons, gamma rays and neutrons can only be measured at certain energies and locations and under limited conditions. Since light transmittance to the PMTs is a function of event position, the energy calibration of SNO must include a detector response function that accounts for the optical effects of the detector. The optical parameters are wavelength dependent, so that the Čerenkov spectrum and light attenuation will evolve as light travels through the detector. The detector gain will depend on factors which could vary over time such as impurities in the water systems, biological activity, deposits on the acrylic or PMT reflectors, water penetration into the acrylic, or gain and efficiency drifts in the PMTs.

SNO is unique in its capabilities as an optical instrument, owing to its large size and nanosecond timing resolution which lead to a high degree of segmentation. In particular, the PMT timing resolution allows the effects of attenuations, bulk scattering and reflections to be separated. Also SNO can be used to study other optical phenomena, for example to measure the event-by-event angular distribution of a sono-luminescence bubble.[1] Other unique SNO events, like flashing PMTs or high voltage breakdown events, can be cut from analysis with a good knowledge of the detector optics.

[1]The sono-luminescence pulser source will be used in SNO to study the fundemental nature of sono-luminescence light.

The optical calibration is the determination of the heavy water, light water and acrylic attenuation coefficients and scattering coefficients. Also, the relative PMT quantum efficiencies and the overall optical 'gain' of the detector will be monitored over time. Details of the Monte Carlo optics are are verified in the measurement of the optical response. This chapter discusses the optical calibration of SNO using the nitrogen/dye laser optical source and PMT timing histograms. Optical absorption, scattering mechanisms and the PMT response are discussed along with the analysis algorithms and monitoring facilities. The nitrogen/dye laserball source, described in detail in this chapter, is also used in the electronics and PMT calibrations discussed in chapter 6.

4.1 Detector Optical Parameters

To account for the optical response of the detector we need to obtain

- The attenuation lengths of the D_2O, the acrylic and the H_2O at several wavelengths between 300 nm and 450 nm. We would like to know these attenuation lengths for each acrylic panel, any across-panel variations and the effects of rope grooves and bonded joints. Also we need to detect if the water attenuation is inhomogeneous.
- The bulk scattering lengths (cross sections) and the angular distributions of scattering for all detector regions and at several wavelengths.
- The position/angular response of the PMTs and relative quantum efficiencies (QE) of all the PMTs.
- The detector optical gain, which is the overall light detection efficiency. The optical gain is the product of the light attenuation and PMT efficiency averaged over all PMTs.

Some of this data will be difficult to obtain reliably, for example the H_2O attenuation, so it is important to understand the response variation to these parameters and any limitations they impose on the neutrino analysis. The most critical optical parameters are the extinction coefficients (absorption plus scattering) in the detector media and the relative PMT quantum efficiencies. The optical analysis will be performed using the pseudo-isotropic laser diffuser ball (the laserball) at near single photo-electron (SPE) light intensity. The SPE PMT response permits the optical effects in the detector to be determined from the PMT pulse arrival times. Also the PMT relative efficiencies must be measured at SPE intensity. By deploying the laserball at certain locations the separate acrylic panels and water regions can be inspected. Cuts on the PMT timing information can be used to separate out scattered and multiple-reflected light.

An overall detector optical gain (or sensitivity, ie. the total number of PMT hits for a given quantity of light) will depend on the absolute quantum efficiency of the PMTs and any systematic errors in determining the attenuation parameters. This detector gain can be measured with the laserball over time, by comparing the laserball output to a standard detector, and can be monitored with the the ^{16}N source for verification and to force convergence.

The light transmission of light and heavy water and the acrylic panels was measured prior to SNO construction [77, 78] and this data will be used to evaluate the expected optical response. The water attenuation is shown in figure 4.1 which is characterized by the well known visible transparency window. In the blue region the transparency comes very close to the Rayleigh scattering limit (density fluctuations), while in the long wavelengths water has an absorption edge (the red cutoff) that begins in the green. In the short wavelength region the small difference between heavy and light water may be due only to slight sample impurities. The absorption edge in heavy water is shifted to the red due to the mass dependence of the vibrational and rotational resonances. The following expressions are used as proxies for the water extinction coefficients

$$\log \mu_{\mathrm{H2O}} = \begin{cases} \frac{1669}{\lambda} - 13.1 & \lambda \leq 430\,\mathrm{nm} \\ \frac{-3385}{\lambda} - 1.35 & \lambda > 430\,\mathrm{nm} \end{cases} \tag{4.1}$$

$$\log \mu_{\mathrm{D2O}} = \begin{cases} \frac{1536}{\lambda} - 11.8 & \lambda \leq 570\,\mathrm{nm} \\ \frac{-3454}{\lambda} - 3.05 & \lambda > 570\,\mathrm{nm} \end{cases} \tag{4.2}$$

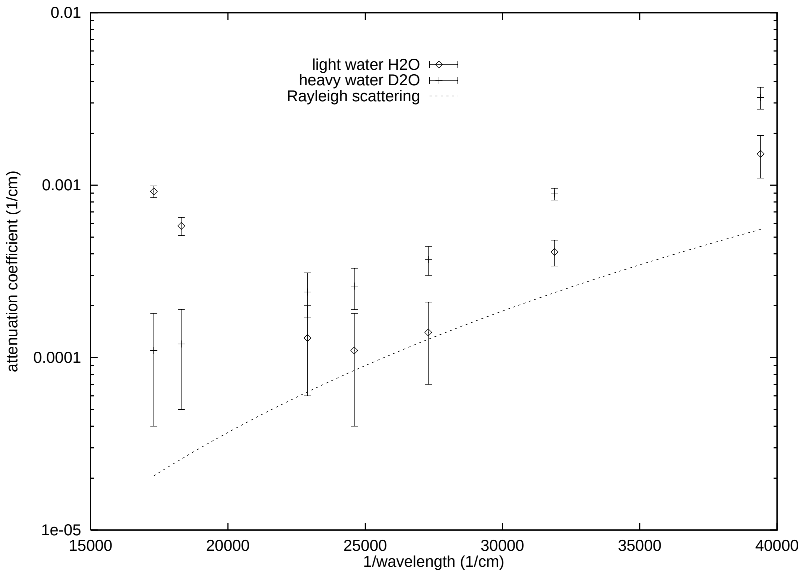

Figure 4.1: Transparency of light and heavy water. The line is the contribution to the extinction from Rayleigh scattering. Data from Boivin [77].

The light transmission through a typical acrylic panel sample is shown in figure 4.2, along with histograms of the measured attenuation coefficients for all the panels. The transmission is characterized by almost perfect transmission in the visible with a blue cutoff. The wavelength dependence of the PMT quantum efficiency [79] (QE) is plotted in figure 4.3 along with the PMT QE weighted by the acrylic transmission and the Čerenkov spectrum as would be detected in SNO. It is clear that the acrylic UV cutoff will dominate the optical response of the detector, so it will be important that some measure of the acrylic optical transparency can be obtained. The weighted PMT QE is then integrated over wavelength to form a figure of merit and shown as a histogram for each delivered acrylic panel. The variation is seen to be about about 2%, with about 20% of the panels being about 6% lower. Panel to panel variations are likely due to slight impurities in the acrylic or variation in the thermo-forming.

The detector response to electrons will be position and direction dependent due to the attenuation and scattering of light. We now estimate the effect of the optical attenuations on the detector response and use this to determine the precision required

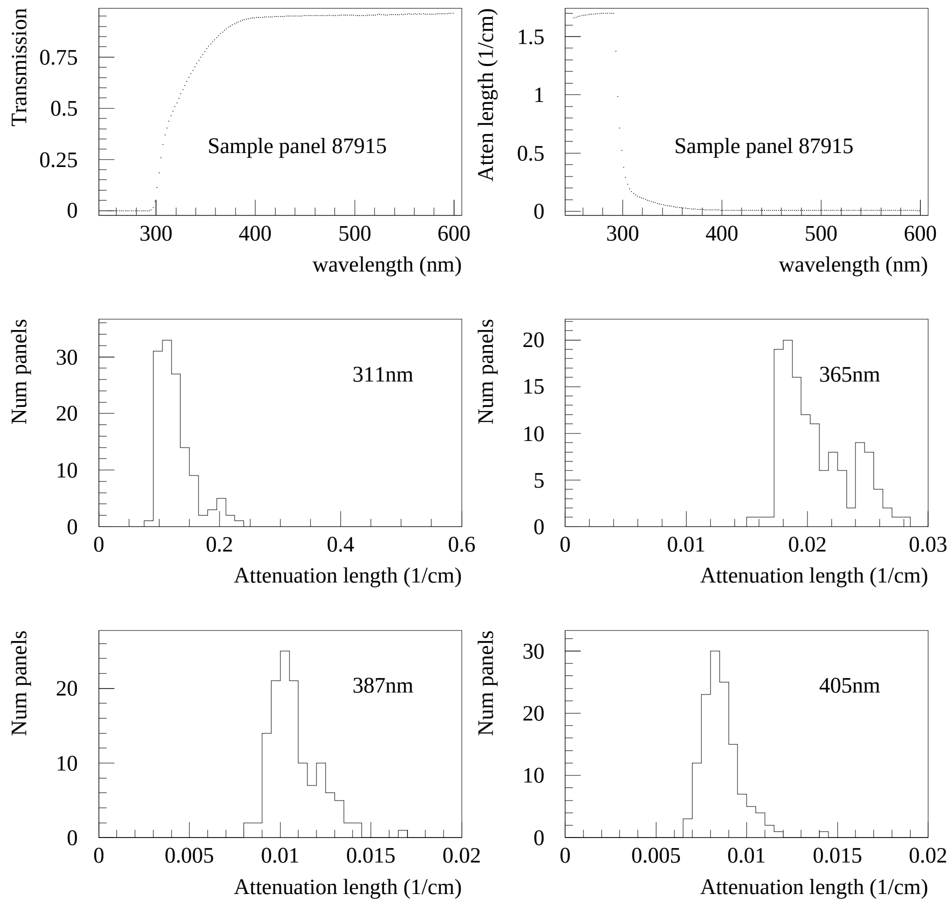

Figure 4.2: The top two plots show the total transmission and attenuation coefficient as a function of wavelength for a 5.84 cm acrylic panel sample. The remaining plots show the distribution of attenuations for all panels measured at several wavelengths.

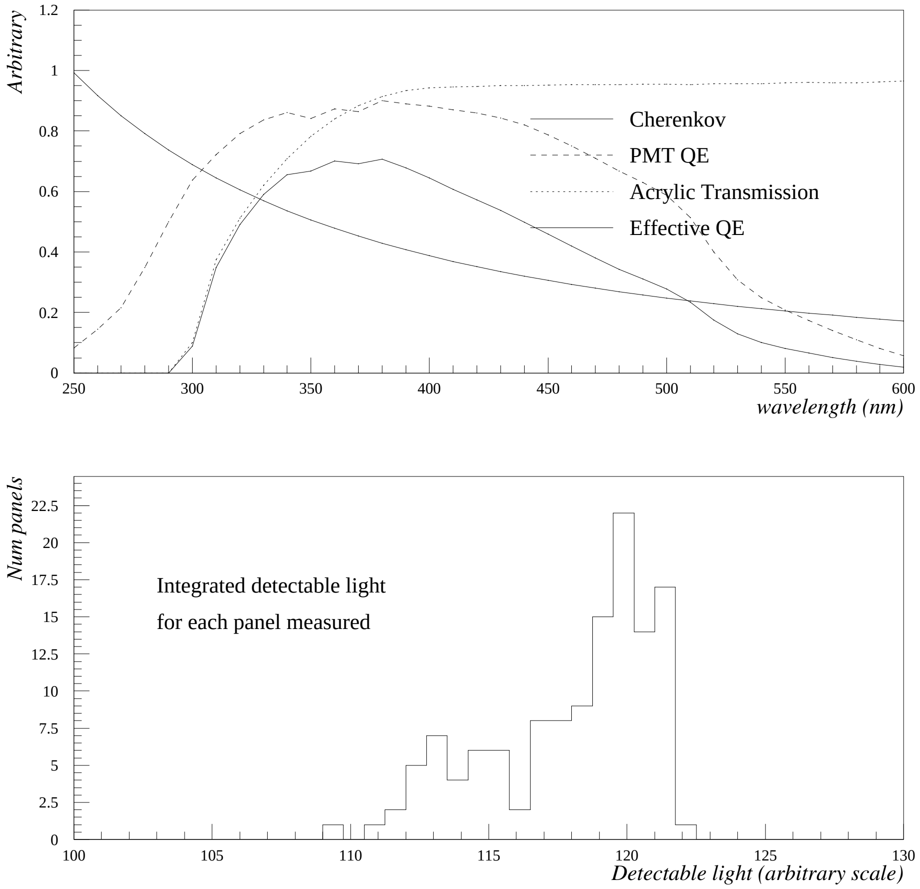

Figure 4.3: Wavelength dependence of PMT QE and acrylic transmission. The upper plot show the measured PMT relative efficiency and the acrylic transmission as a function of wavelength. Also shown is the acrylic/QE product weighted by the $1/\lambda^2$ Čerenkov distribution. It is clear that the acrylic cutoff dominates the short wavelength while the PMT QE cuts off the long wavelength. The second plot is the integral of the weighted acrylic/QE distribution above calculated and histogrammed for all the AV panels.

in measuring the optical parameters. We consider the case of an isotropic light source since the attenuations and derivatives can be integrated directly without the use of Monte Carlo. Consider the total transmitted light from a light source at radius r to a detector sphere at radius R (the PSUP) normalized to the light transmitted for the source at the centre. We refer to this as the isotropic extinction function $J(r, \mu)$

$$J(r, \mu(\lambda)) = \frac{1}{2g} \int_{-1}^{1} dx\, f_1 f_2 f_3 \tag{4.3}$$

where

$$g(\lambda) = \exp\left(-\mu_1 R_1 - \mu_2 (R_2 - R_1) - \mu_3 (R_3 - R_2)\right) \tag{4.4}$$

$$f_n(x, r, \lambda) = \exp\left[-\mu_n(\lambda) \left(\sqrt{R_n^2 + r^2(x^2 - 1)} - \sqrt{R_{n-1}^2 + r^2(x^2 - 1)}\right)\right] \tag{4.5}$$

with $R_3 = 850\,\text{cm}$ (PSUP), $R_2 = 600.5\,\text{cm}$ (D_2O), $R_1 = 606.3\,\text{cm}$ (acrylic) and the μ_n are the extinction coefficients for D_2O, acrylic and H_2O. The isotropic extinction function is then integrated over wavelength, with a weighting for Čerenkov emission and the PMT response, using the water extinctions (equations 4.1 and 4.2) and the data for a typical acrylic panel (figure 4.2) to obtain

$$I(r) = \frac{\int_{\lambda_1}^{\lambda_2} d\lambda\, \frac{\epsilon(\lambda)}{\lambda^2} \int_{-1}^{1} dx\, f_1 f_2 f_3}{2 \int_{\lambda_1}^{\lambda_2} d\lambda\, \frac{\epsilon(\lambda)}{\lambda^2} g(\lambda)} \tag{4.6}$$

Cutoffs at $\lambda_1 = 250\,\text{nm}$ and $\lambda_2 = 600\,\text{nm}$ are used (see figure 4.3). The result is plotted top left in figure 4.4 along with curves generated by setting other extinction coefficients to zero. The D_2O absorption causes an increase in the response with r since the average path length is shorter, while the opposite effect occurs for the acrylic and H_2O. This is fortunate as the response flattens out up to about $r = 450$ due to this absorption cancellation. To further assess this effect we must integrate over volume since more SNO events will occur at larger r. The volume integrated extinction function is

$$H(\lambda) = \frac{3N}{4\pi R_1^3} \int dV\, \frac{\epsilon(\lambda)}{\lambda^2} J(r, \mu) \tag{4.7}$$

and is plotted as a function of wavelength. We see the D_2O effects mostly the mid-wavelengths, the acrylic cutoff dominates the short wavelengths, while the lines converge at the long wavelengths where the PMT QE dominates.

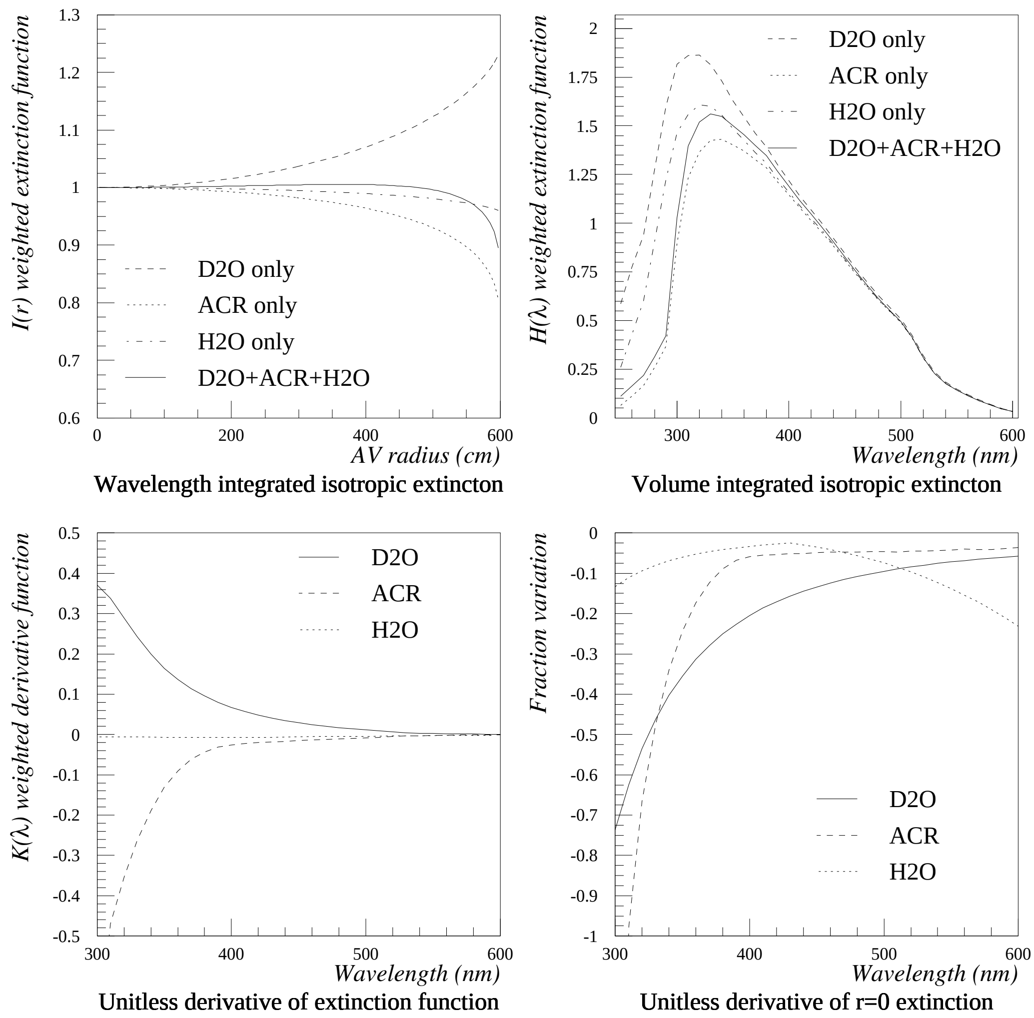

Figure 4.4: Calculated attenuation for an isotropic light source and derivatives weighted by the PMT response and the Čerenkov spectrum (see text).

The sensitivity of the optical response to variation in the attenuation coefficients is evaluated from the derivative function

$$K(\lambda) = \mu_n \frac{1}{H} \frac{\partial H}{\partial \mu_n}(\lambda) \tag{4.8}$$

This function is also evaluated with a weighting for the Čerenkov and PMT response and is shown in the third plot. This is interpreted as follows. At a particular wavelength (say 337 nm) the derivative function $K(\lambda)$ for D_2O has the value 0.18, which means that a position dependent shift in optical gain of 1% corresponds to a change in the D_2O extinction coefficient of $0.01/0.18 = 0.05$, or 5% for that wavelength. The overall required precision is found by integrating $K(\lambda)$ over wavelength; the results are in table 4.1. In general we see that to keep changes in the position dependence of the calibration to less that 1% requires changes in the extinction coefficients to be measured to 14% for the D_2O and acrylic, with little dependence on the H_2O.

We notice that the signs for the derivative are opposite for D_2O and acrylic, as we know that their attenuations tend to compensate. Of course this same property will cause the actual measurements with the laserball to have the same contravariance. The acrylic can be constrained by the conditions that it will not vary rapidly from the external measurements, and that it cannot improve. While it may be possible for the acrylic properties to change slightly by the ingress of water, the most likely apparent change in acrylic will be due to any buildup or plating on the surface. Finally we note that there is almost no sensitivity to variation in the light water attenuation. Furthermore, the light water attenuation covaries with the acrylic attenuation due to degeneracy in the optical path lengths. During the laserball calibration the light water attenuation will be fixed at the current measured values, unless for whatever reason it becomes large and measurable.

Also shown in table 4.1 is the variation of the attenuation at $r = 0$ averaged over wavelength for each of the media

$$\frac{\lambda_1 \lambda_2 N}{\lambda_2 - \lambda_1} \int_{\lambda_1}^{\lambda_2} d\lambda \, \frac{\epsilon(\lambda)}{\lambda^2} \mu_n \left(R_{n-1} - R_n\right). \tag{4.9}$$

For shifts in the total attenuation to be corrected to 1% would require the D_2O and acrylic extinction coefficients to be measured to 3% accuracy. Also the D_2O and

Medium	$\int d\lambda\, K(\lambda)$	Precision for $< 1\%$ shift in position dependence	$\int d\lambda\, \frac{\mu_n \epsilon}{\lambda^2}(R_{n-1} - R_n)$	Precision for $< 1\%$ shift in $r = 0$ attenuation
D_2O	+0.074	14%	-0.306	3%
Acrylic	-0.075	14%	-0.348	3%
H_2O	-0.010	100%	-0.064	16%

Table 4.1: Required precision in monitoring optical parameters.

acrylic attenuations (and the uncertainties) add, rather than cancel, as occurs for the positional dependence. It is for this reason that the optical parameters will be used to calibrate the position dependence, but will not be reliable for monitoring the total energy calibration. Thus, sources such as the ^{16}N will be used to monitor the energy response.

4.2 Nitrogen/Dye Laserball System

4.2.1 Nitrogen Multi-Dye Laser

The main optical source is the nitrogen/dye laser with a diffuser ball and fibre-optic system (figure 4.5) [80]. The primary laser is a TEA thyratron triggered N_2 laser (laser Photonics Inc. LN203C) producing a 600 psec pulse at 337.1 nm wavelength with a peak power of 150kW and 50 Hz repetition rate. This primary beam can be delivered directly to the fibre-optic coupling optics, or it can be used to pump one of four available dye-laser units with four different wavelengths. The dye laser beam paths converge and go through adjustable neutral density filter wheels which provide wavelength independent intensity adjustment. The laser light is transmitted to an optical diffuser (the laserball) through a fibre-optic bundle within a flexible umbilical. The laserball is fixed to the manipulator carriage and can be deployed at various locations within the D_2O volume by the rope manipulator system (see chapter 2.4). The laserball can also access regions between the acrylic and the PSUP down the calibration pipes using the single axis manipulator.

The nitrogen laser has a three level band (see figure 4.6) with very large optical

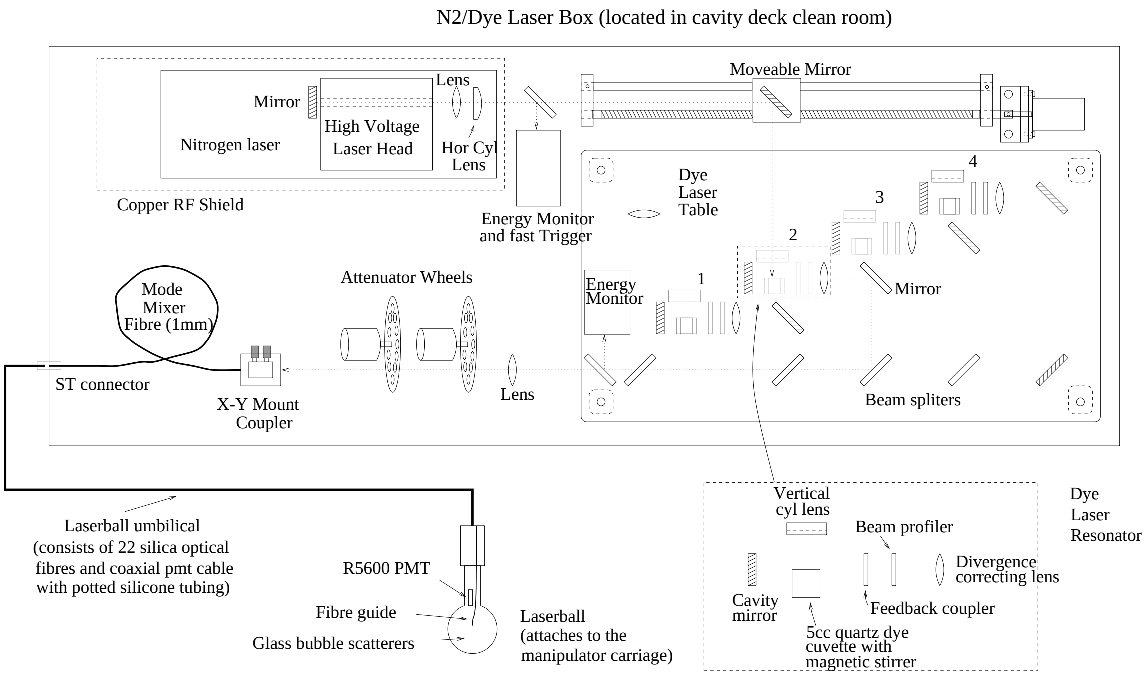

Figure 4.5: Schematic of the N_2/dye laser calibration system.

gain and a short lived upper level state ($C^3\Pi_u$). The laser operates by applying a rapid high voltage discharge across the gas cell which creates a high temperature electron gas [81]. The population inversion proceeds via collisional excitation which preferentially excites the $C^3\Pi_u$ level due to the Frank-Condon principle. The high voltage discharge must be pulsed owing to the meta-stable $A^3\Sigma_g$ level, and it must be very fast ($1-4$ nsec) due to the long lifetime of the $B^3\Pi_g$ level (10 μsec). The laser head is a channel 10 cm long with a 4 mm electrode gap and a feedback mirror between a HV parallel plate capacitor. The charge circuit uses the resonant capacitor transfer method where a thyratron shorts two series capacitors so their charge is delivered by resonance. Since the population inversion time is similar to the optical transit time, coherent cavity modes cannot form, hence the nitrogen laser is a multi-mode super-radiant source. The rapid high voltage discharge requires great care in shielding the RF emissions for use of the laser for PMT calibrations.

The dyes are usually large organic molecules, with energy levels consisting of

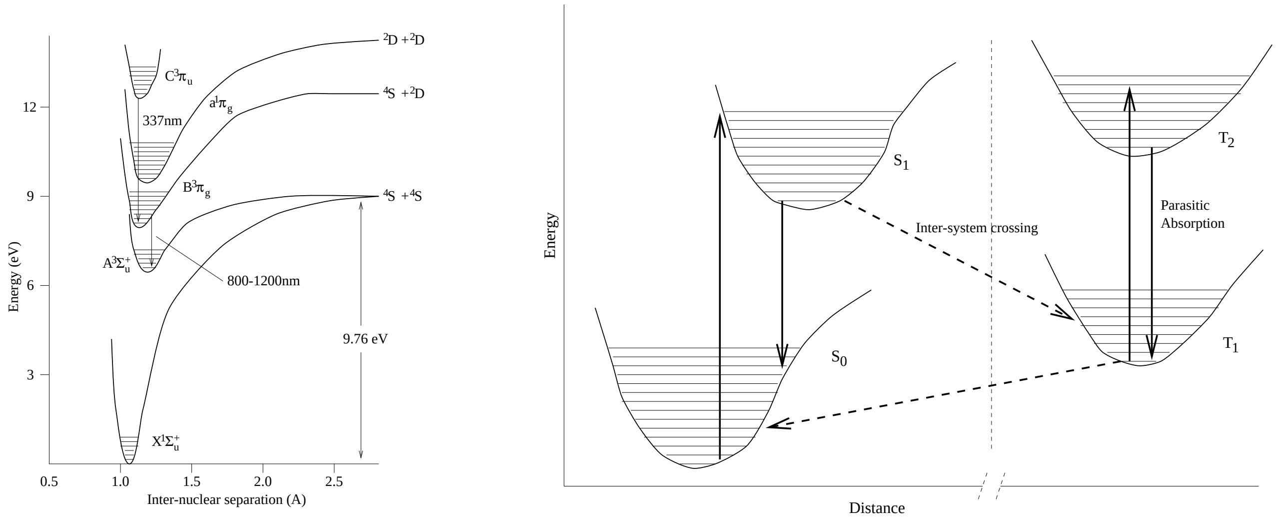

Figure 4.6: (a) Level scheme for the nitrogen laser [82]. (b) Organic dye laser level scheme [83].

wide rotational and vibrational bands. This causes the broad band output and large oscillator strengths [83]. The 337.1 nm radiation is absorbed to provide excitation in the S_1 band, but de-excitation can occur between any combination of states between the S_1 and S_0 bands (figure 4.6). Non-radiative transitions to the bottom of the S_1 band are extremely rapid (picoseconds), so that the dye acts as a wavelength shifter and does not absorb its own radiation. The oscillator strengths are large and so the emission is rapid, hence the resonator cavity with the plain mirror amplifies a large range of modes. The output is super-radiant and lacks the coherence of a cavity mode laser. The dye laser bandwidth can be greatly reduced by using a diffraction grating in place of the mirror to reduce the output bandwidth. The dye laser pulse rate is limited by intersystem crossing to the triplet levels.

The N_2 laser beam is focused through a cylindrical lens to a line just inside the dye cell cuvette wall (figure 4.5). The mirror and optical coupler provide feedback so that the emission has a well defined beam along the focused edge of the fundamental beam. The dye cell cuvettes are mounted at an angle so that feedback from internal reflections are un-amplified. The vertical divergence is limited by the focusing of the multi-mode nitrogen beam (about 0.5 mm), while the horizontal divergence depends on the absorption length which is also the order of 0.5 mm for the correct dye solution concentration. The result is a beam of about 2 mm diameter, approximately 3 mrad half angle divergence, with rectangular diffraction fringes. The pulse length is 500 psec and has about a 20 nm bandwidth (FWHM) dependent on the dye.

The dye laser frequency and attenuation filters can be adjusted remotely by computer control. The nitrogen laser beam is steered by a mirror on a carriage which runs on a motor driven lead screw. The frequency is changed by using the steering mirror to select different laser dye cells. The optical table is configured so that the four dye laser beam axes converge onto the attenuation wheels and output coupler. This is accomplished by using 50%/50% neutral density filters which steer each beam on axis while transmitting the other beams. This method causes the fourth dye cell to be attenuated a factor of $(\frac{1}{2})^3$ compared to the first cell, and the second cell a factor $(\frac{1}{2})^2$ etc. This turns out to be beneficial, since when the dyes are arranged in order of wavelength this attenuation compensates for greater attenuation in the optical fibres at short wavelengths. The fundamental N_2 laser beam can also be steered into the output axis.

The output from the dye lasers is focused into a 1 mm diameter quartz fibre (Fiberguide Ind. SFS-1000N) 1 m long which functions as a mode-mixer before coupling to the higher bandwidth transmission fibres. The power output would not be stable if the beams were coupled directly to the small diameter fibres since the N_2 laser, and in turn the dye lasers, lack the beam structure stability of a cavity mode laser. Looping the SFS-1000N fibre causes greater mode mixing in the fibre, resulting in a uniform power profile which is not very sensitive to the input beam profile.

The laser system also provides a fast negative timing trigger to enable timing calibration of the PMTs. The primary N_2 laser beam is split with a quartz glass plate and a beam is directed to a diffuser box which houses a fast MRD500 PIN diode and a large area (10×10 mm) PIN diode. The small diode is 12V reversed biased with a capacitor in parallel so that the diode conduction produces a fast 1.5V negative pulse with a 0.8 nsec full width. A trigger pulse generated from the laser light provides superior timing compared to command triggering of the laser, which would include about 5 nsec timing jitter due to the logic circuits and the thyratron switch jitter. The large area diode views the diffuser light only to remove beam structure instability. This pulse is integrated with a differential preamplifier to provide a beam energy monitor. A similar diffuser, large area diode and preamplifier provide a beam energy monitor from the dye laser table.

4.2.2 The Laserball

The laser diffuser ball (the laserball) distributes the laser light approximately isotropically (referred to as pseudo-isotropic) into a 4π solid angle to provide a source for PMT calibrations (timing and gain) and optical calibration (attenuation parameters). To be able to move the laserball around in the detector, the laser pulses are transmitted through fibre-optics. Due to the importance of the 337 nm PMT and optical calibration, the fibre-optics must be able to transmit down to this short wavelength without large dispersion. In fact the optical fibre and laserball is designed for 300 nm for the future development of a short wavelength source[2]. Silica fibres become dispersive at short wavelengths (< 400 nm) due to electronic resonances in the UV. We require all dispersion, including the laserball and 35 m of optical fibre, to be smaller than the mean PMT transit time spread of 1.4 nsec. High bandwidth communication fibres have a graded refraction index profile using germanium [84]. However, germanium fluoresces in the UV spectrum causing apparent large dispersion. UV transmission fibres are typically made from quartz glass or fused silica and so they have a step index profile. The pulse dispersion σ in a step index fibre over length l is approximately

$$\frac{c^2\sigma^2}{l^2} = \left(\frac{N\Delta}{2\sqrt{3}}\right)^2 + \left(\frac{\sigma_\lambda}{\lambda}\right)^2 \left(\lambda^2 \frac{d^2 n}{d\lambda^2}\right)^2 \tag{4.10}$$

where $n(\lambda)$ is the index of refraction, $N = n - \lambda\frac{dn}{d\lambda}$ is the group index, Δ is the numerical aperture ($\Delta \approx 0.04$ for a step index fibre with silica clad and gel buffer [85]), and σ_λ is the source bandwidth. The first term is the intermodal (ray-path) dispersion

[2]We have been investigating methods for frequency doubling the 620 nm dye laser, or using a discharge lamp (eg. the 313 nm Hg line).

while the second term is the chromatic dispersion. Using a three term Sellmeier model for the refractive index (with coefficients from Fleming [86]) the dispersion is calculated for several wavelengths, with the results found in table 4.2 for 35 m of fibre. Chromatic dispersion dominates at short wavelengths, while intermodal dispersion dominates at longer wavelengths. The model indicates that it is possible to achieve the required bandwidth with a fused silica step index fibre. In evaluating the total dispersion the l (length) dependence for the intermodal term is changed to $\sqrt{lx}$, where x (estimated $x = 1\,\text{m}$) is the mean path length between mode scattering.

Wavelength (nm)	Intermodal (nsec/m)	Chromatic (nsec/m)	Dispersion in 35 m (nsec)
313	0.0605	0.0159	0.66
337	0.0595	0.0105	0.51
365	0.0588	0.00779	0.44
386	0.0585	0.00650	0.41

Table 4.2: Chromatic and intermodal dispersion values in the dispersion model for pure silica step index fibre-optic.

The selected fibre is a hydrous silica nylon jacketed fibre (Fiberguide Ind. SFS-100/110/240/310N) which offered the best combination of UV transmission, low dispersion and cost. A novel method was used to measure the attenuation and dispersion in samples of the fibre using a fast N_2 pulser lamp (Optitron Inc. OP-NR-10) and a small PMT (Hammamatsu R1635) (see figure 4.7). The fibre is looped over a large drum and the PMT can see the photons at single photo-electron intensity that may scatter out of the fibre for each pass of a light pulse. A constant fraction discriminator, TAC and MCA then collects the spectrum of the pulse time for any observed PMT pulse. The spectrum contains multiple PMT time distributions offset by the loop transit time. The width of the prompt peaks give the dispersions at each distance and the peak heights allow the attenuations to be determined. The results are given in table 4.3 for several wavelengths using 10 nm cavity bandpass filters at the lamp and at the PMT (to investigate any fluorescence).

The laser pulses are transmitted to the laserball with a 35 m 'umbilical' incorpo-

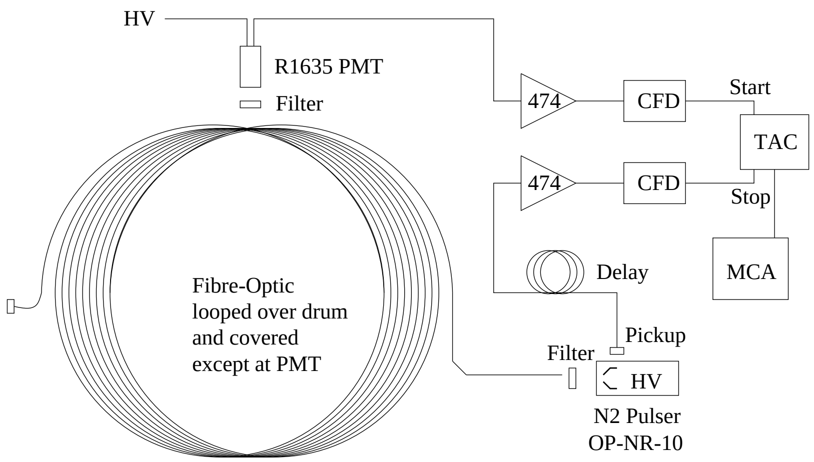

Figure 4.7: Apparatus to measure fibre-optic attenuation and dispersion.

Sample	Wavelength (nm)	Attenuation length (m)	Dispersion ($\times 10^{-3}$ ns/m)	Dispersion in 35 m (nsec)
1	313	8.9 ± 0.3	27 ± 6	0.95 ± 0.2
	337	15.4 ± 0.2	14.9 ± 1.0	0.52 ± 0.04
	365	23.8 ± 0.4	13.5 ± 1.5	0.47 ± 0.05
2	313	19.7 ± 0.3	20.6 ± 1.3	0.72 ± 0.05
	337	23.7 ± 0.2	9.4 ± 0.6	0.33 ± 0.02
	365	33.8 ± 0.5	9.2 ± 1.0	0.32 ± 0.04

Table 4.3: Attenuation and dispersion in SFS-100/110/240/310N fibre-optic.

rating a bundle of 22 fibres to maximize the light available and minimize the risk of fibre fatigue. The fibres are cut to the same length, to ensure the same transit time, and pulled through a number 11 black Teflon tubing. An RG174U cable, with the jacket stripped, a HV and a ground wire are spiral wound on the tubing and then pulled through and potted within a 1/2" OD silicone tubing with RTV silicone (GE-RTV615). This results in a flexible umbilical with mobility for the fibres to reduce the bending stresses. The umbilical is part of the calibration source manipulator system (chapter 2.4) which feeds out the cable as the laserball is moved.

The fibre-optic umbilical is terminated with a 10 cm diameter diffuser ball with an anti-buoyancy weight attached to the manipulator pulley carriage. The laserball diffuser consists of foamed glass bubbles mixed into a soft transparent silicone (GE-RTV6196) cured within a quartz glass boiling flask (figure 4.8). The neck plug contains a fibre-optic positioning guide tube and also houses a miniature monitoring PMT (Hammamatsu R5600). The RG-174U cable serves as the HV and the signal line for the PMT. The PMT can provide long term monitoring of the laserball output and can also provide pulse height corrections for increased pulse-to-pulse stability. The fibre-optic guide tube allows the umbilical cable to be detached from the laserball and reconnected without adjustment to the light output pattern. Figure 4.9 shows a sample laserball light pattern; the plot shows the light intensity over the polar angle at a fixed azimuth orientation. The light output pattern can be adjusted by slightly bending or retracting/protruding the copper guide tube. The density of glass bubbles and the position of the fibre bundle nozzle was designed using a small Monte Carlo to model the light scattering within the ball. The time spread for the fibre-optic and laserball combination was measured at single photo-electron intensity with a small PMT (Hammamatsu R1635) and the PIN diode laser trigger for several wavelengths. The results, in table 4.4, are consistent with the fibre-optics dispersion measurements and the laserball design, and meets the design objectives for PMT and optical calibrations.

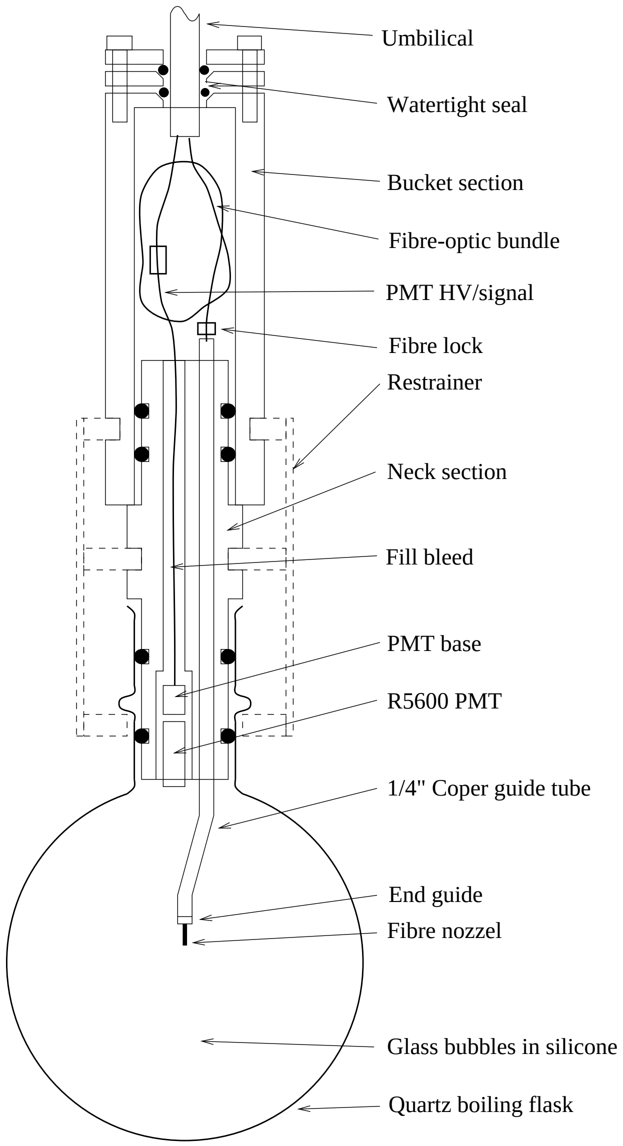

Figure 4.8: The SNO laser pseudo-isotropic diffuser ball (the laserball).

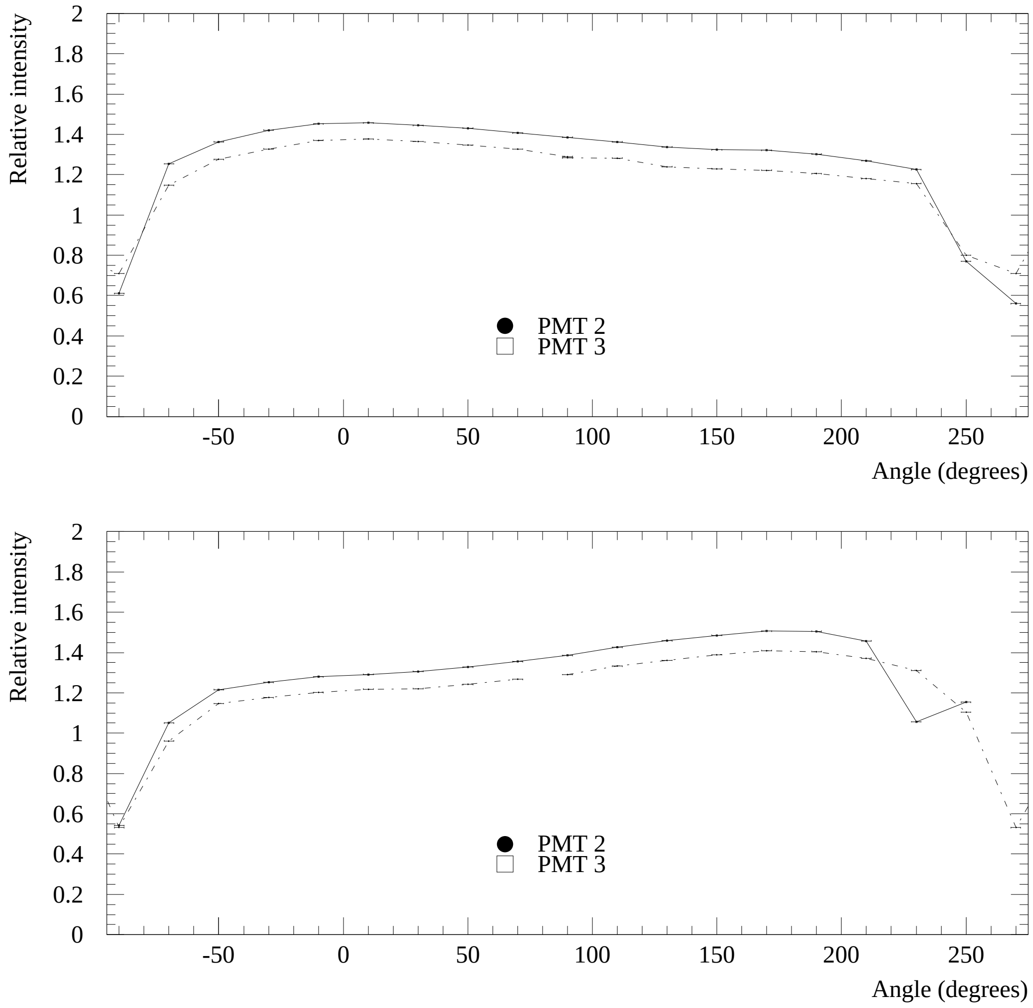

Figure 4.9: Single axis laserball scans in the darkroom with two opposite facing PMTs (PMT 2 and PMT 3) with pulse heights normalized to the laserball internal PMT pulse height. Angles for PMT 3 are displaced 180 degrees from PMT 2. The fibre-optic position in the laserball was adjusted between the two scans to demonstrate how the isotropy can be adjusted. (a) Scan before fibre adjustment, (b) scan after adjustment. The laserball was adjusted back to the first position.

Wavelength	PMT time σ (nsec)	System time σ (nsec)	Fibre + laserball σ (nsec)
500	0.96	0.52	0.81
386	1.04	0.52	0.90
337	1.29	0.52	1.18

Table 4.4: Pulse spreading in the fibre-optic umbilical and laserball.

4.3 PMT Timing Histograms

Most of the PMT and optical calibrations use the laser at single photo-electron intensity (SPE) and require histogramming the time between the laser trigger and the PMT hit time. The PMT calibration must be at SPE intensity since the gain, time offsets and time slewing must be known for neutrino events for which the light is SPE intensity. The optical calibration uses SPE laser runs because the good timing resolution of the SNO PMTs allows specific scattering and reflection phenomena to be observed in the PMT hit times. To collect these timing histograms the SNO detector must be triggered to stop the TACs and read out the channels from the laser trigger, rather than the internal NHIT or charge sum triggers. The SNO trigger system has an asynchronous mode where a global trigger is generated on demand without latching to the 50 MHz clock. The setup is shown in figure 6.2; the ECL line has a large (525 nsec) delay to compensate for the light transit and PMT transit times. The delay time is synchronized to the other trigger modes as described in chapter 6. The method for using these time histograms to calibrate the PMTs is described in chapter 6. It is assumed for the remainder of this chapter that the PMT times are corrected for the channel and cable delay offsets, time slopes and charge versus time (QvT) discriminator slewing.

Figure (4.10) shows the time histograms summed over 9522 PMTs and a single channel histogram for a Monte Carlo of 20,000 laserball events of 1850 3.21 eV (386 nm) photons. With the laserball at the detector centre the histograms can be directly summed to reveal information about the detector optics. The peak at 38 nsec is the prompt light, the other peaks are due to focused reflections, while the remainder of the histogram counts are due to bulk scattering, diffuse reflections and noise. Generally we will require histograms with several thousand counts in the prompt peak to obtain enough statistics for the optical fitting. For the optical analysis we sum the hits over several integration time windows for each PMT set with respect to the prompt peak time. The histograms are not summed for analysis since the prompt peaks are not aligned for the off-centre positions. Although there are not many hits in the scattering and reflection part of the histogram for a single channel, the integrations become significant for the whole ensemble of PMTs.

The largest secondary peak is found at 113.3 nsec which corresponds to the expected three radius transit time. The two earlier peaks are also due to PMT reflections, and are the result of the photocathode-reflector combination discussed below. The 50 nsec fall off from the prompt peak is well understood as Rayleigh scattering (section 4.4.1). The second order reflections are evident before the TAC timeout. The time histogram patterns for some different combinations of scattering and reflections can be studied from figure 4.11 for Monte Carlo data with several conditional cuts. Some individual PMT time histograms are shown in figure 4.12 for the laserball at several positions. Histogram (c) for PMT 9365 is an example of a lensing phenomena which is quite rare but it is expected from the detector geometry and must not be mistaken for prompt light. Histogram (d) shows a common problem with a light source in the H_2O where broad peaks from reflections off the acrylic dominate the spectrum. Other effects due to PMT pre-pulsing and after pulsing are not yet included in the Monte Carlo as they are small compared to the Rayleigh scattering. However, these effects are discussed in chapter 6 for the air-fill calibration.

The optical analysis proceeds by locating the prompt peak with a sliding window algorithm for each PMT time histogram. The algorithm finds the time window with the largest number of hits, and checks if the peak is reasonably distinguished and close to the expected prompt time. Alternate peaks are inspected until the prompt light is identified. The peak is integrated to the number of prompt hits $N_p(i)$ (for PMT i) and the centroid and widths are calculated from the distribution moments. The window width is set empirically at 7 nsec (see figure 4.23) due to the scattering

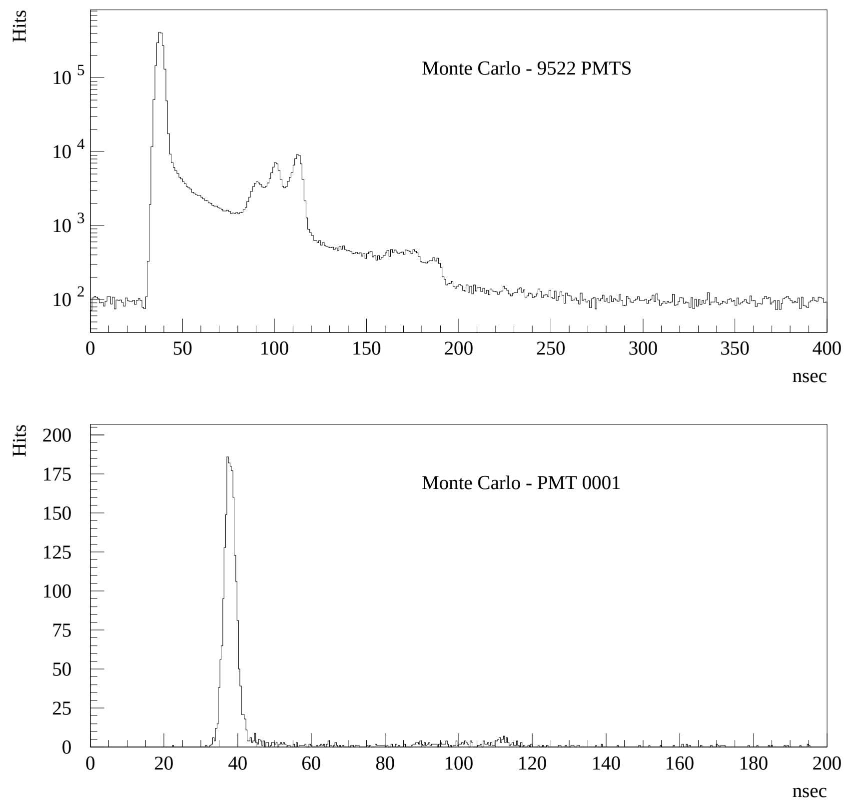

Figure 4.10: (a) Summed time histogram for laserball at centre of the vessel. (b) Single channel histogram (PMT 0001). Data are from Queen's Monte Carlo for 20,000 events of 1852 3.21 eV photons with the complete geometry and the 3D PMT model.

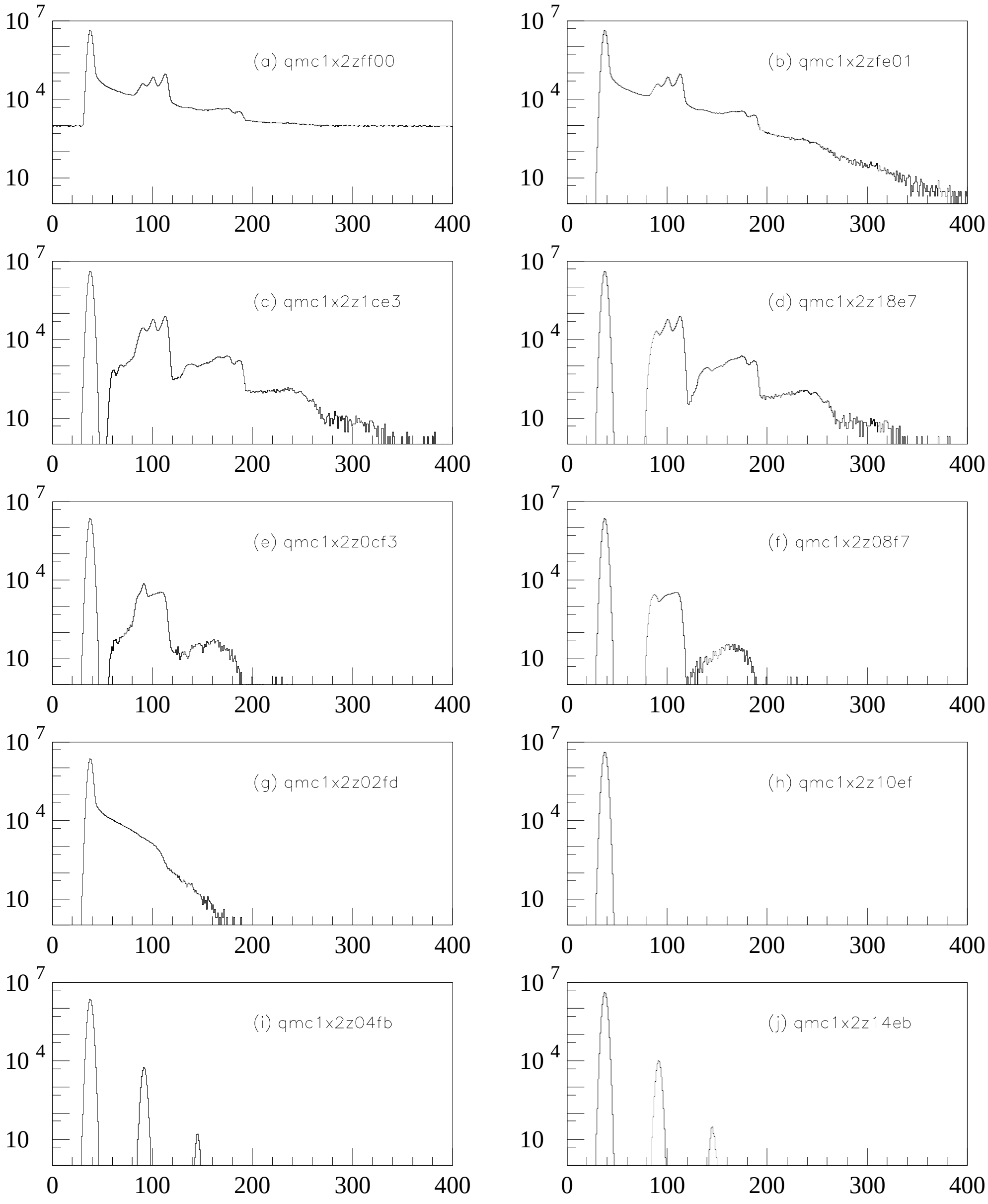

Figure 4.11: Summed Monte Carlo time histograms with cuts on various optical interaction flags. (a) All hits (b) No noise (c) No noise or scattering (d) No noise, scattering or AV reflections (e) No noise, scattering or PMT petal reflections (f) Photocathode reflections only (g) Scattering only (h) PMT petal reflections only (i) AV reflections only (j) AV and PMT petal reflections only

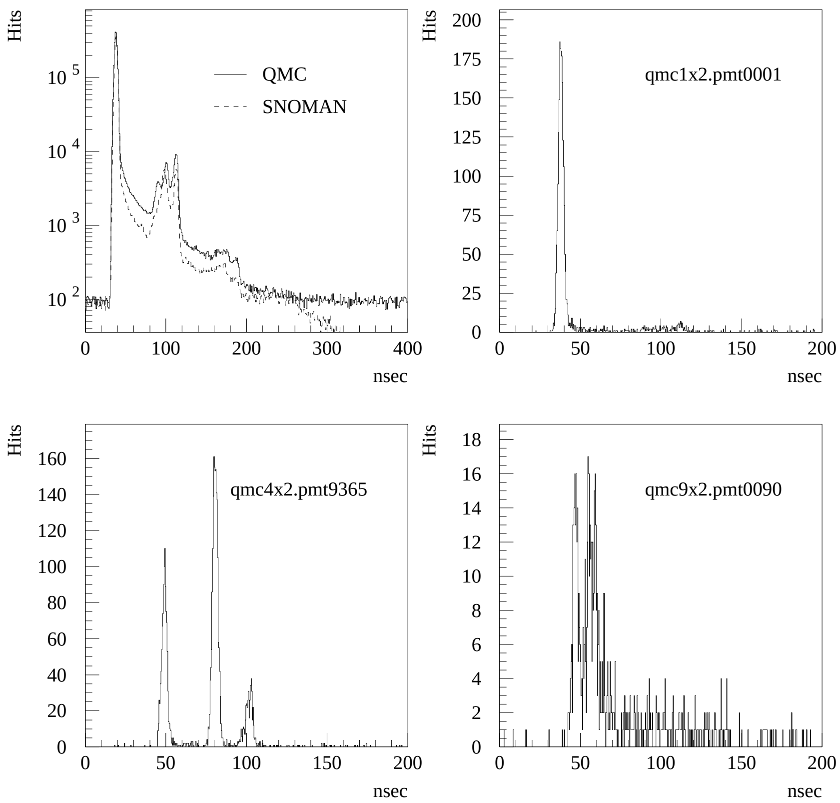

Figure 4.12: a) Summed time histograms for SNOMAN and Queen's Monte Carlo
b) PMT 1 for laserball at (0,0,0)
c) PMT 9365 for laserball at (0,0,-500)
d) PMT 90 for laserball in H_2O at (650,0,374)

tail on the late side of the prompt light. A 30 nsec window following the prompt time is integrated to find the scattering contribution. The scattering component is characterized by the slope at the centre of the 30 nsec window.

The peaks at 91.5 and 99.5 nsec can be understood by taking the photon path to be a detector radius plus a PSUP cord and calculating the PMT reflection angle

$$\cos(\theta) = 0.01336\,t - 0.5 \tag{4.11}$$

The angles are about 44° and 34°. Using ray tracing from a drawing of the PMT/reflector geometry the 44° reflection results from a 50° reflection from the photocathode. The peak is explained as it is well known [87] that the photocathode reflection coefficient rises dramatically at 50° for the parallel polarisation. This reflection is near the PMT reflector bucket cutoff which causes differences in the prominence of this peak between the SNOMAN and Queen's Monte Carlo (top left in figure 4.12).

The peak at 34° is due to a more subtle PMT-reflection interaction that causes the Winston cone reflectors to form an image at about 35°. This effect was verified by shining a flashlight at a PMT 230 cm distant and observing a ring image of the petals projected on the wall with a 165 cm radius. To reflect from a PMT at 35°, the photons must bounce only once off both the photocathode and the aluminized reflector petals, which offers the unique opportunity to use this reflection peak to monitor the average condition of the reflectors. This proposal is evaluated by running the Monte Carlo for the laserball with different values for the PMT petal reflectivity. The reflectivity can then be evaluated by taking the ratio of the prompt peak to the 35° ring image peak and correcting for attenuations. This ratio is actually a bit complicated since both the reflecting and the hit PMT has a dependence on the reflector. The approximation here is that the 35° peak varies with the coefficient squared, while the prompt peak is partially linearly dependent on the reflection coefficient. The result is plotted in figure 4.13; it looks promising that this method would be useful in tracking the aging effects of the aluminized reflectors.

A remaining consideration is the adjustment of light source intensity to maintain SPE PMT response. The photoelectron multiplicity is a Poisson distribution $P(n, \mu)$ with a mean detected light intensity μ. At SPE light intensity μ is the probability

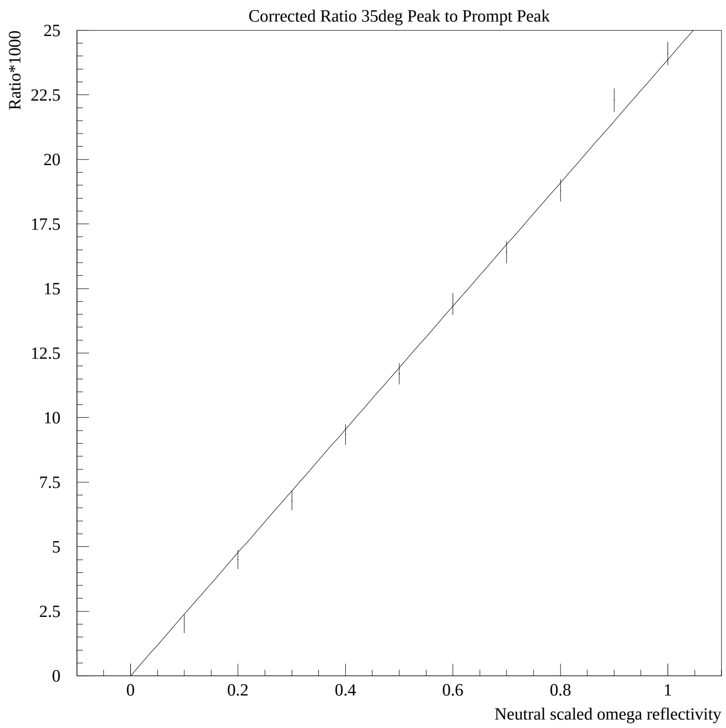

Figure 4.13: Attenuation corrected ratio of hits in the 35° peak to the prompt peak plotted versus the PMT aluminized petal reflectivity.

of an average PMT registering a hit, which is also equal to NHIT divided by the total number of PMTs. If the laser is pulsing at rate R then in time t the number of prompt hits for an average PMT is

$$N_p = Rt\,(1 - P(0,\mu)) = Rt\left(1 - e^{-\mu}\right) \tag{4.12}$$

To keep the probability of two or more photoelectrons to less than 1% would require that the mean event probability be less than 2%-3% everywhere. This would be impractical given the large variation in PMT solid angles when moving the laserball, and would result in very low statistics. Instead we choose the intensity so that most of the PMTs are at SPE intensity and make the correction for each PMT i

$$(N_p')_i = \mu Rt = -Rt \times \log\left(1 - \frac{(N_p)_i}{Rt}\right) \tag{4.13}$$

where Rt is the total number of laser flashes.

Higher photoelectron multiplicities will also distort the time spectrum and so it is important to understand this quantitatively. The time spectrum distortion is due to the discriminator firing on the leading edge of the pulse which results from the first photoelectron. The timing spectrum can be calculated by multiple convolution with a Gaussian for each photoelectron with a cut-off at the time for the first photoelectron. These spectra can then be summed with Poisson weightings. This calculation is easiest to perform as a Monte Carlo, since the first photoelectron time selection imposes awkward cut-offs on the integrals.

Figure 4.14 shows the results of such a calculation assuming a Gaussian shape with a sigma of 0.9 nsec for the laserball pulse and a PMT transit time spread of 1.4 nsec. In the first plot the abscissa is the mean light intensity which is linearly related to the laserball output and equal to the NHIT probability (NHIT divided by the total number of PMTs) in the low intensity limit. In the second plot the abscissa is NHIT probability. The first line plotted is the centroid value of the time peak (with an arbitrary 3 nsec offset) which is seen to shift to earlier times with increasing NHIT. From the second line we see that the sigma also decreases, but only very slowly. The third line is the ratio of the mean intensity to NHIT probability which shows how

NHIT varies with multiple photoelectrons. From linear fits to the plots the following approximate adjustments can be used for NHIT probabilities up to 50%

$$t \longrightarrow t - 0.66 \times \frac{N_p}{\text{Laser pulses}} \tag{4.14}$$

$$\sigma \longrightarrow \sigma - 0.042 \times \frac{N_p}{\text{Laser pulses}} \tag{4.15}$$

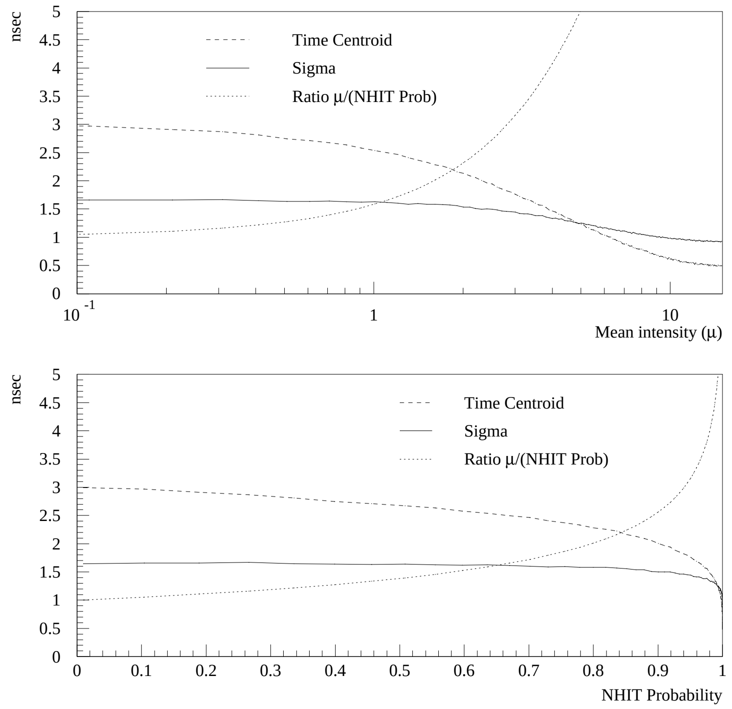

Figure 4.14: The multiple photo-electron time shift. Plot of time centroid shift and sigma versus mean light and NHIT Probability for a single PMT (see text).

Note that the timing issues discussed here are in addition to the electronics Q versus T (QvT) SPE slewing corrections. The issue of unfolding these two effects for neutrino data analysis is discussed further in the PMT calibration section of chapter 6.

4.4 Scattering in SNO

Light scattering in the SNO detector is a difficult phenomenon to measure as it can have many causes and effects. Scattering can be intrinsic to the material, like Rayleigh scattering, or can be due to coherent or incoherent scattering and reflections off particulate matter ranging in size from nanometers to tens of microns. Due to the large size of the SNO detector, even in infinitely clean water, density fluctuation scattering is a common process with over 10% of detected light having been scattered. Scattering can change the resolution and gain of the detector. Fitters that attempt to identify events by hit pattern recognition might be particularly sensitive to scattering distributions that are different from any training sets used.

Instead of attempting to identify and measure all the scattering processes we intend to quantify the effects of scattering guided by how it impacts the interpretation of the SNO data. Any light scattering will cause PMT hits to be out-of-time and out-of-position in a non-random way (unlike noise hits). A pattern recognition fitter wants to know how out-of-time and how out-of-position the hits are; knowing a total scattering cross section is much less useful.

We intend to quantify bulk scattering in SNO with a parameter for the cross section and the angular distribution. Working from the time histograms we concentrate on the height and shape of the hit time distribution in set time windows following the prompt light. From this we can define an effective scattering cross-section. This cross section will be smaller than the real cross section as it will ignore forward scattered light. This is sensible as the SNO data cannot distinguish forward scattered or phase shifted light. The shape of the time distribution, parameterized by the slope at the window midpoint can indicate the broad nature of the angular distributions. Again this is reasonable as there will never be enough detector event data to be sensitive to any fine structure of coherent scattering angular distributions. In future SNO calibration it might be possible to learn more about the angular distribution of scattered light by using a directional (beamed) source. Such a source can be constructed using a laserball mask with a pipe. This is not considered here, but the time distribution analysis for a directional source can be easily obtained from the formalism presented below.

There are three modes of scattering to be considered: dipole (Rayleigh) scattering, Mie scattering and scattering from larger particulate matter. Rayleigh scattering is due to thermally fluctuating electron densities; it is expected to dominate due to the wide $(1 + \cos^2\theta)$ angular distribution. Mie scattering is the intermediate case where the size of the scattering centre is similar to the photon wavelength. The angular distributions must be worked out more rigorously due to phase coherences; the effect is to produce angular distributions that are very forward peaked.

Any larger particulate matter suspended in the water will absorb and reflect light. Assuming a spherical shape of radius a, the reflected light is uniform

$$\frac{dN}{d\Omega} = \frac{a^2}{4} \tag{4.16}$$

Since the distributions will be indistinguishable, we combine specular reflection with Rayleigh scattering by considering the distribution

$$\frac{dN}{d\Omega} = 1 + k\cos^2(\theta) \tag{4.17}$$

where $0 \leq k \leq 1$.

4.4.1 Dipole and Specular Scattering

To study the effects of scattering we start with dipole (Rayleigh) scattering, then try varying distributions keeping with the same general form. For the predicted water purity levels Rayleigh scattering will be the dominant process. For an optical source at the centre of the detector there is a time period of about 40 nsec where there can be no real tube hits unless the photon has made a large angle scatter from within the bulk medium. This suggests an opportunity for determining a characteristic scattering length for dipole scattering in water. Since dipole scattering is due to thermal fluctuations in electron density, scattering should be about the same in D_2O and H_2O. However, the available data is still not reliable [77].

Averaged over polarisations the dipole polar angular distribution has a $(1+\cos^2\theta)$ shape. To permit an admixture of bulk specular scattering we take the distribution

$(1 + k\cos^2\theta)$. Including absorption and transforming the angles into time one finds, for the laserball at the centre of a homogeneous detector, the time spectrum for photons undergoing a single Rayleigh scattering event is

$$\begin{aligned}\frac{dN}{dt} &= \frac{3N_o}{2(k+3)x_s}\exp\left(-\frac{vt}{x_a}-\frac{vt}{s_s}\right)\int_0^R\left[\left(1+k\left\{\frac{v^2t^2+x^2-R^2}{2vtx}\right\}^2\right)\right. \\ &\quad \times\left.\left(\frac{v^2t^2+R^2-x^2}{2xvt^2}\right)\exp\left(-\frac{x}{x_a}-\frac{x}{x_s}\right)\epsilon(\cos\alpha)\right]dx, \qquad (4.18)\end{aligned}$$

where $\epsilon(\cos\alpha)$ is the PMT efficiency and angular response with

$$\cos\alpha = \frac{R^2+v^2t^2-x^2}{2vtR}. \qquad (4.19)$$

The absorption and scattering lengths are given by x_a and x_s. Figure (4.15) shows the results of a computation, where the integral was split into the D_2O and the H_2O regions and integrated across the detector several times. Terms were included for specular reflection from the PMTs, re-transit across the detector and multiple scatters. The spectrum has unphysical sharp secondary peaks since the calculation assumes that all reflected light bounces back from the PMTs at 180°. This time distribution is used in all subsequent analyses since generating these data in the full Monte Carlo (SNOMAN) would take several CPU-weeks.

We now take a window from 45 to 65 nsec and integrate the number of counts for calculated time spectra using a range of D_2O absorption lengths and scattering lengths. A 3D map of this integral versus the absorption length and scattering length is shown in figure 4.16 for $k = 0$ and $k = 1$. The calculation was done also for other k values but are not shown as these are consistent with figure 4.16. We see that for reasonable values of the absorption length (about 60 m) the $45 - 65$ nsec integral is fairly independent of the absorption and k. Thus for all forms of dipole and specular scattering the *effective* scattering length is easily parameterized by the 45-65 nsec integral.

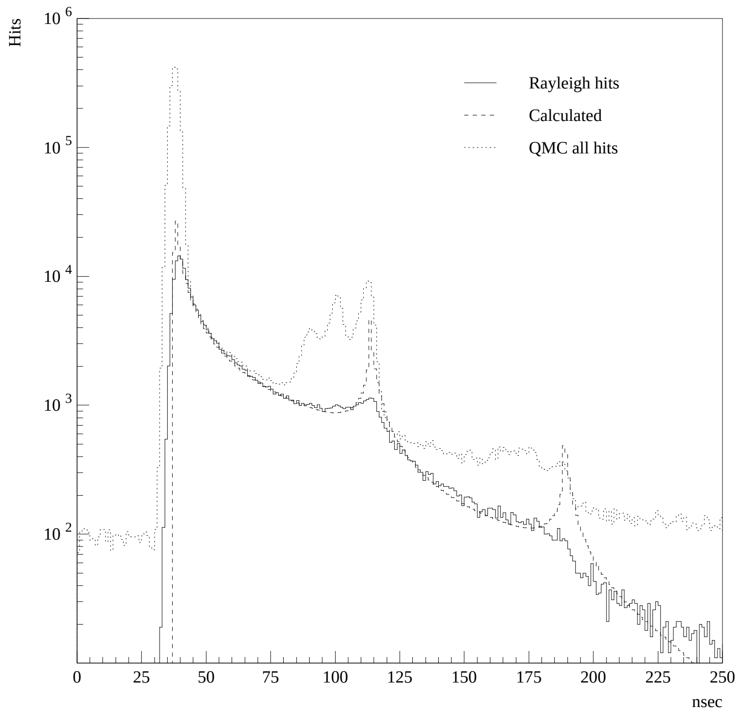

Figure 4.15: Comparison of simple calculated Rayleigh scattering time spectrum to Monte Carlo data.

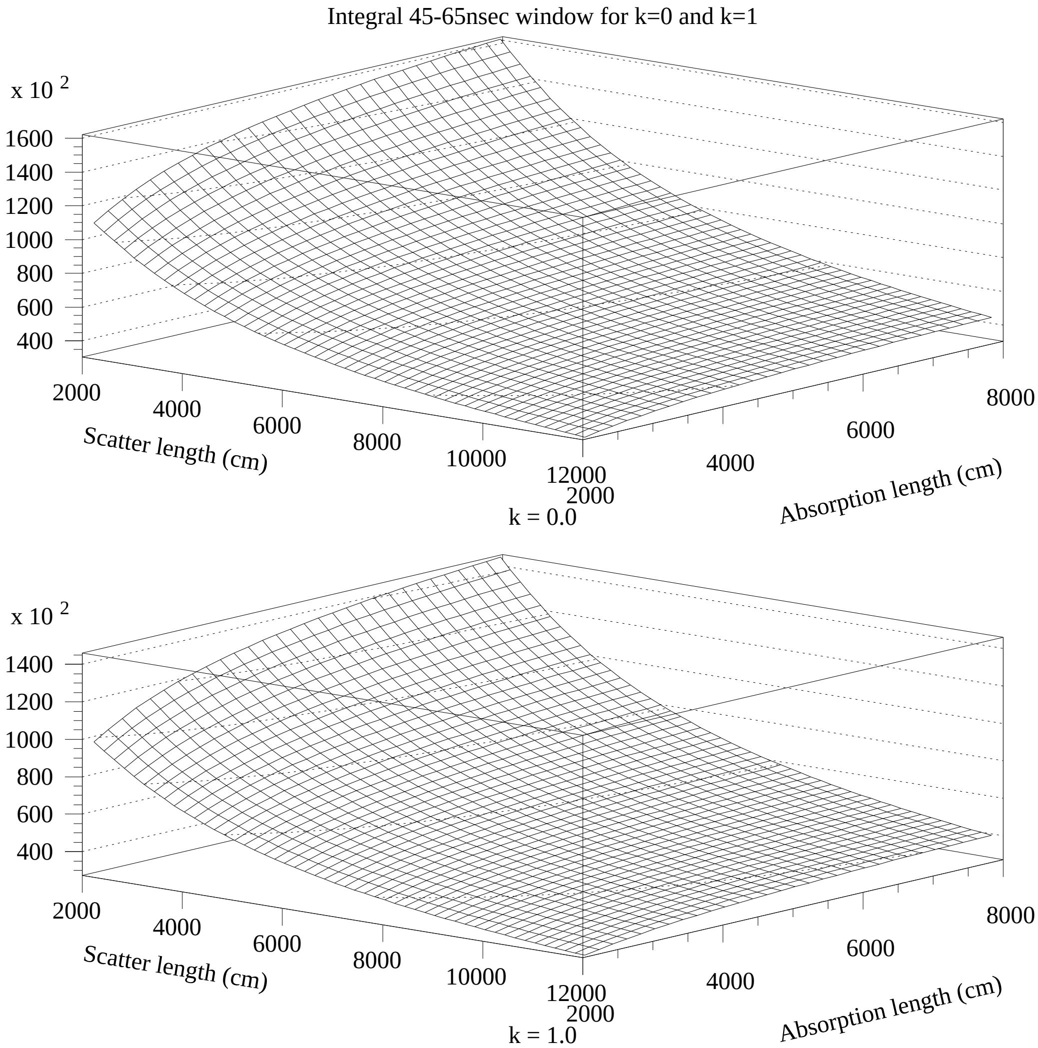

Figure 4.16: Integral of the 45-65 nsec window as a function of scattering length and absorption length for the distribution $1 + k\cos^2(\theta)$. For the upper plot $k = 0$ and for the lower plot $k = 1$. We see that the integral can be specified by a effective scattering length and is fairly independent of k and the absorption.

4.4.2 Non-dipole Scattering

We now turn to the intermediate case where scattering is from foreign impurities in the water of a size comparable to the wavelength of light. This is known as Mie scattering. The problem rapidly becomes intractable unless some simplifying assumptions are made about the scattering object shape and composition. Waltham [88] considered scattering from the bacteria *E.coli* whose refractive index was measured to be $n_b = 1.415$. He found that the total scattering cross-sections calculated for an ellipsoidal shape agreed with measurements.

We now calculate the angular distributions for light scattering off *E.coli* and then determine the hit time distribution in SNO for an isotropic source at the centre of the detector. The light intensity a distance r away from a scattering centre is

$$I = I_{\circ} \frac{|S_1(\theta)|^2 + |S_2(\theta)|^2}{2k^2r^2} \tag{4.20}$$

where $k = 2\pi n_w/\lambda$ and

$$\begin{aligned} S_1(\theta) &= \sum_{n=1}^{\infty} \frac{2n+1}{n(n+1)} \left\{ a_n \pi_n(\cos\theta) + b_n \tau_n(\cos\theta) \right\} \\ S_2(\theta) &= \sum_{n=1}^{\infty} \frac{2n+1}{n(n+1)} \left\{ b_n \pi_n(\cos\theta) + a_n \tau_n(\cos\theta) \right\} \end{aligned} \tag{4.21}$$

The Mie functions (π_n, τ_n) and coefficients ($a_n(x)$, $b_n(x)$) can be found in [89] and are functions of the aspect ratio $x = ka$ with a the particle radius. Some angular distributions are plotted in figure 4.17 for the range of aspect ratios of interest ($x = 4$ to $x = 16$).

Similar to equation 4.18 the time distribution is

$$\begin{aligned} \frac{dN}{dt} &= \frac{2\pi N_o R t \epsilon}{\langle f(\theta) \rangle x_s} \exp\left(-\frac{vt}{x_a} - \frac{vt}{s_s}\right) \int_0^R \left[f\left(\cos^{-1}\left\{ \frac{R^2 - v^2t^2 - x^2}{2vtx} \right\} \right) \right. \\ &\times \left. \left(\frac{v^2t^2 + R^2 - x^2}{2xRvt^2} \right)^2 \exp\left(-\frac{x}{x_a} - \frac{x}{x_s} \right) \right] x\, dx \end{aligned} \tag{4.22}$$

where the PMT angular response has been approximated by $\cos\alpha$. The angular function f is given by

$$f(\theta) = |S_1(\theta)|^2 + |S_2(\theta)|^2 \tag{4.23}$$

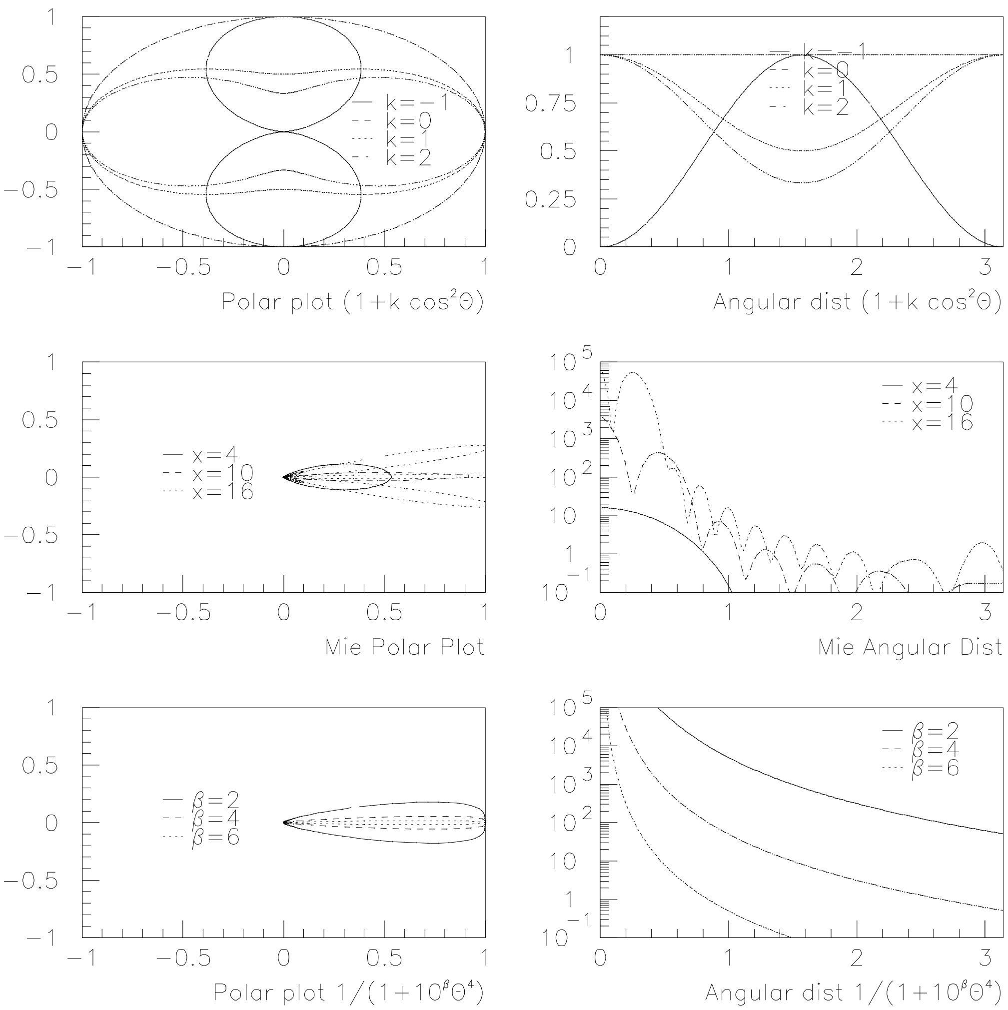

Figure 4.17: The top plots show the polar and angular distribution for dipole-like scattering. The middle plots show the distribution calculated from Mie theory for several aspect ratios. The lower plots shows a simple model for Mie type scattering distributions.

but was actually replaced by a Chebyshev polynomial fit to the angular functions S_1 and S_2. As before, equation 4.22 was integrated to produce a time spectrum including terms for reflection off the PMTs. Again the counts in the 45 to 65 nsec window are summed. These results are shown in figure 4.18, where the integral counts in the 45-65 nsec window is plotted as a function of the scattering particle aspect ratio. In the first case the scattering length is held fixed at $x_s = 6660\,\mathrm{cm}$; we see clearly that the time distribution is insensitive to the aspect ratio (and hence insensitive to the details of the angular distribution). In the second case the bacterial density[3] is held fixed at $8524\,\mathrm{cm}^{-3}$ and the scattering cross-section is calculated from the Mie formula. The integral is linearly dependent on the aspect ratio, hence the time distribution is well characterized by a single parameter: the scattering length. That is, whether any change in scattering length is due to a change in particle (bacteria) size or a change in the bacterial density does not matter. It can be noted that the bacterial density used here ($8524\,\mathrm{cm}^{-3}$) is very high, yet the resulting time distribution integral is down by about an order of magnitude from Rayleigh scattering.

To investigate the sensitivity to the forward peaks in the angular distributions f was replaced with a simple form with a forward peak parameterized by β (see figure 4.17)

$$f(\theta) = \frac{1}{1 + 10^{\beta}\theta^{4}} \tag{4.24}$$

Again calculating time distributions and integrating the 45-65 nsec window the results are seen in figure 4.19. The 45-65 nsec window sum is plotted as a function of the parameter β. We see that when β is negative we essentially have Rayleigh scattering. As β gets to a value of 2 the distribution is becoming forward peaked as in Mie scattering and the integral drops rapidly. For β larger than 2 the integral is constant with a value just the same as for Mie scattering with the same scattering length.

We conclude here that the SNO detector is sensitive only to wide angle scattering like Rayleigh or specular scattering and that this scattering can be parameterized by a single effective scattering length. Scattering then can always be assumed to be

[3] The value $8524\,\mathrm{cm}^{-3}$ was picked for the density because at aspect ratio $x = 10$ it worked out to the same scattering length used in the Queen's Monte Carlo for Rayleigh scattering at 386nm.

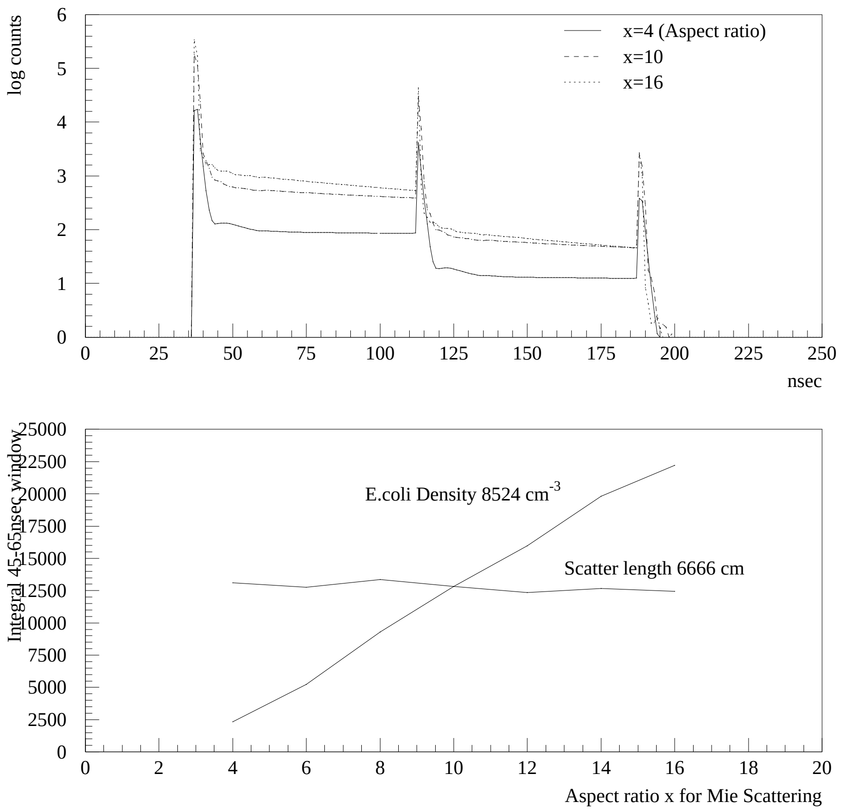

Figure 4.18: The upper plot is the time distribution for Mie scattering with various aspect ratios. The lower plot show the counts in the 45-65 nsec window versus the aspect ratio in Mie scattering for (a) constant density with the scattering length worked out from the aspect ratio, and (b) constant scattering length.

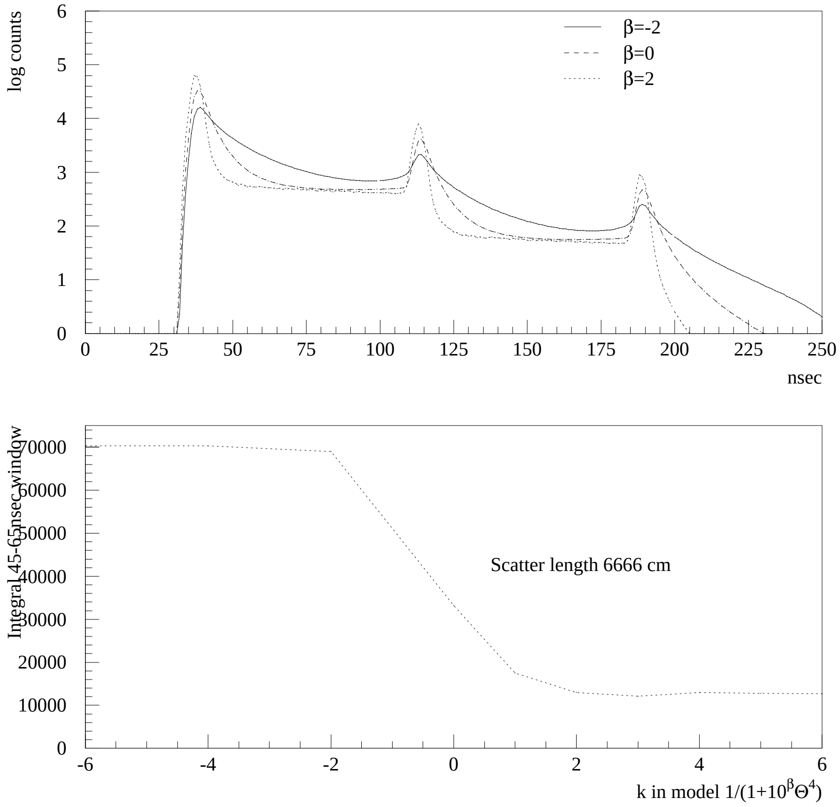

Figure 4.19: The upper plot is the time distribution for the scattering model $1/(1+10^{\beta}\theta^4)$ with several values of β. The lower plot shows the counts in the 45-65 nsec window versus β.

uniform with an *effective* scattering length given by the integral of the time histogram between 45 and 65 nsec. Mie scattering has a very minor effect due to the strong forward peak of the angular distribution. In fact SNO can tolerate bacterial counts an order of magnitude higher than Waltham's initial estimates [88] (10^5 L^{-1}) with the amount of light scattered out of time by Mie scattering still lower than for Rayleigh scattering. High bacterial counts will just add to the effective scattering length while the light distribution within the detector will still be well modeled by a uniform distribution with this *effective* scattering length.

4.5 Optical Fitting Algorithms

For the laserball at position $\vec{L}_j$, over any time the number of hits in PMT i (position $\vec{P}_i$) due only to the light pulses is given by

$$\begin{aligned} (N'_p)_{ij} &= RtN_{ij}\Omega_{ij}\epsilon_{ij} \\ &\times \exp\left(-x_{ij}^{\mathrm{D2O}}\lambda^{\mathrm{D2O}} - x_{ij}^{\mathrm{H2O}}\lambda^{\mathrm{H2O}} - \sum_{k=1}^{\mathrm{NPanels}=125} x_{ijk}^{\mathrm{ACR}}\lambda_k^{\mathrm{ACR}}\right) \\ &\times (1 - R_{1ij})\,(1 - R_{2ij})\,(1 + S_{ij}) \end{aligned} \tag{4.25}$$

where Rt = Number of laserball pulses

N_{ij} = Photons per pulse into unit solid angle (angular distribution of laserball)

Ω_{ij} = Solid angle subtended

ϵ_{ij} = QE including PMT angular response

λ = Extinction coefficient

x_{ij}^{M} = Distance through D_2O or H_2O

x_{ijk}^{ACR} = Distance through acrylic panel k. Note the sum is just for convenience since for a particular i and j only one x_{ijk}^{ACR} is non zero.

R_{mij} = Water-acrylic reflection coefficients

S_{ij} = Hits due to scattered light

In general the extinction coefficients might also depend on $\vec{L}_i$ and $\vec{P}_j$ due to inhomogeneities within the water volumes.

The factor S_{ij} that adds back the detected scattered intensity is a very loose approximation since this does not depend only on the positions $\vec{L}_i$ and $\vec{P}_j$, but it is a complicated function of the entire detector. This is a common problem for all optical photometry experiments. The size of the SNO detector makes it unique as an optical instrument, since an analysis of the arrival times of the PMT hits permits the factor S_{ij} to be partially separated out.

To fit an expression for N'_p with the laserball (equation 4.25) requires calculation of the distances through each medium for every PMT and laserball position. This is not straight forward as the straight line distances between the source and the PMT would always reduce the distance in the acrylic (due to refraction), resulting in a bad fit and a large error in the acrylic attenuation. Even with simple geometry (an acrylic sphere) an analytic solution for the path length is difficult. An iteration method is used which takes path directions to each PMT, propagates the angles due to refractions and then uses the final distance error to adjust the initial direction cosines until convergence at the target.

A problem arises in what coordinate position to take for the PMT location. We want a single target point that well represents the PMT in an average sense. The problem can be significant for finding the correct path distance through the acrylic; it is much less important for the D_2O and H_2O distances. What is required is an average path through the acrylic weighted by the probability of a PMT hit, ie.

$$\overline{x}_{\text{acr}} = \frac{1}{\Omega_0} \int x_{\text{acr}}(\theta, \phi) P(\theta, \phi) \, d\Omega \tag{4.26}$$

where $P(\theta, \phi)$ is the probability of the PMT detecting a hit for a given path, $x_{\text{acr}}(\theta, \phi)$ is the corresponding path length through the acrylic and Ω_0 is the projected PMT solid angle. The SNOMAN Monte Carlo is actually well suited for evaluating such an integral. By running many events with an isotropic source x_{acr} can be weighted with the number of hits. The result is that the optical paths to a PMT are best calculated by assuming the light destination is 4.5 cm in front of the PMT glass evelope.

A further issue is that for laserball positions in the D_2O the path lengths through the acrylic and H_2O are highly correlated, as seen in figure 4.20. Thus it takes high statistics and positions near the acrylic to effectively separate the H_2O and the acrylic attenuations. This degeneracy breaks only at the highest angles into the acrylic, precisely where the errors in the calculated distances will be greatest.

The method is to run the laserball at several locations and sum the hits in the prompt peak for each PMT. The log of the N'_p expression (equation 4.25) is linear in the relative efficiency and the extinction parameters. One can imagine proceeding with a χ^2 fitter by inverting a 128×128 matrix at each wavelength (for 125 acrylic panels plus two extinction coefficients and a gain offset). Unfortunately, drifts in PMT efficiencies, uncertainty in the laserball pattern and covariances between the extinction coefficients make this method all but impossible. The method must be iterative and proceed with human intervention. For example, the D_2O attenuation coefficient can be obtained quite reliably since there is no degeneracy is the distances. With the measured laserball distribution, and averaging over AV panels, the relative efficiencies are obtained. Then a simultaneous fit to the acrylic and D_2O can be performed. These strategies can only be worked out with real data using the tools developed here. The optical analysis tools developed for SNOMAN are discussed at the end of this chapter. Presented here are some examples of optical parameters fitting using Monte Carlo data.

The D_2O extinction can be obtained independent of other optical parameters with laserball runs at positions down the centre axis and using the PMTs directly below the south pole acrylic panels. Then the distance variation in the acrylic and light water is almost zero, as is the angle to the PMTs. The logarithm of prompt N'_p, with solid angle and rate corrections is plotted in figure 4.21 for 105 PMTs that are viewed through the south pole panel at five on-axis laserball positions. A straight line fit yields the extinction coefficient ($-0.000297 \pm 0.000028\,\mathrm{cm}^{-1}$ or $34 \pm 3\,\mathrm{m}$) and a gain offset which is quite arbitrary as the absolute QE is unknown. The Monte Carlo input value for the extinction coefficient at 386 nm is $-0.00031\,\mathrm{cm}^{-1}$. The figure also shows

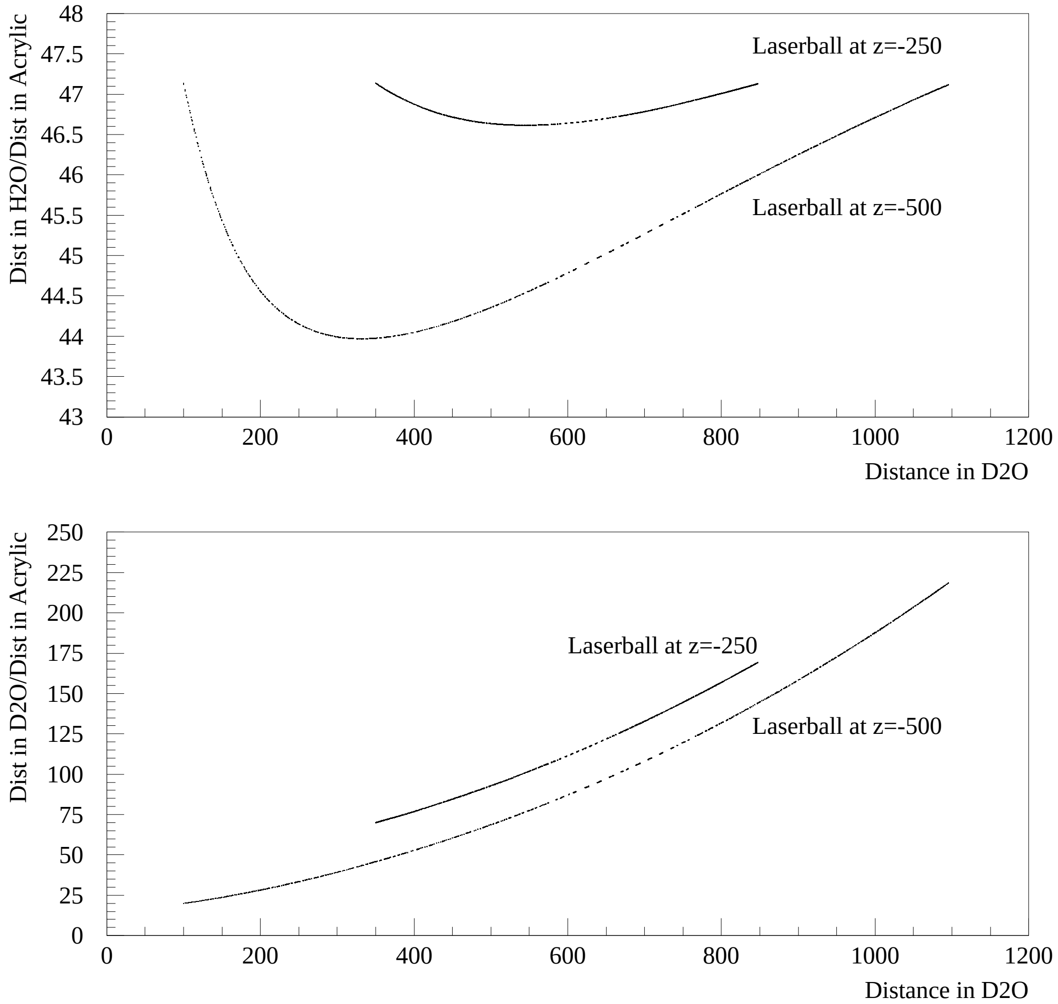

Figure 4.20: (a) Ratio of the distance in H_2O to the distance in acrylic as a function of path length in the D_2O for two laserball positions. This shows that the path lengths are highly correlated so that a determination of the H_2O attenuation is strongly coupled to the acrylic attenuation. (b) Ratio of the distance in D_2O to the distance in acrylic as a function of path length in the D_2O for two laserball positions. These attenuations are not strongly coupled.

the shape of the χ^2 surface where we see that the attenuation does trade off against the QE, but the correlation is not strong. Fitting with all the PMTs offers much better statistics, but does introduce a dependence on other estimated parameters, ie. the acrylic attenuation and the angular PMT response. The fit is seen in figure 4.22 (-0.000286 ± 0.000037 cm^{-1}) with the same QE correlation.

Using this data we can now return to the issue of choosing the width of the integration window for the time histograms. The above fit was repeated with N'_p extracted using varying integration window widths for the prompt peak sum. The result is shown in figure 4.23; empirically 7 nsec is a reasonable choice for the integration width.

A multi-dimensional linear function (equation 4.25) is minimized for three parameters, the D_2O and acrylic attenuations, and a gain figure. The χ^2 surface is plotted in figure 4.24 for the D_2O and acrylic attenuations with the gain fixed at the fit value. The fitted attenuations are $-0.000284 \pm 0.00036\,\mathrm{cm}^{-1}$ for the D_2O and $-0.0172 \pm 0.0033\,\mathrm{cm}^{-1}$ for the acrylic with Monte Carlo values of $-0.00031\,\mathrm{cm}^{-1}$ and $-0.02\,\mathrm{cm}^{-1}$ at 386 nm. Fits to the acrylic have the potential for large systematic errors due to an incorrect PMT response measurement. For off-centre laserball positions the line of sight path to the the majority of PMTs occurs at high angles of incidence. This effect is increase by small angle scattering in the outer volume. The optical calibration code (OCA) removes PMTs with large incidence angles from the fit. The OCA code also includes optional statistical weighting based on the PMT angle and provides a PMT angle correction as an extra free parameter.

4.6 OCA and Online Optical Monitoring

The optical calibration code (OCA) is a SNOMAN processor that calculates the optical parameters discussed in this chapter from the SNO data stream for several laserball runs at different positions. The online optical monitoring is a feature of the SNO event display program that allows the effects of changing the optical parameters to be displayed graphically.

The OCA code is a data driven processor that allows many combinations of optical

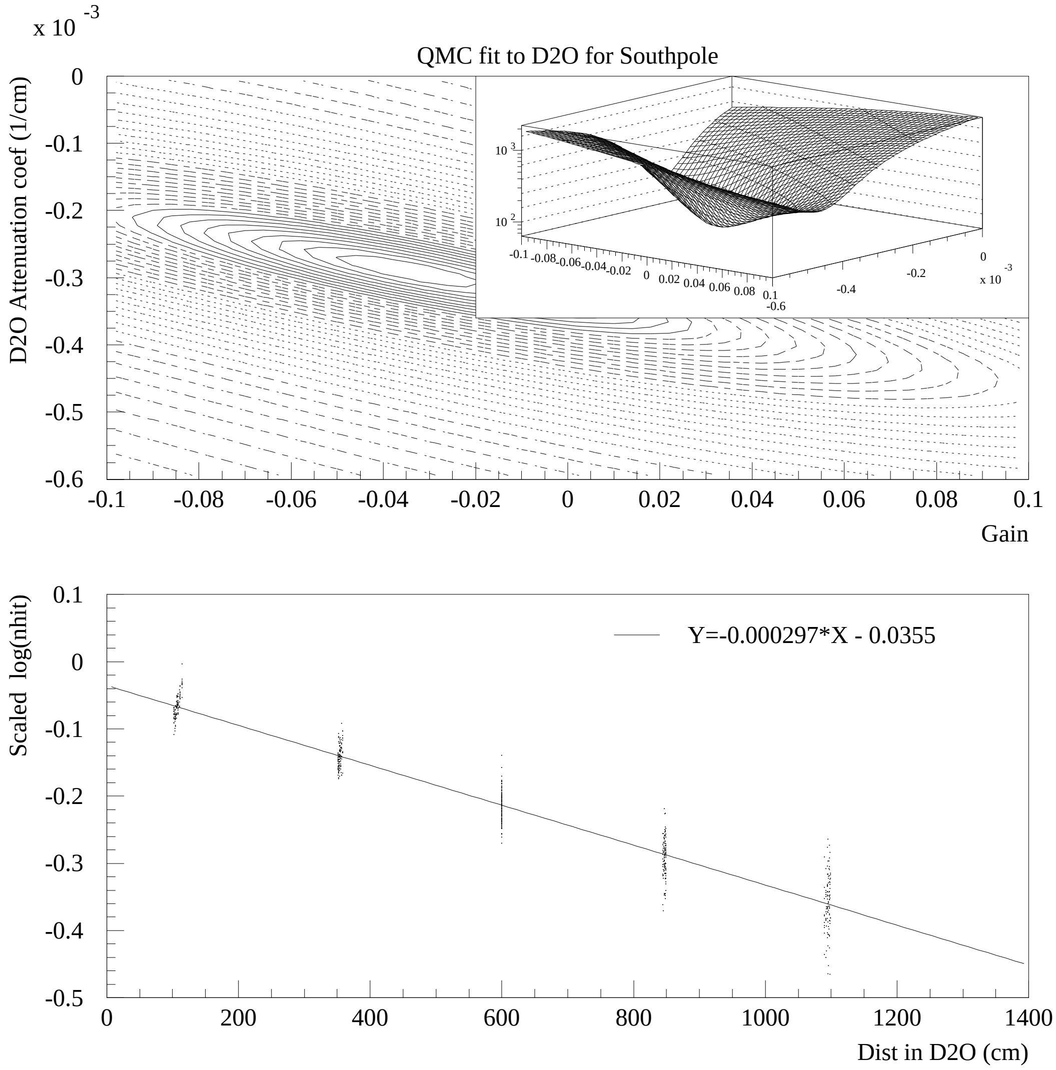

Figure 4.21: Fit to $\log(N'_p)$ and distance in the D_2O from Monte Carlo data with PMTs below the 111 panel (south pole) for the laserball at 5 positions on axis within the D_2O. Fit yields an extinction coefficient of $-0.000297 \pm 0.000028\,\mathrm{cm}^{-1}$ or an attenuation length of $34 \pm 3\,\mathrm{m}$. The upper plot shows the χ^2 surface.

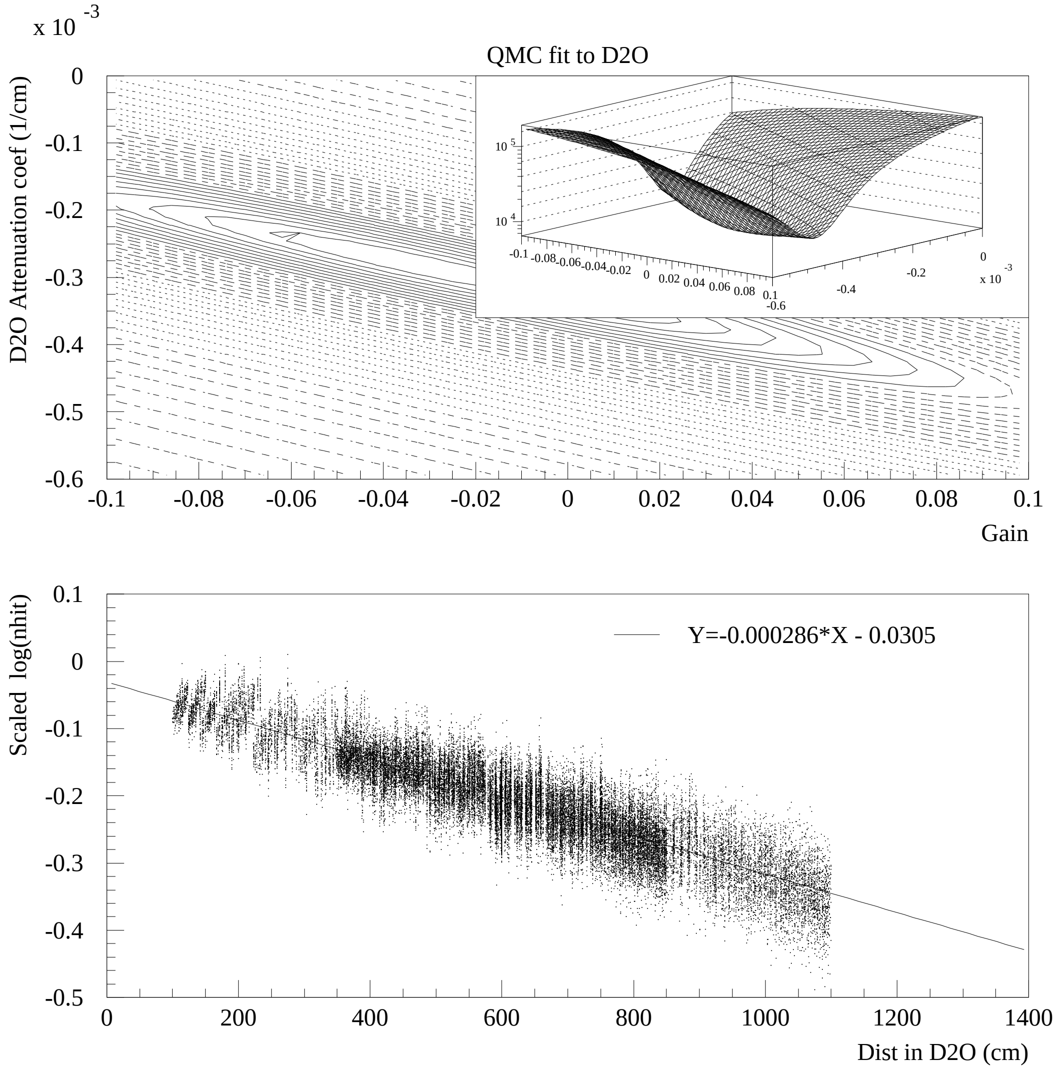

Figure 4.22: Fit to $\log(N'_p)$ and distance in the D_2O from Monte Carlo data for the laserball at 5 positions on axis within the D_2O. Fit yields an extinction coefficient of $-0.000286 \pm 0.000037\,\mathrm{cm}^{-1}$ or an attenuation length of $35 \pm 4\,\mathrm{m}$. The upper plot shows the χ^2 surface.

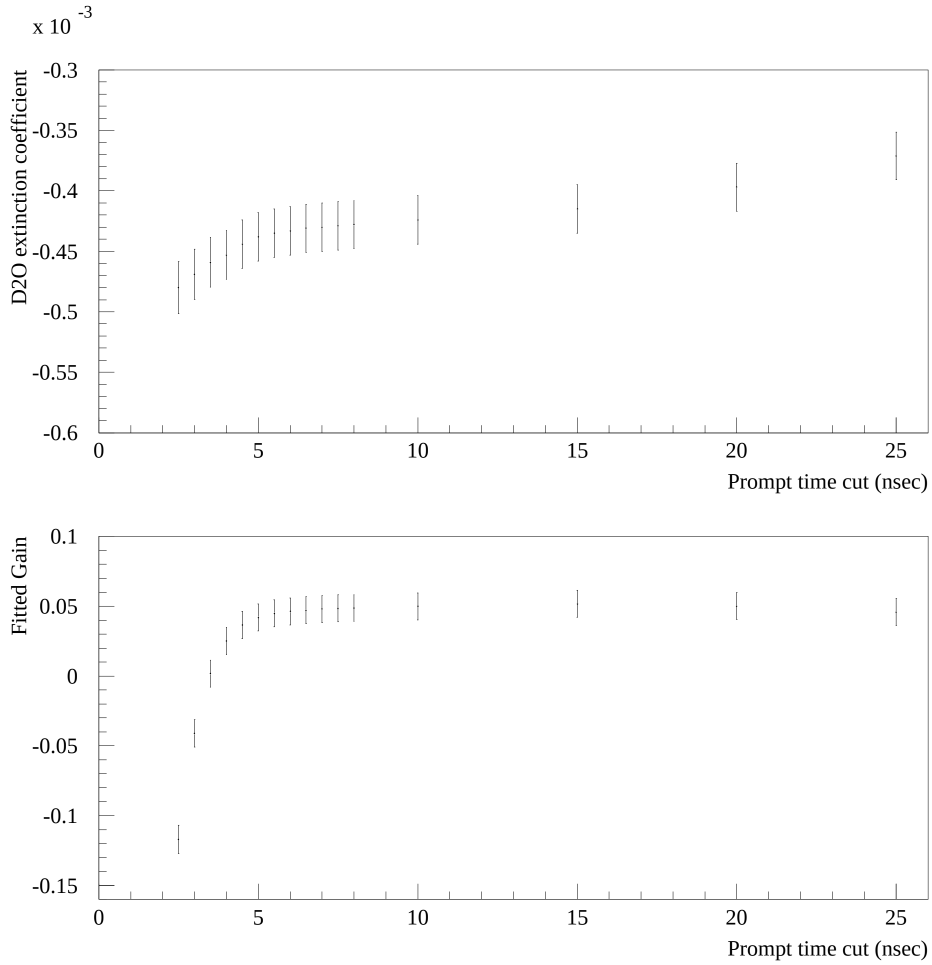

Figure 4.23: Fitted D_2O attenuation and gain versus integration time window width using SNOMAN data for south pole PMTs. A window width of 7 nsec appears to be reasonable choice.

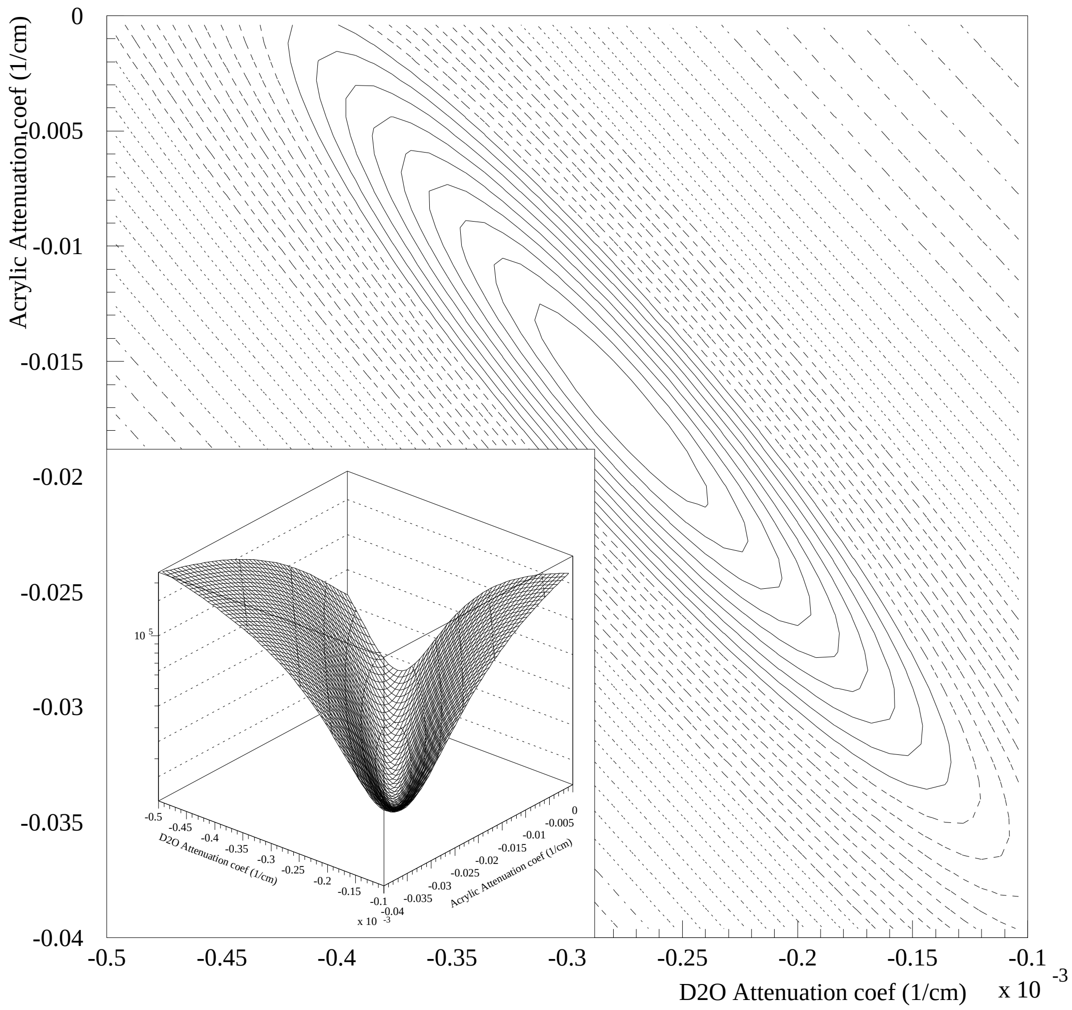

Figure 4.24: χ^2 contours for variations in D_2O attenuation and acrylic attenuation from Monte Carlo data for five laserball positions in the D_2O. Best fit yields $-0.000284 \pm 0.00036\,\mathrm{cm}^{-1}$ for D_2O (35 m) and $-0.0172 \pm 0.0033\,\mathrm{cm}^{-1}$ for acrylic (58 cm).

fitting procedures to be executed in a programmable sequence. The processor first reads in an available run list which describes the laserball positions, wavelengths, pulse rate and intensity for each run. When fully implemented this data can be taken directly from the data stream from banks written out by the DAQ. The OCA code then produces the time histograms, finds the prompt and reflection peaks, and integrates the hits in the time-slice windows. Then the optical path distances are calculated and corrections made for the solid angle, multiple photoelectron, and PMT angular response. The processing sequence is illustrated in figure 4.25. The CERNLIB MINUIT minimization package is used for the extinction parameters fitting. The strategies for the sequence of fitting, freezing parameters and laserball run selections is user programmable. The strategy is selected in the data file, or at the user prompt for a totally user-driven fit. The calculated optical parameters are displayed and can be rejected or accepted for use in further fitting. The OCA processor includes routines for finding various optical parameters by several different strategies. For example, the relative PMT efficiencies can be obtained from laserball runs at the detector centre at a long wavelength (420 nm) where the acrylic attenuations will be small. Then, at shorter wavelengths, the D_2O and acrylic attenuations can be fitted with the methods described in this chapter using several laserball positions. The scattering and PMT reflector parameters can be calculated with routines that integrate windows in the PMT timing histograms. Also, the acrylic attenuation for several AV panels can be determined for runs with the laserball in the PSUP light water region by the transmission technique.

Since the optical calibration will require human intervention to force convergence, a graphical method of finding a good fit is being developed. The event display program uses a large binary file that includes, for a number of preset laserball positions, all the media path distances and a response factor for each PMT. The binary file includes pre-calculations of the solid angle, PMT angular response, multiple photoelectron correction, Fresnel coefficients and a prompt time integration window. This data file is generated by the SNOMAN OCA processor using the geometry and algorithms already developed. With this data the event display program can now sum the hits

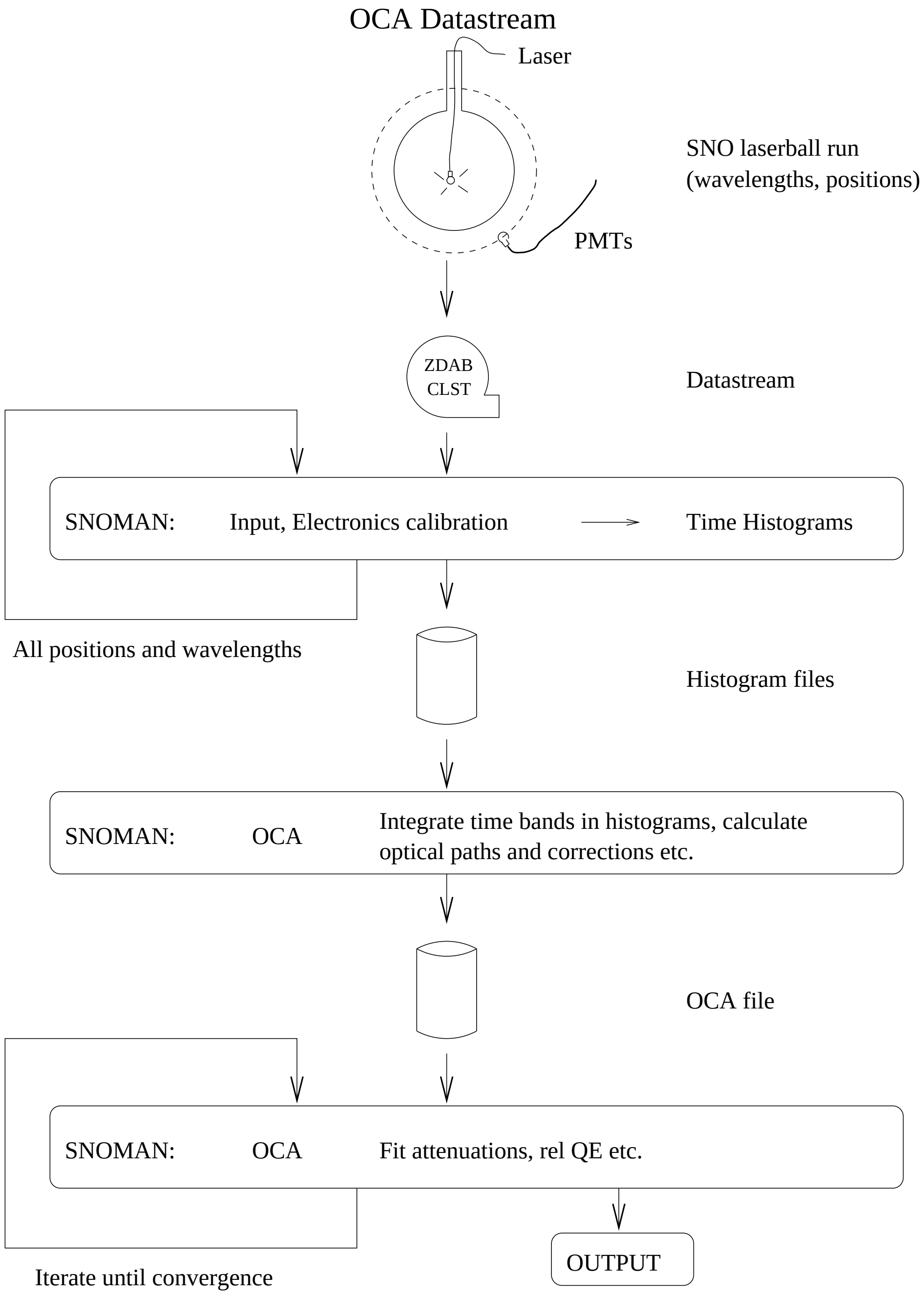

Figure 4.25: The SNOMAN OCA processing sequence.

within the time windows as the data is recorded and rapidly evaluate the expected occupancy from the extinction equation (equation 4.25). The data file also contains the derivatives of the path lengths and angular responses with respect to the x, y, and z laserball position to allow some variation from the preset laserball positions. The display can then represent the PMT in the display with a colour depending on whether the prompt occupancy is high or low, and by how much, for a given set of extinction parameters. The extinction parameters can then be adjusted using graphical slide bars, and the PMT colour map redisplayed for each change. A good optical parameters fit is obtained when all the PMT are the same colour in the display map. This method gives the operator a good feel for for how the detector response is dependent on the optical parameters, and can provide good starting or fixed values for the OCA fitting routines.

Combining equation 4.25 with the multiple photo-electron correction the online display will implement the formula

$$\log\left(1 - \frac{(N_p)_{ij}}{Rt}\right) = A_{ij} Z_{ij} \Omega_{ij} \sum_{n=1}^{3} \exp(-x_n \lambda_n) \tag{4.27}$$

where i and j are the laserball positions and PMT numbers, and Ω_{ij} is the solid angle for each PMT. $(N_p)_{ij}$ will be the continuous accumulation of asynchronously triggered (laser) hits in each PMT within the prompt time window, as supplied in the data file. The factor Z_{ij} includes the laserball pattern, PMT angular response and QE, and the Fresnel transmission factors (as in 4.25). Rt is the total number of laser pulses, which is the number of asynchronous triggered events found in the SNO datastream. The factor A_{ij} is the total laserball output per pulse (which is unknown, but of order 5000 photons for a 5% occupancy SPE run) and will also soak up any residual due to the attenuation, and thus specifies the PMT colour for the graphical map. We write

$$A_{ij} = B(1 + \alpha y_{ij}) \tag{4.28}$$

where B is the constant laserball output and α defines a zero centered colour scale. The first task for the online monitoring code is to collect a distribution in A_{ij}, for an off-centre laserball position, using the best guess values for the attenuation. The factor B is the peak (central) value of A_{ij}, and reasonable bounds on the distribution sets the scale factor α. The user can then scale the attenuations with the graphical slide bars, and the colour map is modified as per

$$\text{PMT colour index}_{ij} = \frac{1}{\alpha}\left(\frac{A_{ij}}{B} - 1\right). \tag{4.29}$$

Chapter 5

Energy Calibration Function

The SNO detector calibration will enable a fitted event to be assigned an electron equivalent energy along with an uncertainty. The fitted event will contain a number of PMT hits with a calculated position and direction. The number of hit PMTs will depend on the event type (electron or gamma ray), the position and direction, the PMT quantum efficiencies, and the optical attenuation and scattering parameters. In this chapter, a detector calibration function is developed that calculates the electron or gamma ray energy of an event assuming the measured optical constants and properties of the PMTs. The calibration function is then compared to a Monte Carlo calculation of the detector response.

In other large volume detectors (eg. Super Kamiokande) the Monte Carlo is used to generate an expected calibration mapping for any position or direction dependence. The Monte Carlo is 'tuned' to match available calibration points, for example by modifying attenuations or the PMT angular response. As SNO is more sensitive to changes in the optics (mostly due to the acrylic), we need to be more careful with such procedures. To use the Monte Carlo would require generating a multi-dimensional grid of the response in x, y and z, but also with as many other dimensions as there are optical parameters which are expected to be important. If we want to investigate any number of parameters beyond the 'tuned' Monte Carlo, then the required amount of Monte Carlo becomes rapidly intractable.

The advantage of the calculated calibration function is that it only needs to be calculated at one point in the parameter space for each event. Thus the calculation takes only milli-seconds to execute and can be built right in to any spectrum analysis code. Another advantage for the calibration function method is that the instantaneous derivatives of the calibration function, with respect to all the inputs, is readily calculated. This permits an event by event uncertainty estimation based on the uncertainties of the inputs.

5.1 Electron Calibration

The geometric part of the calibration function calculates the detector response to an electron at a distance r from the centre and angle θ from the radius to the response for an electron at the centre (see figure 5.1). The response is calculated by integrating over the Čerenkov emission distribution $g(\theta', \phi')$ with a weighted integral over the Čerenkov wavelength spectrum $1/\lambda^2$ and PMT wavelength response. The response function is normalized to the response at the centre of the detector and then can be scaled to a measured calibration point (eg. ^{16}N). The calibration function has the form

$$\mathcal{R}(r,\theta) = \frac{\int_{\lambda_1}^{\lambda_2} d\lambda \, \frac{\epsilon(\lambda)}{\lambda^2} \int d\Omega' \, g(\theta', \phi') e^{-\mu l}}{4\pi \int_{\lambda_1}^{\lambda_2} d\lambda \, \frac{\epsilon(\lambda)}{\lambda^2} e^{-\mu R}} \tag{5.1}$$

where l is the vector distance to the intercept on the PSUP sphere with radius R. Compare this response to the isotropic case used in chapter 4 (equation 4.6) for studying the optical dependences.

Owing to the complex distributions, the integral is performed numerically as a simple Riemann sum. While the calculation does include actual distributions, as in the Monte Carlo, most of the inputs are replaced with simple parameterizations that can be integrated directly. This allows the sum to be formed systematically, instead of random sampling, with the intention that the calculation should be simple and fast. The basic function is

$$R(r,\theta) = \sum_{\theta'} \sum_{\phi'} \sum_{\lambda} \frac{\epsilon(\lambda)}{\lambda^2} g(\theta', \phi') e^{-\mu_1 d_1} e^{-\mu_2 d_2} e^{-\mu_3 d_3} P(r, \theta, \theta', \phi')(1-R_1)(1-R_2). \tag{5.2}$$

Here R_1 and R_2 are the reflection coefficients at the acrylic and μ_i is the attenuation in D_2O, acrylic and H_2O, θ and ϕ are angles relative to the electron trajectory, and $P(r, \theta, \theta', \phi')$ is the PMT angular response.

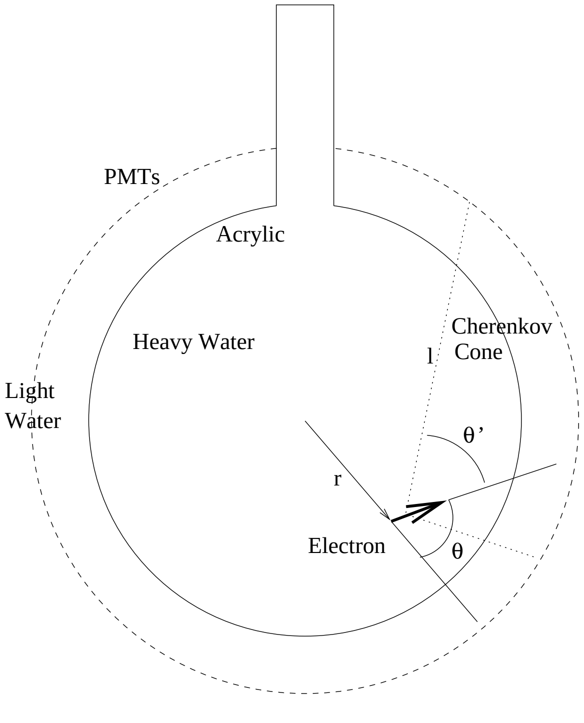

Figure 5.1: Angle definitions for the detector response function.

5.1.1 Čerenkov Angular Distribution

The response of the SNO detector to electrons and gamma rays is different than for an isotropic light source due to the detector geometry. The calculated calibration function is not very sensitive to the detailed shape of the Čerenkov light distribution, $g(x)$, as long as it is distributed in approximately the correct proportion. For example, modeling the Čerenkov distribution as a perfect cone ($x = \cos\theta$)

$$g(x) = \delta(x - x_c) \tag{5.3}$$

does not introduce any backward light. Furthermore, the multiple photoelectron correction would be incorrect because the light intensity would be high for a small number of PMTs. Using the SNOMAN Monte Carlo we can find suitable angular distributions to provide the right energy dependence and extra straggling for gamma rays. The Čerenkov polar angular distribution is shown in figure 5.2 for a couple of electron kinetic energies. We will employ the parameterization

$$g(x) = \begin{cases} p_3 x^2, & x < x_c \\ p_2 \exp(p_1 x), & x \geq x_c \end{cases} \tag{5.4}$$

which actually only has one parameter dependent on the energy. At the Čerenkov angle p_3 is fixed by $p_3 = p_2 \exp(p_1 x_c)/x_c^2$, and p_2 is set by normalizing the distribution. The slope of the tail is given by

$$p_1 = -2.04 - 0.034 T_e, \tag{5.5}$$

where T_e is the electron kinetic energy.

5.1.2 Multiple Photoelectrons

The multiple photoelectron correction (MPE) is important for electrons produced closer to the PMTs. The MPE correction is the only term in the calibration function that depends substantially on the particle energy, the number of photons created, and the absolute quantum efficiency of the PMTs. However, the overall effect of these parameters on the function shape is not large if reasonable numbers are used.

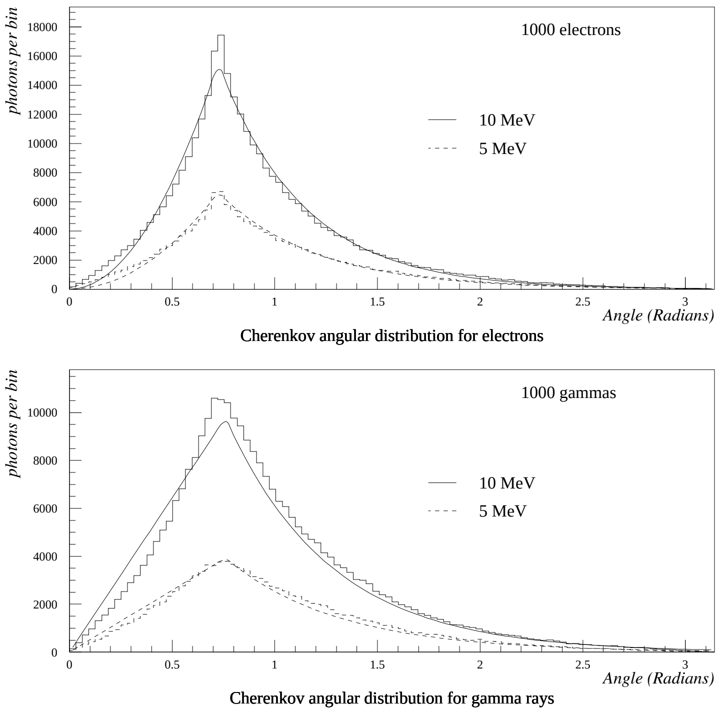

Figure 5.2: Čerenkov polar angle distributions for electrons and gammas in SNO, with the simple parameterizations used in the calibration function calculation.

The MPE correction is calculated from the Poisson statistics for the mean light level μ in photons per PMT. The mean detectable light μ in a direction ($x = \cos\theta$) from the electron path is found to be

$$\mu = \frac{g(\theta')N\epsilon AB\cos\alpha}{2\pi d^2 a \sin\theta'} \tag{5.6}$$

where

where $\epsilon(\lambda)$ = PMT quantum efficiency at wavelength λ
$g(\theta')$ = Čerenkov distribution ($g(x)$ equation 5.4)
N = Total Čerenkov photons (approx $330 \times 10\,\mathrm{MeV}/2.2$)
A = Area of a PMT (589 cm^2)
B = Total attenuation along optical path ($\prod_i (1 - R_i)e^{-\mu d_i}$)
$\cos\alpha$ = Angle to the PMT
d = Distance to PSUP
a = Fraction photocathode coverage (0.65)
$\sin\theta'$ = Solid angle factor

The MPE correction is then a reduction factor M to the mean photon intensity that accounts for multiple photons only getting counted as single hits

$$M = \frac{1 - P(0,\mu)}{\mu} = \frac{1 - e^{-\mu}}{\mu} \tag{5.7}$$

5.1.3 Time Fitter Drive Correction

The time fitter has a systematic shift in the fitted radius r_{fit} and the angle to the radial line θ_{fit} compared to the actual values. This effect, called fitter drive, was discussed earlier in chapter 3.4. The fitter drive effect occurs when scattered light has a longer path length than direct light. Since Čerenkov light is produced in the forward direction, the largest fitter drive occurs for those events where more of the PMTs are behind the electron direction of travel. This occurs at larger event radii for outward trajectories which lead to the simple parameterization offered as equation 3.19. We consider the effect in a bit more detail here in order to find a fitter drive correction factor for the electron calibration function.

The fitter drive effect in θ and r is shown in figure 5.3 using SNOMAN Monte Carlo for a million electrons. The figures shows 2-dimensional histograms of the shift in fit radius (Δr) and direction cosine ($\Delta \cos\theta$) binned by fitted radius and direction. The bins are in the natural volume units of r^3 and $\cos\theta$ so the parameter space is uniform in incident events.

We can parameterize this shift

$$\cos\theta = a\cos\theta_{\text{fit}} \tag{5.8}$$

$$r = r_{\text{fit}} - bZ \tag{5.9}$$

where $a = 0.85$ and $b = 1.5\,\text{cm}$. The pull ratio Z is the ratio of PMTs outside the Čerenkov cone to those inside, and is given by

$$Z = \frac{2}{1-\cos\frac{\Omega}{2}} \tag{5.10}$$

and

$$\Omega = 2\theta_c - \delta + \beta \tag{5.11}$$

$$\sin\beta = \frac{r}{R}\sin(\theta-\theta_c) \tag{5.12}$$

$$\sin\delta = \frac{r}{R}\sin(\theta+\theta_c) \tag{5.13}$$

where R is the PSUP radius (850 cm) and θ_c is the Čerenkov angle in water (41°).

5.1.4 Čerenkov Light Output

The Čerenkov light production is required in the response function to calculate the MPE correction (equation 5.6). Using the Bethe formula with $I = 97\,\text{eV}$ for the ionization potential we can obtain an approximate form for the stopping power in water valid at SNO energies

$$\frac{dE}{dx} = 2.18 + 0.26\log\left(\frac{T_e}{10\,\text{MeV}}\right)\ \text{MeV}\cdot\text{cm}^{-1}. \tag{5.14}$$

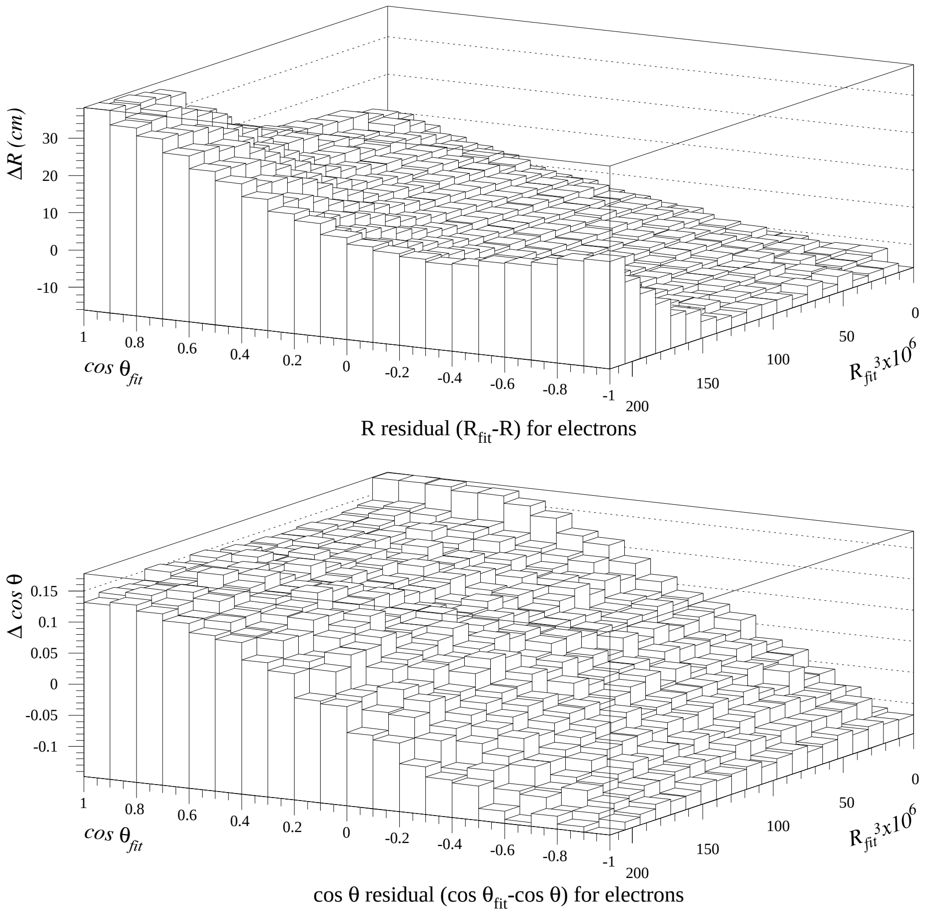

Figure 5.3: Time fitter drive in r and $\cos\theta$ from Monte Carlo of 100,000 electrons. The radius residuals $(r_{\mathrm{fit}} - r_{\mathrm{true}})$ and direction residuals $(\cos\theta_{\mathrm{fit}} - \cos\theta_{\mathrm{true}})$ are binned according to fitted radius and direction.

The Čerenkov photon output for electrons is

$$\frac{d^2N}{dx\,d\lambda} = \frac{2\pi\alpha}{\lambda^2}\left(1 - \frac{1}{n^2\beta^2}\right) = \frac{2.02\times 10^5}{\lambda^2}\,\text{photons}\cdot\text{cm}^{-1}\cdot\text{nm}^{-1} \tag{5.15}$$

which (see figure 5.4) is quite constant down to the threshold of 659 keV (T_e = 148 keV). The small effect due to dispersion of the water refractive index is ignored here.

The range of the electron for Čerenkov production is found from the stopping power by integrating down to the Čerenkov threshold in water T_t

$$R_c = \int_{T_t}^{T_e} \frac{dE}{2.18 + 0.26\log(E/10)} = \frac{e^{-c}}{0.26}\left(\log y + \frac{y}{1\cdot 1!} + \frac{y^2}{2\cdot 2!} + \cdots\right)_{c+\log T_t}^{c+\log T_e} \tag{5.16}$$

where $c = \frac{2.18}{0.26} - \log 10 = 6.08$ and the range is in cm. The electron range is almost linear in energy, with a value of about 5 cm at 10 MeV, but very well fit by a quadratic (figure 5.4). The Čerenkov output spectrum, which is flat in photon energy, is then

$$\frac{dN}{d\lambda} = \left(\frac{10^3}{\lambda^2}\right)\left(-6.2 + 121.8T_e - 1.56{T_e}^2\right)\ \text{nm}^{-1} \tag{5.17}$$

$$\frac{dN}{d\nu} = 98.3\left(-0.051 + T_e - 0.013{T_e}^2\right)\ \text{eV}^{-1} \tag{5.18}$$

where T_e is the electron kinetic energy in MeV. The actual light output is shown by the Monte Carlo to have significant straggling, due to multiple scattering of the electron or Compton scattering, which reduces the mean light production by 8% for electrons and 15% for gamma rays (see figure 5.4).

5.1.5 Electron response function

The resulting calibration function is shown in figure 5.5 for 8 MeV electrons, with a comparison to Monte Carlo. We see agreement in the overall shape of the function compared to the Monte Carlo result, and that the variation of the function over the $\cos\theta$ and r space is significant (10%). We have also plotted a difference distribution between the Monte Carlo and the calibration function and evaluated the χ^2. Note that the χ^2 is usually very large (for 400 bins) since it scales directly with the number

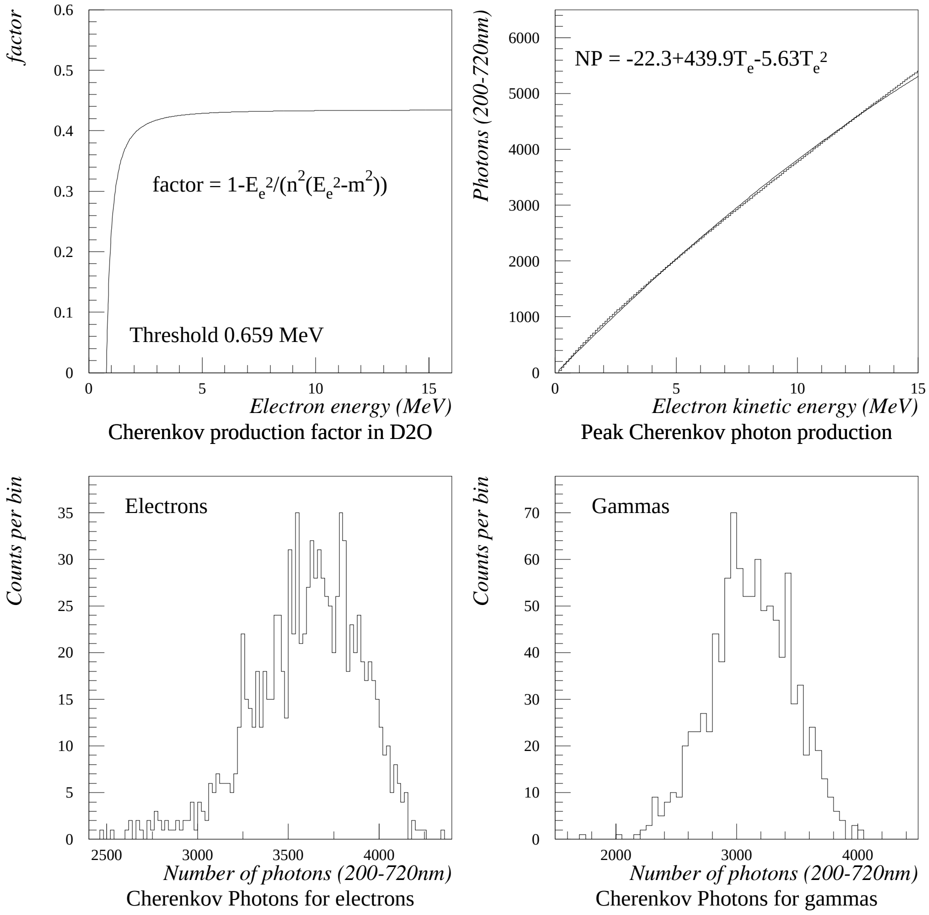

Figure 5.4: The top left plot is the double differential Čerenkov production factor $(1 - 1/n^2\beta^2)$ showing there is little energy dependence above threshold. The top right plot is the energy dependence on the number of photons with a quadratic fit. The bottom plots are photon distributions for Monte Carlo for 1000 10 MeV electron and gammas, showing how scattering (Compton and Moller) causes straggling on the photon production.

of Monte Carlo events. Since the Monte Carlo events are not drawn from the calibration function, then the χ^2 is expected to diverge due to details in the Monte Carlo. However, for a smaller event set (several thousand) the agreement is reasonable, and represents a good improvement over a uniform response.

Figure 5.6 shows the main constituents of the calibration function. We see why the D_2O and acrylic attenuation does not cancel for electrons. However, the multiple photoelectron effect does seem to partly cancel the D_2O attenuation. We illustrate in figure 5.7 how the calibration function can be used to calculate the partial derivative of the function with respect to any of the selected inputs.

5.2 Gamma-Ray Calibration

The gamma ray calibration function differs from the electron function mainly in the Čerenkov angular distribution function, extra straggling in the Čerenkov production (equation 5.17), and different parameter values for the fitter drive correction. The angular distribution function used is (compare 5.4)

$$g(x) = \begin{cases} p_3 x, & x < x_c \\ p_2 \exp(p_1 x), & x \geq x_c \end{cases} \tag{5.19}$$

with p_2 and p_3 eliminated as before and

$$p_1 = -1.65 - 0.031 T_e \tag{5.20}$$

The fitter drive effect from Monte Carlo of a million 10 MeV gamma rays is plotted (figure 5.8) for the shift in fit radius and the shift in $\cos\theta$, binned in $\cos\theta_{\text{fit}}$ and r_{fit}^3 as before. The fitter drive effect is seen to be a bit greater, but with the same shape as for electrons. This is due to Compton scattering which diffuses the light point of origin. As before fitter drive will be related to the ratio of the PMTs inside to outside the main Čerenkov cone, hence the drive is parameterized as before with $a = 0.81$ and $b = 2.0\,\text{cm}$ (equations 5.8 and 5.9). The Čerenkov production is reduced by 11% from 5.17 due to scattering.

The calculated gamma ray response function is shown in figure 5.9, with a break down of the components in figure 5.10. The main features are the same as for the

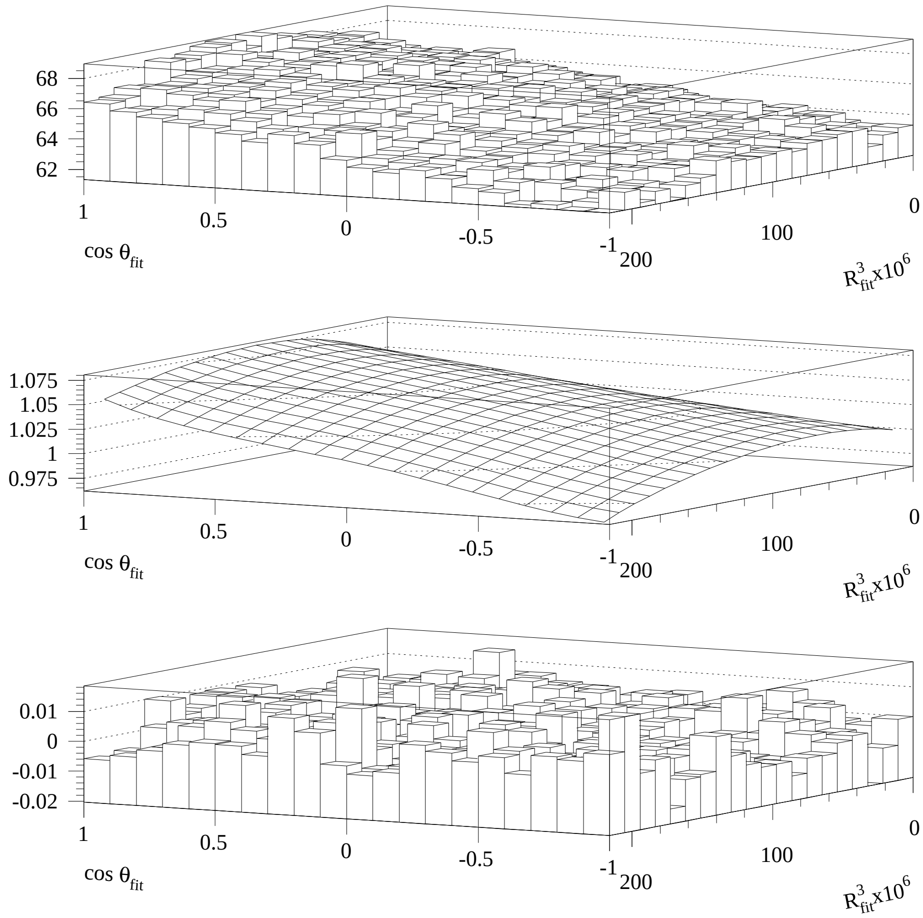

Figure 5.5: Electron response function compared to Monte Carlo. Top plot is the Monte Carlo NHIT response for 100,000 8 MeV electrons. The second plot is the calculated response function. The bottom plot is the difference by subtracting the Monte Carlo form the calculated response with a resulting χ^2 of 1.4 per bin.

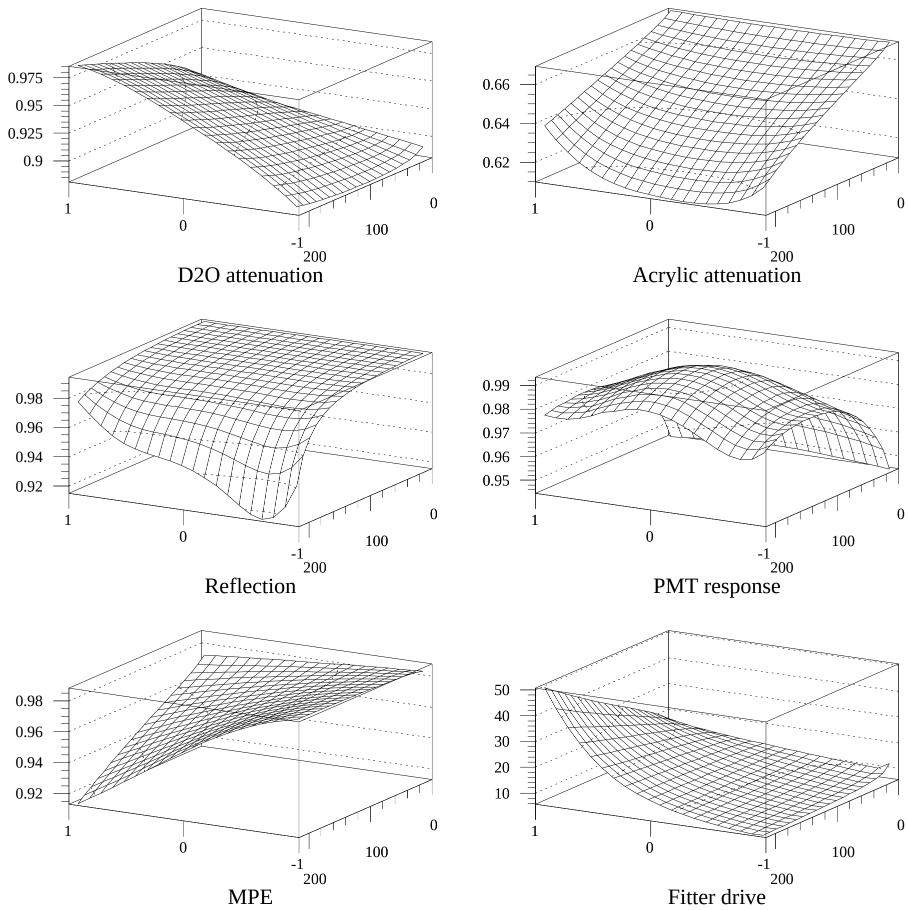

Figure 5.6: The major components of the electron response function. The $\cos\theta$ and r^3 axes (omitted for clarity) are the same as in figure 5.5. The z-axis is a multiplicative factor, except for the fitter drive, where the z-axis is r in cm.

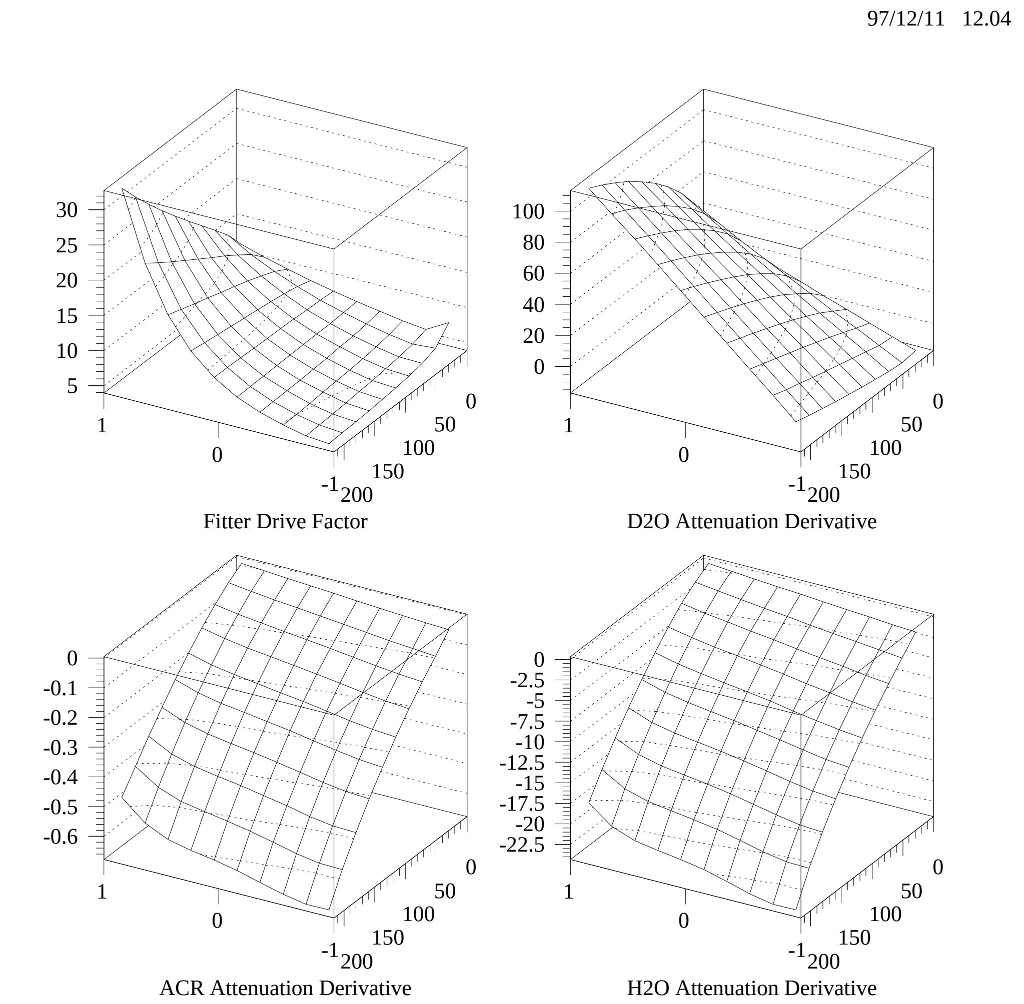

Figure 5.7: Sample derivatives of the electron response function. The axes are the same $\cos\theta$ and r^3 units as in fig 5.5

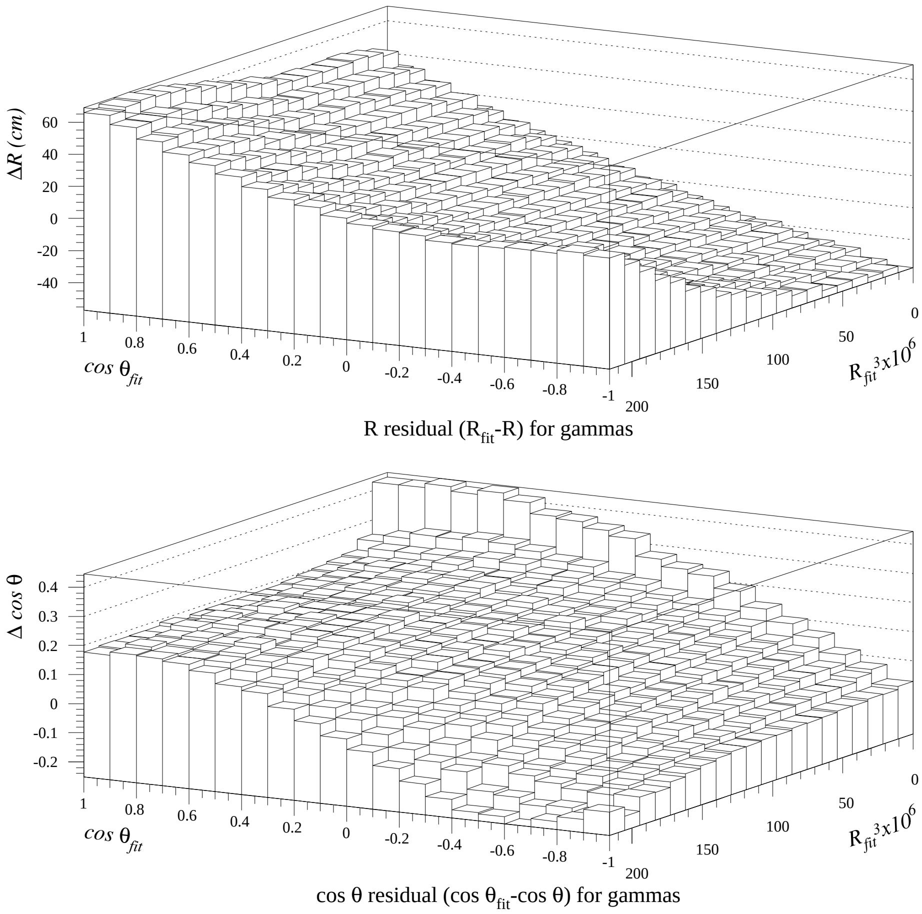

Figure 5.8: Time fitter drive in r and $\cos\theta$ from Monte Carlo of 100,000 gammas. The radius residuals ($r_{\text{fit}} - r_{\text{true}}$) and direction residuals ($\cos\theta_{\text{fit}} - \cos\theta_{\text{true}}$) are binned according to fitted radius and direction.

electron function but with different proportions. As expected the MPE effect is smaller both because the total light output is reduced and because the light is more distributed. However, the fitter drive effect cancels the MPE effect since it has the complementary shape. The distributed light also has the effect of removing some of the directional dependence, due largely to the acrylic absorption.

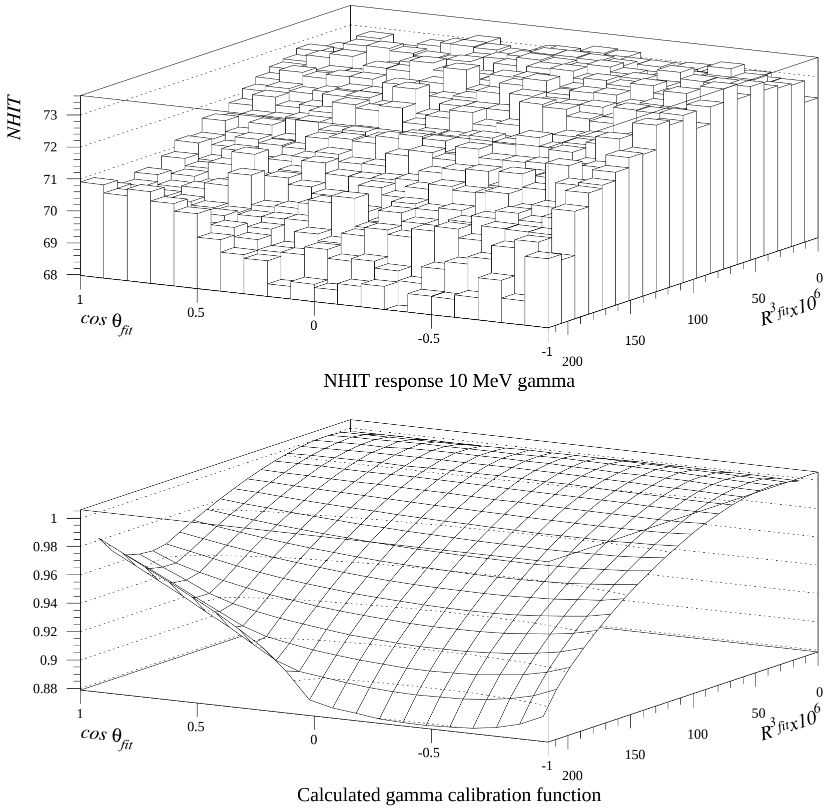

Figure 5.9: The gamma ray response function (bottom) and Monte Carlo of 10 MeV gammas (top).

An additional feature was explicitly added to the gamma ray function to account for the sudden increase in detector response for large radius (at the AV) and outward going direction. The effect is due to gamma rays that convert outside the AV and on average suffer less optical absorption. Note that this effect is averaged; the event variation will be large since the gamma ray usually converts outside the AV, or inside the AV, but not in between.

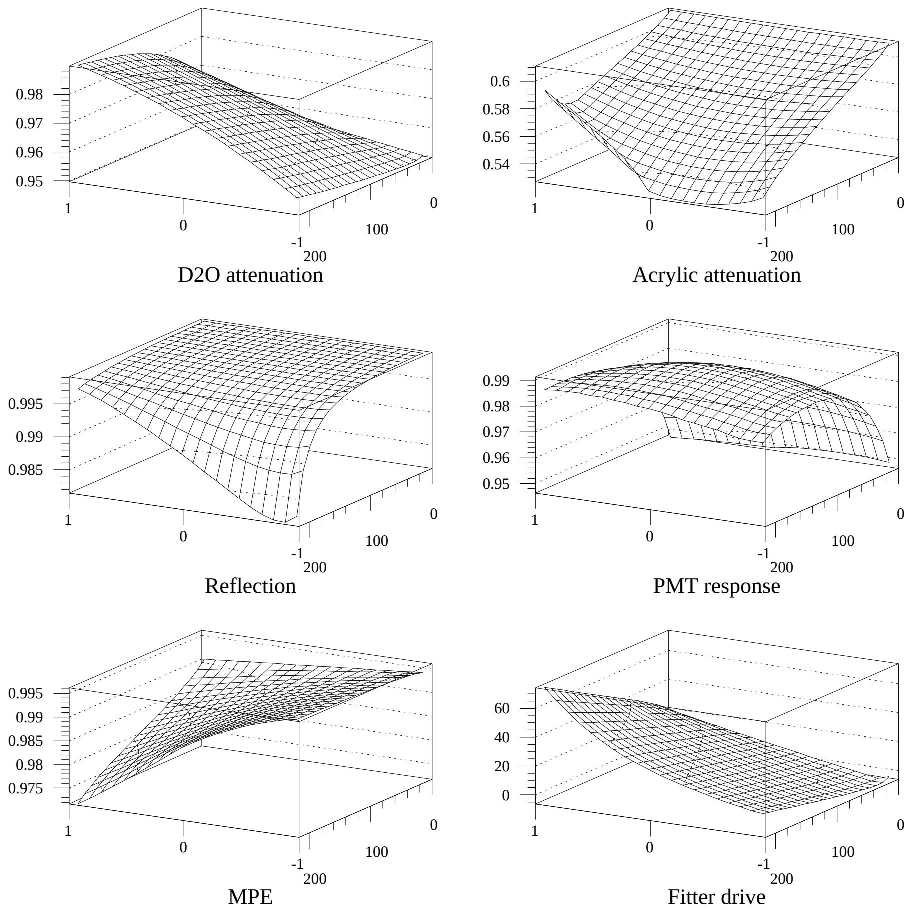

Figure 5.10: The major components of the gamma ray response function. The $\cos\theta$ and r^3 axes (omitted for clarity) are the same as in figure 5.5. The z-axis is a multiplicative factor, except for the fitter drive, where the z-axis is r in cm.

Chapter 6

Airfill Detector Commissioning

During June-October 1998 the SNO detector had entered the commissioning phase. The SNO cavity was complete, including final inspection of the acrylic vessel (AV), installation of all photomultiplier tubes (PMTs) and cables, removal of all construction access and equipment, final cavity cleaning, and sand back-fill of the access ramp. The water systems were complete including all piping through the deck and AV interface and the first shipments of heavy water had been received. There were over 7000 channels (of 9600) electronics channels installed, cabled and high voltage tested. The DAQ system was installed and undergoing commissioning, testing and modification. Calibration systems (manipulator systems and calibration sources) had been delivered underground ready for installation.

The period May to July combined detector turn-on and commissioning with final construction. The detector was operated with alternate dark shifts (complete light blackout to allow high voltage on the PMTs) and construction shifts. The dark shifts periods ranged from several hours to several days of continuous detector operation. There were several goals for the airfill commissioning dark shifts:

- Testing of PMTs and electronics channels to ensure proper connections, signal gain and detection, and elimination of any high voltage breakdown or channel noise problems.

- Testing of complete electronics system, including front end card operation, data readout and the trigger system.

- Data acquisition system (DAQ) testing, including detector control, event building, data recording and detector monitoring.
- Test operation of the primary calibration sources.
- Electronics and PMT calibrations.
- To provide a baseline for the SNO experimental backgrounds, ie. the basic background signal level in the absence of the target (the D_2O).
- Attempt to use these backgrounds (particularly muons) to gain information about absolute light detection efficiency.
- Use calibration sources to test calibration systems and to get an early indication of detector performance.
- Some analysis of the detector optics, which is unique during airfill.
- Testing and further development of all analysis software.

In this chapter we will present and discuss some of the airfill commissioning data as it relates to the work of this thesis. While an attempt is made to give an overview of all the airfill analysis, only the work of the author is discussed in detail. This work consists of PMT and electronics calibration, time histograms and optical analysis, event reconstruction and detector performance, and event spectrum analysis.

6.1 Photomultiplier and Electronics Calibration

Rapid calibration and characterization of the PMT and electronics channels was critical during the air-fill commissioning to provide PMT time spectra and reconstruction capability. For each of the 16 analogue cells for every electronics channel the charge to digitization function and pedestal (zero offset) must be determined. Also the time offset, time digitization function, and time walk (time versus charge, also called time slewing) must be measured. Then the PMT properties have to be determined: the gain, transit time spread, SPE response, noise rate, threshold and relative efficiency.

Finally, features such as high voltage breakdown, channel pickup and induced noise, and flashing PMTs must be identified and their effects on final data taking quantified.

Each PMT electronics channel has three reconfigurable charge integrators (see chapter 2.2.5), currently set to (i) high gain, short integrate time (QHS), (ii) high gain, long integrate time (QHL), and (iii) low gain, long integrate time (QLX). The integrate times are reconfigurable to tune out any non-linearities that may result from any front end oscillation response. Charge pedestals are accumulated for each of the 16 analogue cells on each channel during a detector pedestal run. An external pulser triggers each channel in turn 640 times to get 40 counts in each cell. In off-line analysis, a sliding window algorithm is used to locate the pedestal and the pedestal value calculated as the window mean value. The pedestal charge, with the mean pedestal values subtracted, is shown in figure 6.1 for QHL at a typical crate. The pedestal full width is about 2-3 ADC channels, or about a tenth of a PE. The linear relationship to convert the charge ADC counts to pico-Coulombs (pC) is found by fitting a line to the charge measured by injecting pulses of known charge. This step was not performed in the following analysis as there is no reason to do so until the PMT gains have been determined.

The electronics timing calibrations and PMT response are measured using the nitrogen/dye laserball system (described in chapter 4.2). The laserball is deployed at precisely the centre of the PMT support structure (about 5 cm precision) and the light activated trigger is plugged directly into the master trigger system. The trigger is configured as in figure 6.2 using the trigger utility board (TUB) for fast pulse discrimination and conversion to positive edge ECL. The cable delays were adjusted so that the synchronous laser trigger[1] causes a detector trigger at the same time as the NHIT sum trigger condition is met. This ensures that the time and PMT calibrations are performed in the part of the TAC window where neutrino or background events would occur.

The dye laser is set at 386 nm wavelength and the neutral density filters set to

[1]This external trigger is actually called the ASYNCHRONOUS TRIGGER; so named because it is not latched (synchronized) to the 50 MHz clock. An external SYNCHRONOUS TRIGGER is also available, which is latched to the 50 MHz clock and not synchronized with the actual device.

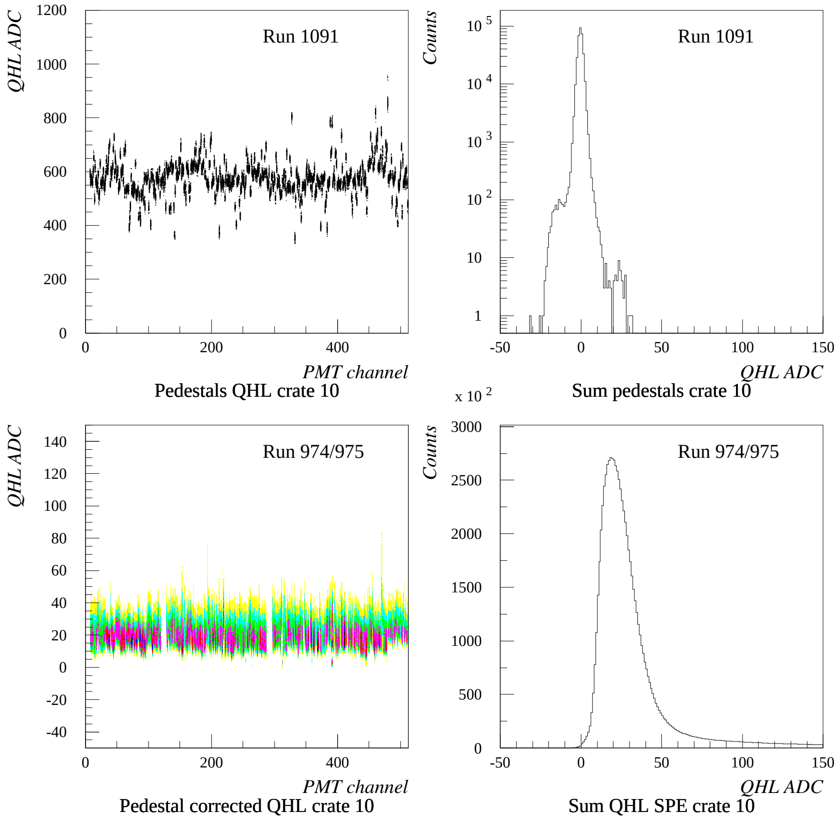

Figure 6.1: Top left: raw pedestal data for QHL. Top right: summed pedestal corrected pedestal data. Bottom left: pedestal corrected data for an SPE laserball run. Bottom right: summed data for QHL showing SPE spectrum.

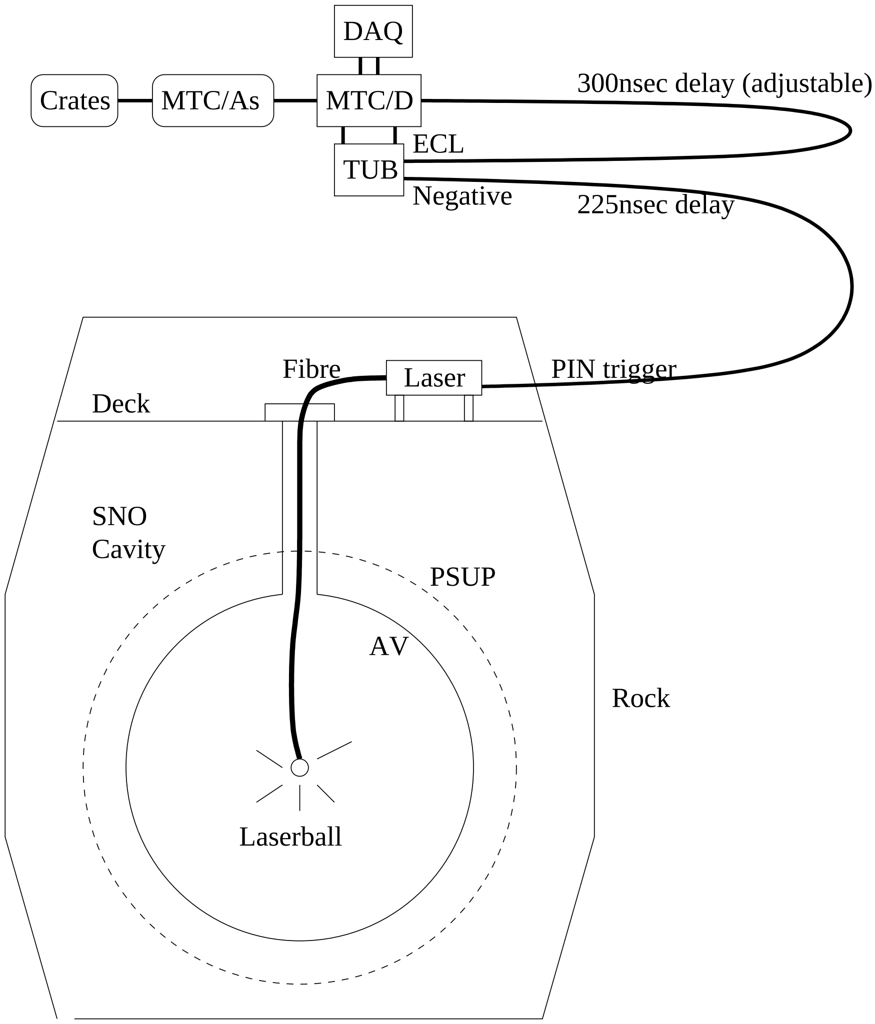

Figure 6.2: The nitrogen/dye laserball system with triggering setup for a photomultiplier and electronics timing calibration.

obtain 3% to 5% detector occupancy, this produces single photoelectron charge and timing distributions with neglible effects due to double photoelectrons. At 50 Hz laser pulse rate it takes about 3 hours to get good statistics, about 1000 counts per channel cell. While the relative time offsets could be obtained more quickly from higher intensity (MPE) light, it is preferable to have the time offsets centered for a distribution of SPE charge. This is because detector optical phenomena, the time walk correction and real event data all have PMT times centered on a SPE time distribution.

A sliding window algorithm, similar to the charge pedestal analysis, is used to locate the prompt light peak. The time offset is calculated as the window mean value, which will have a slight (0.2 nsec) bias due to the peak asymmetry resulting from scattering and PMT late-pulsing. However, this offset inclusion is appropriate since the same time bias will exist in the time walk correction and in real event data. The time TDC slope is obtained from a separate advanced trigger run, where the ECL laser trigger delay cable is shortened by 75 nsec (measured precisely with an oscilloscope). This provides a two point slope calibration,[2] bounding the most active portion of the TACs for normal event data. Calibrated and uncalibrated time spectra are shown in figure 6.3. The final time spectra plot has structure associated with the detector optics for airfill (discussed next section) summed with the PMT noise. The ridging (curl-up) of the noise spectrum at the ends of the TAC range is due to TAC non-linearities at the extreme range. The effect, called TAC curl, is small, and is beyond the time range of normal event phenomena.

The final step in the time calibration is the correction for pulse amplitude dependence of the threshold crossing time, this is the time walk (or slewing) effect. The time dependence on charge can be seen in figure 6.4. For each PMT the pedestal corrected charge is binned against time with the time offset correction and time slope calibration; this is called the Q versus T map (QvT map). The QvT map is first fit to a Gaussian in each charge bin to provide a set of Q versus T points with error

[2]The official SNO analysis utilizes internal electronic timer-pulsers to determine the time digitization function. However, this author's independent calibration algorithms used the delay method as described.

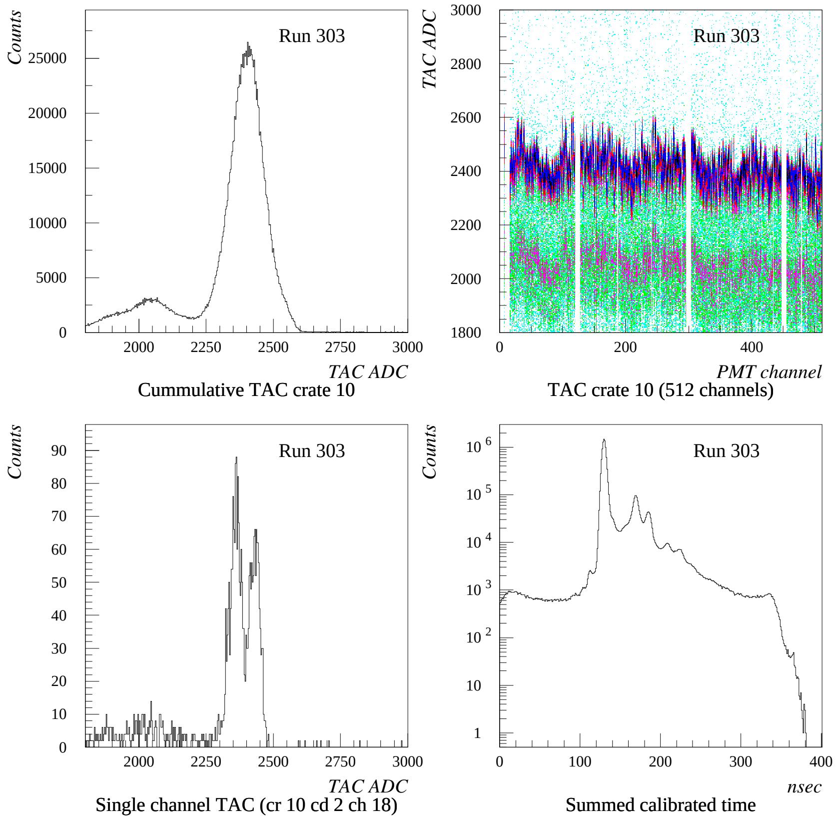

Figure 6.3: (i) Raw cumulative TAC spectrum for a single photo-electron intensity laserball run. The right peak is the prompt light while the second peak is light reflected off the acrylic vessel (note that TACs are 'common stopped' so that time runs from right to left). (ii) uncalibrated times for a typical crate (crate 10). (iii) uncalibrated time for a typical channel. Note that the cell variation is small, while the variation between the alternate TACs causes the double peaks. (iv) Summed TAC spectra with calibrated times. Reflections from the acrylic and PMTs, and the second order reflections are easily distinguished.

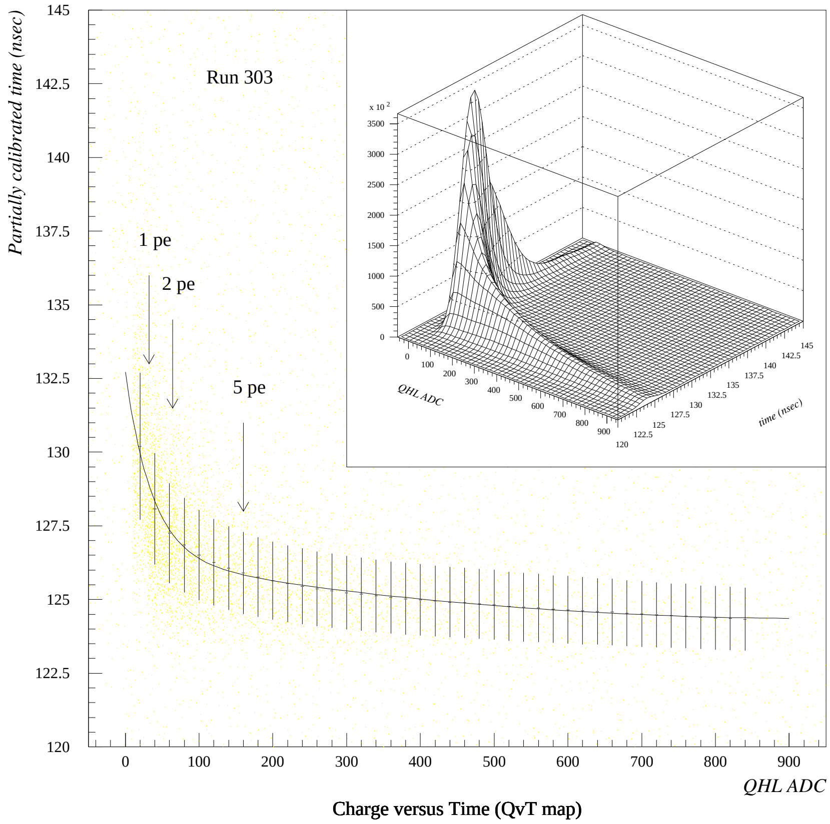

Figure 6.4: Offset and slope corrected PMT time versus pedestal corrected charge (QHL). This is the QvT map that shows the time threshold walk effect; the same data is shown in the surface plot in the upper right corner. Each charge bin slice is fitted to a Gaussian and the centroids and widths are plotted on the same axes. The data are then fitted with a three exponential function for use in time walk PMT calibrations.

bars. Then the QvT map is fit to a three exponential function up to about 25 PE, and from there a straight line to the charge rail (about 120 PE). The three exponent form of the function is found to fit well to all the channel variations in the QvT with the available free parameters. These functions are matched at 25 PE to provide the walk function used in the PMT calibration. The function is continued at the origin to provide a calibration below threshold to accommodate any front end oscillation effect which should still yield a well calibrated PMT time. We note that the data is more sparse for higher charge, and the question arises as to whether one should use higher occupancy laser runs to provide better continuation of the function. The caveat is that higher occupancy charges generally result from higher photo-electron multiplicities, which will have different pulse shapes than SPE pulses, even for the same charge. This effect was considered in chapter 4, and a calculation provided a parameterized (and small) correction factor (equation 4.14). While this gives confidence that the effect is small, it is better not to rely on the assumptions in that calculation for providing the primary PMT calibration. I argue that the QvT map should be produced at a detector occupancy that results in a similar level of MPE hits as for ordinary events throughout the detector (about 5% occupancy). Also at higher occupancy the probability of early pulsing increases due to the photoelectric effect at the first dynode. The time shift is large (about 12 nsec, see figure 6.13), but cannot be subtracted event-by-event. At 5probability is about 10^{-3}.

To minimize the timing sensitivity to bad fits or drifting gains it is preferable that on average the net walk correction is zero, especially since the walk correction becomes a steep function near the SPE level. This is achieved by shifting the time offset so that the zero time correction is referenced to the peak of the SPE spectrum. In this work the QHL integrator was used for the walk function, as this combination of gain and integration time seemed to be the most reproducible during the commissioning.

These PMT calibration constants are stored in files so that for events the PMT times can be calculated as follows. For PMT i

$$t_{ik} = t_0 + \frac{d_i}{v} - \frac{(\mathrm{TAC}_{ik} - \tau_{ik})}{S_{ik}} - \exp(p_1 + p_2 Q_i) - \exp(p_3 + p_4 Q_i) - \exp(p_5 + p_6 Q_i) \quad (6.1)$$

where TAC_{ik} is the raw time ADC with k specifying the CMOS cell, τ_{ik} is the offset,

S_{ik} is the time slope, and the exponential term are the QvT correction using the pedestal correction charge Q_i. An offset d_i is applied to account for the distance from the laserball to the PMT.

For commissioning and first turn on of the the detector the PMT channel thresholds are set quite high (at estimated 0.4-0.5 PE) while some initial problems with high voltage breakdowns and pickup noise are investigated. In this mode of operation the thresholds are set with rate monitoring tools for both the quiescent state and in response to readout bus and trigger line activity. The thresholds will be set later as a fraction of SPE gain. Presently we can see the variation of the gains and thresholds in the individual channel occupancies plotted in figure 6.5 for both a normal NHIT run and a asynchronous triggered laserball run. The variation is about 17% for the NHIT triggered run, and a more even 12% for the laserball data. The variation is mostly caused by several channels with very high occupancies due to noise or trigger line pickup. The channels surrounding these high rate channels often have the threshold set high due to inductive pickup, and thus have low occupancy for in-time light. The occupancy variation is expect to improve once the thresholds are set according to the SPE gain.

In figure 6.6 the occupancies for the laserball are grouped and plotted by electronics crate, card, channel and position angle cosine for the laserball. Card 15 and slots 0, 13 and 31 have lower occupancies since they have systematically higher thresholds, while the $\cos\theta$ plot shows the expected laserball variation (see also figure 4.9).

We next need to determine the actual charge gains and thresholds as a fraction of a PE. This is investigated first using the laserball at SPE intensity and the trigger in 'gated charge' mode where the integrators are opened and read out on every asynchronous trigger (the laser). The charge spectra will then consist of the pedestal peak plus the SPE charge. A series of laserball runs were performed with the usual asynchronous trigger and different threshold settings. (The threshold settings are referred to as 'DAC clicks' which are incremental voltage reference settings above baseline set by the digital to analogue converter on the DBs. The DAC is programmed by the FEC eCPU via the DAQ Macintosh dual port memory. The baseline is deter-

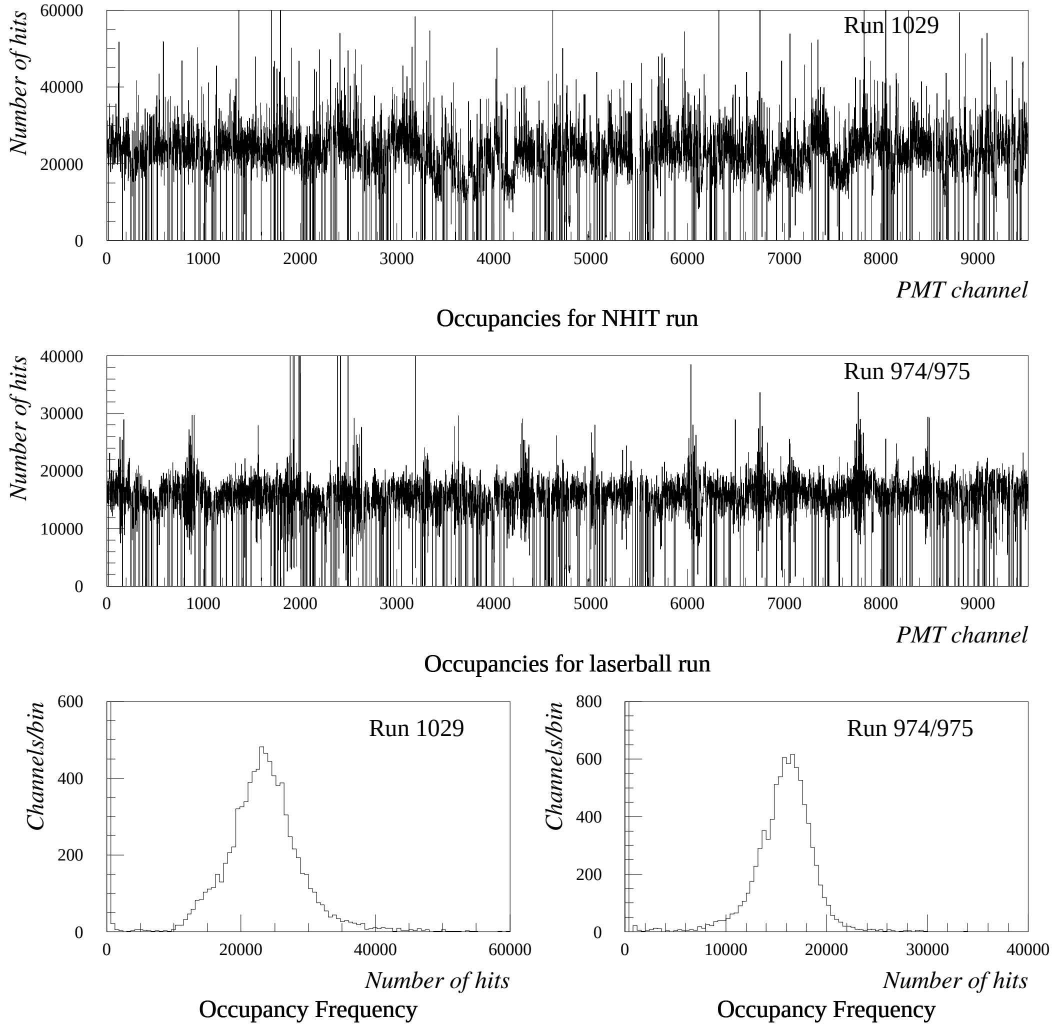

Figure 6.5: PMT occupancies for NHIT and laserball runs.

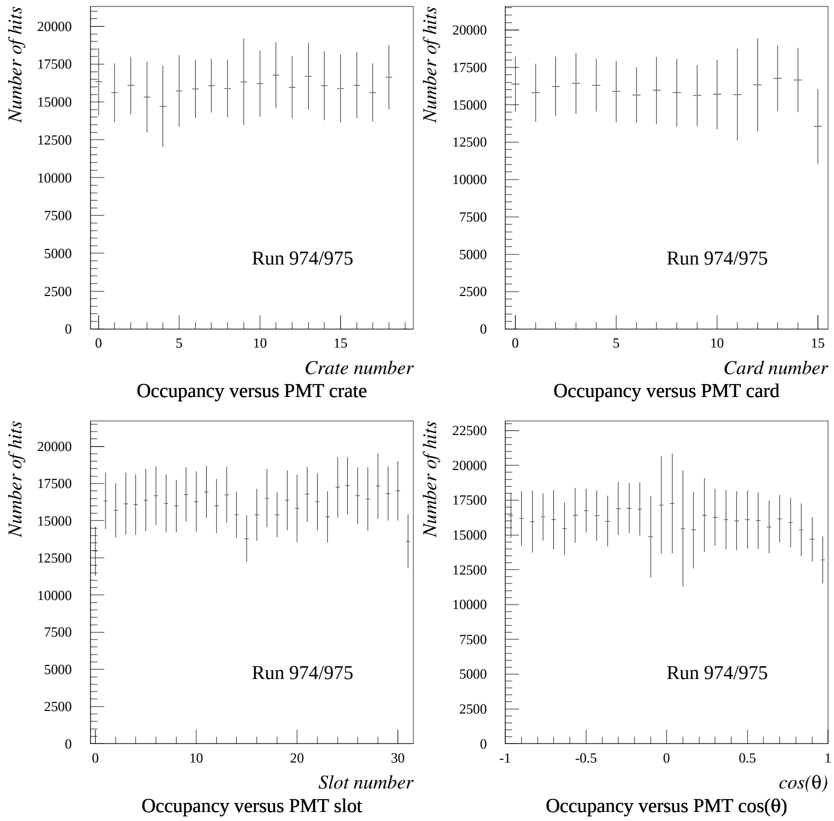

Figure 6.6: PMT occupancies by crate, card, channel and $\cos\theta$.

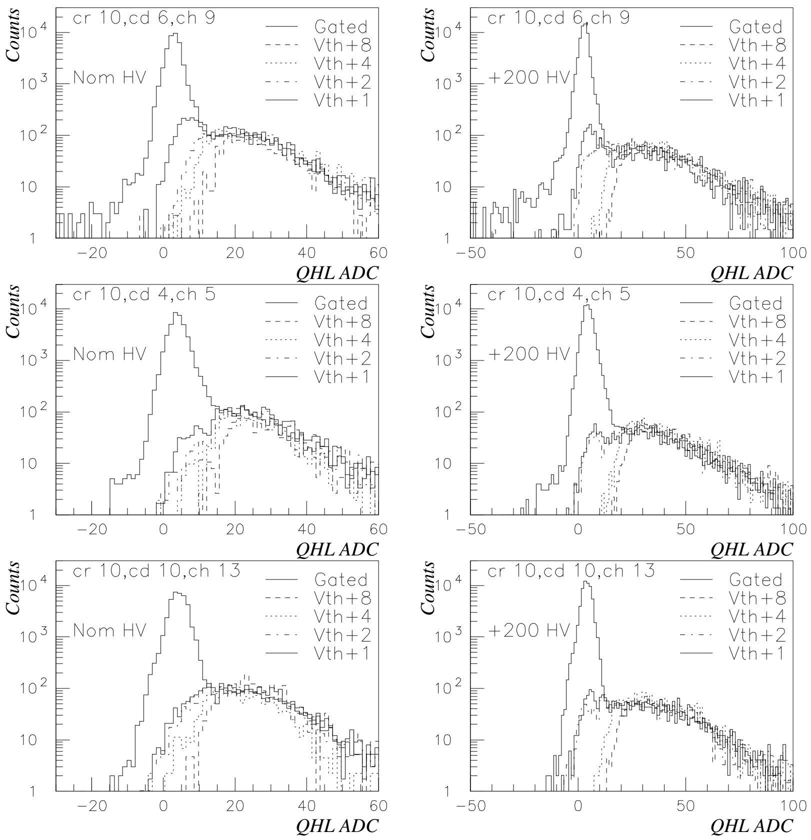

Figure 6.7: The QHL charge is plotted separately for three PMTs for a gated charge run and threshold scan runs at normal (nominal) HV and at nominal +200 V. Note the log scale.

mined by the eCPU using an algorithm that scans the voltage until discriminator saturation. The DAC click increments are chosen to roughly correspond to an ADC channel value.) Charge spectra (QHL) for these runs were normalized for the high charge region and overlaid. The plots for three typical channels are given in figure 6.7 for runs at regular (nominal) HV and with the PMT voltage raised by +200 V. We see that at the nominal voltage the SPE mean is roughly at channel 25 (ADC above zero) while a threshold of eight (Vth+8), which is typical, is just below $\frac{1}{2}$ PE. At +200 V the SPE mean is about 40; however, since the pedestal intercepts the SPE peak at the same PE fraction, there seems to be no advantage to operating at higher than nominal voltage.

A method for calculating the charge gain was developed that will work for untuned channels with high thresholds. The problem in determining the SPE calibration is that an SPE charge spectrum convolved with a threshold function still looks like an SPE spectrum, but with a larger mean. So without either a calibrated gain or a calibrated threshold the SPE gain cannot be determined. The method employs the observation that even in a potentially noisy spectrum, the charge resolution should be sufficient so that above the threshold the charge spectrum shape is not very different than the standard R1408 spectrum shape. Then the SPE mean can be found by comparing the ratio of the mean to threshold for a given charge distribution to the standard spectrum.

The whole procedure and results are presented in figures 6.8 to 6.11. First we define the SPE mean and a threshold ratio function. The SPE mean is the mean of the charge spectrum for single photoelectrons with no threshold. In practice we adopt the convention that the mean is calculated by integrating from $\frac{1}{4}$ of the mean to $2\frac{1}{2}$ times the mean, and iterate the calculation, which usually convergences on the second pass. Thus any threshold larger than $\frac{1}{4}$ PE, will result in a distribution mean value larger than the SPE mean, but it is the SPE mean that we seek. The ratio function is the ratio of mean to threshold, in any units, which we are claiming is the same for all PMTs (see figure 6.8).

The analysis then proceeds by taking the QHL for every SNO PMT in a run and

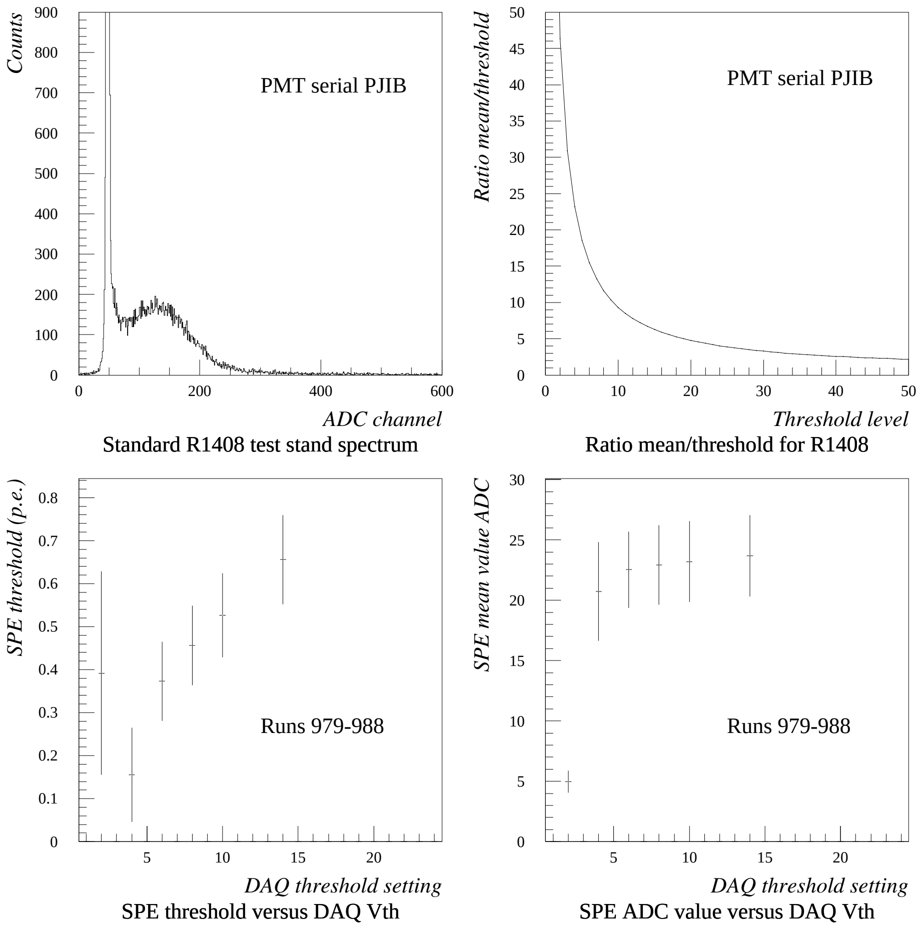

Figure 6.8: A typical R1408 charge spectrum from the Queen's PMT testing, and the mean/threshold ratio as a function of threshold. The bottoms plots show the average threshold and SPE mean as a function of DAC setting calculated using a method that compares the mean/threshold ratio between the PMT test data and SNO data.

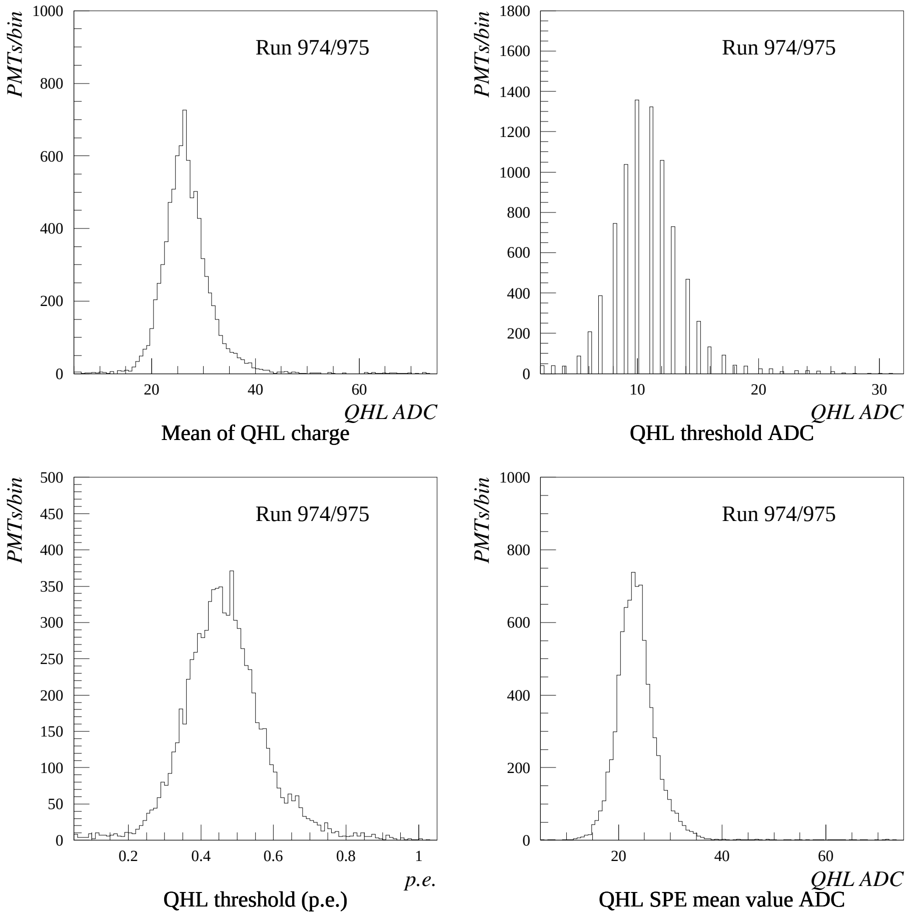

Figure 6.9: The QHL ADC mean and thresholds (top), and calculated PE thresholds and SPE means (bottom) using the mean/threshold ratio method.

finding the threshold and the mean. The threshold is calculated with an algorithm that finds where the spectrum raises above 0.4 times the maximum using a 3 channel window for noise immunity. The distribution mean is calculated by iterating the integration between 0.25 to 2.5 times the mean. The ratio of the mean to the threshold can then be used by the ratio function to find the corresponding threshold (or mean) in ADC channels for the standard PMT. We now have a rescaling for each PMT that sets the SPE mean and threshold, and provides a gain calibration for each channel. The ADC mean and threshold, and the rescaled SPE mean and threshold as a fraction of a PE are shown as histograms for all channels in figure 6.9. These results are re-histogrammed and fitted to a Gaussian to present averages by crate, card and channel in figure 6.10. The global average is an SPE mean of 23.2 ADC and a threshold of 0.46 PE. The same analysis is performed for each run of a threshold scan, with the global averages plotted as a function of DAC setting in figure 6.8. We see the SPE mean is independent of threshold, as it should be, and that fractional PE threshold decreases with DAC setting until the calculation fails at low values (<Vth+5). We find also that obtaining thresholds of 0.25 PE requires DAC thresholds of about 5-6 DAC clicks.

As a test, we perform the same analysis for the summed spectrum, summed by crate and a global sum (figure 6.11). The summing slightly spreads the peak which results in larger SPE mean (roughly 24 ADC for each crate and 23.8 ADC global) and a lower threshold. I take this to be a conservative upper bound for the uncertainty of this procedure. As a final consistency check we sum the total charge for each event between the calibrated 0.25 - 2.5 PE range and divide by the number of hits. This converges on the mean by the central limit theorem, the value 24.7 ADC is obtained, for an SPE mean of 21.8 ADC.

Finally we plot (lower left figure 6.11) the PMT efficiency compared to the efficiency with a threshold at 0.25 PE as a function of mean value threshold. We see that with thresholds at 10.7 ADC (0.46 PE) the efficiency is about 90% compared to thresholds at 0.25 PE. The entire analysis has been repeated using a different standard PMT, and purposely selecting a PMT from the test database with a poor

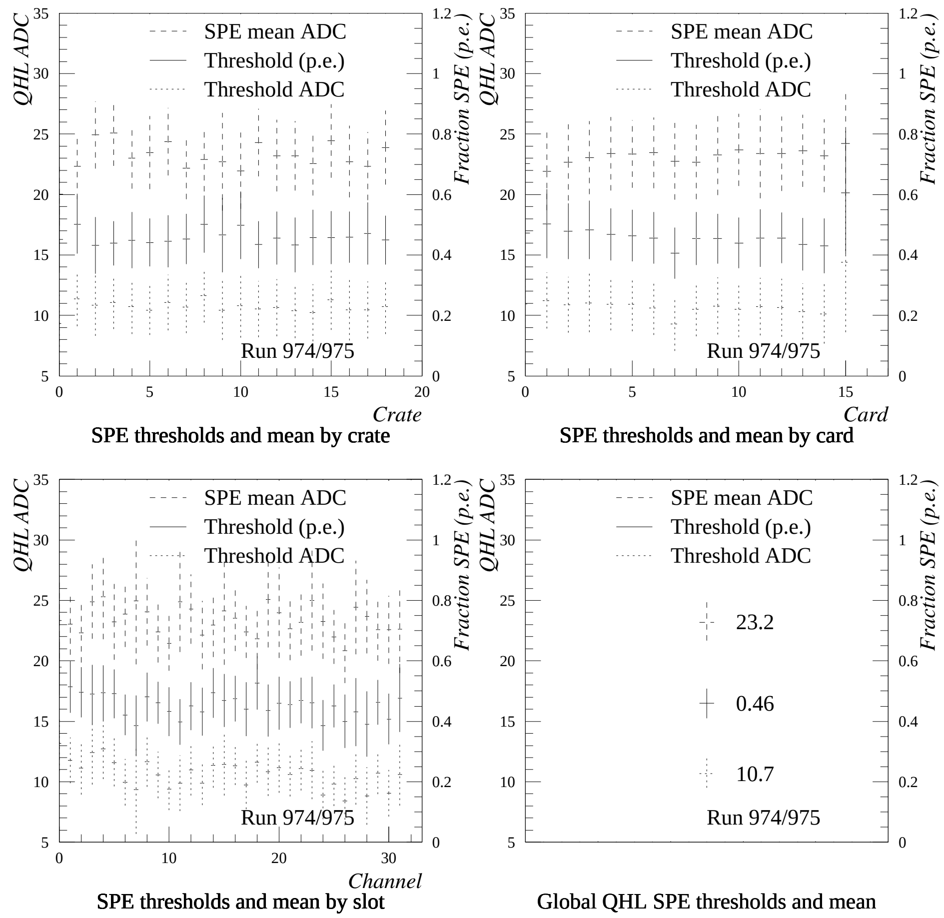

Figure 6.10: Calculated PE thresholds and SPE means by crate, card and channel, and the global average. The SPE mean and threshold in ADC counts use the left scale, while the threshold is also given in PE on the right scale.

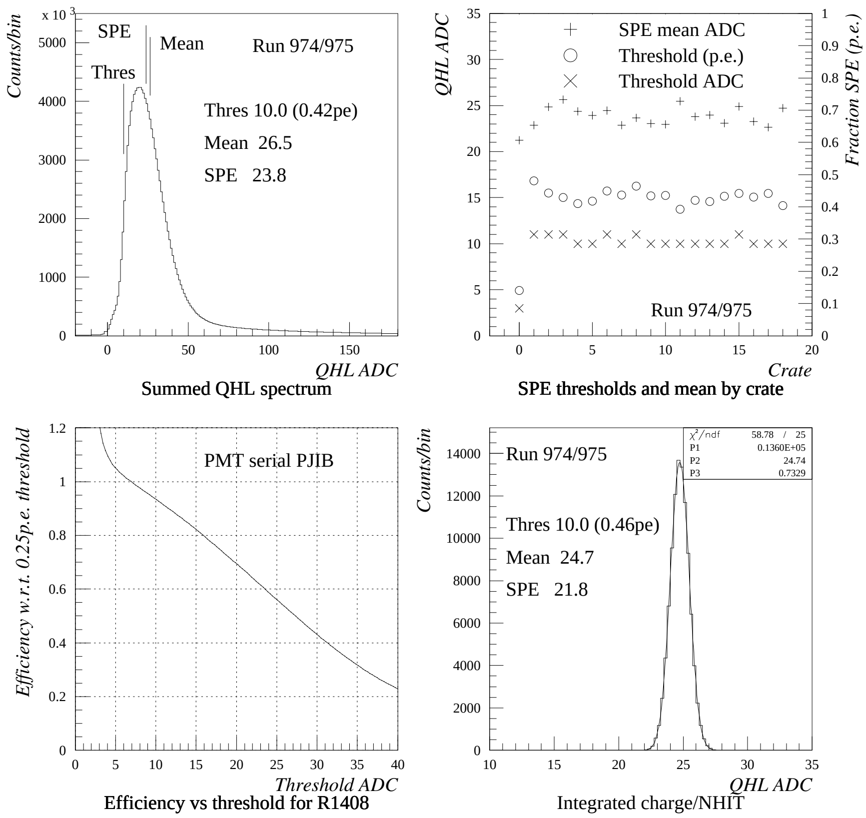

Figure 6.11: (i) Calculated SPE mean and threshold for summed QHL spectrum. (ii) Calculated SPE mean and thresholds for summed QHL spectra by crate. (iii) PMT threshold efficiency as function of threshold. (iv) Average SPE mean from the central limit theorem.

peak-to-valley ratio. The change in the results was small compared to the distribution widths.

6.2 Timing Histograms and Optical Analysis

One of the commissioning tasks is to verify the expected detector PMT time distribution due to optical effects. In airfill the detector response (number of hits per event), PMT time distributions and reconstruction resolution is highly dependent on optical effects like refraction at the AV and reflections from PMTs. Also this is the first chance to verify if a proper understanding of the late-light components has been obtained so that the second order optical effects (scattering and PMT reflections) can be measured as described in chapter 4.

The cumulative time histogram for an SPE laserball run at 386 nm is shown in figure 6.12 compared to a Monte Carlo calculation. The data is fully time calibrated and offset to light emission at 100 nsec. This cannot be compared to the distributions in chapter 4 (figures 4.10 and 4.12), as the optical effects for airfill are different than for waterfill. The biggest change is the reflection from the AV, the peak at 167 nsec which reflects about 9% of the light. Also the airfill data does not have any significant Rayleigh scattering, instead the 130 nsec window following the prompt peak is filled by multiple reflections between the PSUP and the AV. While the overall agreement with the Monte Carlo is good, there are two significant regions of disagreement, at the tail for 15 nsec following the prompt peak, and the broad 10 nsec shoulder before the AV peak.

The small peaks at 237 and 246 nsec are due to RF pickup from the laser at a couple of channels transmitted through the command trigger line. This has since been fixed by providing additional electrical isolation at the laser.

To further investigate disagreement with the Monte Carlo we next investigate PMT late pulsing. The time distributions for 200 PMTs from the Queen's PMT testing data were summed and plotted in figure 6.13. Some late pulsing[3] is seen in

[3]We distinguish late pulsing from after pulsing. PMT after pulsing is a better known phenomena where pulses occur several micro seconds after the original pulse, due to ionized residual gas attracted

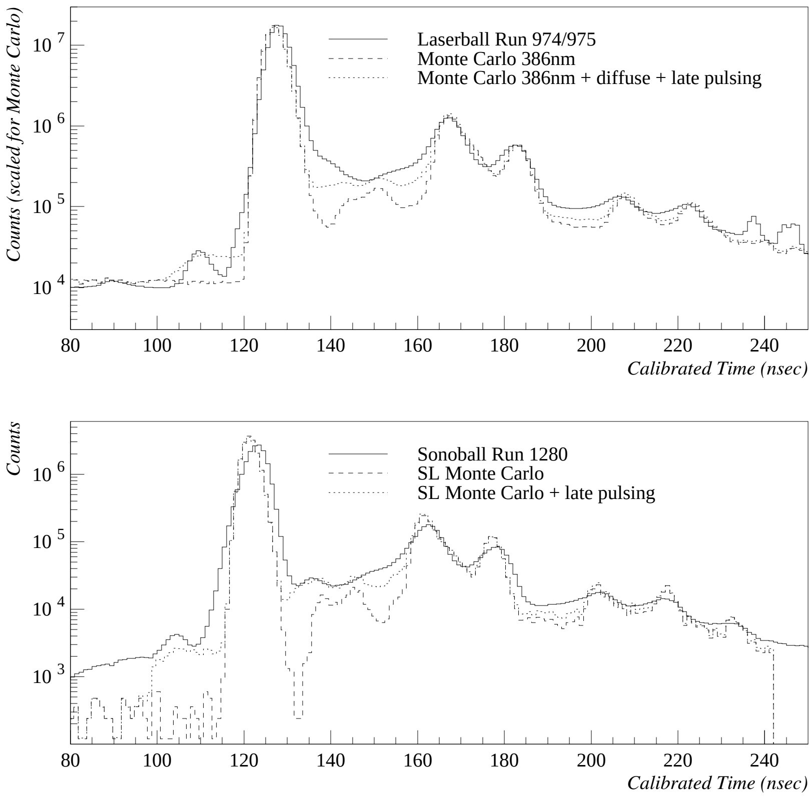

Figure 6.12: Airfill time histograms for the laserball and sonoball compared to Monte Carlo data.

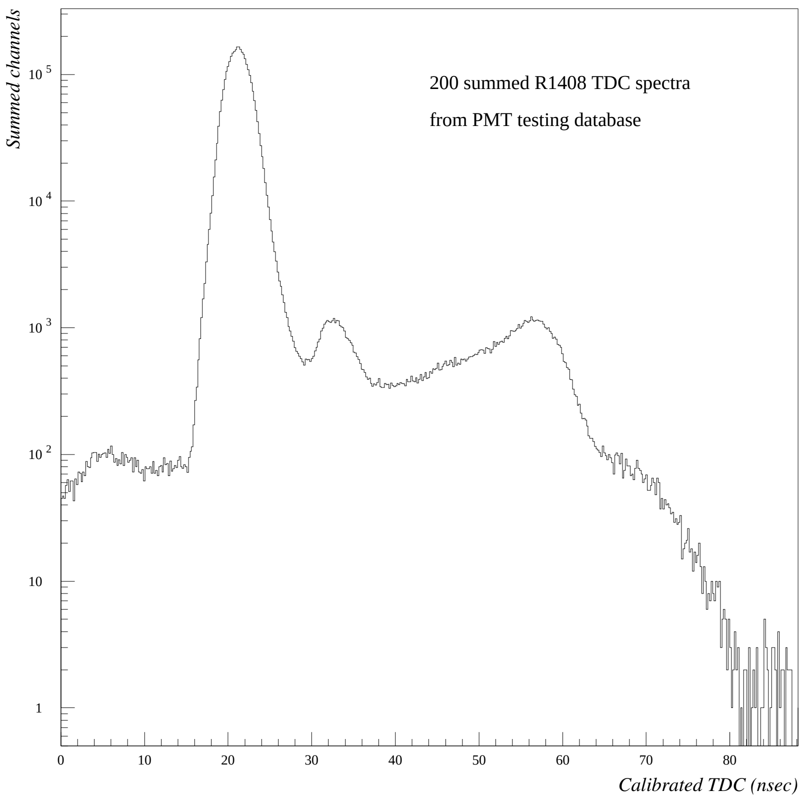

Figure 6.13: Summed R1408 time distribution from the Queen's PMT testing database showing the early and late pulsing peaks.

peaks at 15 and 40 nsec after the prompt signal, and some early pulsing at 15 nsec before the signal. The late pulsing mechanism is still unknown, but is thought to be due to soft x-ray emission from the dynodes striking the photocathode (note that 15 nsec is about the transit time to the 1st dynode, while 40 nsec is about the full transit time). You see this pulse either because the original pulse is below threshold, or because the original pulse is non-amplified (remember the anode efficiency is not 100%). The peaking structure is likely because some dynode segments are more visible to the photocathode than others. The late pulsing rate is about 1.5%, and has less than 0.5% of the pulses in the second largest peak. Early pulsing is due to amplification of a first dynode photon interaction, and will increase with increased light intensity. Late pulsing was not included in the discussion of optics in chapter 4 since it does not extend to the reflection peaks for water, and is small in the selected scattering time window.

While the effect was thought to be small, diffuse scattering (about 2% reflection and transmission) was added to the Monte Carlo for the AV surface. From figure 6.12 we see that the late pulsing and diffuse scattering improve the agreement, but do not solve the two cases of disagreement noted earlier. Studies of airfill muons actually indicated a much larger amount (about 8%) of diffuse scattering at the acrylic. Muons are sensitive to AV diffuse scattering because part of the produced light is trapped by total internal reflection and must scatter out before absorption to be detected. However, the laserball data rules out such a large diffuse scattering, since the PSUP-AV reflection at 150 nsec would be increased much more than this data allows.

The airfill optics was also investigated with the sonoluminescence source (the sonoball) which is broadband, but has a very sharp intrinsic light duration. The prompt peak width is due to PMT transit time spread, NHIT trigger jitter and chromatic dispersion (figure 6.12). The prompt peak is asymmetric since the sonoball uses the NHIT trigger (pre-scaled and input to the ASYNCH trigger) with a high NHIT cut. The sonoball reproduces the disagreement at the shoulder on the AV peak,

to the photocathode. The after pulsing rate is expected to be dependent on total anode current. For the SNO R1408 the after pulsing rate is about 0.1%/PE.

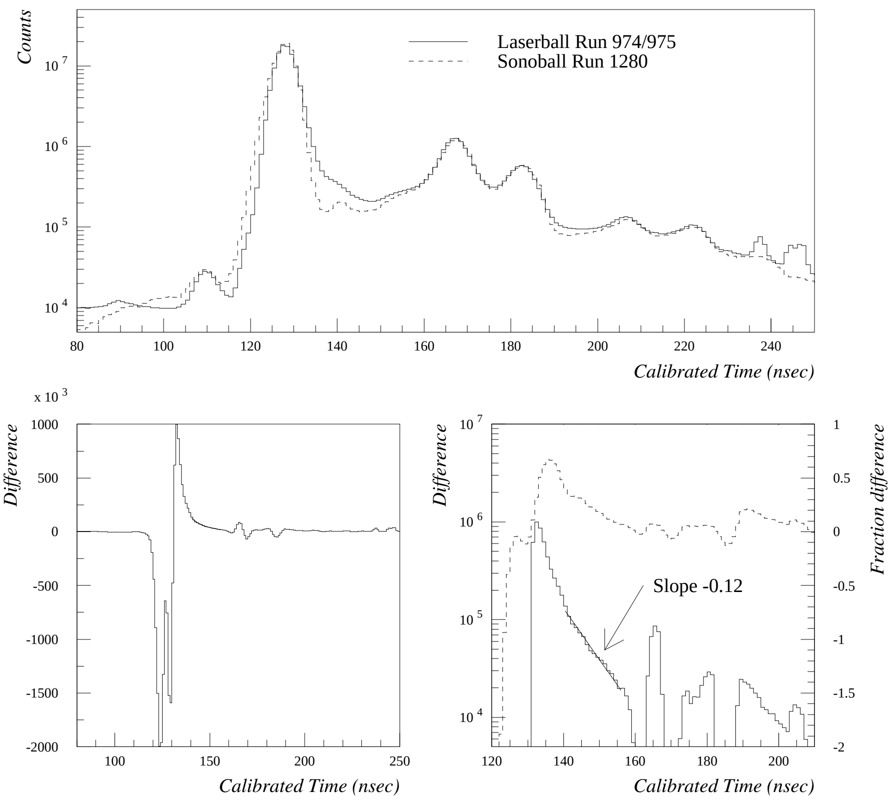

Figure 6.14: The sonoball time distribution is subtracted from the laserball time distribution to yield decay tails (fluorescence) from the source and reflection peaks.

but does not have the tail following the prompt peak. This suggests that the light tail is due to the laserball. Taking the difference between the laserball and the sonoball (figure 6.14 produces an exponential which can be fit to a slope of -0.12 ± 0.01 in the region after the transit time spread).

We next overlay laserball runs for different wavelengths (337, 365, 386 and 500 nm), shown in figure 6.15. The decay tail is a strong function of wavelength and clearly indicates short wavelength fluorescence, likely in the fibre optics. Taking the difference between the 500 nm and the 337 nm distributions yields the decay curve with a -0.11 ± 0.01 slope, consistent with the laserball/sonoball fit. Both the 500 nm and the 337 nm runs have increased light in the secondary reflections. This is due to the longer wavelengths absorbing less in the AV, where the 337 nm is mostly converted to longer wavelengths by fluorescence after 200 nsec. The fluorescence tail will not interfer with the prompt peak analysis at 337 nm but will be a significant correction for the scattering measurement. We have purchased a second hydrous silica fibre-optic with an acrylate jacket (Fiberguide Ind. SFS-100/140/250Y) to test if a different fibre geoemtry may reduce the UV fluorescence.

A measurement using a 337 nm cavity filter and a small PMT was performed by placing the filter at the laser and at the PMT. There was a $12.8\% \pm 4\%$ difference in light transmission through the fibre-optic cable and laserball between the two configurations. This indicates that up to 13% of the light at 337 nm may be lost due to flourescence.

The shoulder on the AV peak at 160 nsec is likely due to the $50°$ PMT reflection. It was already noted in chapter 4 that this reflection peak was sensitive to the PMT glass envelope shape, and differs between SMOMAN and Queen's Monte Carlo.

6.3 Event Reconstruction

The PMT calibration and time fitter reconstruction were tested in airfill for the laserball, a PSUP LED and an Americium source. The laserball was moved to several positions inside the AV, and outside the AV using the west calibration port. The LED was a Nichia blue NSPB500 LED installed on the PSUP steel and externally

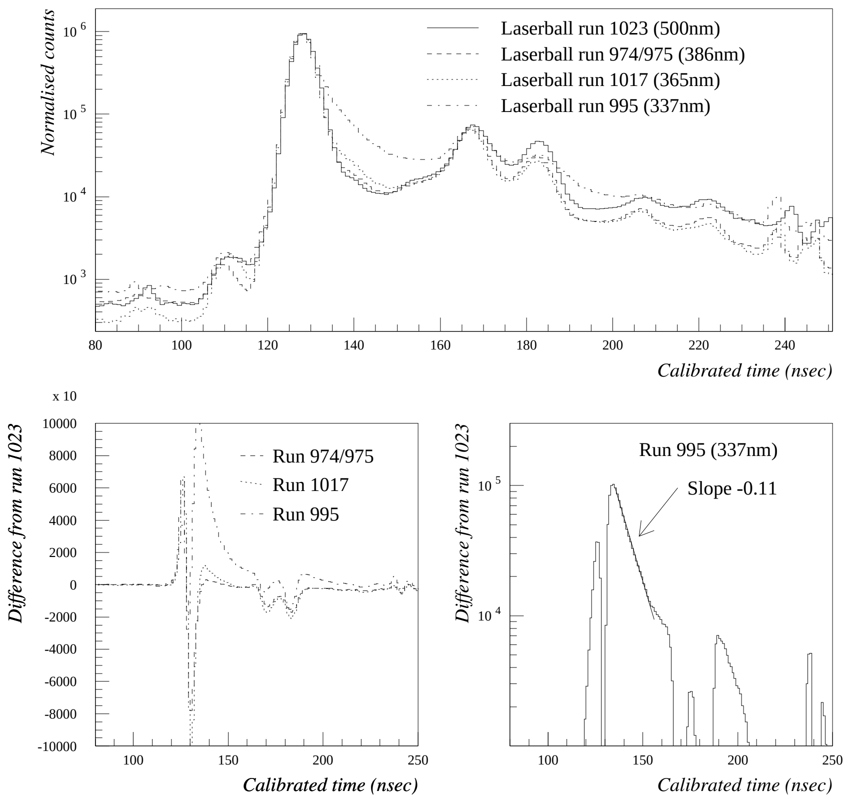

Figure 6.15: Laserball time distributions at several wavelengths, and the difference distributions by subtracting the 500 nm distribution.

pulsed with 10 nsec pulse width. The Americium source was a 100 Bq toluene based scintillator cocktail encapsulated in a 5.5 cm diameter quartz flask. The source has a 10 nsec scintillation time and produces an NHIT of 65. A summary of the fitter results are given in table 6.1 where the uncertainties represent the RMS of the distributions. The good fits for the laserball are expected for an isotropic source and demonstrate that the detector is functioning and has a good PMT calibration. The ^{241}Am and LED fits suffer from the poor source time response, but show no problem with fitting low NHIT events or events on the PSUP.

Run	Source	ID	Source and Fitted Position			
			X	Y	Z	T
340	Laser	Source	0.0 ± 3	-13.0 ± 3	0.0 ± 3	100.0 ± 0.5
		Fitted	-4.4 ± 7.5	-2.8 ± 9.0	-0.8 ± 9.1	98.3 ± 0.25
341	Laser	Source	0.0 ± 3	-13.0 ± 3	-300.0 ± 3	100.0 ± 0.5
		Fitted	0.5 ± 7.3	-4.1 ± 8.8	-302.2 ± -9.7	98.9 ± 0.25
342	Laser	Source	0.0 ± 3	-13.0 ± 3	300.0 ± 3	100.0 ± 0.5
		Fitted	-0.8 ± 7.8	-6.9 ± 8.9	300.0 ± 9.3	97.7 ± 0.25
372	Laser	Source	-586.6 ± 3	222.2 ± 3	0.0 ± 3	100.0 ± 0.5
		Fitted	-610.3 ± 11.7	209.3 ± 10.4	5.8 ± 10.9	99.5 ± 0.25
364	Laser	Source	-586.6 ± 3	222.2 ± 3	-176.6 ± 3	100.0 ± 0.5
		Fitted	-611 ± 11	210 ± 10	-170 ± 10	99.3 ± 0.25
375	Laser	Source	-586.6 ± 3	222.2 ± 3	176.6 ± 3	100.0 ± 0.5
		Fitted	-605 ± 12	209 ± 12	183 ± 12	99.6 ± 0.27
196	LED35	Source	-168.5 ± 3	716.9 ± 3	-408.9 ± 3	128.8 ± 1.0
		Fitted	-170 ± 90	695 ± 162	-499 ± 132	132 ± 6
379	^{241}Am	Source	0.0 ± 3	-13.0 ± 3	0.0 ± 3	100.0 ± 1.0
		Fitted	2.9 ± 46.9	-5.6 ± 48.1	-7.1 ± 49.8	91 ± 12

Table 6.1: Source position reconstruction for several calibration sources.

Longer runs with the regular NHIT and ESUM triggers were analyzed using event reconstruction. Using the time minimization fitter resulted in the fitted radius distribution shown in figure 6.16 plotted against NHIT with a cut NHIT> 40 for run 1029. The radius R distribution peak at 600 cm is expected in airfill due to high energy rock wall gammas that convert in the AV. The low energy events that fit uniformly in R will be due to the tail on radon scintillation that dominates the event rate in air.

Radon emits about 250 scintillation photons in air and is expected to be about 5% of the 3 pCi activity of mine air. The high energy tail is due to detector resolution and pile-up, while the large number of mis-fit events ($R > 850\,\mathrm{cm}$) is due to pile-up and geometry. Pile-up events will mis-reconstruct since there is not a single origin, while events outside the AV will suffer from light absorption in the AV, and reflections off the AV surface.

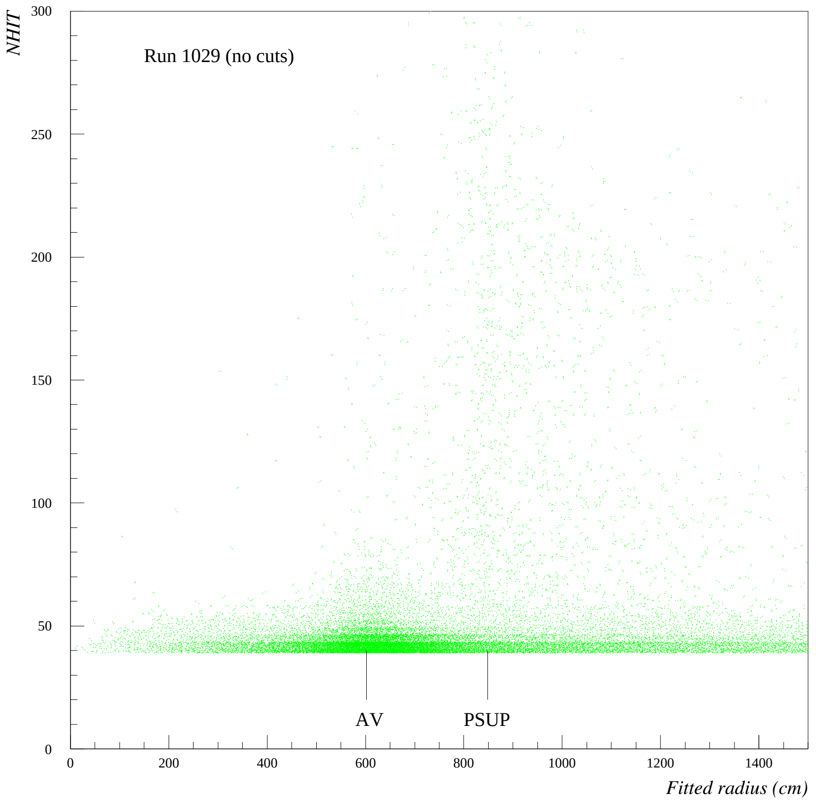

Figure 6.16: Run 1029 NHIT versus fitted radius.

There are also many higher NHIT events due to high voltage breakdown burster events and PMT flashing. The high voltage breakdown events are called bursters because the detector usually retriggers to cause several high NHIT events with decaying intensity. The paddlecard with the breakdown can be identified on the crate display map as the whole paddlecard or frontend card usually have large charges that saturate the ADCs (railed charges). The induced pickup on neighboring cards and crates have channel times that are consistent with the speed of light for the rack configuration on deck. These events rarely reconstruct as the channel times bear no relation to detector transit times. These events are cut by looking for 200 or more channels that fire in a single crate, and by removing any events within 100 μsec of a breakdown event.

The events that fit at the PSUP ($R = 850$ cm) are identified as flashing PMTs. The flashing PMT phenomenon appears to be a feature of a subset of the PMTs. Other large unsegmented detectors (S-K, IMB) have had similar PMT behavior. These flashing PMT events are different from failed PMT flashers[4] in that the flashers are less intense (50-400 NHIT), and the flashing is often periodic (periods 15 minutes to hours). The flashing can come and go, but otherwise the tube operates normally, with typical gain, noise and occupancy. Most flashers are easily identified on the detector or crate display map as a small cluster of triggered channels with one channel having a railed or negative[5] charge (presumably the flashing PMT). The other channels in the cluster usually have zero charge, indicating inductive pickup. There is also a scattering of SPE hits on the opposite side of the detector consistent with the speed of light transit time from the cluster. This timing relation also proves the event is initiated at the PMT, and not at the PMTIC. The railed charge channel appears to fire 15 nsec before the time that would correspond to the light emission, even in the uncalibrated time (as the QvT correction would be obviously wrong for negative railed channel). This is a bit puzzling as the induced neighbour channels must be exactly synchronous, unless there is an unusual and very specific PMTIC response to the flasher pulse. Flashers can be cut by elimination of events with negative or railed charges, or by cutting events with a row of adjacent (FEC) fired channels. Also we

[4]Flashing is a well known phenomenon in PMTs that are about to fail. Usually the flashes are quite intense due to internal arcing, likely due to gas or vapour buildup in the PMT.

[5]Channels often have negative charges in response to presumably large pulse heights. This wrap around effect is either due to the saturated integrator, or is a specific system response to the flasher pulse shape.

have shown that the flasher events fit at the PSUP and will mostly get eliminated in the reconstruction cut ($R < 550\,\mathrm{cm}$).

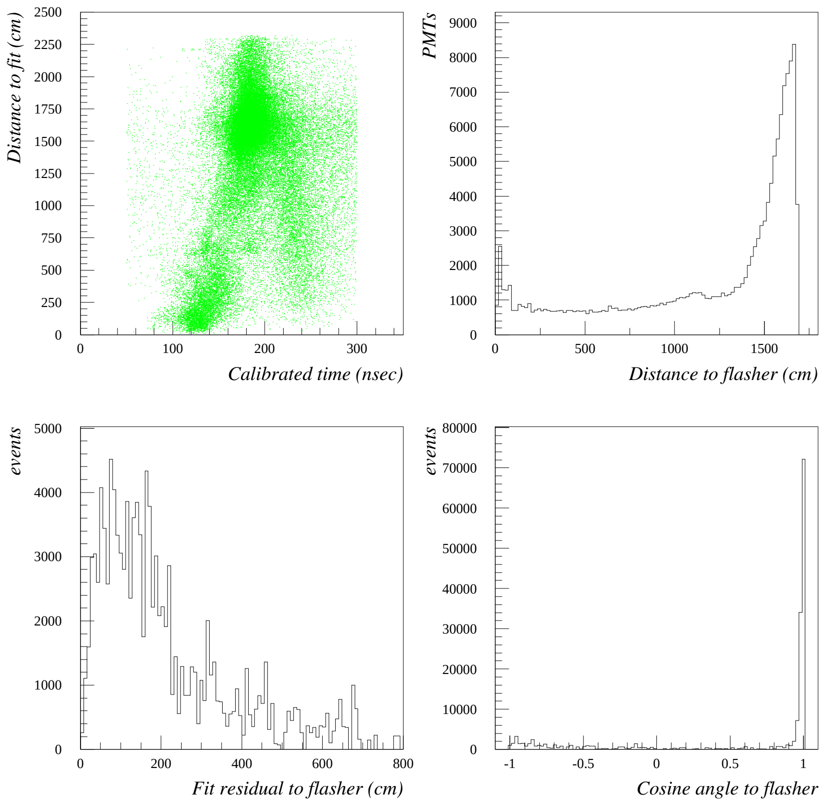

Figure 6.17: The distance of each PMT to the flasher identified by railed or negative charge versus the PMT time for several hundred flashers. The second plot is the distance projection. The third plot is the distance from the fitted position to the railed/negative charge PMT. The bottom right plot is the angle cosine between each PMT and the railed/negative charge PMT.

The time/distance topology for several hundred identified flasher events is plotted in figure 6.17, where the distance and time of all PMTs is plotted relative to the fitted position and time. We see most PMTs appear on the speed of light line with origin at 128 nsec. There is a large peak across the detector at 18 m and with a width corresponding to a light cone of about 40° half angle. There is a shadow band at late times which correspond to the time line for internal reflection from the outside of the AV. The small peak at 1150 cm is the AV tangent. There is also a peak very close to the flasher PMT which turns out to be significant. The PMTs near the flasher are either induced pickup, or are due to light reflecting off the AV. There is a class of flasher events (called silent flashers) where the flashing PMT pulse is not large enough to rail the channel or cause much induced pickup. Without the induced channels, the nearby hit PMTs are mostly out of time due to AV reflections and cause the fitter to reconstruct the event at the AV. From the time/distance topology we can see how this comes about. Most of the hits in the peak across the detector are degenerate in distance and don't contribute much to the fitter χ^2. Thus, if the near side PMT hits are reflected off the AV, then moving the fit position to the AV reduces the χ^2.

We now develop a modification to the fitter that can properly reconstruct flasher events for the very small number of flashers that may pass all the conventional cuts. The algorithm works as a pre-processor to the time fitter by adjusting the hit times of the reflected PMT hits to account for the extra transit distance. The essential ingredient is a model for finding the reflected PMT hits. The method uses the funnel nature of the flasher light, by taking the average PMT position vector as the centre of the funnel. The point on the PSUP opposite the average position vector then becomes the predicted flash origin. The distance of each PMT from the flash origin is calculated. We then adjust the times for all PMTs whose distance is less than a PSUP cord tangent to the AV. The time adjustment is the time assuming a reflection path off the AV minus the straight path time. Fortunately, this time adjustment is insensitive to the predicted flasher origin. This fitter is called the reflection fitter, since it works by correcting for reflected light trajectories. Results for simple Monte Carlo flashers are plotted in figure 6.18; none of the 10,000 events are reconstructed within the AV.

The reflection fitter was tested on a set of "fake" silent flashers from NHIT run 567. The large sample of fake silent flashers was generated by removing the railed and induced charge hits from flasher events so that they deliberately failed the usual cuts.

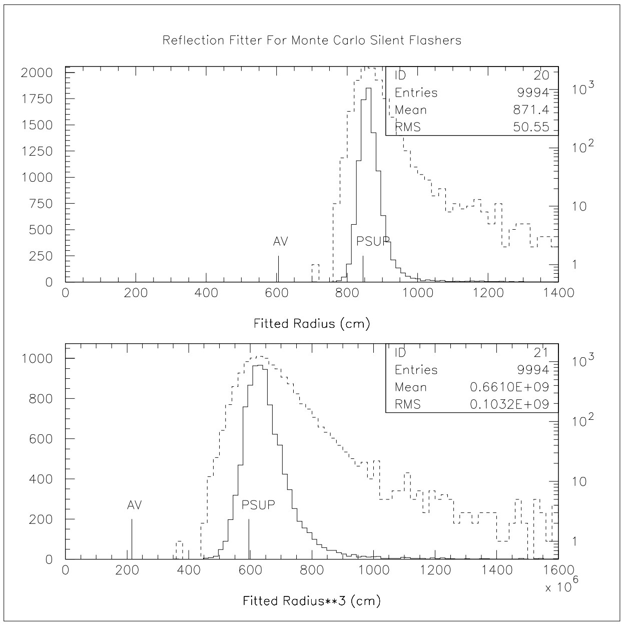

Figure 6.18: Reconstructed radius using the reflection fitter for Monte Carlo flashers.

The reconstructed radius plot is figure 6.19. The reflected fitter was 93.4% efficient for a cut at 600 cm (AV) and 97.3% efficient for a 550 cm cut (fiducial).

Figure 6.20 is the reflection fitter results for the silent flashers in run 570 that did pass the regular cuts (the events all fitted with radius less than 700 cm with the regular time fitter because that was one of the cuts). Out of the 32 events the reflection fitter reconstructed 30 outside the AV. The fitter was then improved by using a peak searching algorithm to identify the funneled light in the event time histogram. The new reconstruction for the 32 silent flasher events in run 570 is given in figure 6.21. The events are now more closely grouped at the PSUP, and none reconstruct within the AV.

The reflection fitter was tested on a sample of Monte Carlo high energy gammas from the cavity walls. The detected events are mostly from conversion with the AV acrylic. The reconstruction distribution in radius is presented in figure 6.22. The fitter does not appear to bias non-flasher events. This is expected as non-flasher events will not have many hits directly opposite the mean hit location. In fact, even for regular

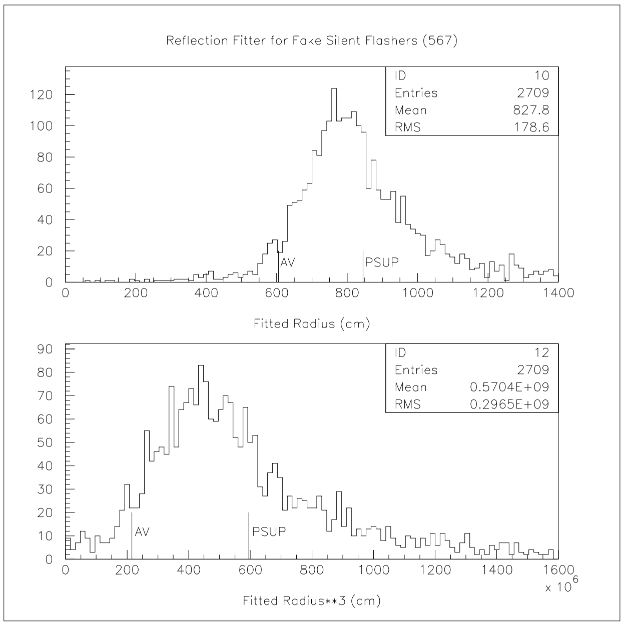

Figure 6.19: Reconstructed radius using the reflection fitter for fake silent flashers.

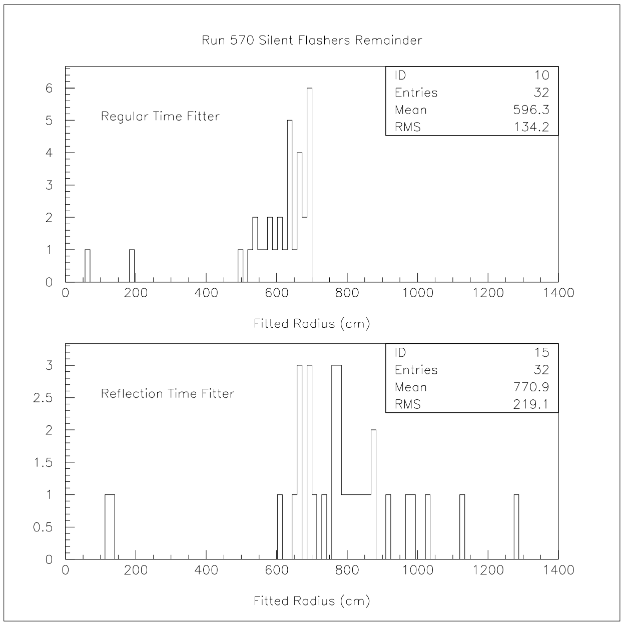

Figure 6.20: Reconstructed radius using the time fitter and the reflection fitter for run 570 silent flashers.

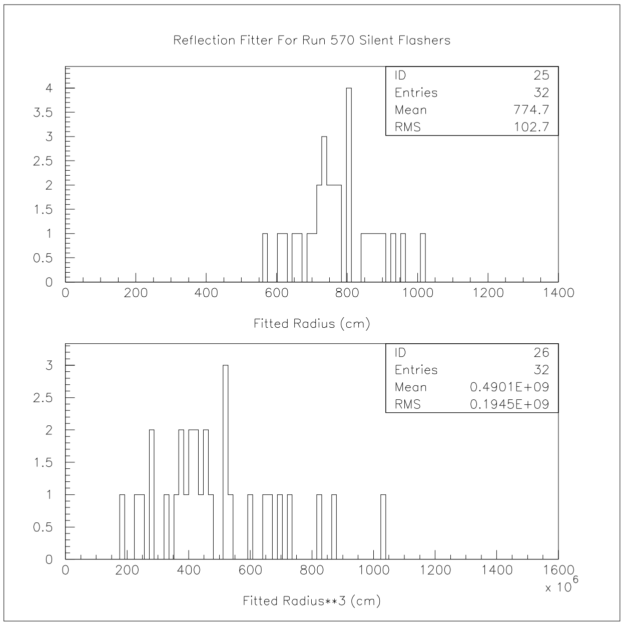

Figure 6.21: Reconstructed radius using the improved reflection fitter for run 570 silent flashers.

events, the hits opposite the mean location are usually reflected or scattered light, and will be brought closer in time by the time adjustment. This suggests the possibility of developing a generalized reflection fitter.

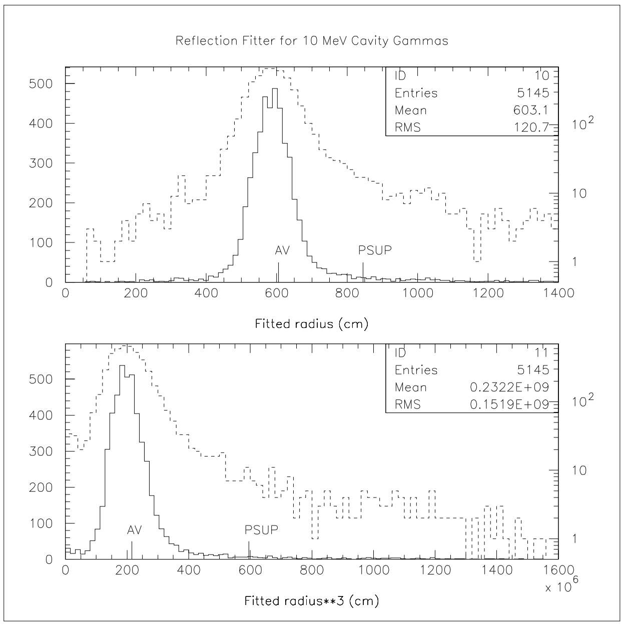

Figure 6.22: Reconstructed radius using the reflection fitter for Monte Carlo cavity gammas.

Chapter 7

Conclusions and Discussion

In this thesis we have presented the hardware, software, and methodology for the calibration of the Sudbury Neutrino Observatory. The calibration begins with the electronics and PMT calibrations: charge pedestals and slopes, time offset, times slopes and slewing corrections, PMT gains and efficiencies. The position and angular resolution is then obtained by reconstruction of the laserball and ^{16}N sources. These will be followed by optical attenuation and scattering measurements. The optical measurements will be used to adjust the Monte Carlo and for long term detector monitoring. The optical measurements are also used in the detector calibration function, which corrects the detector position and direction dependence for electrons and gammas. The calibration function will be scaled to the absolute energy response by using the ^{16}N gamma source, and later the ^{8}Li and pT sources. The energy resolution can then be measured with gamma ray sources. Finally, neutron or background sources (eg. Th) can be used can be used to measure these specific efficiencies.

In this thesis we have accomplished the following

1. We have reviewed the solar neutrino problem and current experiments. Despite new experimental results, the scientific impact for SNO has continued to increase. This is due to SNO's unique ability to separately measure the neutral current neutrino reaction and the energy spectrum for the charged current reaction.

2. We have used the SNO Monte Carlo to fully characterize the detector response,

and have provided parameterizations for the sensitivity, energy resolution, position and angular resolution, and systematic fitter effects.

3. Calculation of the ^{8}B neutrino spectrum has been reviewed. The expected spectrum for SNO has been calculated, along with spectra for the best fit MSW oscillation parameters.

4. A nitrogen/multi-dye laser diffuser ball (laserball) calibration system has been designed, fabricated, installed underground, and tested. The laserball delivers short (1 nsec σ) pulses pseudo-isotropically in to the detector with 5 wavelengths from $337 - 500$ nm, 20 nm bandwidth, and pulse rates up to 50 Hz. The laser is shielded to prevent RF pickup at the PMTs, and operates remotely via the DAQ or any computer TCP/IP client.

5. Optical absorption, reflections, scattering and the PMT response have been studied in detail, and methods developed to measure the important optical parameters using SPE time histograms. Algorithms have been developed, with SNOMAN driver tools, for the extraction of optical attenuation coefficients, water scattering length and PMT relative efficiencies. Software has also been developed for the SNO event display to use the optical algorithms to provide a graphical on-line calibration.

6. We have developed detector calibration functions for electrons and gammas that corrects for the position and direction NHIT response. The calibration function uses simplified or parameterized distributions for the Čerenkov output and detector geometry. The calculation is rapid and can be built in to a neutrino spectrum analysis. Also the derivatives with respect to any of the inputs can be calculated to enable a proper uncertainty calculation.

7. The laserball system has been used in airfill to calibrate the PMTs for electronics commissioning and other airfill detector testing and analysis. The PMTs were calibrated for charge and time, and a method developed to obtain the SPE gains and thresholds.

8. The method of using the time histograms to measure optical properties was shown to be feasible, by investigating some of the optics from the first airfill laserball runs.

9. The calibrated time and charge were used to characterize the SNO PMT flasher events, and develop cuts.

10. The performance of the event fitters for airfill were tested. We then developed a reflection biased version of the time fitter (the reflection fitter) to improve the reconstruction of silent flasher events.

The next six months will be an important time for SNO. As the detector fills with water it will be imperative that the detector can be calibrated and the efficiencies of the charge and reconstruction cuts established. There is further work to be done in installing the algorithms developed in this thesis into the production version of SNOMAN, ready for testing when the detector is filled. Almost certainly the optical algorithms will require tuning at that time. Specifically, the optical algorithms make assumptions that large subgroups of PMTs have the same average efficiencies, in order that the relative PMT efficiencies can be determined for the optical analysis. These will likely need to be redistributed by crate after the correct gains have been established.

The laser system should run without problems except for regular maintenance. A system manual is provided which sets out a maintenance schedule and all the procedures [80]. The newly acquired acrylate Superguide-G silica fibre (Fiberguide Ind.) should be installed to improve the short wavelength fluorescence in the present fibres. Upgrades to the laser system maybe considered to provide shorter wavelengths ($300 - 340$ nm). One possibility is to use one of the dye resonators (no. 4) with a frequency doubling crystal, for example Rhodamine 610 can be used to produce 305 nm radiation. This would require a beam expander and diffraction grating to reduce the dyelaser bandwidth. A second possibility is to install a high power Hg lamp with a 313 nm line filter and beam modulator to couple in to the present fibre optic system.

After calibration with the ^{16}N source, the calibration response function can optimized. There are adjustable parameters in the calibration function that relate to the amount of scattered light accepted in the events. The PMT event time cuts will be optimized during the first ^{16}N calibration. This can be accomplished by setting a window around the prompt time peak such that the number of included PMTs as a fraction of the event NHIT is not a strong function of source position.

The idea of biasing the PMT times in the reflection fitter can be extended to a generalized reflection fitter applicable to water fill. Such a fitter may be useful for improved reduction of PMT $\beta - \gamma$ events, or other background events near the AV.

Appendix A

The Standard Solar Model

The standard solar model (SSM) was discussed in section 1.1, including the assumptions, iteration, convergence and uncertainties. We present in this appendix the main equations for the SSM and the thermonuclear reactions.

A model for stellar evolution is solved by iteration of the differential equation over spherical shells. Assuming hydrostatic equilibrium the force of gravity is everywhere balanced by radiation and thermal pressure. The gravitational pressure across a shell dr is

$$dP = -\frac{\rho(r)GM(r)}{r^2}\,dr \tag{A.1}$$

where ρ is the density and $M(r)$ the mass contained within the radius r. The mass increment across the shell is

$$dM = 4\pi r^2 \rho\, dr \tag{A.2}$$

while the energy generated within the shell is

$$dL = 4\pi r^2 \epsilon \rho\, dr, \tag{A.3}$$

where ϵ is the energy generation per unit mass by nuclear fusion. In equilibrium the integral over dL is the luminosity, which is equal to the total energy production rate.

In regions of high opacity (where the temperature gradient is small) the energy transport through a surface at radius r is [3]

$$L = -\frac{16\pi ac}{3\kappa\rho} r^2 T^3 \left(\frac{dT}{dr}\right) \tag{A.4}$$

where a is the Stefan-Boltzmann constant, c the speed of light and κ is the opacity. The opacity has a radiative and a conductive component, $\frac{1}{\kappa} = \frac{1}{\kappa_{\rm rad}} + \frac{1}{\kappa_{\rm cond}}$, although heat transport by electron conduction is negligible except at the solar centre [3]. The opacities, calculated from atomic physics, are quite complex and introduce uncertainties of several percent. In regions of low opacity, where the temperature gradient is larger than the adiabatic temperature gradient,

$$\frac{dT}{dr} > \frac{T}{P}\left(1 - \frac{C_v}{C_p}\right)\frac{dP}{dr}, \tag{A.5}$$

energy is transported by convection. The theory of stellar convective flow is still not well understood, and I use here some ideas from Harwit [90]. Plumes of buoyant material would transport heat at a rate

$$H = C\rho v\,\Delta T \tag{A.6}$$

where ΔT is the temperature difference between the convective cell and the surrounding medium. The velocity v can be given in terms of a mixing length λ

$$\begin{aligned} v &= \sqrt{2r\ddot{d}} \\ &= \left[\frac{2GM}{r^2}\,\frac{\Delta T}{T}\,\lambda\right]^{\frac{1}{2}} \end{aligned} \tag{A.7}$$

so that

$$H \sim C\rho\left(\frac{GM}{Tr^2}\right)^{\frac{1}{2}}\lambda^2\left(\frac{d\,\Delta T}{dr}\right)^{\frac{3}{2}} \tag{A.8}$$

where $d\,\Delta T/dr$ is taken to be the difference between the actual and the adiabatic gradient. The mixing length is usually scaled to the pressure height [12]

$$\lambda \equiv \alpha\left(\frac{d\,\log P}{dr}\right)^{-1} \tag{A.9}$$

with the mixing length parameter α calibrated in the model to match the surface temperature.

In the equation of state the pressure is the sum of the thermal and radiative pressure [3]

$$P = \frac{\rho kT}{m_H}\left(2X(r) + \frac{3}{4}Y(r) + \frac{1}{2}Z(r)\right)(1+D) + \frac{aT^4}{3} \tag{A.10}$$

where D is a correction for degeneracy of electrons and screening interactions and $aT^4/3$ is the radiation pressure. The number density is evaluated in terms of X, Y and Z which are the mass fractions of hydrogen, helium and heavy elements. Using the equation of state, and eliminating the opacity κ and energy production ϵ in terms of the thermodynamic variables, leaves four differential equations (A.1,A.2,A.3,A.4 or A.8) as functions of four variables (say P, T, L and Z). These equations are iterated from the initial conditions to the observed boundary conditions as discussed in section 1.1.

The reaction rate between two nuclei is the velocity integrated product of the cross section and flux

$$R_{12} = \int_0^\infty n_1 n_2 v \sigma(E) f(v)\, dv, \tag{A.11}$$

The distribution $f(v)$ is the Maxwell function since the nuclei are not degenerate, and v is the relative velocity

$$f(v) = v^2 T^{-\frac{3}{2}} \exp^{-\mu v^2/2kT}, \tag{A.12}$$

where μ is the reduced mass. The cross section is usually written in terms of an exponential Coulomb penetration factor and $1/v^2$ for the phase space overlap

$$\sigma(E) = \frac{S(E)}{E} \exp\left(\frac{-2\pi Z_1 Z_2 e^2}{hv}\right). \tag{A.13}$$

The factor $S(E)$ is a smoothly varying function that depends on the nuclear matrix element, and the value $S(0) = S_0$ is known as the cross-section factor or the astrophysical S-factor. The $\langle v\sigma \rangle$ integrand (A.11) has the form $\exp(-\frac{a}{v} - bv^2)$ where the Maxwell distribution decreases rapidly and the cross-section increases rapidly. Thus the integral is essentially zero except for a small overlap called the Gamow peak.

The energy released is then the Q-value of the reaction with the neutrino energy subtracted. The average energy per unit volume is

$$\epsilon_{12} = (Q_{12} - \langle q \rangle) R_{12}, \tag{A.14}$$

where $\langle q \rangle$ is the neutrino energy integrated over the emitted spectral shape.

Appendix B

The MSW Effect

If neutrinos have mass, then in general the weak flavour eigenstates will not be the mass eigenstates. The mass states can be transformed to the flavour states with a rotation matrix with a mixing angle, as in the CKM matrix. For two flavours it is

$$U = \begin{pmatrix} \cos\theta & \sin\theta \\ -\sin\theta & \cos\theta \end{pmatrix} \tag{B.1}$$

The following formalism is the same for 3 flavours, but gets more complicated. However, the two flavour oscillation treatment is usually justified, since the neutrino masses are expected to be hierarchical in order to explain both the solar neutrino problem and atmospheric neutrino data [11]. Then the level crossings will not interfere for MSW conversion in the sun or the earth. Note that while we discuss $\nu_e \longrightarrow \nu_\mu$ conversion, the mixing angle and Δm^2 may actually correspond to oscillation with ν_τ.

The equation of motion is given by the outward going solution of the Klein-Gordon equation

$$j\frac{d}{dt}\left|\nu_i\right\rangle_t = \frac{m^2}{2E}\left|\nu_i\right\rangle_t \tag{B.2}$$

for mass states $i = 1, 2$ with the same 3-momentum (and practically the same energy). The propagation in the flavour basis is then written

$$j\frac{d}{dt}\left|\nu_\alpha\right\rangle_t = \frac{1}{2E}U\begin{pmatrix} m_1^2 & 0 \\ 0 & m_2^2 \end{pmatrix}U^{-1}\left|\nu_\alpha\right\rangle_t \tag{B.3}$$

Using solutions $\left|\nu_i\right\rangle_t = e^{-jE_it}\left|\nu_i\right\rangle$ we evaluate the survival probability

$$P(\nu_e \longrightarrow \nu_e)_t = \left|\left\langle\nu_e(0)\right|\nu_e(t)\rangle\right|^2$$

$$= \quad 1 - \frac{1}{2}\sin^2 2\theta\,[1 - \cos(E_2 - E_1)t]\,. \tag{B.4}$$

The probability can be written as a function of the distance L

$$P(\nu_e \longrightarrow \nu_e) = 1 - \sin^2 2\theta \sin^2\left(\frac{L}{L_v}\right) \tag{B.5}$$

where L_v is the characteristic vacuum oscillation length

$$L_v = \frac{2\pi}{|E_2 - E_1|} = \frac{4\pi E}{\Delta m^2} = 2.48\left(\frac{E}{\mathrm{MeV}}\right)\left(\frac{\mathrm{eV}^2}{\Delta m^2}\right) \text{ meters.} \tag{B.6}$$

If L_v is roughly the earth-sun distance ($D_\odot$), then $P(\nu_e \longrightarrow \nu_e)$ can take any value from 0-1 and thus provides a probe of Δm^2 down to $10^{-12}\,\mathrm{eV}^2$ for solar neutrino energies. If L_v is much larger than the earth-sun distance then $P(\nu_e \longrightarrow \nu_e) = 1$, while if L_v is much smaller the phases become totally mixed and $P(\nu_e \longrightarrow \nu_e) = 1 - \frac{1}{2}\sin^2 2\theta$.

While the "just so" case of $L_v \approx D_\odot$ can provide spectral distortions, the coincidence is unlikely. Otherwise, even with an unexpectedly large mixing angle, we can only achieve an overall factor of two flux suppression, which does not solve the solar neutrino problem.

In a dense medium, electron neutrinos have a larger cross-section for electron scattering than $\nu_{\nu,\tau}$, due to the weak charged current. Thus, in a neutrino mass eigenstate of mixed flavour the electron component will gain an extra phase shift which alters the oscillation probability. In the flavour basis the electron neutrino therefore has an extra potential $\sqrt{2}G_F n_e$ in the Hamiltonian. The equation of motion is then

$$j\frac{d}{dt}\,|\nu_\alpha\rangle_t = \frac{1}{2E}\left[U\begin{pmatrix} m_1^2 & 0 \\ 0 & m_2^2 \end{pmatrix}U^{-1} + \begin{pmatrix} 2\sqrt{2}G_F n_e E & 0 \\ 0 & 0 \end{pmatrix}\right]|\nu_\alpha\rangle_t\,. \tag{B.7}$$

We rotate back to the mass basis with a matrix U_m defined with an angle θ_m (as in equation B.1), we have then

$$\begin{aligned} j\frac{d}{dt}\,|\nu_i\rangle_t &= \frac{1}{2E}U_m^{-1}\left[Um^2U^{-1} + \begin{pmatrix} \beta & 0 \\ 0 & 0 \end{pmatrix}\right]U_m\,|\nu_i\rangle_t \\ &= \frac{M^2}{2E}\,|\nu_i\rangle_t \end{aligned} \tag{B.8}$$

where $\beta = 2\sqrt{2}G_F E n_e$. Diagonalizing M^2 we obtain the eigenvalues

$$2M^2_{2,1} = \beta \pm \sqrt{(\beta - \Delta m^2 \cos 2\theta)^2 + (\Delta m^2 \sin 2\theta)^2} \tag{B.9}$$

and matrix unitarity provides the rotation angle in the medium

$$\tan 2\theta_m = \frac{\Delta m^2 \sin 2\theta}{\Delta m^2 \cos 2\theta - \beta} \tag{B.10}$$

The eigenvalues are plotted in figure B.1.

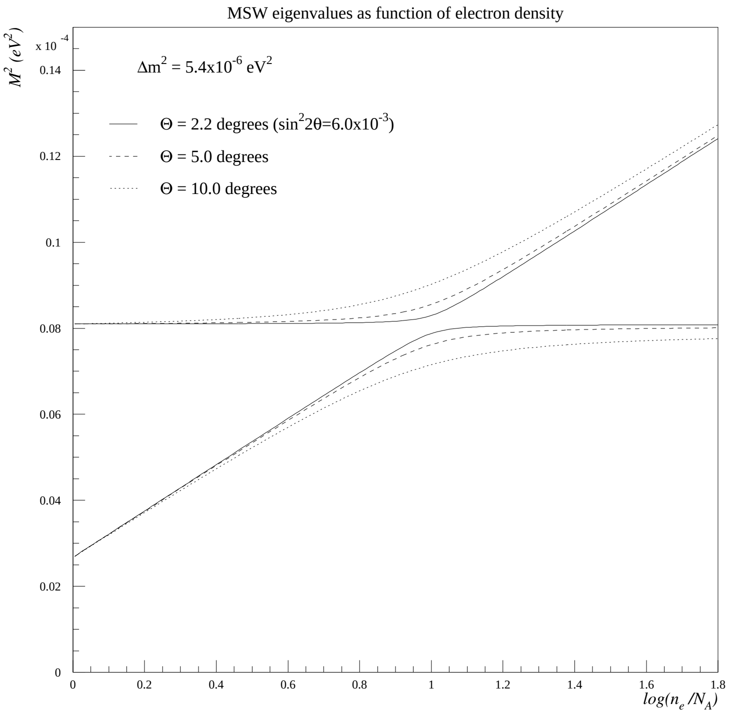

Figure B.1: The mass eigenvalues for the MSW effect plotted as a function of electron density ($\log(n_e/N_A)$ where N_A is Avogadro's number). An arbitrary mass ($5.4 \times 10^{-6}\,\mathrm{eV}^2$) is added to make the eigenvalues positive in vacuum.

As before we can define an oscillation length

$$L_m = \frac{L_v}{\sqrt{(\beta/\Delta m^2 - \cos 2\theta)^2 + \sin^2 2\theta}} \tag{B.11}$$

and the survival probability

$$P(\nu_e \longrightarrow \nu_e)_t = 1 - \frac{1}{2}\sin^2 2\theta_m \left(1 - \cos\left(\frac{2\pi t}{L_m}\right)\right). \tag{B.12}$$

Note that this equation would only be applicable when the electron density (in the β term) is constant, which is not the case for the sun or earth. However, from equation B.10 we have

$$\sin^2 2\theta_m = \frac{(\Delta m^2)^2 \sin^2 2\theta}{\sqrt{(\beta - \Delta m^2\cos 2\theta)^2 + (\Delta m^2 \sin 2\theta)^2}} \tag{B.13}$$

so that when $\beta \sim \Delta m^2 \cos 2\theta$ we get $\sin^2 2\theta_m \approx 1$ and $L_m \approx L_v/\sin 2\theta$. This is the resonance condition, and for a large L_v (small Δm^2 or large E) we can get complete depletion of ν_e. We see that the resonance depends on both the neutrino energy and the electron density. In particular, significant oscillation can occur in the sun if neutrinos are produced in a region where the density is greater than

$$n_e > \frac{\Delta m^2 \cos 2\theta}{2\sqrt{2}G_F E} \tag{B.14}$$

so that the resonance region is crossed before the solar surface. Furthermore, the the resonance condition must be met for at least several oscillation lengths. This means that at resonance the density must be only slowly varying, which is called the adiabatic condition. From equation B.13 we can obtain the half width of the resonance ($\sin^2 2\theta_m = \frac{1}{2}$) as

$$|\delta\beta| = \Delta m^2 \sin 2\theta \tag{B.15}$$

so that the resonance distance $d = |\delta n_e| \frac{dx}{dn_e}$ is

$$d = \frac{dx}{dn_e}\frac{|\delta\beta|}{2\sqrt{2}G_F E} = \frac{n_e \tan 2\theta}{|dn_e/dx|}. \tag{B.16}$$

The oscillation length at resonance is $L_m = 4\pi E/\Delta m^2 \sin 2\theta$ so that the adiabatic condition $d \ll L_m$ gives

$$\gamma \equiv \frac{\Delta m^2 \sin 2\theta \tan 2\theta}{2E\left|\frac{1}{n_e}\frac{dn_e}{dx}\right|_r} \ll 1 \tag{B.17}$$

where γ is defined as the adiabatic parameter.

Parke has provided a formula for calculating the survival probability with non-adiabatic corrections due to level crossing jumps between the eigenstates [37]. In figure B.1 the eigenvalues are close together at resonance if the adiabatic condition above is not met. Then the jump probability becomes large, which is known as level crossing. The Parke formula is

$$P(\nu_e \longrightarrow \nu_e) = \frac{1}{2} + (1 - P_c)\cos 2\theta \cos 2\theta_m. \tag{B.18}$$

The tunneling probability was first calculated by Landau and Zener in atomic collisions for a linear density variation, where they obtained $P_c = \exp(-\frac{\pi}{2}\gamma)$ [37]. In a similar way, the jump probability can be worked out for other density functions. The solar density is very well represented by an exponential in radius, which leads to the jump probability

$$P_c = \frac{\exp(-\frac{\pi}{2}\gamma F) - \exp(-\frac{\pi}{2}\gamma(F/\sin^2\theta))}{1 - \exp(-\frac{\pi}{2}\gamma(F/\sin^2\theta))} \tag{B.19}$$

with $F = 1 - \tan^2\theta$. The formula B.18 was plotted in chapter 1 figure 1.8 for the present best fit values of Δm^2 and $\sin^2 2\theta$.

Bibliography

[1] H.H. Chen, Phys. Rev. Lett. 55 (1985) 1534. H.H. Chen, Nucl. Instr. and Meth. **A264** (1988) p48. G.T. Ewan *et al*, *Sudbury Neutrino Observatory Proposal*, SNO-1987-12 (1987).

[2] SNO Collaboration, *Scientific and Technical Description of the Mark-II SNO Detector*, SNO-1989-15 (1989). G.T. Ewan, Nucl. Instr. and Meth. **A314** (1992) p373. G.T. Ewan *et al*, Physics in Canada **48** (1992) p112. A.B. McDonald, in *Proceedings of the 9th Lake Louise Winter Institue*, ed. A. Astbury *et al.*, World Scientific (1994) p1.

[3] J.N. Bahcall, *Neutrino Astrophysics*, Cambridge University Press (1989).

[4] J.N. Bahcall and H. Bethe, Phys. Rev. D **44** (1991) p2962.

[5] Particle Data Group, *Review of Particle Physics*, Eur. Phys. J. C. **3** 1-794.

[6] F. Boehm and P. Vogel, *Physics of Massive Neutrinos*, Cambridge University Press (1987).

[7] B. Schwarzschild, Physics Today, **51** 6 (1998) p17.

[8] K. Zuber, Phys. Rep. **305** (1998) 295.

[9] J.N. Bahcall, P.I. Krastev and A. Yu. Smirnov, preprint hep-ph/9807216 (1998).

[10] V. Berezinsky *et al*, Phys. Lett. **B365** (1996) p185. G. Fiorentini *et al*, Phys. Rev. D **49** (1994) p6298. N. Hata and P. Langacker, Phys. Rev. D **50** (1994) p632.

[11] G.L. Fogli *et al*, Phys. Rev. D **56** (1997) p4365.

[12] S. Turck-Chièze *et al*, Astrophys. J. **335** (1988) p415. S. Turck-Chièze and I. Lopes, Astrophys. J. **408** (1993) p347. S. Turck-Chièze *et al*, Physics Reports **230** (1993) p57.

[13] J.N. Bahcall and R.N. Ulrich, Rev. Mod. Phys. **60** (1988) p297.

[14] J.N. Bahcall and M.H. Pinsonneault, Rev. Mod. Phys. **64** (1992) p885.

[15] A.S. Brun, S. Turck-Chièze and P. Morel, Astrophys. J. **506** (1998) p.

[16] C.R. Proffitt, Astrophys. J. **425** (1994) p849.

[17] J.N. Bahcall and M.H. Pinsonneault, Rev. Mod. Phys. **67** (1995) p781.

[18] J.N. Bahcall, S. Basu and M.H. Pinsonneault, Phys. Lett. **B433** (1998) p1.

[19] A. Dar and G. Shaviv, Astrophys. J. **468** (1996) p933.

[20] J. Christensen-Dalsgaard *et al.*, Science **272** (1996) p1286.

[21] S. Basu *et al*, Mon. Not. R. Astron. Soc. **292** (1997) p234.

[22] F. Hill *et al*, Science **272** (1996) p1292.

[23] S. Turck-Chièze *et al*, Sol. Phys. **175** (1997) p247.

[24] E. Adelberger *et al*, Rev. Mod. Phys. **70** (1998) p1265.

[25] J.N. Bahcall, M. Fukugita and P.I. Krastev, Phys. Lett. **B374** (1996) p1.

[26] R. Davis, Phys. Rev. Lett. **12** (1964) p303.

[27] J.N. Bahcall, Phys. Rev. Lett. **12** (1964) p300. J.N. Bahcall, Phys. Rev. B **135** (1964) p137.

[28] R. Davis, Prog. Part. Nucl. Phys. **32** (1994) p13. B.T. Cleveland *et al*, Nucl. Phys. (Proc. Suppl.) **B38** (1995) p47. B.T. Cleveland *et al*, Astrophys. J. **496** (1998) p505.

[29] K.S. Hirata *et al*, Phys. Rev. Lett. **65** (1990) p1297; **66** (1991) p9. K.S. Hirata *et al*, Phys. Rev. D **44** (1991) p2241; **45** (1992) p2170. Y. Fukuda *et al*, Phys. Rev. Lett. **77** (1996) p1683.

[30] A. Suzuki, in *Physics and astrophysics of Neutrinos*, ed. M. Fukugita and A. Suzuki, Spinger-Verlag, Tokyo (1994) p414. Y. Totsuka, Nucl. Phys. (Proc. Suppl.) **B48** (1996) p547. K. Inoue, in *TAUP'97 5th Intermnational Workshop on Topics in Astroparticle and Underground Physics*, Gran Sasso, Italy (1997) in Proceedings. Y. Fukuda *et al*, Phys. Rev. Lett. **81** (1998) p1158. Y. Suzuki *et al*, Nucl. Phys. **B** *Proceedings Neutrino 98*, ed. Y. Suzuki and Y. Totsuki, Takayama, Japan (1998).

[31] Y. Fukuda *et al*, Phys. Rev. Lett. **81** (1998) p1562. Y. Fukuda *et al*, Phys. Lett. **B433** (1998) p9.

[32] J.N. Bahcall, Phys. Rev. C. **56** (1997) p3391.

[33] P. Anselmann *et al*, Phys. Lett. **B285** (1992) p376; **B314** (1993) p445; **B327** (1994) p377; **B342** (1995) p440; **B357** (1995) p237; **B361** (1996) p235E. W. Hampel *et al*, Phys. Lett. **B388** (1996) p384. T. Kirsten *et al*, Nucl. Phys. **B** *Proceedings Neutrino 98*, ed. Y. Suzuki and Y. Totsuki, Takayama, Japan (1998).

[34] A.I. Abazov *et al*, Phys. Rev. Lett. **67** (1991) p3332. J.N. Abdurashitov *et al*, Phys. Lett **B328** (1994) p234. J.N. Abdurashitov *et al*, Phys. Rev. Lett. **77** (1996) p4708. V. Gavrin *et al*, Nucl. Phys. **B** *Proceedings Neutrino 98*, ed. Y. Suzuki and Y. Totsuki, Takayama, Japan (1998).

[35] B. Pontecorvo, Sov. Phys. JETP **7** (1958) p172; **26** (1968) p989.

[36] S.P. Mikheyev and A.Yu. Smirnov, Sov. J. Nucl. Phys. **42** (1985) p913. S.P. Mikheyev and A.Yu. Smirnov, Nuovo Cimento **9C** (1986) p17. L. Wolfenstein, Phys. Rev. D **17** (1978) p2369; **20** (1979) p2634.

[37] S.J. Parke, Phys. Rev. lett. **57** (1986) p1275. H.A. Bethe, Phys. Rev. lett. **56** (1986) p1305. W.C. Haxton, Phys. Rev. lett. **57** (1986) p1271. W.C. Haxton, Phys. Rev. D **35** (1987) p2352; **36** (1987) p2283. T.K. Kuo and J. Pantaleone, Rev. Mod. Phys. **61** (1989) p937.

[38] A. Dar and S. Nussinov, Particle World **2** (1991) p117.

[39] S.M. Bilenky and C. Giunti, preprint hep-ph/9407379 (1994). S. Parke, Phys. Rev. lett. **74** (1995) p839.

[40] A. Cumming and W.C. Haxton, Phys. Rev. Lett. **77** (1996) p4286.

[41] M.M. Guzzo, A. Masiero and S.T. Petcov, Phys. Lett. **B260** (1991) p154. P.I. Krastev and J.N. Bahcall, Proceedings Symposium of FCNC (1997) UCLA, Santa Monica.

[42] K.S. Hirata *et al*, Phys. Rev. Lett. **58** (1987) p1490.

[43] R.S. Raghavan, Science **267** (1995) p45. G. Alimonti *et al*, Nucl. Instr. and Meth. **A406** (1998) p411.

[44] M. Apollonio *et al*, Phys. Lett. **B420** (1998) p397.

[45] C. Athanassopoulos *et al*, Phys. Rev. C **58** (1998) p2489. C. Athanassopoulos *et al*, Phys. Rev. Lett. **81**, (1998) p1774.

[46] B. Armbruster *et al*, Phys. Rev. C **57** (1998) p3414.

[47] J. Altegoer *et al*, Phys. Lett. **B431** (1998) p291.

[48] K. Daum *et al*, Z. Phys. **C66** (1995) p417.

[49] M. Aglietta *et al*, Europhys. Lett. **8** (1989) p611.

[50] R. Becker-Szendy *et al*, Phys. Rev. D **46** (1992) p3720.

[51] W.W.M. Allison *et al*, Phys. Lett. **B391** (1997) p491.

[52] C. J. Jillings *et al.*, Nucl. Instr. and Meth. **A373** (1996) p421.

[53] G. Doucas *et al.*, Nucl. Instr. and Meth. **A370** (1995) p579.

[54] T. Ekenberg *et al.*, IEEE Nuclear Science Symposium and Medical Imaging conference, IEEE Conference Record, **1**, (1995) 30. T. Ekenberg *et al.*, Transactions on Nuclear Science, **42**, (1995) 925.

[55] P. Skensved and B.C. Robertson, *Summary of Backgrounds in SNO*, SNO-STR-94-013 (1994).

[56] B.P. Barber *et al*, Phys. Rep. **281** (1997) 65.

[57] Y. Sato, N. Takahashi and S. Sato, Jpn. J. Appl. Phys. **35**, 7A (1996) L838.

[58] B. Sur *et al*, Bull. Am. Phys. Soc. **39**, (1994) 1389.

[59] A.W.P. Poon *et al.* in Particles and Cosmology, ed. E.N. Alexeev, V.A. Matveev, Kh. S. Nirov, V.A. Rubakov, World Scientific, page 248 (1996).

[60] L.S. Erhardt, *A High Energy Gamma Ray Calibration Source for SNO*, M.Sc. Thesis, Queen's University (1994).

[61] F. Dalnoki-Veress, *Investigation of the Triggered Source Technique for the Calibration of SNO*, M.Sc. Thesis, Carleton University (1996).

[62] F.C. Barker, Aust. J. Phys. **42** (1989) p25. E.K. Warburton, Phys. Rev. C. **33** (1986) p303. D.H. Wilkinson and D.E. Alburger, Phys. Rev. Lett. **26** (1971) p1127.

[63] J.N. Bahcall and B.R. Holstein, Phys. Rev. C. **33** (1986) p2121.

[64] J. Napolitano, S.J. Freedman and J. Camp, Phys. Rev. C. **36** (1987) p298.

[65] J.N. Bahcall *et al.*, Phys. Rev. C. **54** (1996) p411.

[66] L. De Braeckeleer, preprint (1998) *Not yet available.*

[67] G. Jonkmans, I.S. Towner and B. Sur, Phys. Rev. C. **58** (1998) p1278.

[68] F.J. Kelly and H. Überall, Phys. Rev. Lett. **16** (1966) p145.

[69] S.D. Ellis and J.N. Bahcall, Nucl. Phys. **A114** (1968) p636.

[70] S. Ying, W. C. Haxton, and E.M. Henley, Phys. Rev. C. **45** (1992) p1982. K. Kubodera and S. Nozawa, Int. J. Mod. Phys. **E3** (1994) p101.

[71] J.N. Bahcall and E. Lisi, Phys. Rev. D. **54** (1996) p5417.

[72] M.D. Lay, D.L. Wark and N. West, *It's Alive – The Birth of SNOMAN*, SNO-STR-91-077 (1991). T. Anderson *et al.*, *SNOMAN User Guide*, SNO Internal Document (1998).

[73] P. Skensved, private communication (1996).

[74] M. Thorman *et al.*, *submitted to NIM*, (1998).

[75] W.H. Press *et al.*, *Numerical recipes*, Cambridge University Press, Cambridge (1986).

[76] J.N.Bahcall and E. Lisi, neutrino-deuterium cross-section code is kindly made available at J.N. Bahcall's WWW site http://www.sns.ias.edu/~jnb/.

[77] L.P. Boivin *et al.*, Appl. Optics **25** (1986) p877.

[78] E.D. Earle and D. Sinclair, Acrylic transmission measurements were made at AECL Chalk River Laboratory for the SNO collaboration (1995).

[79] M.D. Lay, *Creation and Detection of Čerenkov Light in the Sudbury Neutrino Observatory*, PhD. Thesis, Oxford (1994).

[80] R.J. Ford, *System Manual for the SNO N_2/Dye Laser*, SNO-STR-96-056 (1997).

[81] *LN203C Operator's Manual*, Laser Photonics, Inc., Orlando, Florida (1991).

[82] J.T. Verdeyen, *Laser Electronics*, Prentice-Hall, New Jersey (1989).

[83] P.W. Milonni and J.H. Eberly, *Lasers*, Wiley, New York (1988).

[84] G. Keiser, *Optical Fiber Communications, 2nd Edition*, McGraw-Hill, New York (1991).

[85] J. Gowar, *Optical Communications Systems*, Prentice-Hall, London (1984).

[86] J.W. Fleming, Appl. Opt. **23** (1984) p4486.

[87] M.E. Moorhead, N.W. Tanner and A.P. Ferraris, *Reflections from a Bialkali Photocathode*, SNO-STR, Oxford (1988).

[88] C. Waltham *et al.* Appl. Opt. **33** 31 (1994) p7536.

[89] H.C. van de Hulst, *Light Scattering by Small Particles*, Dover, New York (1981).

[90] M. Harwit, *Astrophysical Concepts*, Concepts, Ithaca, NY (1982).

Curriculum Vitae

Name:	Richard James Ford
Place and Year of birth:	Colchester, England, 1968
Education:	Ph.D, Experimental High Energy Physics Queen's University, Kingston, Ont. 1998
	Master of Science, Physics Queen's University, Kingston, Ont. 1993
	Bachelor of Science (Co-op Honours Applied Physics, Mathematics Minor) University of Waterloo, Waterloo, Ont. 1991
	Ontario Secondary School Honours Graduation Diploma Orangeville District Secondary School, Ont. 1985
Experience:	Teaching and Research Assistant (Physics Department) Queen's University, Sept 1991 - Sept 1998
	Technical Assistant (Simulator Services) Ontario Hydro, Sept 1989 - Sept 1990
	Research Assistant (Data Acquisition Division) Canada Centre for Remote Sensing, Sept 1988 - Apr 1989
	Laboratory Technician/Research Assistant Chembond Limited, Jan 1988 - May 1988
Awards:	Queen's Graduate Award 1991-1996 Ontario Graduate Scholarship 1995-1996 NSERC PGSB (1993-1995) Reinhardt Fellowship (1993-1994)